

Investigations of Nonlinear Surface-Wave Phenomena and Anisotropic Photoluminescence of Nano-Film Structures via Two-Dimensional k -Space Spectroscopy

vorgelegt von

Diplom-Physiker Jan Heckmann
aus Frankfurt am Main

von der Fakultät II – Mathematik und Naturwissenschaften
der Technischen Universität Berlin
zur Erlangung des akademischen Grades

Doktor der Naturwissenschaften
Dr. rer. nat.

genehmigte Dissertation

Promotionsausschuss:

Vorsitzender: Prof. Dr. Andreas Knorr

Gutachterin: Prof. Dr. Ulrike Woggon

Gutachter: Prof. Dr. Kurt Busch

Gutachter: Dr. habil. Vasily Temnov

Tag der wissenschaftlichen Aussprache: 05.05.2017

Berlin 2017

Acknowledgements

I like to thank all those involved with the research presented in this work for their help, guidance, friendship, patience, and criticism. As head of the group Prof. Ulrike Woggon has initiated this research and provided the necessary infrastructure and funding. She has influenced this work with many ideas and recommendations and gave me the opportunity to present my work at workshops and conferences. I want to thank Prof. John Sipe and Prof. Elaine Li for their contribution to the analysis of the experimental results. Dr. Nicolai Grosse who has supervised many parts of this work by closely following the experiments in all stages. Discussions with him are always a pleasure and have proved to be crucial for a deeper understanding and progress of the presented work. Beyond that he has always encouraged me and supported this work as a supervisor, a colleague and a friend. Riccardo Scott for his commitment while proofreading this work, productive times in the lab and for being a close friend. Dr. Oliver Schöps for his incredible patience and for just being a good soul. Dr. Alexander Achtstein for the fruitful collaboration, illuminative discussions and constructive comments. I wish to thank all under-graduate students that have worked with me and contributed to the findings presented here, especially Marie-Elena Kleemann, Karsten Pufahl, Philipp Franz and Simon Kubitza. All members of the AG Woggon for productive discussions, good teamwork and the good times I spent in the group. Finally I want to thank my parents for their support and especially Kathrin and Charlotte who gave me the energy to write this thesis and always supported me with an incredible energy, love and endless tolerance.

Abstract

The investigation of surfaces and thin films is of particular interest in current research as it provides a basis for a multiplicity of applications such as waveguides, sensors, solar cells and optoelectronics. The origins of complex phenomena on surfaces and in thin films can be revealed by applying angle-resolved spectroscopy in two dimensions: the angle of incidence is scanned while analyzing the full emission spectrum in terms of exit angle and emission energy.

The interface of a metal layer and a dielectric can support collective electron plasma resonances, i.e. surface plasmon polaritons, which are accompanied by giant field enhancement while propagating along the interface. We characterize the Kretschmann and the Otto coupling configuration in terms of their coupling efficiency and their impact on the surface plasmon resonance as a function of wave-vector. Although being commonly considered as equivalent in terms of plasmonic coupling, we identify differing dependencies of their respective coupling efficiency on the coupling layer thickness and the excitation wavelength which is fundamental for sensing applications.

Provided that a metal layer is embedded in a symmetric cladding in terms of its dielectric function and the film thickness is reduced to the order of $\lambda/10$, modes from both interfaces can couple and propagate as long-range surface waves. Surprisingly, even intrinsically absorbing films support low-loss surface waves, whose propagation length can become arbitrarily long in the limit of vanishing film thickness. This phenomenon requires only that the material's dielectric function be predominantly imaginary over that particular range of optical frequencies.

Furthermore we show that the orientation of transition dipole moments inside thin monolayer films of effective media that contain oriented CdSe nano-platelets can be determined by applying k -space spectroscopy. Thus we determine electronic and dielectric contributions to the emission anisotropy and reveal the intrinsic nature of the directionality in the emission. We show that this phenomenon is related to the anisotropy of the electronic Bloch states that govern the transition dipole moment of the exciton.

Beyond the linear investigation of surfaces and thin films, 2D- k -space spectroscopy can provide an insight into the principles of nonlinear wave-mixing interactions. The role of surface plasmons in second harmonic generation, whether they act as field-enhancing catalysts or as quasiparticles converted in the interaction can be revealed by k -space spectroscopy: by way of the signature in k -space, we identify a nonlinear interaction where two surface plasmons annihilate to create a second-harmonic photon as well as the interaction of a plasmon and a photon by virtue of a degenerate three-wave mixing process.

We analyze the intrinsic origin of surface plasmon enhanced second harmonic generation in metal films by comparing the absolute nonlinear yield in attenuated internal reflection configurations to theoretical calculations based on the hydrodynamic model. A first estimation of the nonlinear parameters in the hydrodynamic model is given and the contributions of the bulk and surface source are determined, showing that the in-plane surface source is stronger than predicted.

For absorbing thin films however, we report the first evidence of field enhancement and long-range surface wave enhanced second harmonic generation. Here, we identify the out-of-plane surface source to have the strongest contribution to the second harmonic yield. As the nonlinear susceptibility of a material can greatly increase if the probing frequency approaches an absorption resonance, absorbing materials can indeed be considered as low-loss optical media for doing surface-wave optics in the nonlinear regime.

We show further, that, in contrast to the isotropic linear absorption, the two-photon absorption in oriented nano-platelets is highly anisotropic. This transition dipole orientation is dependent on the probabilities of the involved processes and their selection rules. We demonstrate that an additional silver layer covered with SiO_2 enables surface plasmon enhanced excitation of oriented nano-platelets, boosting the photoluminescent emission which is highly directed through coupling to the plasmonic mode. The combination of TPA and the plasmonic resonance even leads to further concentration of the absorption range as a function of excitation wave-vector.

In summary, this work has shown that 2D- k -space spectroscopy –as applied to solid surfaces, thin films and nano-particles– provides insight into the intrinsic material properties, as well as the surface- wave and radiation phenomena supported by these structures.

Zusammenfassung

Die Erforschung von Oberflächen und dünnen Schichten ist für die Forschung besonders interessant, da zahlreiche Anwendungen wie Wellenleiter, Sensoren, Solarzellen oder optisch-elektronische Geräte darauf beruhen. Die Ursprünge komplexer Oberflächenphänomene können durch winkelaufgelöste Spektroskopie in zwei Dimensionen aufgedeckt werden: während der Anregungswinkel durchgestimmt wird, wird das gesamte Emissionsspektrum als Funktion der Austrittswinkel und der Energie analysiert.

An der Grenzschicht zwischen einem Dielektrikum und einem Metall können Resonanzen kollektiver Elektronenschwingungen, so genannte Oberflächenplasmonen auftreten. Während ihrer Propagation entlang der Grenzschicht, werden sie von großen Feldverstärkungen begleitet. Wir charakterisieren die Otto- und die Kretschmann-Koppelanordnung bezüglich ihrer Kopplungseffizienz und ihres Einflusses auf die Oberflächenplasmon-Resonanz. Obwohl beide Anordnungen gewöhnlich als äquivalent in Bezug auf die Anregung von Plasmonen angesehen werden, identifizieren wir Unterschiede: die jeweiligen Koppleffizienzen unterscheiden sich deutlich in ihrer Abhängigkeit von der Dicke der Kopplungsschicht und der Anregungswellenlänge, was ausserordentlich wichtig für z.B. Sensoren ist.

Für dünne Metallschichten in dielektrisch symmetrischer Umgebung und unter der Voraussetzung sehr dünner Schichten von der Grössenordnung $\lambda/10$, können Moden von beiden Grenzschichten miteinander koppeln und sich als langreichweitige Oberflächenwellen ausbreiten. Überraschenderweise existieren solche Oberflächenwellen auch in absorbierenden Materialien, in denen die Propagationslänge sogar beliebig lang werden kann, wenn die Schicht infinitesimal dünn wird. Die einzige Bedingung ist, dass der Imaginärteil die dielektrische Funktion in dem entsprechenden Frequenzbereich dominiert.

Darüber hinaus zeigen wir, dass die Orientierung von Übergangsdipolmomenten in dünnen Monolayer-Schichten, die orientierte Nano-Plättchen beinhalten, durch k -Raum-Spektroskopie bestimmt werden kann. Wir unterscheiden elektronische von dielektrischen Beiträgen zur Emissions-Anisotropie und enthüllen den Ursprung gerichteter Emission, der auf die Anisotropie der elektronischen Bloch-Zustände zurückzuführen ist, die das Dipol-Übergangsmoment des Exzitons bestimmt.

Zusätzlich zur linearen Erforschung von Oberflächen und dünnen Schichten, gewährt 2D- k -Raum-Spektroskopie Einblick in die Grundlagen nichtlinearer Wellenmisch-Prozesse. Die Rolle des Oberflächenplasmons in der Wechselwirkung, ob es sich um einen feldverstärkenden Katalysator oder ein Quasiteilchen, das umgewandelt wird, handelt, kann

durch k -Raum-Spektroskopie geklärt werden. Durch ihre Signatur im k -Raum identifizieren wir das Entstehen eines frequenz-verdoppelten Photons durch die Auslöschung zweier Plasmonen und auch die Wechselwirkung eines Plasmons mit einem Photon in entarteten Drei-Wellen-Mischprozessen.

Wir analysieren weiter den intrinsischen Ursprung der Verstärkung von harmonischer Strahlung zweiter Ordnung durch die Anregung von Oberflächenwellen in metallischen Filmen, indem wir Absolutwerte der harmonischen Intensität, gemessen in veränderter Totalreflexion, mit Berechnungen basierend auf dem hydrodynamischen Modell vergleichen. Eine erste Abschätzung der nichtlinearen Parameter des hydrodynamischen Modells wird gegeben und die Beiträge von Quellen an den Oberflächen und innerhalb der Schicht werden bestimmt, wobei sich die in der Grenzschicht liegende Oberflächenquelle als Stärkste erweist.

Für absorbierende dünne Schichten erbringen wir den ersten Nachweis von Feldverstärkung durch langreichweitige Oberflächenwellen und daraus resultierende frequenz-verdoppelte Strahlung. Hier liefert die aus der Oberfläche heraus gerichtete Quelle den größten Beitrag. Da die Nichtlineare Suszeptibilität im Bereich einer Absorptions-Resonanz deutlich erhöht sein kann, kommen absorbierende Materialien tatsächlich für nichtlineare Optik mit langreichweitigen Oberflächenwellen in Frage.

Darüber hinaus zeigen wir, dass im Gegensatz zur isotropen linearen Absorption, die zwei-Photonen-Absorption in orientierten Nano-Plättchen stark anisotrop ist. Diese Orientierung der Übergangs-Dipolmomente führen wir auf die Übergangs-Wahrscheinlichkeiten und die Auswahlregeln zurück. Wir zeigen, dass eine zusätzliche Silberschicht, bedeckt mit einer dünnen SiO_2 -Schicht, die Oberflächen-Wellen-verstärkte Anregung orientierter Nano-Plättchen ermöglicht, was zu erhöhter Photolumineszenz führt, welche gleichfalls an die plasmonische Mode koppelt und stark gerichtet abstrahlt. Die Kombination von Zwei-Photonen-Absorption und Plasmonischen Resonanzen führt sogar zu noch stärkerer Konzentration der Absorption in Bezug auf ihren Wellen-Vektor.

Zusammenfassend haben wir gezeigt, dass 2D- k -Raum-Spektroskopie –angewendet auf Festkörper-Oberflächen, dünne Schichten und Nano-Teilchen– Einblicke in intrinsische Materialeigenschaften gewährt und die Analyse von Oberflächenwellen und damit zusammenhängender Strahlung ermöglicht.

Contents

1	Introduction	1
1.1	Nonlinear 2D k -Space Spectroscopy	3
1.2	Experimental Setup	10
2	Linear Analysis of Surface Plasmon Polaritons	11
2.1	Surface Plasmons at the Interface of Two Semi-Infinite Media	12
2.2	Attenuated Total-Internal-Reflection Coupling Configurations	15
2.2.1	Fabry-Pérot Model	16
2.3	Linear Measurements	18
2.3.1	Spectroscopic Measurements	18
2.3.2	Gaussian Beam Excitation	22
3	Theoretical Analysis of Second Harmonic Generation	27
3.1	SHG in the Hydrodynamic Model	27
3.1.1	Bulk Sources	29
3.1.2	Surface Sources	31
3.1.3	Harmonic Emission And Nonlinear Parameter	32
3.2	Mode analysis	33
4	Plasmon-Enhanced Second Harmonic Generation	35
4.1	Absolute Nonlinear Yield from ATR Coupling Configurations	36
4.1.1	Influence of the Nonlinear Parameters	40
4.1.2	Mode Analysis	43
4.2	Plasmon-Photon Wave Mixing in 2D- k -Space Spectroscopy	44
4.2.1	Enhanced SHG from Plasmon-Photon Interactions	45

4.2.2	Degenerate Three-Wave Mixing from Plasmon-Photon Interactions	49
5	Long-Range Surface Modes On Thin Films	57
5.1	Theoretical Analysis	59
5.2	Experimental Analysis	62
5.2.1	Spectroscopic Measurements	63
5.2.2	Excitation at High Intensities	64
5.2.3	Analysis of Propagation Lengths	67
5.2.4	Nonlinear Source Terms and Driving Electric Fields	68
6	Anisotropic Emission of Oriented Nano-Platelets	73
6.1	Analysis of Monolayer CdSe Nano-Particle Samples	74
6.1.1	Two-Dimensional k -space analysis	76
6.2	Experimental Results and Discussion	82
6.3	Analysis of Dielectric and Electronic Contributions	86
6.3.1	Microscopic Origin of the Anisotropy	87
7	k-Space Resolved Two-Photon Absorption in Oriented Nano-Platelets	91
7.1	Two-Photon Absorption Of Oriented CdSe Nano-Platelets	92
7.1.1	Sample Characterization And Experimental Setup	93
7.1.2	Transition Dipole Distributions for TPA Excitation	94
7.2	Surface Plasmon Enhanced TPA and Directed Emission	98
8	Conclusion	103
	Publications	109
A	SHG in the Hydrodynamic Model	111
A.1	Conventions	111
A.2	The linear fields	111
A.3	The Bulk Metal Source and its Radiated Fields	114
A.4	The Surface Sources and Their Radiated Fields	121
A.5	The Total Fields and the Second Harmonic Reflection Coefficients	123
B	Anisotropy in the Emission of CdSe-Nano-Platelets	127
B.1	Sample Analysis	127
B.1.1	Influence of the Effective Medium	127

B.1.2	In and Out-of Plane Local Field Factors for Radiation Pattern Calculation	130
B.1.3	Radiation Patterns	131
B.2	Analysis Of Optical Interband Transitions	132
B.2.1	Theoretical Considerations	134
C	Orientation of TPA in CdSe-Nano-Platelets	137
C.1	Two-Photon Absorption Probability	137
C.2	Selection Rules	138
	References	141
	List of Figures	157

1 | Introduction

The surfaces of bodies are the field
of very powerful forces of whose
action we know but little - *Lord Rayleigh*

The study of thin films and solid surface phenomena has become the basic science behind many engineering branches and technologically ambitious industries. A sample of solid material is always in contact with other media via its surface and it is through this interface that interactions with the environment occur. The physical and chemical properties of a surface can be strongly altered by the surrounding medium. Thus the surface of a solid plays an important part in key physical and chemical processes [1–4].

Surface science is vital in many materials-based industries such as optoelectronics, molecular sensing industries and any industry working in nanotechnology. Modern communication technology based on semiconductor devices and microelectronics with its increasing trend towards greater miniaturization would be unthinkable without surface and interface research [5, 6].

But how can a solid surface be defined?

A simple definition would be the plane at which the solid terminates. In practice, however, this boundary is not limited to the last atom layer before the adjacent phase but extends into it. Thus the surface is commonly regarded as consisting of that number of the solid's atomic layers after which bulk properties are reached. This decay distance in general is of the order of 5 to 20 nm [7].

Multiple methods have been developed to identify the surface compositions and to characterize their physical and chemical properties. Among them a multiplicity of spectroscopic methods based on direct particle interaction such as Auger electron spectroscopy, electron energy-loss spectroscopy, low-energy electron diffraction but also static and dynamic secondary ion mass spectroscopy and many others [8–11]. These methods can

provide detailed information about surface composition and physical properties but require high vacuum and are thus not easy to apply. Besides, modification of the sample by way of particle interaction cannot always be excluded during the analysis.

A different approach is used for scanning probe techniques where the surface is interrogated by a sharp tip, realized, for example, by atomic force microscopy, scanning near-field microscopy or scanning tunneling microscopy [12–14]. The surface’s composition as well as its profile can be explicitly determined with these techniques. However, surface modification through physical contact or deposition of conductive coatings is often inevitable and large-area scanning is very time-consuming.

Proven alternatives for surface and thin film analysis are angle-dependent scattering techniques. They have the advantage of being non-invasive, applicable at standard atmospheric pressure, suitable in scanning setups, and adaptable to large areas. A distinction in terms of excitation wavelength can be drawn between X-ray measurements (total reflection X-ray fluorescence analysis, grazing incidence X-ray reflectivity, energy-dispersive x-ray spectroscopy and others) and the optical regime (ultraviolet, visible and near-infrared, for transmission, reflection and scattering) [15–17].

In this work, we focus on angle-dependent techniques in the optical regime which can be referred to as k -space spectroscopy due to the imaging properties of the setup. Well-established methods such as surface enhanced Raman spectroscopy, sum-frequency generation spectroscopy or UV-vis-IR ellipsometry are also based upon this principle [18–22]. They enable the analysis of compositions at the nano-scale, orientation distributions, structural information about the surfaces and their environment. Related properties such as refractive index, concentration, film thickness, optical dispersion and nonlinear susceptibility can be determined. As such, k -space spectroscopy is finding the way for applications not only in surface and material science but also in environmental analysis, art research, explosives and drug detection, and high-sensitivity detection of molecular interaction [23–28].

The special aspect of our approach is the principle of *two-dimensional* k -space spectroscopy which combines tunable incident angles with wavelength and angle resolved detection. Even complex phenomena such as collective charge oscillations, nonlinear interactions, transition dipole orientations or coupled surface wave resonances which exceed the simple composition of the topmost layers can be revealed by these k -space spectroscopic measurements. Furthermore, nonlinear interactions in thin films and at the surface can be resolved and the contributing source terms can be quantitatively determined [29, 30]. This approach cannot be categorized into one of the afore-mentioned

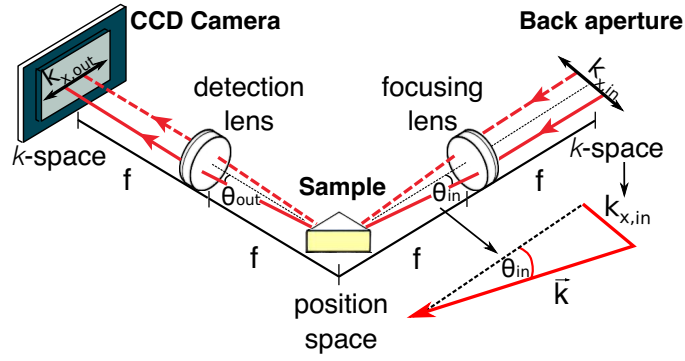


Figure 1.1: k -space spectroscopy excitation and detection scheme. The beam position in the back aperture is related to the incident angle in the lens focus via the wave-vector projection $k_{x,in} = \bar{k} \sin(\theta_{in})$. Analogous the exit angle can be imaged to the CCD camera via its wave-vector projection. Here, f is the focal length of the identical focusing and detection lenses.

angle-dependent techniques because it combines properties such as surface-enhancement, nonlinear wave-mixing and polarization-dependent excitation and detection. Further information on the principle of k -space spectroscopy and the examined phenomena can be found in the next section. Our experimental setup is illustrated in section 1.2.

1.1 Nonlinear 2D k -Space Spectroscopy

The principle of k -space spectroscopy relies on the relation of a well-defined beam's position in the back aperture of an objective to the angle under which a sample in its focus is encountered [29, 31]. This angle-dependent wave-vector projection can be understood as a Fourier transform between k -space and position space. Two-dimensional k -space spectroscopy means scanning of the incident angle while simultaneously analyzing the reflected intensity in terms of its emission wave-vector as shown in Fig 1.1. In addition, dispersive components can be integrated in the detection path to identify nonlinear interactions and luminescent emission by their spectral distribution in energy. What follows now is a discussion of the most prominent surface phenomena that have been investigated in this work.

Surface Plasmons: A prominent example of surface phenomena is the surface plasmon polariton (SP), a surface wave confined to the interface between a metal and a dielectric [32, 33]. The sub-wavelength confinement of SPs to the interface can lead to giant field enhancement. The latter property has provided a basis for applications such as plasmonic

sensor devices, microscopes, waveguide couplers, modulators and improved solar cells. It is valuable in boosting the yields of nonlinear frequency conversion, such as in harmonic generation and the sensing of molecular vibrations via surface enhanced Raman scattering [29, 34–47]. Recently, SPs are used for optical switching, self-assembly of nano-films, quantum plasmonic sensing and plasmonic superlenses [48–52]. Future applications and combinations of effective media, surface waves and single photon emitters require further investigation of fundamental linear and nonlinear properties of surface waves and coupled propagating waves in thin films.

A detailed analysis of SP-excitation via evanescent fields is given in Chapter 2, revealing analogies and differences for the two common coupling configurations, namely the Otto and the Kretschmann configuration [53, 54]. SP excitation in these attenuated total internal reflection (ATR) setups allows the determination of pronounced surface and thin film characteristics such as dielectric function, film thickness, concentrations and radiative losses which are the basis for sensing devices [55–62]. Although being established as standard coupling configurations in many applications, the coupling properties and especially the sources of nonlinear effects are of current interest in research and development.

We demonstrate the existence of fundamental differences between the Otto and the Kretschmann coupling configurations, which are commonly considered as identical. The differences concern the coupling properties for SP excitation which are examined for white-light and pulsed laser excitation. As a result, the dependence of the coupling efficiency on material parameters and configuration parameters such as dielectric function and film thickness is revealed.

Nonlinear Plasmonics: The combination of plasmonic field enhancement at the surface and the breakup of the inversion symmetry of noble metals at an interface led to the consequential application of SP's to nonlinear optics. The fast developing field of nonlinear plasmonics comprises harmonic generation from surfaces and thin films, wave-mixing and its applications in microscopy and sensing techniques, generation of high harmonic atto-second pulses, two-photon absorption, surface structuring and down conversion. [46, 63–68].

The yield of nonlinear conversion processes is strongly dependent on the intensity of the driving fundamental field and its phase-matching to the emitted harmonic radiation. Hence, second harmonic generation (SHG) is often used as indication for plasmonic field enhancement [69]. As the total interaction length at a single surface or in a thin film is orders of magnitude less compared to the sizes of typical nonlinear crystals employed in frequency conversion, can there be a significant yield of harmonic generation? Can

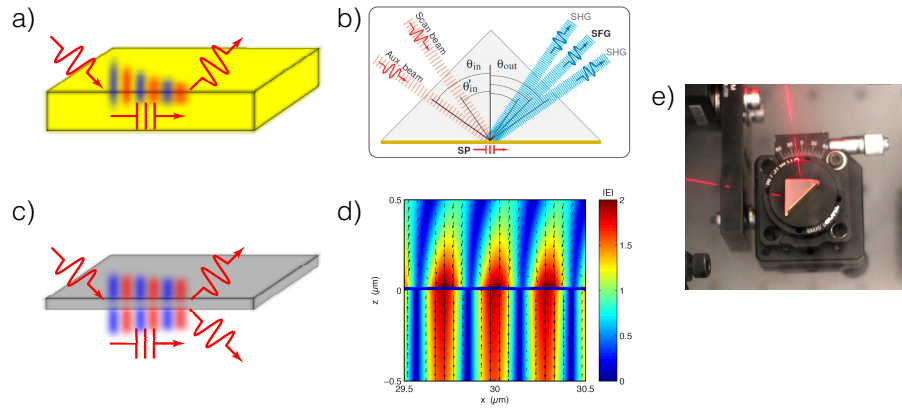


Figure 1.2: Illustration of surface waves. a) Surface plasmon polariton at two semi-infinite media. b) Second-harmonic generation and degenerate sum-frequency generation as example of surface plasmon enhanced nonlinear interactions. c) Long-range surface wave in a thin film. d) Electric field enhancement at the long-range surface wave resonance. e) Photography of a prism sample in the Kretschmann configuration.

the huge field enhancement provided by the SP resonance be used to boost nonlinear phenomena so that it can compete against established converters such as beta barium borate (BBO) crystals? And if yes, what are the specific sources of nonlinear polarization that are involved in the nonlinear conversion process?

In Chapters 3,4 and 5, we focus on surface plasmon enhanced SHG and wave-mixing processes on single interfaces and in thin films. The groundwork for the theoretical analysis of surface SHG was laid by Bloembergen et al. [70, 71] and has thereupon been applied to plasmonics [18, 72, 73]. An established theoretical concept to calculate surface plasmon enhanced SHG is to describe the electron dynamics with the hydrodynamic theory [72–74]. This approach is adapted in Chapter 3 to determine the surface and bulk contributions to the out-coupled SHG.

In Chapter 4 the harmonic conversion efficiency is compared to experimental results from ATR coupling configurations both qualitatively and quantitatively. A direct comparison of absolute values for the conversion efficiency is given and the nonlinear source parameters following the notation of Rudnick and Stern are determined [74]. Furthermore, the interactions involved in the nonlinear conversion process are analyzed and the role of the surface plasmon, being a catalyst or an active participant is revealed. For this purpose, the setup is modified to enable excitation with two independent laser beams and hence investigation of degenerate three-wave-mixing.

Long-range surface waves in thin films: Thin films with symmetric cladding in terms of their dielectric function are known to support coupled surface waves at both interfaces [75–79]. Long propagation lifetimes have been reported in the visible regime for very thin films (< 20 nm) if embedded in transparent media [76, 80, 81]. As the electric field is suppressed inside the film, strongly absorbing media whose dielectric function is dominated by its imaginary part, can also support low-loss surface waves [82–84]. Close to an absorption resonance, the nonlinear susceptibility of a material can greatly exceed those values found off-resonance which could make absorbing thin films interesting for nonlinear optics [85].

In Chapter 5, such long-range surface waves (LRSW) are investigated for thin chromium, molybdenum and gold films. A modified ATR coupling configuration is applied to determine linear coupling properties, propagation lengths and mode profiles [86–89]. In addition, we examine to what extent field enhancement originates from the surface wave resonance. Here, the second harmonic radiation coupled to the far-field is acting as indicator for field enhancement that is local to the film and its interfaces [90–92]. These results are compared to SP enhanced SHG from Chapter 4 and it is discussed if intrinsically absorbing materials can be considered as low-loss optical media for surface-wave optics in the nonlinear regime.

Oriented nano-platelets: Colloidal nano-particles have become a promising field of research and have already been implemented in light emitting devices, solar cells, biological sensors and electronics [93–95]. Recently, new 2D materials such as II-VI nano-platelets, nano-belts and transition metal dichalcogenides have emerged [96–99] which have been found to share the exciting properties of being nearly ideal quantum wells. Additionally, high carrier mobilities [100, 101], very short (radiative) exciton lifetimes [102–105] and high exciton binding energies have been reported for these 2D materials [98, 106–108]. The latter were attributed to the strong dielectric confinement in 2D nano-crystals.

Quantum confined systems have also been found to have anisotropic distributions of their transition dipole moments [109–111]. The existence of a bright plane and a dark axis has been reported for wurzite CdSe/ZnS quantum dots (QDs) and nano-rods. These observed properties have been attributed to the symmetry and the fine structure of the electronic states. Hence, the orientation or distribution of transition dipole moments and their coupling to the density of photon states determine the emission characteristics and radiative rates [112, 113]. In addition, theoretical predictions for strongly anisotropic particles show that the dielectric contrast between the nano-particles and the surrounding

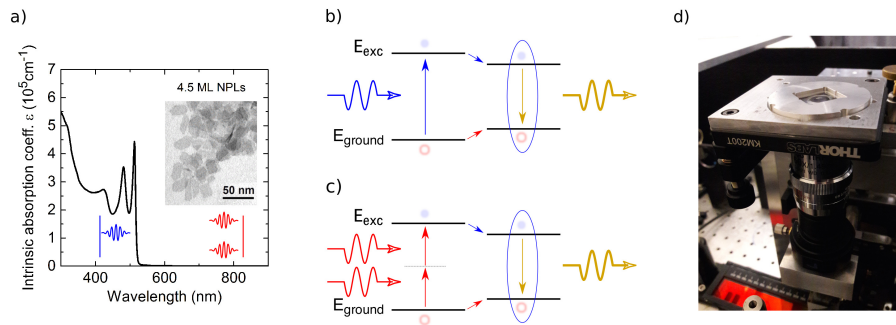


Figure 1.3: Absorption and emission characteristics of oriented NPs. a) Absorption spectrum of our nano-platelets. A TEM image is shown in the inset. b) Scheme of the linear absorption process, relaxation by phonon-scattering and emission from excitonic recombination. c) Scheme of two-photon absorption and the respective emission. d) Photography of our confocal setup (high-NA objective and sample).

ligands strongly alters the angular emission properties [114]. This is in strong contrast to the case of highly symmetric spherical particles, such as PbSe dots, where isotropic internal dipole distribution and local fields result in isotropic emission [115]. For applications in photonics such as lasing and efficient display technology intrinsically directional emitters of light will become increasingly important.

In Chapter 6 we apply 2D k -space spectroscopy to characterize the absorption and emission patterns of a monolayer of oriented CdSe nano-platelets. Our investigation reveals photoluminescence that is strongly anisotropic in terms of its k -space distribution, while the off-resonant absorption into the energetically higher 2D-continuum of states is isotropic. The internal distribution of transition dipoles can be reconstructed including consideration of the local density of photon states, and local field and Fresnel effects. Thus dielectric and electronic effects can be separated and the intrinsic nature of directed emission can be revealed. Having these contrasting properties of isotropic absorption, yet anisotropic emission, makes oriented CdSe nano-platelets, or superstructures of similarly parallel-oriented platelets, an interesting, and potentially useful class of semiconductor-based emitter for optical technologies.

SP enhanced TPA in oriented nano-platelets: Strong enhancement and directed emission have been shown for colloidal nano-particles on top of plasmonic layers [116–124]. The combination of individual photon-emitters and subwavelength-confined plasmon modes promises improvement in numerous fields such as sensing, microscopy, photovoltaics and

spectroscopy [125–128].

In Chapter 7 we combine monolayers of oriented nano-platelets with silver layers that support propagating surface plasmons. With the results from the previous chapters, we can determine the plasmon-enhanced absorption and emission characteristics. Distinguishing dielectric effects attributed to the sample geometry and the surrounding ligands from electronic effects, we can analyze the coupling of propagating surface waves to transition dipoles in oriented nano-platelets.

Furthermore, nano-platelets have been identified to offer remarkably high two-photon absorption (TPA) cross sections which has likewise become important in various applications, e.g. micro-fabrication, lithography, polymerization, data storage and spectroscopy []. The selection rules for this multi-photon process are investigated and compared to the case of linear excitation.

Plasmonic resonances in combination with two-photon absorption are of actual interest in fluorescence microscopy, sensing applications and nano-lithography [129–134]. Highly oriented nano-platelets with their distinct radiation pattern on top of plasmonic thin films promise boosted excitation and directed emission normal to the interface. Thus we compare linear excitation and TPA excitation of oriented nano-platelets with and without plasmonic layers in terms of their efficiency, field enhancement and directionality of the emission.

Nonlinear 2D- k -space spectroscopy is a powerful tool for studying surface and thin film phenomena. Beyond the determination of material and sample properties such as the dielectric function, the surface structure or the film thickness, it delivers insight into the intrinsic nature of the sample. Surface wave resonances, second harmonic yield, photonic and plasmonic interactions as well as transition dipole orientations can thus be characterized and will be the subject of this thesis.

Applying k -space spectroscopy, we could quantify the influence of ATR coupling configurations on the excitation of SP and especially on the generation of second harmonic radiation. In this context, the first direct comparison of absolute values for the SHG yield to the nonlinear parameters from the hydrodynamic model in the Otto and Kretschmann coupling configurations is presented. In a next step, absorbing thin films are shown to support low-loss surface waves, that are confined to the surface and reach long propagation lengths. Even SHG from field enhancement is observed for LRSW in the Otto configuration which, to our knowledge, has not been reported before.

Finally, composite monolayer films of effective media that contain oriented nano-platelets

are investigated and it is shown how 2D- k -space spectroscopy enables access to the intrinsic Bloch states of these 2D confined nano-particles. Thereby, the origins of the anisotropy in the photo-luminescent emission and even for the nonlinear process of two-photon absorption could be revealed.

The combination of 2D- k -space spectroscopy with different excitations and spectroscopic analysis in the detection thus enables a large variety of measurements. It provides an insight into the intrinsic properties of surface and thin film phenomena which are analyzed in the following chapters.

1.2 Experimental Setup

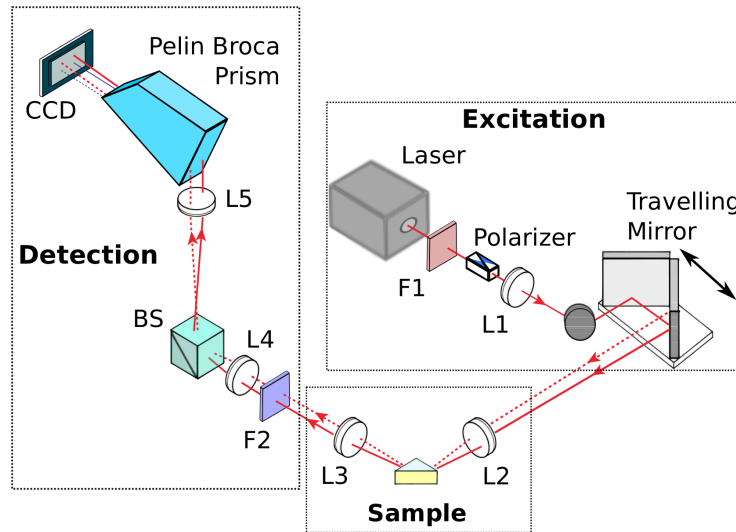


Figure 1.4: Experimental setup for k -space spectroscopy. A Ti:sapphire laser provided pulsed radiation (150 fs) with wavelengths tunable from 780 nm to 960 nm and a repetition rate of 75,4 MHz, which was polarized with reference to the plane of incidence on the sample. A cut-on filter F1 removed residual pump and second-harmonic radiation. A pre-focusing-lens L1 adjusted the beam's spot size in the back aperture of the objective lens L2 (0.075°) and thus the beam's waist on the sample ($190 \mu\text{m}$). The input fundamental beam was displaced in the back aperture of the objective lens by a traveling mirror thereby scanning the angle of incidence with respect to the sample. The outgoing light was collected by another, symmetrically-arranged, achromatic lens L3 and a filter F2 removed the majority of fundamental intensity. A beam splitter BS was used to divide the signal into one half going to a monitoring camera, and the other half transferred to a Pellin Broca prism which separated fundamental and harmonic radiation, and luminescence. The relay lenses L4 and L5 project the back aperture of L3 and hence the k -space information of the emission onto a cooled CCD camera. By using the full 1024x256 pixel CCD-array, the excitation can be scanned while the full emission is detected at once and analyzed as a function of wave-vector (long axis) and wavelength (short axis). The excitation can be selected between white-light excitation, two-beam excitation and pulsed frequency-doubled excitation in the visible regime. The objective lens L3 can be replaced by a high NA immersion oil objective, enabling confocal excitation.

2 | Linear Analysis of Surface Plasmon Polaritons

Surface plasmon polaritons (SP's) are known as solutions of Maxwell's equations since the work of Zenneck and Sommerfeld [135, 136]. Perhaps their simplest manifestation occurs at the planar interface between a conductor and a dielectric, where the plasma oscillations in the conductor are coupled to an evanescently confined electromagnetic field. Due to their evanescent field profile and the plasmon wave-vector larger than that of propagating light waves in the surrounding dielectric, SP cannot directly be excited from the far-field. However, there are several options to match the wave-vector of the incident light to that of the SP [137]. Excitation of SP via the method of attenuated total-internal-reflection (ATR) was first demonstrated by Otto [54], closely followed by Kretschmann and Raether, who developed an alternative ATR configuration [53]. Matching of the incident wave-vector's projection onto the interface to that of the surface plasmon can also be achieved by the use of diffraction gratings or other appropriate excitation configurations that can provide a larger wave-vector component [138, 139]. It has even been shown that free-space excitation by four-wave mixing is possible [66].

The strong confinement of SP's to the surface can further lead to huge enhancement of the electromagnetic field while undergoing the plasmonic resonance. Applications such as plasmonic sensor devices, modulators, solar cells and the sensing of molecular vibrations via surface enhanced Raman scattering are based on plasmonic field enhancement [29, 34, 46, 140–142]. For all these applications, efficient coupling and well-defined mode properties are indispensable, while easy implementation without manipulation of the sample is highly desirable. Few experimental configurations enable tuning of essential coupling properties without substantially changing the propagation properties or inserting additional resonances.

Fundamentals of coupling from free-space radiation to propagating SPs, as well as ef-

efficient out-coupling, are discussed in this chapter for the Otto and the Kretschmann configuration. A short definition of SPs is followed by a detailed analysis of linear coupling efficiencies in both configurations. Therefore, we experimentally investigate plane-wave excitation of SP realized with white-light illumination as well as Gaussian beam illumination from a pulsed Ti:Sapphire laser. The results are compared to a detailed multi-layer calculation.

2.1 Surface Plasmons at the Interface of Two Semi-Infinite Media

The treatment that follows can be found in greater detail in the books of e.g. Raether [32] and Maier [33]. The physical properties of SP's can directly be derived from Maxwell's Equations. Starting with the curl equations in the absence of external charge and current densities[143]

$$\begin{aligned}\nabla \times \mathbf{E} &= -\frac{1}{\mu_0} \frac{\partial \mathbf{H}}{\partial t} \\ \nabla \times \mathbf{H} &= \frac{\partial \mathbf{D}}{\partial t}\end{aligned}\quad (2.1)$$

where \mathbf{E} is the electric field, $\mathbf{D} = \epsilon \epsilon_0 \mathbf{E}$ the dielectric displacement and \mathbf{H} the magnetic field, we can calculate the equation for a surface wave, that is confined to an interface between two infinite media. Assuming harmonic time dependence,

$$\mathbf{E}(\mathbf{r}, t) = \mathbf{E}(\mathbf{r})e^{-i\omega t}\quad (2.2)$$

and inserting this ansatz into the wave equation

$$\nabla^2 \mathbf{E} - \frac{\epsilon}{c^2} \frac{\partial^2}{\partial t^2} \mathbf{E} = 0\quad (2.3)$$

yields

$$\nabla^2 \mathbf{E} + k_0^2 \epsilon \mathbf{E} = 0\quad (2.4)$$

where $k_0 = \omega/c$ is the wave-vector in vacuum and c is the speed of light. Without loss of generality, the plane of incidence is chosen to be the xz -plane (Fig 2.1). Now, an electromagnetic wave, that is confined to the surface and propagates in the x -direction, can be described as

$$\mathbf{E}(x, y, z) = \mathbf{E}_0 e^{i(k_x x + k_z z)}\quad (2.5)$$

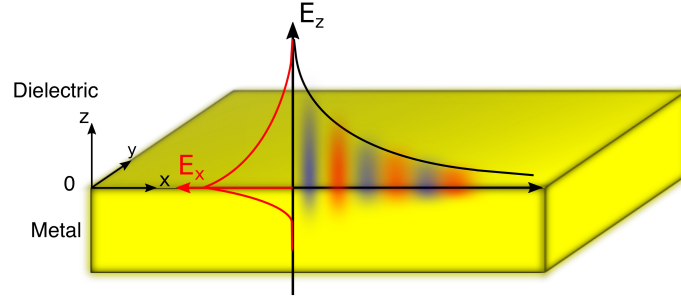


Figure 2.1: Geometry of a surface wave, that is confined to the interface between a metal $z < 0$ and a dielectric $z > 0$. The wave propagates in x-direction and the electric field amplitudes are defined as $E_x(0, 0, z)$ and $E_z(x, 0, 0)$.

and the wave equation 2.4 results in

$$\frac{\partial^2 \mathbf{E}(x, y, z)}{\partial z^2} + (k_0^2 \epsilon - k_x^2) \mathbf{E}(x, y, z) = 0. \quad (2.6)$$

which yields

$$k_z = \sqrt{k_0^2 \epsilon - k_x^2} \quad (2.7)$$

A similar equation exists for the magnetic field \mathbf{H} . It is well known [32, 33, 144], that transverse magnetic (TM) polarization (here referred to as p-polarization) is needed to excite surface plasmons. For this case ($E_y = H_x = H_z = 0$), Eqs. 2.1 reduce to

$$\begin{aligned} \frac{\partial H_y}{\partial x} &= \frac{\partial D_z}{\partial t} \\ \frac{\partial H_y}{\partial z} &= -\frac{\partial D_x}{\partial t} \end{aligned} \quad (2.8)$$

First, we consider the simple configuration of two infinite half-spaces (Fig. 2.1), a dielectric with ϵ_d for $z > 0$ and a metal with ϵ_m for $z < 0$, with their interface at $z = 0$ in the xy -plane. Inserting Eqs. 2.2 and 2.5 into 2.8 then leads to

$$\begin{aligned} ik_{d,x} H_{dy} &= i\omega D_{d,z} \\ ik_{d,z} H_{dy} &= -i\omega \epsilon_0 \epsilon_d E_{d,x} \end{aligned}$$

inside the dielectric medium $z > 0$. For the metal $z < 0$, the respective equations are

$$\begin{aligned} ik_{m,x} H_{d,y} &= i\omega D_{m,z} \\ ik_{m,z} H_{d,y} &= -i\omega \epsilon_0 \epsilon_m E_{m,x}. \end{aligned}$$

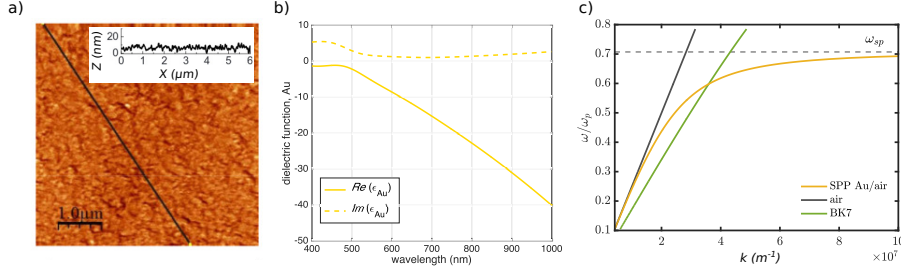


Figure 2.2: AFM image (a) dielectric function of a thermally evaporated gold film (b) and related SP dispersion relation (c). The averaged roughness of the gold film is 3 nm. The dispersion relation is shown for a surface plasmon at the interface between an infinite gold layer and air. The dielectric function of gold was obtained experimentally by ellipsometric measurements and is shown in b).

The boundary conditions at $z = 0$ require continuity of H_y , E_x and D_z . The first one leads to continuity of the k_x -components,

$$k_{d,x} = k_{m,x}$$

which is equivalent to Snell's law. The latter ones result in

$$\frac{k_{d,z}}{k_{m,z}} = -\frac{\epsilon_d}{\epsilon_m}. \quad (2.9)$$

With Eqs. 2.9 and 2.7, we can calculate the wave-vector of a surface wave, that propagates in the x -direction and is confined in the z -direction

$$k_{SP} = k_0 \sqrt{\frac{\epsilon_m \epsilon_d}{\epsilon_m + \epsilon_d}} \quad (2.10)$$

In contrast to this ideal conception, the measured SP resonance and propagation properties are highly affected by the respective coupling configuration. The actual plasmon wave-vector slightly differs from this exemplary wave-vector, which is defined at the interface between infinite media. In addition, intrinsic SP mode properties are particularly sensitive to surface roughness and contamination of the metal surface—both of which significantly affect the SP's propagation speed, lifetime and resonant field enhancement. Fig. 2.2a) shows an atomic-force microscopy (AFM) image of an exemplary gold film. The averaged surface roughness was measured to be 3 nm. Ellipsometric measurements were performed to obtain the gold's dielectric function (see Fig. 2.2 b), which was used in the following calculations. Fig. 2.2c) shows the dispersion relation of a surface plasmon (Eq. 2.10), which propagates at the interface between gold and air, and the respective light-lines of free-space propagation in air and BK7 glass.

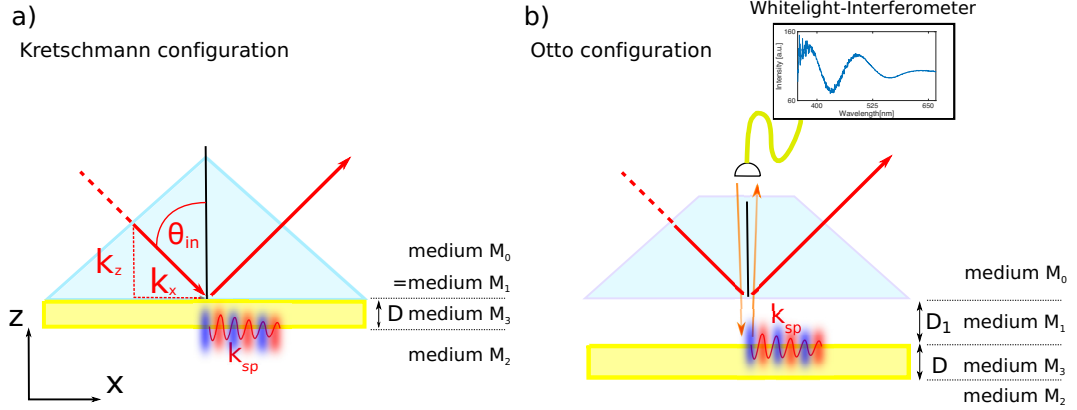


Figure 2.3: Standard ATR coupling configurations. a) shows the Kretschmann configuration, which consists of a BK7-glass coupling prism, a thermally evaporated gold film of thickness D and the surrounding dielectric (air). b) shows the Otto configuration, which is based on the same principle, yet the layer order is inverted. Below the BK7-prism is an air gap of size D_1 for adjustable coupling of the generated evanescent field to a gold film of thickness D . The gap size D_1 is controlled via white-light interferometry. For both configurations, the SP can be excited on the gold-air interface: By varying the angle of incidence θ_{in} , the wave-vector's projection k_x to the interface can be matched to k_{SP} .

2.2 Attenuated Total-Internal-Reflection Coupling Configurations

Established as the standard ATR-coupling configurations are the Otto and the Kretschmann-Raether configurations that are considered to be equivalent in terms of their plasmonic coupling, and relation to near-field enhancement. Due to its simplicity, the Kretschmann configuration (Fig. 2.3a) is often employed for excitation of SP's, where a collimated light beam interrogates the metal film via a glass prism [53].

In our experiment, the Kretschmann configuration consisted of a BK7-glass coupling prism (layer M_0) on which a thin gold film (M_3) of thickness D was thermally evaporated. SP's can be excited at the interface between the metal and the surrounding dielectric (M_2), which was air in this case.

$$\left. \begin{array}{l} z > 0 \quad \text{glass } M_0 \text{ with } \epsilon_0 \\ 0 > z > -D \quad \text{gold } M_3 \text{ with } \epsilon_3 \\ z < -D \quad \text{air } M_2 \text{ with } \epsilon_2 \end{array} \right\} \text{Kretschmann}$$

Driven as a total internal reflection setup, the larger wave-vector in the glass (ϵ_0)

reaches the interface between metal (ϵ_3) and dielectric (ϵ_2) as an evanescent wave.

$$k_x = k_0 \sqrt{\epsilon_0} \sin(\theta_{\text{in}}) \equiv k_{\text{sp}} \quad (2.11)$$

As described by Eq. 2.11, the wave-vector's component parallel to the surface can thus be matched to that of the SP by varying the angle of incidence θ_{in} . When this condition is met, the surface plasmon resonance (SPR) leads to a strong local enhancement of the fundamental field.

The Otto configuration (Fig 2.3b) was based on the same principle, yet the layer order was inverted. On a Quartz coupling prism (M_0) followed an adjustable air gap (M_1), that was used to vary the coupling to SP's on a gold-air-interface, resulting in the order

$$\left. \begin{array}{l} z > D_1 \quad \text{glass } M_0 \text{ with } \epsilon_0 \\ D_1 > z > 0 \quad \text{air } M_1 \text{ with } \epsilon_1 \\ 0 > z > -D \quad \text{gold } M_3 \text{ with } \epsilon_3 \\ z < -D \quad \text{substrate } M_2 \text{ with } \epsilon_2 \end{array} \right\} \text{Otto}$$

While the Kretschmann configuration is easier to apply, the Otto configuration offers the advantage of tunability. The coupling strength can be changed by varying the air gap (M_1). Concomitant with a change to the coupling properties, the SP's dielectric environment also changes, leading to a shift of the plasmon resonance. Due to this dependence, we studied a series of different metal thicknesses in the Kretschmann configuration and of varying air gap in the Otto configuration.

2.2.1 Fabry-Pérot Model

The model in section 2.1 tells us about surface plasmon modes but does not contain information about the reflected intensity in ATR coupling configurations. Thus we use a theoretical model, where we consider a general 2D configuration with the above mentioned 3 layers for the Kretschmann and 4 layers for the Otto configuration (Fig 2.3). To take multiple reflections inside the air gap M_1 and the metal M_3 into account, we apply a multi-layer Fabry Pérot model [145] to analyze our data. The reflectivity for an electric field, incident as plane-wave from medium M_0 is then

$$\bar{r}_{02} = r_{01} + \frac{t_{01} \bar{r}_{12} t_{10} e^{2ik_{1,z} D_1}}{1 - r_{10} \bar{r}_{12} e^{2ik_{1,z} D_1}} \quad (2.12)$$

where

$$\begin{aligned} \bar{r}_{12} &= r_{13} + \frac{t_{13} r_{32} t_{31} e^{2ik_{3,z} D}}{1 - \bar{r}_{30} r_{32} e^{2ik_{3,z} D}} \\ \bar{r}_{30} &= r_{31} + \frac{t_{31} r_{10} t_{13} e^{2ik_{1,z} D_1}}{1 - r_{10} r_{13} e^{2ik_{1,z} D_1}} \end{aligned} \quad (2.13)$$

The Fresnel coefficients for reflection and transmission from medium i to medium j are defined as

$$\begin{aligned}
 r_{ij}^s &= \frac{k_i - k_j}{k_i + k_j} \\
 t_{ij}^s &= \frac{2k_i}{k_i + k_j} \\
 r_{ij}^p &= \frac{k_i\epsilon_j - k_j\epsilon_i}{k_i\epsilon_j + k_j\epsilon_i} \\
 t_{ij}^p &= \frac{2\sqrt{\epsilon_i}\sqrt{\epsilon_j}k_i}{k_i\epsilon_j + k_j\epsilon_i}
 \end{aligned} \tag{2.14}$$

All coefficients are functions of their respective wavelengths and incident angles. From Eq. 2.12, we can calculate the reflected intensity as

$$I_R = |\bar{r}_{02}|^2 I_0 \tag{2.15}$$

For the special condition $|\mathcal{R}e(\epsilon_3)| \gg 1$ and $|\mathcal{I}m(\epsilon_3)| \ll |\mathcal{R}e(\epsilon_3)|$, the plasmonic resonance can be approximated [32] by a Lorentzian type relation of the form

$$I_R(k_x) = 1 - \frac{4\Gamma_i\Gamma_{rad}}{[k_x - (k_{SP} + \delta k_{SP})]^2 + (\Gamma_i + \Gamma_{rad})^2}, \tag{2.16}$$

where δk_{SP} accounts for the finite metal layer thickness and the related resonance shift with respect to the plasmon wave-vector k_{SP} for a semi-infinite metal. The real part of the plasmon wave-vector $\mathcal{R}e(k_{SP}) + \mathcal{R}e(\delta k_{SP})$ defines the resonance position, whereas the damping terms

$$\begin{aligned}
 \Gamma_i &= \mathcal{I}m(k_{SP}) \\
 \Gamma_{rad} &= \mathcal{I}m(\delta k_{SP})
 \end{aligned} \tag{2.17}$$

are related to the imaginary part of the plasmon wave-vector. Here, we distinguish internal damping Γ_i caused by electron-electron and electron-phonon scattering and therefor thermal dissipation, and radiative damping Γ_{rad} from out-coupling to the prism and scattering on surface roughness. The characteristic plasmon absorption for impedance matching is found as a minimum in Eq.2.16, which is zero for

$$\Gamma_i = \Gamma_{rad} \tag{2.18}$$

and fixes the optimum metal layer thickness for a given excitation wavelength. The damping terms are also responsible for the finite surface plasmon propagation length, given by

$$L_{SP} = \frac{1}{2(\Gamma_i + \Gamma_{rad})} \tag{2.19}$$

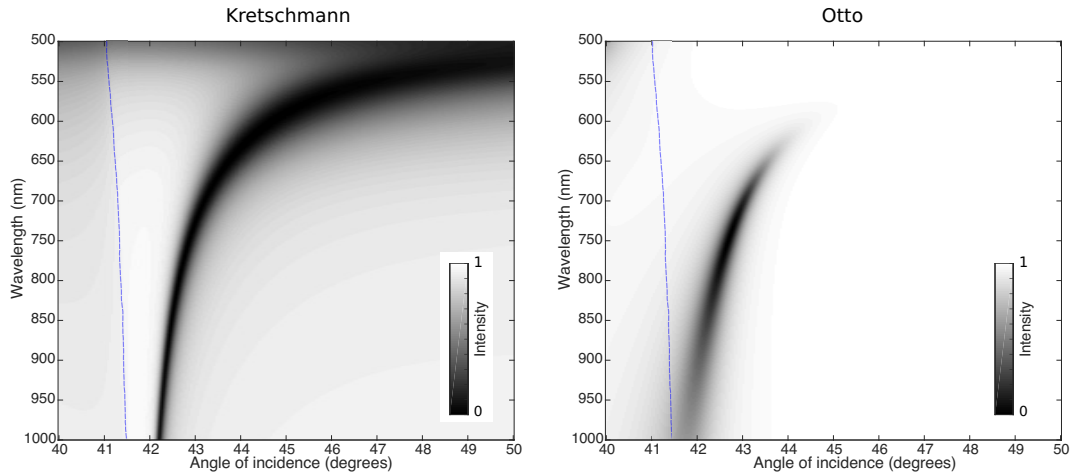


Figure 2.4: Calculated reflected intensities as a function of wavelength and incident angle for a 50 nm gold layer in the Kretschmann configuration (on the left-hand side) and an air gap of 1000 nm in the Otto configuration (on the right-hand side). The dashed lines mark the angle of total internal reflection at glass-air interface.

which also determines the width of the plasmon resonance. A calculated white-light map of the reflected intensity (Eq. 2.15) for several wavelength and incident angles is shown in Fig. 2.4. Here, the calculations for the Kretschmann configuration were performed with a gold film thickness D of 50 nm, and for the Otto configuration with an air gap size D_1 of 1000 nm. The excitation of propagating surface plasmons can clearly be seen as strong absorption feature beyond the angle of total internal reflection (dashed blue line). A detailed comparison to the experimental results can be found in the next section.

2.3 Linear Measurements

For the linear analysis, two different k -space configurations were applied. A white-light excitation setup (Fig. 2.5), which provides an overview of the linear coupling efficiency to propagating surface plasmons, and a pulsed laser setup (Fig. 1.4) for Gaussian beam excitation at a single wavelength.

2.3.1 Spectroscopic Measurements

In the white-light setup (Fig. 2.5), the emission from an incandescent filament lamp is linearly polarized and focussed on the sample, containing a whole wavelength spectrum from 400 nm to 1000 nm and a broad angular width from 35 to 55 degrees. The reflected

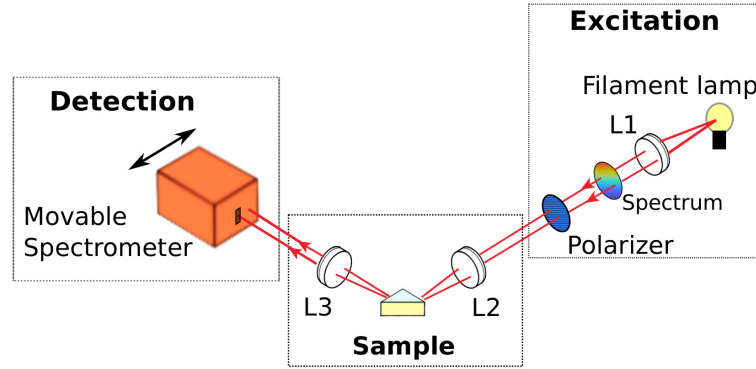


Figure 2.5: Experimental Setup for linear reflectivity measurements with white-light excitation. A filament lamp provides a broad spectrum, which is collimated with the lens L1, linearly polarized and focussed on the sample with the lens L2. In a symmetric configuration, the reflected intensity is collected and collimated with another lens L3. The signal is detected with a spectrometer scanning the k -space. The resolution is limited by the entry slit of the spectrometer, the source size and the precision of the translation stage.

intensity is collimated and then collected with a spectrometer in k -space. By shifting the spectrometer's position, the emission is scanned by the spectrometer's entry slit which also determines the angular resolution.

On the left-hand side of Fig. 2.6, the experimental results for different thicknesses of 34 nm, 54 nm, and 74 nm in the Kretschmann configuration are shown. The right-hand side shows the results for air gap sizes of 450 nm, 750 nm, and 1000 nm in the Otto configuration. For a wavelength below 450 nm, strong absorption features from inter-band transitions are known for gold [146].

The blue-dashed lines represent the calculated angle of total internal reflection (TIR). To eliminate fluctuations in the excitation spectrum, the results were normalized to a reference measurement of an uncoated BK7-glass prism. Due to the lower reflection coefficient of bare glass beneath the TIR-angle, the normalized reflection appears to be higher in the red-shaded areas, where it effectively vanishes. The characteristic plasmonic absorption feature can be found beyond the TIR-angle for all measured parameters.

In the Kretschmann configuration, the plasmonic coupling efficiency remains almost constant over the measured spectral range and bends towards larger incident angles for shorter wavelengths, as expected from the dispersion relation (Eq. 2.10, Fig. 2.2). Variation of the gold film's thickness strongly affects the coupling strength, which is maximum for $D = 50$ nm. Here, the incident light is phase-matched to the propagating surface plasmon, leading to nearly complete extinction of the reflected intensity. An increase

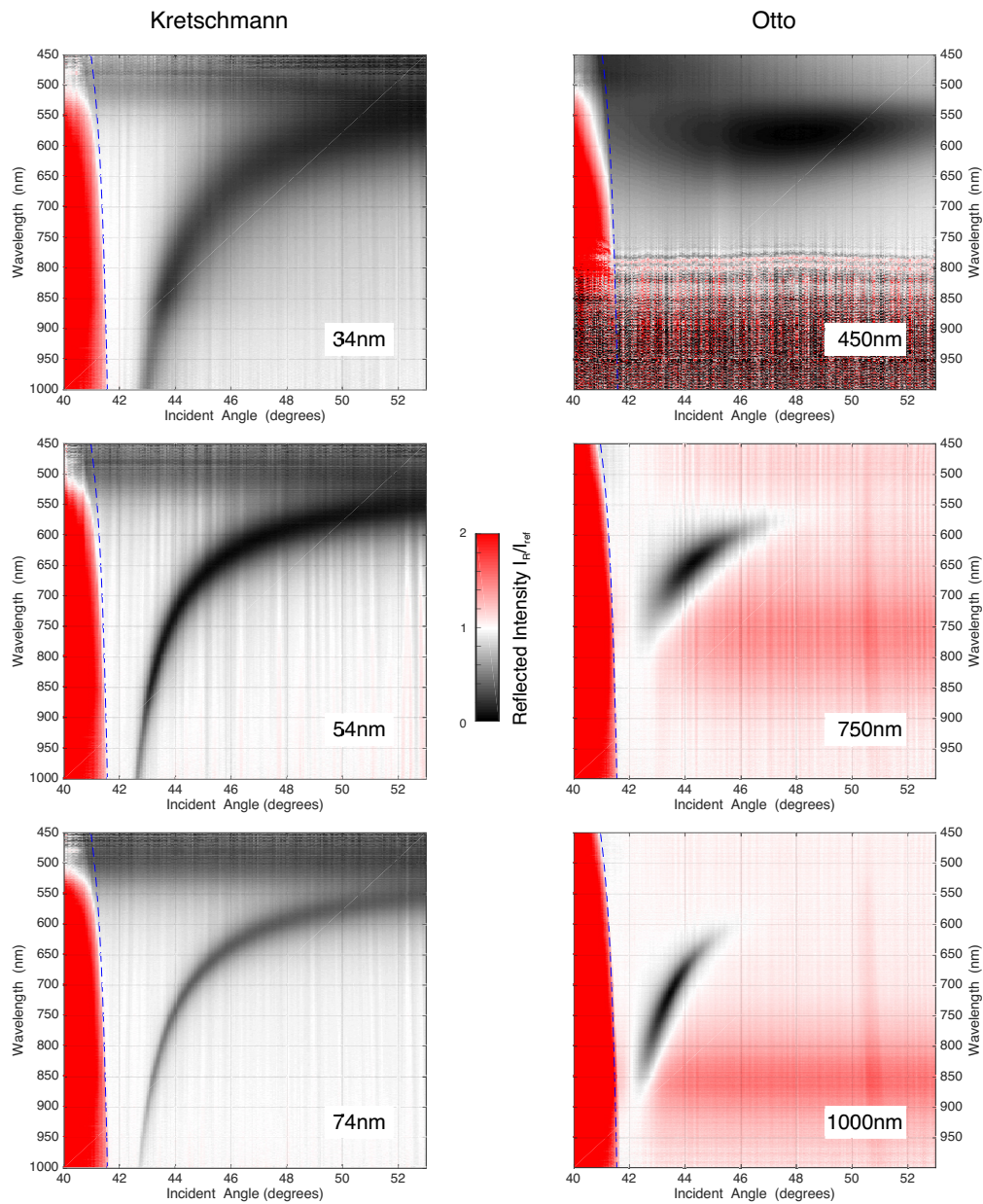


Figure 2.6: White-light reflection measurements for varying gold layer thickness in the Kretschmann configuration (on the left-hand side) and different air gap sizes in the Otto configuration (on the right-hand side). The dashed blue line marks the angle of total internal reflection from BK7 glass to air. Due to normalization effects, the red-shaded areas diverge in their intensities, while the actual reflected intensity vanishes.

in the thickness leads to weaker coupling and narrowing of the feature, while thinner layers cause broadening of the plasmonic resonance at a likewise decrease in the coupling strength.

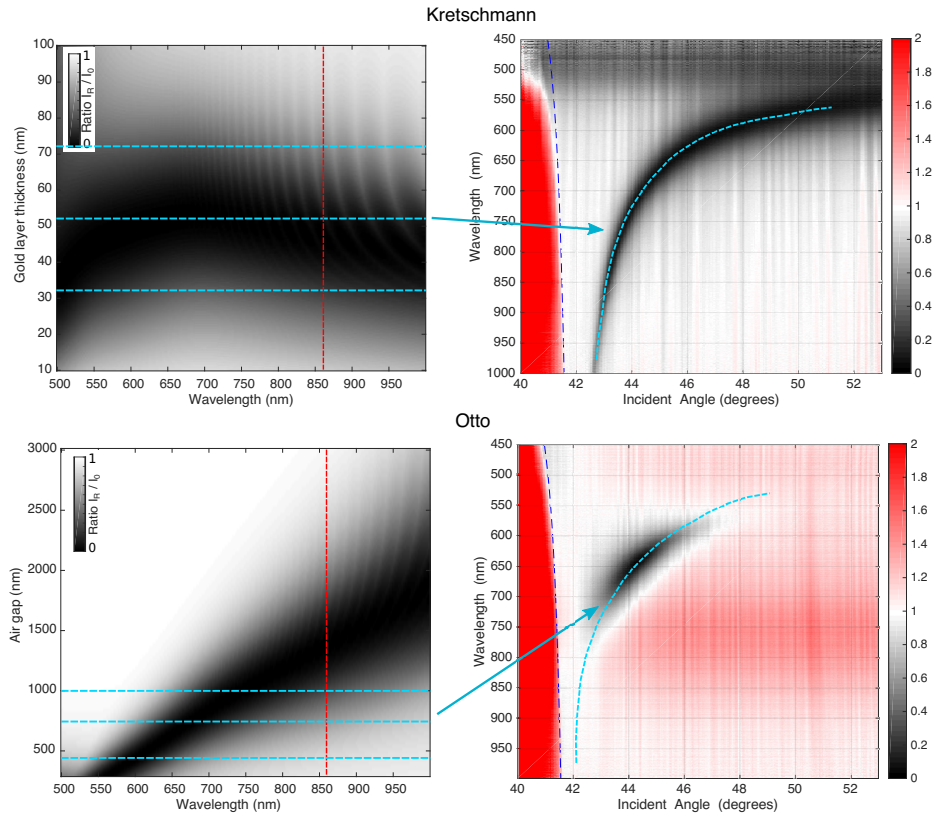


Figure 2.7: Comparison of coupling efficiencies as a function of wavelength and coupling layer thickness for the Otto and the Kretschmann configuration: Reflected intensity as a function of wavelength and gold layer thickness for the Kretschmann configuration (upper image) and air gap size for the Otto configuration (lower image). To obtain these images, the SP resonance was tracked for every coupling layer thickness (D and D_1 , respectively) and plotted as a function of wavelength. Thus the dashed blue lines mark the development of the measured plasmonic resonances as a function of wavelength, which is exemplary shown on the right side for 54 nm gold layer and 750 nm air gap, respectively. The red line designates the position of Gaussian beam excitation for the measurements in section 2.3.2.

A different behavior can be found for the Otto configuration. Here, the coupling efficiency has an optimum for every air gap D_1 . Shorter wavelengths require smaller air gaps for efficient coupling, while increasing gap sizes lead to a resonance shift towards larger wavelengths. As for the Kretschmann configuration, the plasmonic absorption feature broadens as a function of the incident angle as the gap size is decreased. However, as a function of wavelength, the opposite dependence can be found: while the coupling strength is nearly constant in the Kretschmann configuration, a confinement can be found for smaller gap sizes in the Otto configuration.

This trend can be confirmed by calculating the ratio I_R/I_0 (Fig. 2.7) as a function of wavelength and either gold layer thickness or air gap for the respective configurations. Here, the minima in the reflected intensity which identify the SP resonance were tracked for every coupling layer thickness (D and D_1 , respectively) and plotted as a function of wavelength, as schematically shown on the right hand side. Following the dashed blue lines, which mark the measured layer thicknesses, the trend of the respective plasmonic resonance can be recognized. For the Kretschmann configuration at 74 nm layer thickness, the coupling strength is increasing up to a relative maximum at a wavelength of 650 nm and then decreases again. For 54 nm thickness, the coupling remains constant over the whole spectral range, while for a thickness of 34 nm, it starts at a higher level, decreases to find a minimum at a wavelength of 700 nm and then rises again. While for the Kretschmann configuration, the thickness for optimal coupling differs only a little around 50 nm, the plasmonic coupling in the Otto configuration shows a strong spectral dependence on the size of the air gap: at a specific distance, coupling can only occur for a distinct spectral range. Shorter wavelengths require smaller air gaps for efficient coupling. As observed in Fig. 2.6, the resonance as a function of wavelength also is narrower for smaller gaps and shows broadening when the air gap is increased.

In summary, the linear coupling in the Kretschmann configuration strongly depends on the gold layer thickness but shows minor dependence on the excitation wavelength. In the Otto configuration, efficient plasmonic coupling occurs for specific combinations of gap size and wavelength: the optical pathway determines the coupling strength.

2.3.2 Gaussian Beam Excitation

While white-light excitation can be approached by plane wave calculations, laser beams usually have a Gaussian beam profile in terms of incident angle, transverse as well as in position. This distribution function of incident angles tends to broaden the observed absorption features in k -space. Experimental results and calculations with pulsed excitation from a Ti:Sapphire laser at 855 nm wavelength are shown in Fig. 2.8 for varying gold film thickness in the Kretschmann configuration (upper images) and different gap distances in the Otto configuration (lower images). The angular beam width was measured to be 0.075 degrees and the spectral full-width-half-maximum (FWHM) 8 nm, which relates to a pulse length of 150 fs and a pulse energy of 2 nJ at a repetition rate of 75.4 MHz. Since the theoretical model was fully determined by the experimental parameters, no degree of freedom was left in the calculations. The experimental results are compared to calculations of the reflected intensities with Gaussian beam excitation for the respective coupling configu-

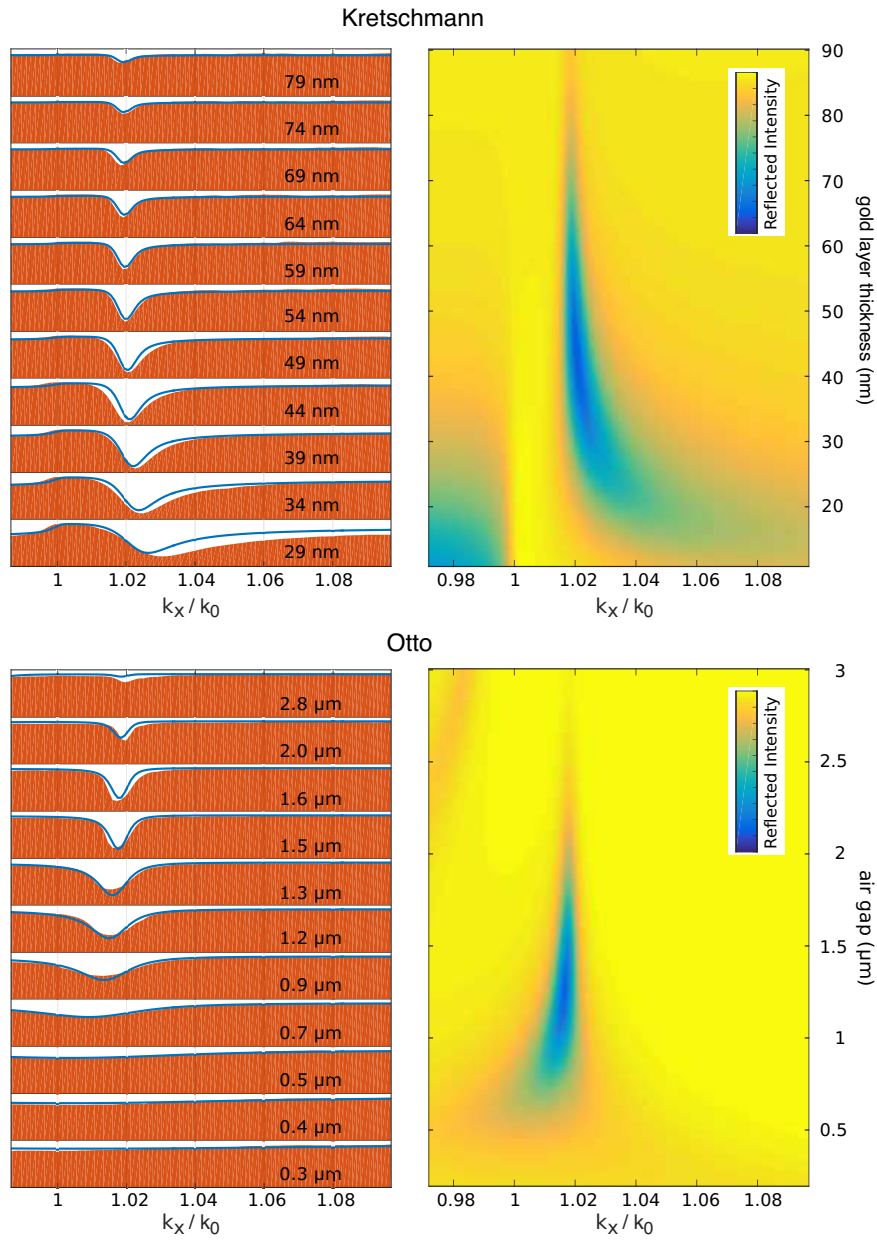


Figure 2.8: Comparison of measured reflected intensities (on the left) and calculations (on the right) for Gaussian beam excitation at 855 nm in the Kretschmann configuration (upper images) and in the Otto configuration (lower images). The beam parameters were: angular beam width: 0.075 degrees, spectral FWHM: 8 nm. Here, $k_x/k_0 = 1$ corresponds 41.8°, the TIR-angle at aBK7-glass-air interface.

rations. The right-hand side of Fig. 2.8 shows the calculations for a broad range of layer thicknesses. As for the white-light measurements, the coupling to propagating surface plasmons can be identified by the decrease in the reflected intensity beyond the TIR-angle

($k_x/k_0 = 1$), which corresponds to 41.8° for BK7-glass at a wavelength of 855 nm..

In the Kretschmann configuration, only weak coupling is observed for thick gold layers above 80 nm. When the film thickness is reduced, the coupling efficiency increases up to a maximum across 90 % at 44 nm. Further reduction again leads to lower coupling efficiency, increased radiative damping and thus to a broadening of the resonance, which is also shifted towards larger incident angles. Below 50 nm film thickness, a decrease in the reflected intensity can be found below the TIR-angle ($k_x/k_0 < 1$), which is due to partial transparency of very thin layers. Both, qualitatively (on the right) and quantitatively (blue lines on the left), the calculation fits the experiment very well.

As expected from Fig. 2.7, the optimum coupling in the Otto configuration at a wavelength of 855 nm can be found around 1400 nm air gap size. Variations in both directions lead to reduction of the coupling efficiency. In the under-coupled regime of thicker coupling layers narrowing of the resonance can be observed. Over-coupling in the region of smaller spacings causes broadening of the absorption feature whilst being shifted towards smaller incident angles and thus closer, to and even beyond, the TIR-angle. The calculations show the same characteristics and also match the quantitative coupling efficiency very well. In addition, the first order Fabry-Pérot resonance is visible in the theory at small incident angles $k_x/k_0 < 1$ and large air gaps in excess of $2.5 \mu\text{m}$.

The coupling efficiencies are compared in Fig. 2.9 as a function of gold layer thickness and air gap for the Kretschmann configuration and the Otto configuration, respectively. The air gap in Otto and the metal thickness in the Kretschmann configuration tune the coupling strength from under-coupling to impedance matching, to over-coupling. Here, the experimental data is compared to Gaussian beam calculations performed with the measured beam parameters and to plane-wave calculations (red lines at 855 nm in Fig. 2.7). For monochromatic excitation and negligible surface roughness (plane waves), perfect coupling can be observed. Critical coupling for plane-wave excitation is found at a gold layer thickness of 48 nm in the Kretschmann configuration. In the Otto configuration, an $1.4 \mu\text{m}$ air gap enables impedance matching.

However, a finite beam width leads to reduced coupling efficiency. In addition, a resonance shift towards smaller coupling layer thickness can be observed compared to plane-wave excitation. As determined from the white-light measurements and the respective calculations, the plasmon resonance is very sharp in terms of incident angles for matched coupling layers and excitation wavelengths. A Gaussian beam in contrast, which contains a broader range of incident angles has greater overlap with the broadened resonance in the over-coupled regime. This results in the resonance shift and the decrease of the coupling

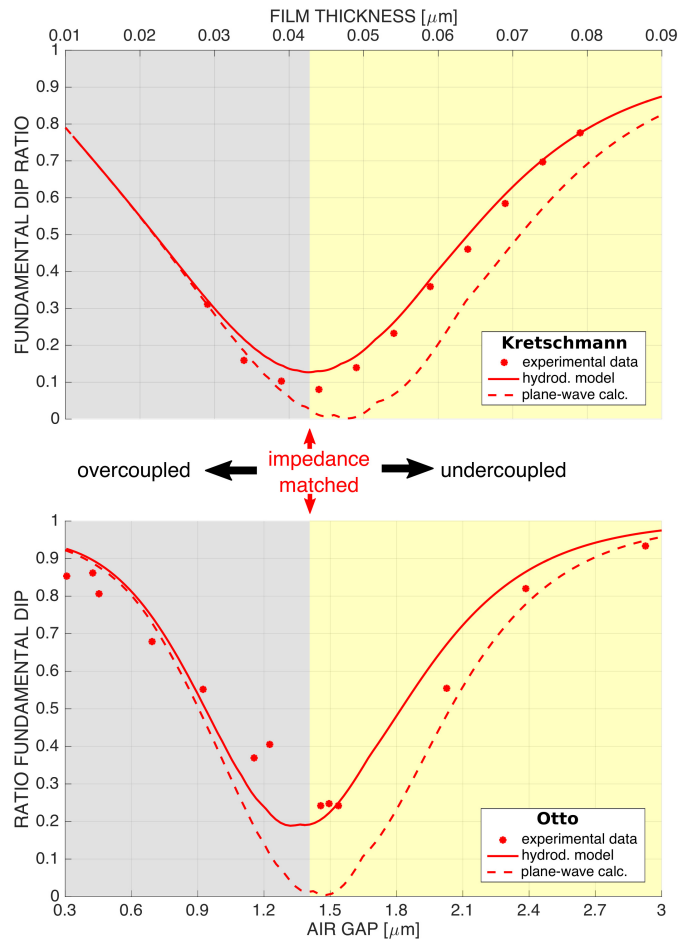


Figure 2.9: Comparison of the measured and the calculated coupling efficiency determined by the dip in the reflected intensity. The Kretschmann configuration (at the top) and the Otto configuration (at the bottom) are compared in terms of coupling efficiency for Gaussian beam excitation at a wavelength of 855 nm and for plane-wave excitation.

efficiency compared to the case of plane-wave excitation. A maximum coupling efficiency of 90% is reached for a gold layer thickness of 42 nm in the Kretschmann configuration. In the Otto configuration, optimum coupling of 80% is observed for an air gap of 1.35 μm . Hence, the overall coupling efficiency depends on the matching of the incident beam's waist to the angular width of the plasmonic resonance. Despite this, the model matches the experimental results very well.

Knowledge about linear coupling efficiency, the dependence on layer thickness, beam-shape, wavelength and material properties is indispensable for all applications that exploit surface plasmon resonances. Strong influences of the above mentioned parameters on the

overall coupling efficiency of free-space radiation to propagating SPs have been observed and analyzed. This detailed characterization of ATR coupling configurations enables further investigations of waveguide-like thin films (see Chapter 5) and second harmonic generation (Chapter 4).

3 | Theoretical Analysis of Second Harmonic Generation

In this chapter, we present a theoretical analysis of SP-enhanced SHG which is supported by a stringent calculation based on the hydrodynamic model. Reinterpreting the pioneering experiment from Simon et al. [72], we give an insight into the local nonlinear polarization for both, bulk and surface contributions. Discrepancies between harmonic conversion efficiencies for both configurations can be explained, if source terms driven by the fundamental field and harmonic out-coupling efficiencies are taken into account. We give an estimate of the nonlinear conversion parameters established by Rudnick and Stern [74] and expanded by Sipe et al. [73, 147–149] by comparing measured absolute conversion efficiencies to the hydrodynamic model. Additionally, resonances below and on the light-line are analyzed, as evidenced by their nonlinear signature [83].

3.1 SHG in the Hydrodynamic Model

The yield of SHG and the excitation of surface waves strongly depend on the matching of the incoming wave-fronts to that of the generated wave. For SHG, matching is more difficult to achieve as the nonlinear polarization is generated at every point in the nonlinear medium and interferes with the already propagating harmonic radiation. The problem is thus broken up into three tasks: (1) we have to calculate the local fields at the fundamental frequency – from which (2) the nonlinear source terms are evaluated. Here, we distinguish between sources of nonlinear radiation at the interfaces (**Q**) and in the bulk material (**A**, **B**), which are depicted in Fig. 3.1. The coupling efficiency of this radiation out to the far-field has to be included (3), which depends on the matching conditions of the generated evanescent field’s wave-vector to that of the propagating harmonic field. The hydrodynamic approach [73, 150] is adapted to investigate the second harmonic genera-

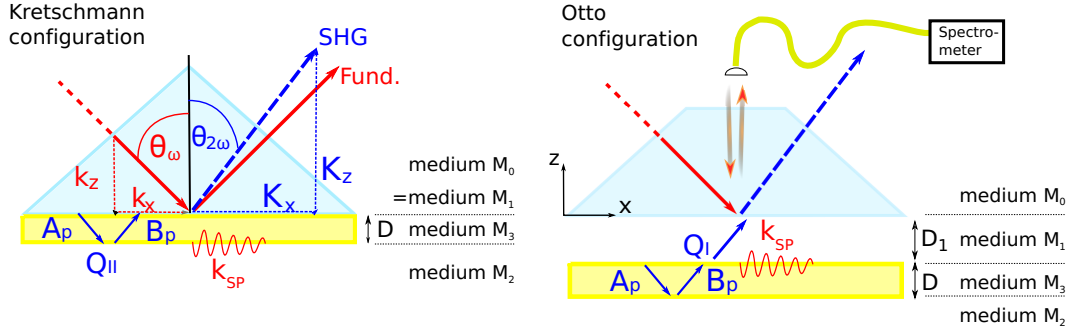


Figure 3.1: ATR excitation configurations with nonlinear sources. In the left image the Kretschmann configuration consisting of a glass prism and a thermally evaporated gold layer with thickness of order $\lambda/10$, surrounded by air. In the right image, the Otto configuration composed of a glass prism, an air gap of thickness D_1 (on the order of the wavelength λ) and a gold layer of a fixed thickness D . Here, k_x and K_x are the wave-vector projections onto the interface, relating to the incident angles θ_ω and $\theta_{2\omega}$, at the fundamental frequency ω , and harmonic frequency 2ω , respectively. **A** and **B** are the harmonic sources from the bulk metal and the **Q**s are the respective surface sources.

tion and the conversion efficiencies in both the Otto and the Kretschmann configuration. Here, cgs units are used for all calculations. A detailed derivation can be found in Appendix A.

As in chapter 3, we consider a general 2D configuration with 3 layers for the Kretschmann configuration and 4 layers for the Otto configuration:

$$\left. \begin{array}{l} z > 0 \quad \text{glass } M_0 \text{ with } \epsilon_0 \\ 0 > z > -D \quad \text{gold } M_3 \text{ with } \epsilon_3 \\ z < -D \quad \text{air } M_2 \text{ with } \epsilon_2 \end{array} \right\} \text{Kretschmann}$$

and

$$\left. \begin{array}{l} z > D_1 \quad \text{glass } M_0 \text{ with } \epsilon_0 \\ D_1 > z > 0 \quad \text{air } M_1 \text{ with } \epsilon_1 \\ 0 > z > -D \quad \text{gold } M_3 \text{ with } \epsilon_3 \\ z < -D \quad \text{substrate } M_2 \text{ with } \epsilon_2 \end{array} \right\} \text{Otto}$$

The coupling to surface waves requires p-polarized excitation, so we limit the calculation to this case. Without loss of generality, we define the plane of incidence to lie in the x - z -plane. The polarization vector for the linear and nonlinear wave is therefore given by

$$\begin{aligned}\hat{\mathbf{P}}_{i\pm} &= \frac{k_x \hat{\mathbf{z}} \mp k_{i,z} \hat{\mathbf{x}}}{k_0 \sqrt{\epsilon_i}} \\ \hat{\mathbf{P}}_{i\pm} &= \frac{K_x \hat{\mathbf{z}} \mp K_{i,z} \hat{\mathbf{x}}}{K_0 \sqrt{\mathcal{E}_i}}\end{aligned}\quad (3.1)$$

The minus sign identifies a p-polarized plane wave, that propagates “downward” in positive x-direction and negative z-direction. As the wave-vector components parallel to the interface are continuous the z-components vary for different media i such that

$$k_{i,z} = \sqrt{k_0^2 \epsilon_i - k_x^2} \quad (3.2)$$

For the SP-enhanced second harmonic, which is emitted at $\theta_{2\omega}$, the wave-vector components are given by

$$\begin{aligned}K_x &= 2k_x \\ K_{i,z} &= \sqrt{K_0^2 \mathcal{E}_i - K_x^2}\end{aligned}\quad (3.3)$$

where $K_0 = 2k_0$. For the second harmonic components, capital letters will be used throughout this work.

Now, to calculate the emitted second harmonic radiation, we have to determine the generated nonlinear polarization

$$\mathbf{\Pi}^{\text{II}}(\mathbf{r}, t) = \mathbf{\Pi}^{\text{II}}(\mathbf{r}) e^{-i\Omega t} + c.c., \text{ where } \Omega = 2\omega \quad (3.4)$$

which can be separated into a time-dependent and a time-independent part.

3.1.1 Bulk Sources

The relevant contribution from the bulk material in M_3 , which was defined to contain the nonlinear sources, is given by

$$\begin{aligned}A_p &= \int_{-D}^0 e^{-iK_{3,z} z'} \hat{\mathbf{P}}_{3+} \cdot \mathbf{\Pi}^{\text{II}}(z') dz' \\ B_p &= \int_{-D}^0 e^{iK_{3,z} z'} \hat{\mathbf{P}}_{3-} \cdot \mathbf{\Pi}^{\text{II}}(z') dz'\end{aligned}\quad (3.5)$$

for the down- (\mathbf{A}_p) and up-propagating (\mathbf{B}_p) sources, respectively. From the hydrodynamic model, the nonlinear polarization in M_3 is defined as

$$\mathbf{\Pi}^{\text{II}}(\mathbf{r}) = \gamma \nabla(\mathbf{E}_3(\mathbf{r}) \cdot \mathbf{E}'_3(\mathbf{r})) + \delta'(\mathbf{E}_3(\mathbf{r}) \cdot \nabla) \mathbf{E}'_3(\mathbf{r}) \quad (3.6)$$

To allow different options for the exciting beam’s finite angular width and to distinguish it from the related wave-mixing processes, we have to mark the second field as \mathbf{E}'_3 here.

The material parameters δ' and γ , first introduced by Bloembergen [71] can be considered as independent constants and are defined as:

$$\begin{aligned}\gamma &= \chi(\Omega) \frac{\chi(\omega)}{2en_0} \bar{\gamma} \\ \delta' &= -\chi(\Omega) \left(\frac{\chi(\omega)}{en_0} + \frac{m\omega^2 \chi^2(\omega)}{e^3 n_0^2} \right) \bar{\delta}'\end{aligned}\quad (3.7)$$

where $\bar{\delta}'$ and $\bar{\gamma}$ are phenomenological parameters, that can parameterize physics not included in the hydrodynamic model. Here, $-e$ is the charge of the electron and $n_0 = 5.9 \cdot 10^{22}/\text{cm}^3$ is the number density of electrons in gold, that are involved in the optical response. The actual linear susceptibilities of the metal at ω and 2ω are given in cgs units by

$$\begin{aligned}\chi(\omega) &= \frac{\epsilon(\omega) - 1}{4\pi} \\ \chi(\Omega) &= \frac{\epsilon(\Omega) - 1}{4\pi}\end{aligned}\quad (3.8)$$

With an incident electric field in M_0

$$\mathbf{E}_{\text{inc}}(\mathbf{r}) = \hat{\mathbf{p}}_{0-} E_{0-}^p e^{-ik_{0,z}z} e^{ik_x x} \quad (3.9)$$

where E_{0-}^p is the field amplitude, the fundamental electric field in medium 3 can be calculated by

$$\begin{aligned}\mathbf{E}_3(\mathbf{r}) &= \hat{\mathbf{z}}(e^{-ik_{3,z}z} + r_{32}^p e^{2ik_{3,z}D} e^{ik_{3,z}z}) C_z E_{0-}^p e^{ik_x x} \\ &+ \hat{\mathbf{x}}(e^{-ik_{3,z}z} - r_{32}^p e^{2ik_{3,z}D} e^{ik_{3,z}z}) C_x E_{0-}^p e^{ik_x x}\end{aligned}\quad (3.10)$$

The components

$$\begin{aligned}C_s &= \frac{t_{13}^s}{1 - \bar{r}_{30}^s r_{32}^s e^{2ik_{3,z}D}} \frac{t_{01}^s e^{ik_{1,z}D_1}}{1 - r_{10}^s \bar{r}_{12}^s e^{2ik_{1,z}D_1}} \\ C_z &= \frac{k_x}{k_0 n_3} \frac{t_{13}^p}{1 - \bar{r}_{30}^p r_{32}^p e^{2ik_{3,z}D}} \frac{t_{01}^p e^{ik_{1,z}D_1}}{1 - r_{10}^p \bar{r}_{12}^p e^{2ik_{1,z}D_1}} \\ C_x &= \frac{k_{3,z}}{k_0 n_3} \frac{t_{13}^p}{1 - \bar{r}_{30}^p r_{32}^p e^{2ik_{3,z}D}} \frac{t_{01}^p e^{ik_{1,z}D_1}}{1 - r_{10}^p \bar{r}_{12}^p e^{2ik_{1,z}D_1}}\end{aligned}\quad (3.11)$$

are Fabry Pérot coefficients, that contain multiple reflections inside the air gap M_1 and the metal M_3 :

$$\begin{aligned}\bar{r}_{12} &= r_{13} + \frac{t_{13} r_{32} t_{31} e^{2ik_{3,z}D}}{1 - r_{31} r_{32} e^{2ik_{3,z}D}} \\ \bar{r}_{30} &= r_{31} + \frac{t_{31} r_{10} t_{13} e^{2ik_{1,z}D_1}}{1 - r_{10} r_{13} e^{2ik_{1,z}D_1}}\end{aligned}\quad (3.12)$$

Here, the Fresnel coefficients for reflection and transmission from medium i to medium j are defined following Eq. 2.14.

3.1.2 Surface Sources

Next, we calculate the surface sources. The tradition in characterizing the surface source, going back to Rudnick and Stern[74], is to put the source in vacuum just beyond the metal surface, but to characterize its response in terms of the linear fields on the metal side of the interface. The effective dipole moment per unit area source is placed just outside the metal. In general, we get

$$\begin{aligned} \mathbf{Q}(\mathbf{R}) &= \mathbf{Q}e^{i\mathbf{K}_x \cdot \mathbf{x}} \\ &= -\Gamma^T \hat{\mathbf{x}} E_3^x(\mathbf{R} - z\hat{\mathbf{z}}) E^z(\mathbf{R} - z\hat{\mathbf{z}}) - \Gamma^z \hat{\mathbf{z}} (E^z(\mathbf{R} - z\hat{\mathbf{z}}))^2 \end{aligned} \quad (3.13)$$

where z is the z -position of the corresponding interface. The Γ variables are nonlinear parameters for the surface source which are defined as:

$$\begin{aligned} \Gamma^T &= -\frac{m}{e^2 n_0} \chi \omega \left(\frac{e}{m} - \frac{\omega^3 \chi(\omega)}{en_0} \right) \chi(\omega) \bar{b} \\ \Gamma^z &= -\frac{e^3 n_0}{4m^2 \omega^4} \bar{a} \end{aligned} \quad (3.14)$$

where \bar{a} and \bar{b} are additional phenomenological parameter for the out-of-plane and the in-plane component of the surface source. \bar{a} is directly corresponding to the parameter a and \bar{b} is developed from the phenomenological parameters b introduced by Rudnick and Stern [74]. While \bar{b} is expected to be of order unity, there is no prediction for \bar{a} unless the dynamics at the surface are worked out completely, as it depends on the details of the electron motion near the surface. An explicit minus sign is introduced here, as Γ is usually defined to point from the metal to the surrounding dielectric, whereas here, it points from M_2 to M_3 .

For the Kretschmann configuration, where the SP propagates along the interface between M_3 and M_2 , the surface source is defined as

$$\begin{aligned} \mathbf{Q}_{\text{Kr}}(\mathbf{R} - D\hat{\mathbf{z}}) &= \hat{\mathbf{x}} Q_{\text{Kr}}^x e^{i\mathbf{K}_x \cdot \mathbf{x}} + \hat{\mathbf{z}} Q_{\text{Kr}}^z e^{i\mathbf{K}_x \cdot \mathbf{x}}, \\ Q_{\text{Kr}}^x &= -\Gamma^T (1 - r_{32}^p)(1 + r_{32}^{p'}) e^{i(k_{3,z} + k'_{3,z})D} C_x E_{0-}^p - C'_z E_{0-}^{p'} \\ Q_{\text{Kr}}^z &= -\Gamma^z (1 + r_{32}^p)(1 + r_{32}^{p'}) e^{i(k_{3,z} + k'_{3,z})D} C_z E_{0-}^p - C'_z E_{0-}^{p'} \end{aligned} \quad (3.15)$$

The surface source in the Otto configuration is given by

$$\begin{aligned} \mathbf{Q}_{\text{Ot}}(\mathbf{R} - 0\hat{\mathbf{z}}) &= \hat{\mathbf{x}} Q_{\text{Ot}}^x e^{i\mathbf{K}_x \cdot \mathbf{x}} + \hat{\mathbf{z}} Q_{\text{Ot}}^z e^{i\mathbf{K}_x \cdot \mathbf{x}} \\ Q_{\text{Ot}}^x &= Q_{\text{Ot,up}}^x + \bar{R}_{12}^p Q_{\text{Ot,down}}^x \\ Q_{\text{Ot}}^z &= Q_{\text{Ot,up}}^z + \bar{R}_{12}^p Q_{\text{Ot,down}}^z \end{aligned} \quad (3.16)$$

Here, the source term pointing from M_3 to M_1 as well as the one pointing from M_1 to M_3 and being reflected there have to be considered, resulting in

$$\begin{aligned}
 Q_{Ot,\text{down}}^x &= \Gamma^T (1 - r_{32}^p e^{2ik_{3,z}D}) (1 + r_{32}^{p'} e^{2ik'_{3,z}D}) C_x E_{0-}^p - C'_z E_{0-}^{p'} \\
 Q_{Ot,\text{down}}^z &= \Gamma^z (1 + r_{32}^p e^{2ik_{3,z}D}) (1 + r_{32}^{p'} e^{2ik'_{3,z}D}) C_z E_{0-}^p - C'_z E_{0-}^{p'} \\
 Q_{Ot,\text{up}}^x &= -\Gamma^T (1 - r_{32}^p e^{2ik_{3,z}D}) (1 + r_{32}^{p'} e^{2ik'_{3,z}D}) C_x E_{0-}^p - C'_z E_{0-}^{p'} \\
 Q_{Ot,\text{up}}^z &= -\Gamma^z (1 + r_{32}^p e^{2ik_{3,z}D}) (1 + r_{32}^{p'} e^{2ik'_{3,z}D}) C_z E_{0-}^p - C'_z E_{0-}^{p'}
 \end{aligned} \tag{3.17}$$

With all source terms being defined, the emitted second harmonic radiation can be calculated.

3.1.3 Harmonic Emission And Nonlinear Parameter

With this preliminary work, the radiated second harmonic field

$$\mathbf{E}_{0+}^{II}(\mathbf{r}) = (E_{0+}^{pII} \hat{\mathbf{P}}_{0+}) e^{i\mathbf{K}_x \cdot \mathbf{x}} e^{iK_{1,z}z} \tag{3.18}$$

can be calculated. Combining Eqs. (3.5,3.6,3.10,3.13,3.15,3.16), we obtain

$$\begin{aligned}
 E_{0+}^{pII, Kr} &= \frac{T_{31}^p}{(1 - \bar{R}_{30}^p R_{32}^p e^{2iK_{3,z}D})} \\
 &\quad \left[\frac{K_0}{K_{3,z}} (A_p + R_{32}^p e^{iK_{3,z}D} B_p) + \frac{K_0 T_{23}^p e^{iK_{3,z}D}}{K_{2,z}} \left(\frac{K_x Q_{Kr}^z - K_{2,z} Q_{Kr}^x}{K_0 N_2} \right) \right] \\
 E_{0+}^{pII, Ot} &= \frac{\bar{T}_{10}^p}{(1 - \bar{R}_{30}^p R_{32}^p e^{2iK_{3,z}D})} \\
 &\quad \left[\frac{K_0 T_{31}^p}{K_{3,z}} (A_p + R_{32}^p e^{iK_{3,z}D} B_p) + \frac{K_0 \bar{T}_{10}^p}{K_{1,z}} \left(\frac{K_x Q_{Ot}^z - K_{1,z} Q_{Ot}^x}{K_0 N_1} \right) \right]
 \end{aligned} \tag{3.19}$$

for the Kretschmann and the Otto configuration, respectively. \bar{T}_{10}^p is the harmonic Fabry-Pérot out-coupling coefficient given by

$$\bar{T}_{10}^p = \frac{T_{10}^p e^{iK_{1,z}D_1}}{(1 - R_{10}^p \bar{R}_{12}^p e^{2iK_{1,z}D_1})} \tag{3.20}$$

and \bar{R}_{30} and \bar{R}_{12} follow their respective linear definitions at frequency ω . For the SHG efficiency, we expect the strongest influence in variations of the coupling layer's thickness, D and D_1 respectively, as been discussed by Tzeng et al. [151] and Jensen [150]. Another question is how the nonlinear parameters \bar{a} , \bar{b} , $\bar{\delta}'$, and $\bar{\gamma}$ influence the harmonic emission characteristics and the absolute conversion efficiency. In Chapter 4, an experiment is designed to investigate second harmonic generation from ATR configurations. The experimental results are compared to our theoretical model and a discussion of the different source contributions will be presented in section 4.1.1.

3.2 Mode analysis

Due to SP hybridization, thin metal films support four modes of SP propagation which are labelled as: the symmetric bound s_b and leaky s_l ; and the anti-symmetric bound a_b and leaky a_l [83]. The modes are typically non-degenerate in their k -vectors, which are found by solving the dispersion relation

$$\tanh(k_{2,z}D)(\epsilon_1\epsilon_3k_{2,z}^2 + \epsilon_2^2k_{1,z}k_{3,z}) + \epsilon_2k_{2,z}(\epsilon_1k_{3,z} + \epsilon_3k_{1,z}) = 0 \quad (3.21)$$

where ϵ_1 and ϵ_3 are the dielectric functions of the cladding and ϵ_2 of the thin film with the solution k_x complex ($k_{i,z} = \sqrt{\epsilon_i k_0^2 - k_x^2}$). The modes a_b and a_l are not accessible via the Kretschmann configuration due to their large wave-vector component. However, the symmetric modes are accessible, and also happen to possess field-enhancement localized to the metal-air interface. The k -vector degeneracy for s_b and s_l is lifted as D is reduced or ϵ_2 is made lossy. The bound mode s_b (also known as the Brewster mode) has energy flow only into the metal, from both the air and glass media, and as such, is absorbed. Consequently, the excitation of s_b via a photonic plane-wave is the cause for ATIR, which occurs at the s_b plasmon angle.

In contrast, the leaky mode s_l transports energy away from the metal, and into the glass. Unlike for the s_b mode, it is expected that only a fundamental field in the s_l mode, which drives a second-order polarization in the metal surface, will be able to radiate a second-harmonic field into the glass prism, and subsequently be detected. Henceforth, the solution to (3.21) for the fundamental s_l mode will be selected for k_x^{ω} as an ansatz for SP-induced SHG from the metal-air interface.

However, for a modified Otto configuration with symmetric cladding around the metal film in terms of its dielectric function, bound long-range modes (s_b) and bound short-range modes (a_b) are accessible [79]. These long-range surface waves can exceed the propagation lengths of SP at single interfaces by orders of magnitudes.

A theory to determine the modes, that are supported by a three-layer structure was developed by Burke et al.[83]. To ensure continuity of the tangential magnetic fields, the boundary conditions and therefore the dispersion relations

$$\begin{aligned} \tanh(k_{3,z}D)(\epsilon_1\epsilon_2k_{3,z}^2 + \epsilon_3^2k_{1,z}k_{2,z}) + (k_{3,z}(\epsilon_1k_{2,z} + \epsilon_2k_{1,z})\epsilon_3) &= 0 \\ \tanh(k_{1,z}D_1)(\epsilon_0\epsilon_3k_{1,z}^2 + \epsilon_1^2k_{0,z}k_{3,z}) + (k_{1,z}(\epsilon_0k_{3,z} + \epsilon_3k_{0,z})\epsilon_2) &= 0 \end{aligned} \quad (3.22)$$

have to be satisfied for the Kretschmann and the Otto configuration, respectively. Applying this theory on both structures, potential resonances can be calculated and compared to the experimental results and the hydrodynamic model.

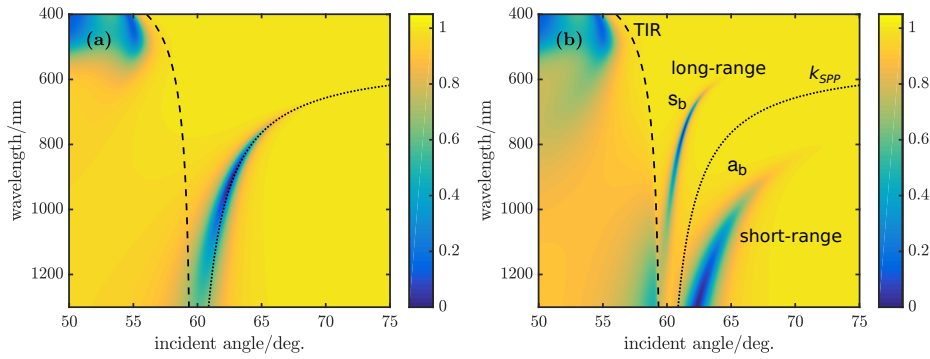


Figure 3.2: Calculated reflected intensities for thin and thick films in the Otto configuration. a) An SF-11 coupling prism is followed by a BK7 matching fluid spacer of 750 nm and a thick (bulk) gold film. b) configuration consisting of a SF11-prism, 750 nm BK7 matching-fluid, a 40 nm gold film and BK7-glass substrate. Coupled modes (long-range and short-range) can be determined by their characteristic absorption feature.

An exemplary calculation for a four-layer coupling configuration, which consists of a high-index SF-11 glass-prism, a 40 nm thick gold film and a symmetric BK7-glass cladding with a 750 nm gap between gold and prism, is shown in Fig. 3.2 b). Both modes, long-range and short-range can clearly be identified by their typical absorption feature. They lie on both sides of the plasmonic resonance for two infinite layers (k_{SPP}), to which they converge for increasing gold film thicknesses. For comparison, a calculation for SP-excitation on a thick (bulk) gold film in the Otto configuration is shown in a). As shown in section 2.3.1, the different propagation lengths can be determined from the respective resonance width. A sharp resonance implies long propagation lengths. Unfortunately, our experimental setup did not provide illumination wavelengths in excess of 1000 nm, such that we could not measure the short-range mode. Experimental results of thin-film measurements and long-range surface waves are discussed in detail in chapter 5.

On the basis of these calculations, experimental results of surface plasmon-enhanced second harmonic generation can be interpreted: Supported surface modes can be identified and the absolute nonlinear yield can be related to either surface or bulk sources. This paves the way for an experimental analysis to quantify the nonlinear parameters \bar{a} , \bar{b} , $\bar{\delta}'$, $\bar{\gamma}$. Furthermore, surface-waves in thin films with symmetric cladding can be analyzed in terms of their mode profile, propagation length and field enhancement.

4 | Plasmon-Enhanced Second Harmonic Generation

In 1968, Bloembergen et al. [71] published their pioneering work on second harmonic generation (SHG) in reflection from media with inversion symmetry, a phenomenon, that is strongly dependent on the intensity of the driving fundamental field and its matching to the emitted harmonic radiation. Because of the sub-wavelength confinement to the interface which can lead to a huge field enhancement and the inversion symmetry of noble metals, the consequential application of surface plasmons (SP) to SHG has led to the fast developing field of nonlinear plasmonics [60, 67, 68, 152, 153]. In return, SHG is often used as indication for plasmonic field enhancement [29, 69].

In this chapter, the surface plasmon enhanced nonlinear yield is analyzed in terms of absolute conversion efficiency, form of the nonlinear resonance and particle interactions, that are involved in the actual conversion process. First, the two basic ATR configurations (Otto and Kretschmann) are investigated in their second harmonic yield and out-coupling efficiency to the optical far-field, which are then compared to the theoretical model, Chapter 3. In this context, the nonlinear parameters \bar{a} , \bar{b} , $\bar{\delta}'$, and $\bar{\gamma}$ are determined for gold and their influence on the emitted radiation is investigated. The modes which are supported in the respective configurations are then evaluated in their contribution to SHG. Beyond that, the origin of the second harmonic emission is rigorously investigated: A detailed analysis of incident and exit angles provides an insight into the nonlinear conversion processes. This attempt is supported by a study of two-beam excitation measurements and a subsequent interpretation of degenerate four-wave mixing interactions.

The measurements were performed with a the short-pulsed laser setup from section 1.2 (see Fig. 1.4).

4.1 Absolute Nonlinear Yield from ATR Coupling Configurations

We constrain the theoretical model from Chapter 3 with the absolute second harmonic yield from the experiment to arrive at estimates for the nonlinear parameters. Combined with the linear analysis from chapter 2 we can also evaluate linear and nonlinear coupling efficiencies in the Kretschmann configuration and the Otto configuration. The experimental data and calculated intensities can be found in Fig. 4.1 a-c) for the Kretschmann and Fig. 4.1 d-f) for the Otto configuration, respectively.

Figure 4.1a) shows the reflected fundamental intensity and the emitted SHG in the Kretschmann configuration. A k -space intensity spectrum over the relevant angular range was measured for different gold layer M_3 thickness. All other parameters were kept constant. In the investigated wavelength range, metal layers over 100 nm could not provide coupling to SP's, as the evanescent field was not penetrating to the relevant interface. Beginning from 79 nm Au thickness, the fundamental signal (red curve on the left-hand side) was weakly coupled as a small dip of 5% ratio could be found at $k_x/k_0 = 1.02$, which is close to the calculated ideal plasmon wave-vector and corresponds to 42.2° for the used BK7-glass coupling prism. A reduction in thickness led to increased fundamental coupling, which was optimum at 44 nm (i). Simultaneously, the dip broadens (iii) and its position slightly shifts to larger wave-vectors. As M_3 is almost transparent for very thin layers, the edge of total internal reflection $k_x/k_0 = 1$ becomes visible.

The emitted second harmonic radiation (filled blue area) is weakly visible starting from 64 nm layer thickness. In general, the harmonic peak follows the fundamental dip in terms of broadening (iii) and displacement as the thickness is decreased further. For a film thickness 50 nm and thinner layers, the wave-vector position of the individual peaks starts to shift towards smaller values with reference to the corresponding dips. However, the optimal yield of SHG, which shows a maximum at gold layer thickness of 39 nm (ii), occurs for thinner layers as the optimal coupling to the fundamental. The experimental results for SHG are supported by results from the theoretical model in Fig. 4.1b), which includes the complete intensity from bulk (A_p, B_p from Eq. 3.5) and the respective surface source (Q_{Kr} from Eq. 3.17). The maximum peak position in the calculation can similarly be found around 40 nm (ii) and broadening for thin layers is likewise visible (iii). Fig. 4.1c) shows the harmonic source signal at the interface (A_p, B_p and Q_{Kr} 's) in M_2 (which is air) as red lines and the out-coupling coefficient T_{31}^p (Eq. 3.19) as logarithmic contours. Similar to the measurement, the field strength from the theory clearly follows the fundamental intensity, and

4.1. ABSOLUTE NONLINEAR YIELD FROM ATR COUPLING CONFIGURATIONS

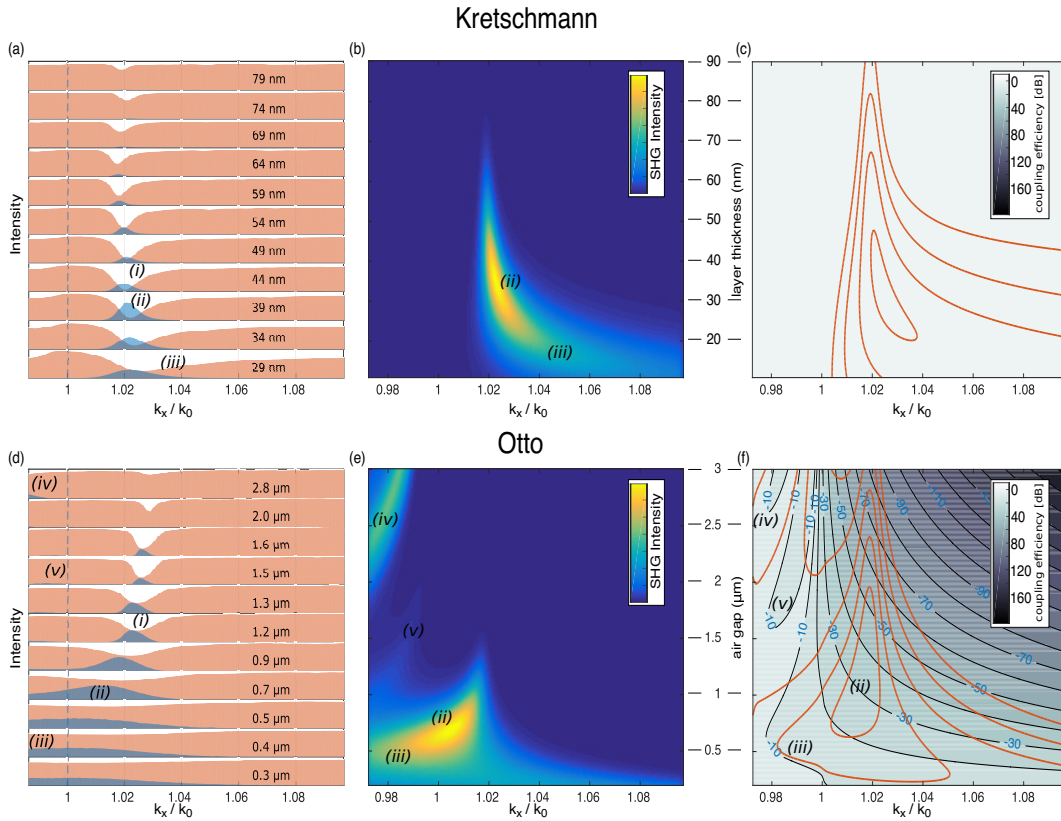


Figure 4.1: Comparison of theory and experimental data for fundamental coupling and second harmonic emission in the Otto and the Kretschmann configuration (a) Experimental data for varying layer thickness in Kretschmann configuration, red = reflected fundamental intensity, blue = emitted second harmonic intensity. (b) Theoretical calculation for SHG according to the hydrodynamic model. (c) Calculation of the harmonic source's intensity at the metal surface (red) and out-coupling coefficient as contours with logarithmic scale. Every full step is a power of 10. (d) Experimental data for different air gaps in Otto configuration. (e) Theoretical calculation for SHG according to the hydrodynamic model. (f) Calculation of the harmonic source's intensity at the metal surface (red) and out-coupling coefficient through air gap and prism as contours with logarithmic scale. Every full step is a power of 10.

in the case of the Kretschmann configuration, the effect of out-coupling parameter leads to only small increase of the harmonic intensity for very small layer thickness.

Concerning variation of the air gap in the Otto configuration, shown in Fig. 4.1(d-f), a behavior similar to the Kretschmann configuration was observed for the fundamental intensity. Starting at an air gap of $2.8 \mu\text{m}$, only a small absorption feature is visible, where the last Fabry-Pérot mode was expected (iv). Furthermore, a small harmonic Fabry-Pérot contribution (v) can be seen, that is also due to the out-coupling parameter. The linear coupling strength to the fundamental SP, which theoretically lies at $k_x/k_0 = 1.02$ for two

infinite media, found a maximum (i) around a $1.5 \mu\text{m}$ air gap. The dip broadens upon reducing the air gap and shifts slightly to smaller wave-vectors, contrary to the Kretschmann case.

While the lowest order Fabry-Pérot mode could be identified by its characteristic SHG peak (iv), the SP-related SHG (ii) improves at a $0.7 \mu\text{m}$ air gap, due to the better out-coupling efficiency for this wavelength. As the air gap is minimized still further, the absorption and SHG features in k -space broaden (iii). Below $0.5 \mu\text{m}$ the SP mode (as evidenced by its SHG peak) was even inside the angle for total internal reflection ($k_x/k_0 = 1$), where a propagating wave is expected. Here, hybridization with a waveguide like mode in the coupling layer leads to further broadening of the peak. Evidence of strong out-coupling can be revealed if the hydrodynamic theory is considered. In Fig. 4.1e) the calculated emitted second harmonic radiation is shown, which is in good agreement with the experimental data.

The harmonic sources and individual coupling parameters have been examined more closely to identify the cause of the broadening: Fig. 4.1f) shows the nonlinear source terms from bulk and surfaces (A_p, B_p and Q_{Ot} 's) at the interface of the metallic M_3 and the surrounding air gap M_1 before coupling through air into the prism M_0 . In contrast to the Kretschmann configuration, the out-coupling efficiency \bar{T}_{10}^p (Eq. 3.20) which is given by the black contour lines, effectively acts as a selection effect for the emitted radiation and is responsible for the large broadening (iii) of the harmonic radiation's emission at small gap sizes.

In Fig. 4.2, the ratio of the dip-intensity to an off-resonant reference at the fundamental wavelength and the absolute values of second harmonic yields for the Otto and the Kretschmann configurations are collected. Thus the second harmonic conversion efficiency is compared to the fundamental coupling. It can clearly be seen, that both harmonic contributions have their relative maximum in an over-coupled regime beyond impedance matching of the exciting fundamental with the surface plasmon. Both configurations show up to 80% coupling efficiency for the fundamental wavelength while the second harmonic yield is one order of magnitude greater for the Kretschmann configuration. The harmonic signal in the Kretschmann configuration has its maximum value at a film thickness of 35 nm, which is close to the fundamental optimum at a film thickness of 42 nm but is already in the over-coupled regime.

The hydrodynamic model matches the fundamental data for both configurations very well. For the Otto configuration, impedance matching at the fundamental wavelength is found at an air gap of $1.35 \mu\text{m}$, while the SHG maximum is located at an air gap of

4.1. ABSOLUTE NONLINEAR YIELD FROM ATR COUPLING CONFIGURATIONS

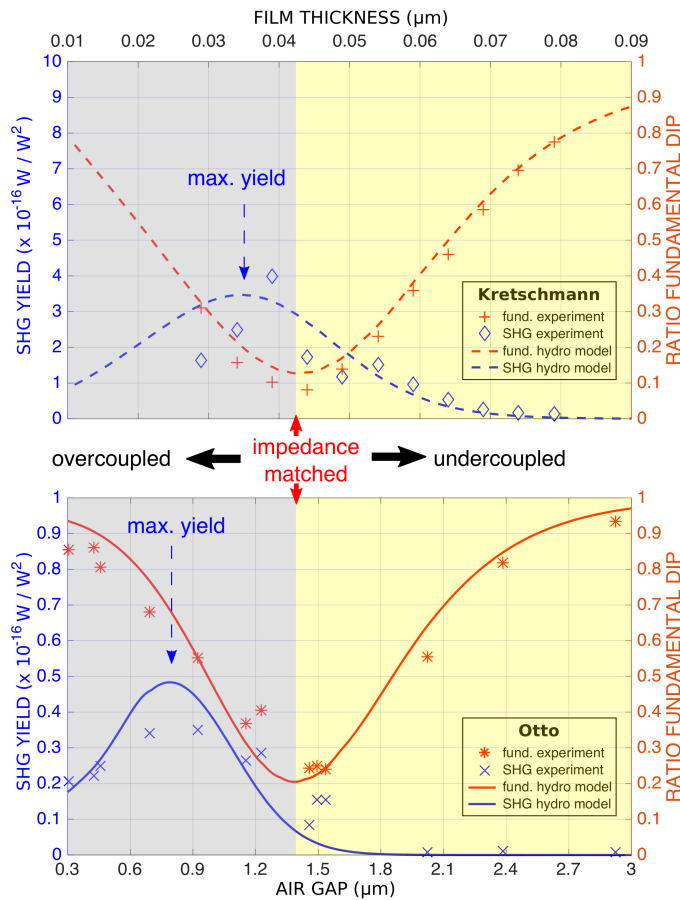


Figure 4.2: SHG yield and fundamental impedance matching in the Otto and the Kretschmann configuration. The linear coupling efficiency and the absolute nonlinear conversion efficiency are compared for the Kretschmann (upper image) and the Otto configuration (lower image). Both values are a function of incident angle and the thickness of the coupling layer, the gold film and the air gap, respectively.

$0.8 \mu\text{m}$. The difference between the optimal coupling conditions for the fundamental and the harmonic is much larger for the Otto than for the Kretschmann configuration. The gap size plays a larger role for shorter wavelengths (i.e. the second harmonic), so the influence of the out-coupling efficiency to the second harmonic yield is carrying weight, as it was shown in Fig. 4.1f). Although the source strengths are comparable for both configurations inside the metal, the absolute yield is less in the Otto configuration. This difference is reproduced by the hydrodynamic model and the harmonic yield as a function of layer thickness, and is in good agreement with the experiment.

The nonlinear parameters are obtained by using the least square method to fit the reduced data set in Fig. 4.2 for both configurations collectively. The following orders of

magnitude were found:

$$\begin{aligned}\bar{\gamma} &\approx 1 \\ \bar{\delta}' &\approx 1 \\ \bar{b} &\approx 5 \\ \bar{a} &\approx 10^{-2}\end{aligned}$$

These values match the predictions for the hydrodynamic model very well. The parameter for the in-plane surface source \bar{b} is above the expected value of order unity, which can be explained by surface imperfections (i.e. so-called hot-spots of greater local intensity) and roughness, that are not contained in the model. As mentioned above, there is no precise prediction for \bar{a} . A further analysis of the nonlinear parameters can be found in the following section.

4.1.1 Influence of the Nonlinear Parameters

The nonlinear parameters were obtained as follows: \bar{a} could be constrained by noting its waveguide-like resonance (Fig. 4.3b), which is very weak in the experimental data. This feature, in combination with the out-coupling coefficient, leads to the broadening of the harmonic signal, which was observed in Fig. 4.2. For values greater than 0.05, a "waveguide" - like resonance appears in the Otto configuration at the angle of total internal reflection which is not observed in the experimental data. This resonance can be much stronger than the plasmonic resonance for values of order unity and above but has only minor influence here.

In the Kretschmann configuration, the conversion efficiency decreases for increasing values of $\bar{\delta}'$. A minimum can be found around $\bar{\delta}' \approx 65$, then the efficiency starts increasing again. For values ~ 60 , the influence of the plasmon resonance is sufficiently lowered, so that a second resonance at larger incident angles can be seen (Fig. 4.3a). This resonance is not visible in the experiment and can be used to adapt the parameter. Variation of $\bar{\delta}'$ has negligible influence in the Otto configuration.

The parameters with the largest influence on the nonlinear yield, \bar{b} and $\bar{\gamma}$ are determined, using a least square routine for both experimental data sets, Kretschmann and Otto. The different nonlinear parameters are varied one by one while the other values are kept constant. The conversion efficiencies shown here are the maximum values obtained by variation of film thickness and incident angle for each set of parameters.

Variation of \bar{b} has a strong influence in both configurations (Fig. 4.4a). In the Kretschmann configuration, it is strictly increasing while for the Otto configuration, there is a minimum

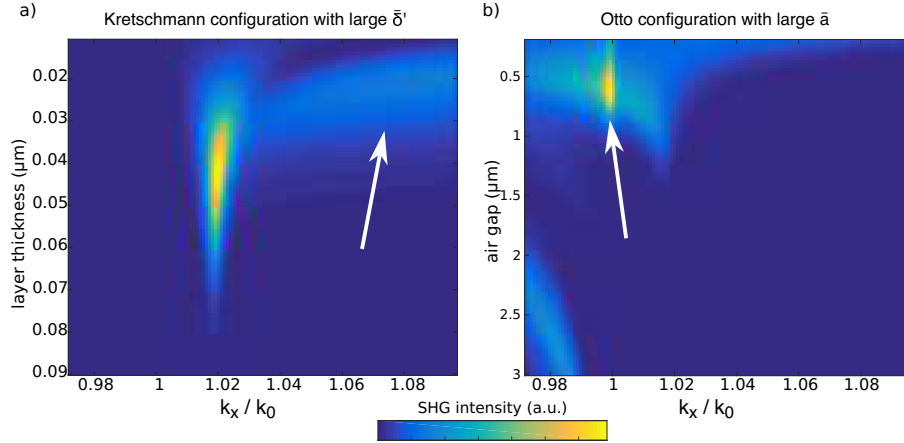


Figure 4.3: Calculated second harmonic emission for overly large values of the nonlinear parameters: $\bar{\delta}' = 60$ in (a) for the Kretschmann configuration. Additional emitted radiation is visible for incident angles larger than the plasmon resonance. (b) shows a calculation in the Otto configuration with $\bar{a} = 0.1$. Here, a “waveguide”-like resonance is visible at the TIR angle.

intensity around $\bar{b} = 0.5$. As the model gives smaller values for the conversion efficiency than expected from the experiment, if all parameters are set to one, \bar{b} has to be increased to a value ~ 5 to match the experimental results. In Fig. 4.4b), one can see, that for values of order unity, the conversion efficiency is decreasing for increasing $\bar{\gamma}$ in the Otto configuration. It actually has a minimum at around ~ 8 , while it is strictly rising in the Kretschmann configuration. The nonlinear parameters antagonize each other and \bar{b} and $\bar{\gamma}$ are identified to have the greatest influence on the conversion efficiency. The exact parameters for the final fits calculated by least squares are:

$$\begin{aligned}
 \bar{b} &= 5.96 && \text{in - plane component of surface SHG} \\
 \bar{\delta}' &= 0.8 && \text{bulk SHG} \\
 \bar{\gamma} &= 0.77 && \text{bulk SHG} \\
 \bar{a} &= 0.01 && \text{out - of - plane component of surface SHG}
 \end{aligned}$$

By comparing the different harmonic contributions, the bulk term B_p and the surface sources Q_{Kr}^x, Q_{Ot}^x have been identified to be the dominant driving sources in both configurations. The influence of the source A_p is much weaker in the Kretschmann configuration and negligible in the Otto configuration. Q_{Ot}^z has to be treated carefully as it contains additional “waveguide”-like resonances. The theory now matches both experimental results very well, which can be seen in the comparison with the experimental results (Fig. 4.2). The difference of one order of magnitude in the conversion efficiencies is included as well as the angular dependence of the resonances.

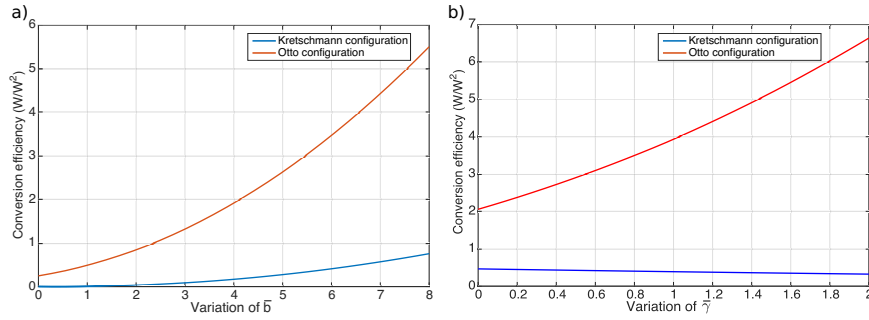


Figure 4.4: Absolute harmonic conversion efficiency as a function of the nonlinear parameters \bar{b} in (a) and $\bar{\gamma}$ in (b) for the Otto and the Kretschmann configuration.

Given the similarity of their linear responses in k -space, it has generally been thought that both coupling configurations, Otto and Kretschmann, are equivalent. However, as demonstrated experimentally in this work, the second-harmonic responses in the two configurations differ markedly in their qualitative behavior (as a function of coupling strength), and quantitatively in terms of their radiated nonlinear yield. These surprising results can be understood in terms of the nonlinear sources in and on the metal, how they are driven by the fundamental field and SP resonances, and the limitations imposed by the out-coupling efficiency of the second-harmonic to the far-field. The analysis using the hydrodynamic model of the metal film, treated in the respective configurations, confirms that the harmonic out-coupling efficiency dominates in SHG yield from the Otto configuration, while the fundamental SP resonance governs the yield in the Kretschmann configuration.

In addition, both coupling methods also show perturbations to the fundamental's SP momentum and lifetime in the limit of strong radiative damping. Curiously, these deviations from the ideal un-coupled SP are caused by the strong influence of the coupling layer and SP hybridization with a photonic mode in the Otto configuration, while the Kretschmann configuration is only affected for very thin metal layers.

Although the Otto configuration is considered to be the most non-invasive method of coupling SP to the far-field, thereby guaranteeing the longest SP lifetimes and greatest field enhancements, those field enhancements do not lead to a proportionately higher yield of second-harmonic radiation. The hydrodynamic model enables a qualitative analysis of the experimental data as well as a quantitative calculation of the absolute second-harmonic yield. Consequently, a classification of the nonlinear parameters could be given, showing, that the in-plane surface source is stronger than predicted by the hydrodynamic model.

4.1.2 Mode Analysis

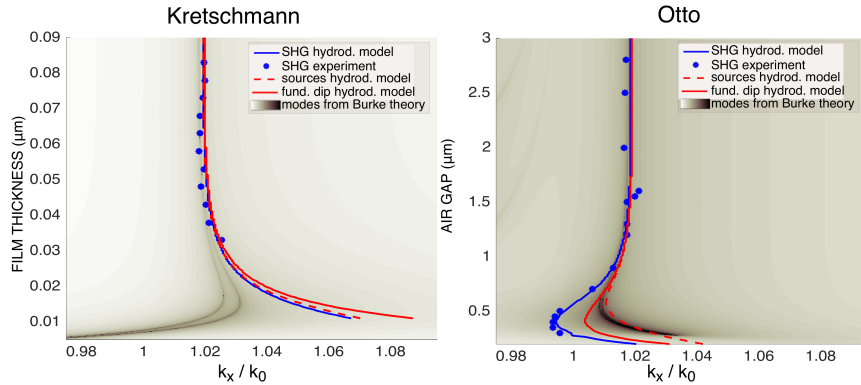


Figure 4.5: Comparison of the SHG peak positions for experimental data (blue dots) and theory. Solutions from Burke’s theory for the modes, that are supported by the Kretschmann (left-hand figure) and the Otto configuration (right-hand figure) are shown as shaded background. The radiated second harmonic’s position (blue lines), source terms at the interface, where the SP is propagating (dashed red lines) and fundamental dip position (red line) are calculated with the hydrodynamic model.

Fig. 4.5 shows a comparison of the measured peak positions and the calculation for different layer thicknesses. The blue lines represent the maximum of the calculated harmonic radiation from Fig. 4.1b) and (e), while the dashed red lines show the source terms from Fig. 4.1c) and (f), all calculated with the hydrodynamic model. The solutions for the supported modes from Burke’s theory (shaded background, the residual of Eq. 3.22) are also included.

For the Kretschmann configuration, the experimental data is in good agreement with the theory. The out-coupled second harmonic radiation directly follows the harmonic source terms at the interface, where the SP is excited. For a film thickness below 30 nm, the Gaussian beam calculation diverges from the mode analysis. In this regime, the solutions of the mode analysis can only be approached by plane-wave calculations which can be explained by the short lifetime of surface plasmons in very thin films, seen as broadened SP resonances in Chapter 2. The second harmonic yield in this regime is very low and therefore the peak’s position is dominated by the resonance in the Fresnel coefficients. Due to technical reasons, no samples could be manufactured below 25 nm layer thickness to investigate this regime experimentally. For very thin layers, vapor deposition leads to island growth of the metal and produces rather rough surfaces. In this regime, the Burke theory also contains mode splitting between the bound and the leaky solution of Eq. 3.22.

As expected from Fig. 4.1f), the harmonic radiation in the Otto configuration does not directly follow the source terms but is strongly influenced by the out-coupling parameter (Eq. 3.20). This parameter, included in the hydrodynamic model (blue line), fits the experimental results (blue dots) remarkably well. Below $1.5 \mu\text{m}$ air gap, it does not directly follow the source terms at the interface (dashed red line) but is shifted to smaller wave-vectors and even crosses the light-line for the fundamental wavelength. The maximum for the source terms lies on the solution for the supported modes of Burke's theory. Solutions for the Fabry-Pérot modes already analyzed in Fig. 4.1e), (iv) and (v) were also found. The fundamental dip position is found in between the out-coupled radiation and the source terms. This influence of the effective layer thickness was already found for the intensities in Fig. 4.2. The proximity of the coupling prism affects the dielectric environment and hence the plasmonic resonance.

4.2 Plasmon-Photon Wave Mixing in 2D- k -Space Spectroscopy

In this section, experimental results are presented, that uncover the plasmon-photon nonlinear interactions which are responsible for the enhanced SHG from a metal nano-film. What makes this approach distinctive is that the pioneering experiments [72] are revisited where SP propagate with well-defined k -vectors on the surface of bulk metal; and the application of k -space spectroscopy in the Kretschmann configuration to examine the emitted SHG in a way that provides precise information on SP nonlinear phase-matching. To promote SHG from a surface, the nonlinear phase matching conditions have to be taken into account [18]. Similar to SHG in bulk-materials [154], the phase of the fundamental field and the related nonlinear polarization have to be matched to the excited second harmonic light's phase.

For the Kretschmann configuration, the maximum intensity of SHG will therefore be obtained for both SP-excitation and nonlinear phase-matching. Because each type of nonlinear interaction conserves momentum, they can be distinguished by their unique signature in k -space. The results show that the role of the surface-plasmon is not merely to provide a local field enhancement for driving SHG at the metal surface, but it is the fundamental SP themselves that are annihilated and convert into the second-harmonic photon [29]. This knowledge not only has didactic value, but is the key to developing new structures that fully exploit SP nonlinearities. A striking example would be the inverse process to plasmon SHG, namely parametric down-conversion, which could be a source of entan-

gled SP pairs at compact length scales.

4.2.1 Enhanced SHG from Plasmon-Photon Interactions

The analysis is restricted to SP in the Kretschmann configuration, which comprises a glass prism coated with a metal film, exposed to air. As in the chapters 2 and 3, the media are described by their complex dielectric functions: glass ϵ_1 , metal ϵ_3 of thickness D , and air ϵ_2 .

Assuming that all permutations of surface plasmon (p) and photon (f) are allowed in the second-order nonlinear process of SHG, which can generate either p or f ; and that each process can be identified by its condition for momentum conservation.

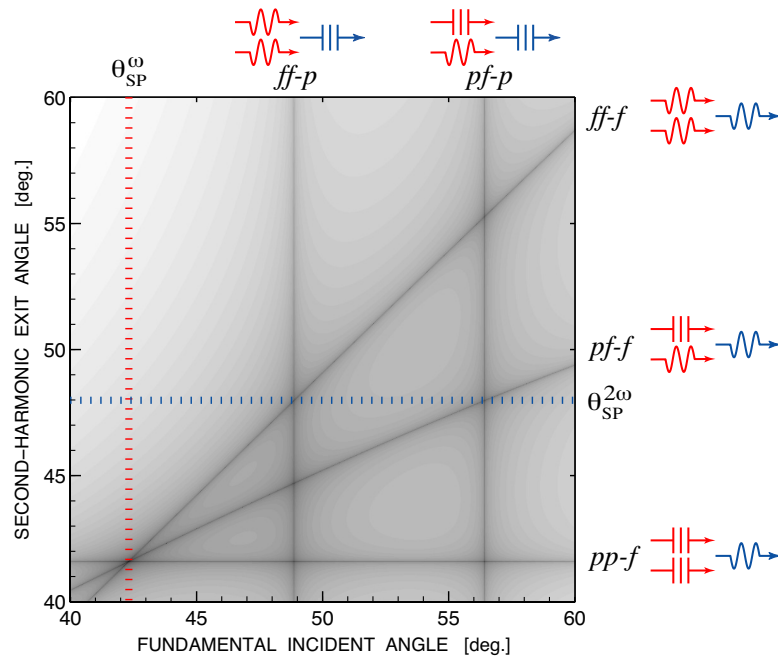


Figure 4.6: Feynman diagrams and nonlinear phase-matching conditions for surface plasmons (p) and photons (f) interacting for SHG. Exemplary, the grand residuals of the phase-matching conditions for SHG are mapped across the angles for an input fundamental of 800 nm and an output second-harmonic of 400 nm. Each interaction is identified by its own dark line. Dashed lines mark the angles θ_{SP} for linear phase-matching between (p) and (f). Calculation for pure silver on BK7 glass in the Kretschmann configuration (thick-film limit).

The following nonlinear phase-matching conditions for the set of SHG processes are

introduced:

$$2k_f^\omega(\theta_{\text{in}}) - k_f^{2\omega}(\theta_{\text{out}}) = \Delta_{ff-f} \quad (4.1)$$

$$k_p^\omega + k_f^\omega(\theta_{\text{in}}) - k_f^{2\omega}(\theta_{\text{out}}) = \Delta_{pf-f} \quad (4.2)$$

$$2k_p^\omega - k_f^{2\omega}(\theta_{\text{out}}) = \Delta_{pp-f} \quad (4.3)$$

$$2k_f^\omega(\theta_{\text{in}}) - k_p^{2\omega} = \Delta_{ff-p} \quad (4.4)$$

$$k_p^\omega + k_f^\omega(\theta_{\text{in}}) - k_p^{2\omega} = \Delta_{pf-p} \quad (4.5)$$

$$2k_p^\omega - k_p^{2\omega} = \Delta_{pp-p} \quad (4.6)$$

where k_p^ω and $k_p^{2\omega}$ are the k -vectors of the SP for the fundamental ω and second-harmonic 2ω frequencies, where in the thick-film limit $k_{SP} = k_0 \sqrt{\epsilon_3 \epsilon_2 / (\epsilon_3 + \epsilon_2)}$. Photon plane-waves propagate into and out of the glass medium with angles θ_{in} and θ_{out} (to the normal) which project k -vector components parallel to the surface: $k_f^\omega = k_0 (\epsilon_1^\omega)^{1/2} \sin \theta_{\text{in}}$ and $k_f^{2\omega} = 2k_0 (\epsilon_1^{2\omega})^{1/2} \sin \theta_{\text{out}}$ (see Chapter 2). Here, silver [146] was used for the metal layer due to its sharp resonance, which enables the study of the pf - f -interaction and produces enough SHG to enable tracking in k -space. But silver samples also show degradation (tarnish) over two weeks not visible with the naked eye, but measurable. In the SP resonance this leads to increased imaginary components of the dielectric function, and thus to increased losses, which weaken the SP resonance, and hence the field enhancement. Therefore, a quantitative study of pf - f -interaction strength over varying auxiliary beam angles was not possible.

The plasmon angle θ_{SP} is defined as the angle for linear phase-matching of the photon to the SP, by solving for $k_f = k_{SP}$. The nonlinear phase-matching conditions, as given by the Δ in equations (4.1–4.6), were multiplied together and plotted in Fig. 4.6 as a gray-scale map across θ_{in} and θ_{out} . Momentum conservation for each nonlinear interaction (e.g. $\Delta_{ff-f} = 0$) thus appears as a dark line. Given that momentum conservation is a general requisite for strong SHG, it is anticipated that k -space measurements of SHG from a metal film will adhere to the dark lines, and therefore allow identification of the various plasmon-photon nonlinear interactions.

A typical image taken by the setup is shown in Fig. 4.7 b), where a prism sample with 30 nm silver layer was illuminated at an angle of 45.0° with 86 mW, a wavelength of 800 nm and p-polarization. Additional tests were performed with colored filters to determine the wavelengths of the spots on the image. The spot I^ω was identified as the reflected fundamental and $I^{2\omega}$ as the generated second-harmonic which was emitted by the sample at 44.3° . This offset is due to the dispersion of the metal and the coupling prism. Varying the input power from 20 mW to 320 mW revealed a linear response for

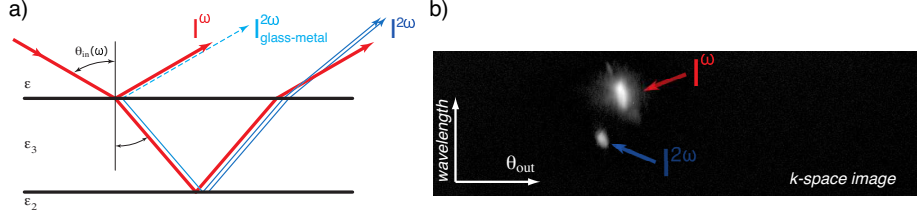


Figure 4.7: Optical path and CCD image for one-beam excitation in the Kretschmann configuration with a silver sample a) shows the three-layer system with reflections and second harmonic contributions from both interfaces. b) shows raw data from the CCD for illumination at 45.0° . Fundamental and second harmonic signal are clearly resolved in wavelength and k -space.

I^ω , and quadratic responses for the $I^{2\omega}$, which confirms the second-order nonlinear process. Changing the input beam to s-pol at constant power caused the harmonic emission to vanish. In s-pol, the lack of an electric field component normal to the surface denies the generation of SP and also annuls the quadrupolar source of nonlinearity at the metal surfaces.

The SHG emission from the silver film sample was mapped in k -space using a high resolution angle scan of the incident fundamental field (241 steps, 10 s exposures). An integration of the recorded intensity was performed only in wavelength around the second-harmonic, thereby preserving greater angular resolution.

In Fig. 4.8a), the strong SHG, $I^{2\omega}$, adheres to an offset diagonal line $\theta_{\text{out}} = \theta_{\text{in}} - 0.7^\circ$. As mentioned above, the offset is caused by the dispersion of the glass and metal media. A weak harmonic emission can be seen lying on a diagonal line $\theta_{\text{out}} = \theta_{\text{in}}$, which is generated at the prism-metal interface and results from corrugation of the silver. Because both harmonic contributions follow a diagonal, they originate from a purely photonic process (SHG via $ff-f$). However, the prominent spot at $\theta_{\text{in}} = 43^\circ$ displays elongation in the θ_{in} axis, which indicates a contribution other than the $ff-f$ interaction. In Fig. 4.8b), profiles along the θ_{out} axis were normalized to the maximum value in each curve. Near the corners of Fig. 4.8b), $I^{2\omega}$ follows the diagonal $\theta_{\text{out}} = \theta_{\text{in}} - 0.7^\circ$, which comes from the $ff-f$ interaction. However, there is a strong off-diagonal component that remains fixed at $\theta_{\text{out}} = 42.3^\circ$. An explanation can be given with regard to Fig. 4.6. The off-diagonal component originates from the nonlinear interaction where two fundamental SP are converted into a second-harmonic photon ($pp-f$). Furthermore, this technique can be extended to probe the full gamut of interactions, far from the plasmon angle, by introducing an additional excitation that ensures a supply of fundamental SP.

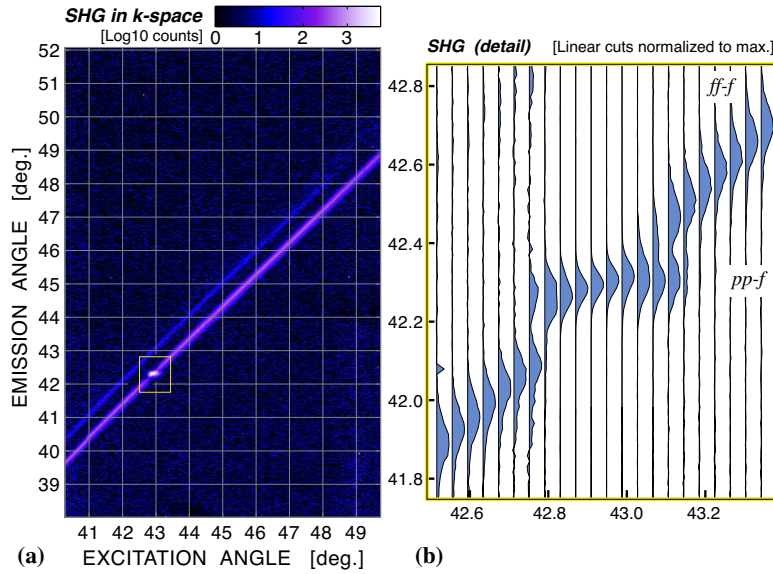


Figure 4.8: Revealing pp - f interaction by analyzing incident and exit angles of second harmonic radiation. (a) shows the harmonic emission as a function of incident and exit angle. By undergoing the plasmonic resonance, enhanced emission and horizontal elongation is visible. Cuts in (b) distinguish purely photonic conversion from plasmonic interaction.

By moving to a lower dispersion region (fundamental wavelength at 925 nm), absorption features for the second-harmonic became accessible in the limited angle range. In Fig 4.9, the beams I^ω and $I^{2\omega}$ were tracked and integrated to get the optical power while the incident angle of the fundamental beam was scanned (173 mW, 121 steps, 20 s exposures). The reflected harmonic intensity $I^{2\omega}$ shows a background contribution due to the ff - f interaction. A strong narrow peak is visible at 42.8° that is attributed to the excitation of SP, which caused a local field enhancement at the air-metal interface and therefore boosted SHG. As identified earlier in the k -space maps, the interaction is pp - f . Adjacent to the peak is a sharp notch at 42.6° which is destructive interference between the source contributions from the glass-metal and metal-air interfaces. A broad minimum is visible in the background at 46.8° , which stems from ATR at 2ω . The fundamental curve I^ω shows the characteristic dip at 42.9° . As indicated in chapter 2, this absorption feature is assigned to the ATR effect arising when the mode for ω is excited at its plasmon angle, thus delivering energy to the metal film wherein it is absorbed.

The only indication for the direct creation of a second harmonic plasmon (Eqs. 4.4-4.5) is the absorption feature $\text{ATR}(2\omega)$ in the harmonic signal $I^{2\omega}$. However, no enhanced emission was detectable at the predicted exit angle. Rather the background SHG of pho-

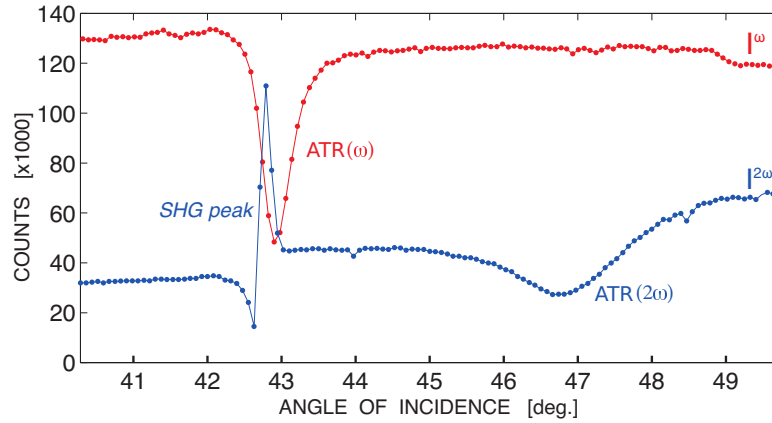


Figure 4.9: Fundamental and second harmonic radiation from a 57 nm silver sample. The excitation beam at 925 nm is scanned in terms of incident angle. Its integrated intensity is detected simultaneously with the generated second harmonic intensity for each angular position.

tonic origin was absorbed like in ATR. Whereas the direct excitation by absorption of two-photons $ff-p$, respective a plasmon and a photon $pf-p$ apparently was not sufficiently efficient, purely plasmonic frequency doubling $pp-p$, Eq. 4.6, was impossible due to the dispersion of the metal.

It has been demonstrated how k -space spectroscopy can identify the combinations of elementary excitations (photons, surface-plasmons) which contribute to nonlinear frequency conversion in metal surfaces. SHG was investigated from an optically-excited metal nano-film in the Kretschmann configuration. The results revealed an interaction where two surface-plasmons annihilate to create a second-harmonic photon. Knowledge of the relevant nonlinear interactions that occur in nano-metallic structures is vital for the development of applications in quantum plasmonics, such as sub-wavelength sources of entangled surface-plasmons.

4.2.2 Degenerate Three-Wave Mixing from Plasmon-Photon Interactions

It was predicted in the previous section, that the different types of plasmon-photon interaction can be clearly identified by their signatures in k -space [29]. The special case of two plasmons that generate a photon of twice the frequency was shown. The nature of the nonlinear process, that the plasmon acts not only like a far-field enhanced catalyst but as an active partner, has recently been revealed by Palomba et al. for $\chi^{(3)}$ -processes like FWM [46].

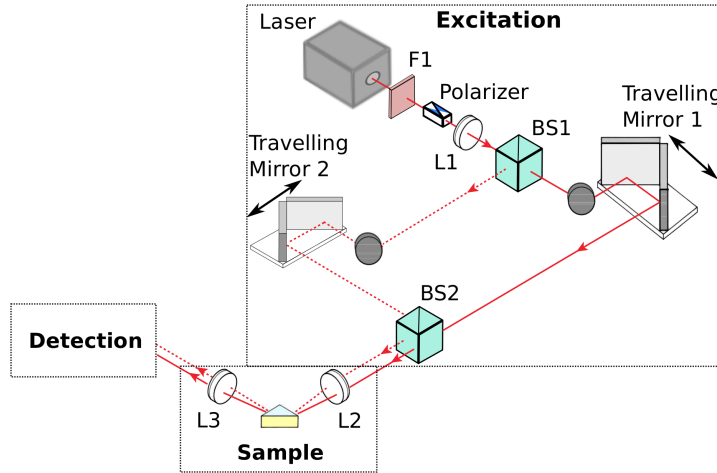


Figure 4.10: Experimental setup for degenerate three-wave mixing with two incident beams. Beam-splitter BS1 divides the beam into two parts, which both are independently displaced in horizontal direction by traveling mirrors. Beam-splitter BS2 reunites both beams which then impinge on the sample with incident angles dependent on their earlier displacement. The temporal delay is controlled via a large band-gap photodiode at the remaining beam-splitter port.

Here, the focus lies on the $\chi^{(2)}$ -conversion process, where the direct interaction of a propagating SP and an incoming photon, both of fundamental frequency ω , leads to the emission of a photon of the sum-frequency 2ω . The occurrence of sum-frequency generation (SFG) is in contrast to ordinary SHG, where two photons of fundamental frequency ω merge into a harmonic photon. As for SFG not only energy but also momentum have to be conserved. For the purpose of investigating plasmon-photon interactions in degenerate SFG, two independent laser beams are required. Here, the wave-vector-projections that fulfill the matching conditions and identify the associated conversion processes originate from a modified setup (Fig. 4.10) with two incident beams that are separately adjustable in terms of incident angle and femtosecond-pulse delay. A beam-splitter was integrated, to divide the laser into two equal parts, each of them impinging on individually adjustable traveling mirrors. Subsequently, the beams were reunited by a second beam-splitter BS2 and oriented towards the focussing lens L2, which transferred the particular translation of both beams into corresponding incident angles with respect to the sample. The remaining outcome of BS2 was sent to a photodiode to monitor the temporal delay. An exemplary CCD image is shown in Fig. 4.11b), which was detected identically to one-beam excitation (Fig. 1.4).

Thus degenerate SFG could be measured and it was determined how it is influenced

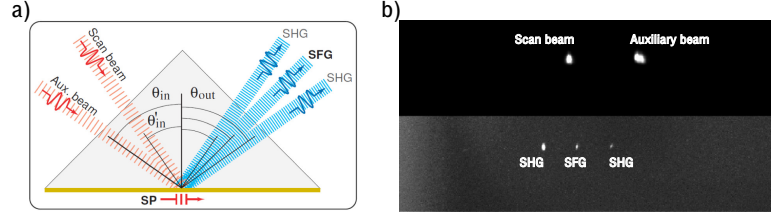


Figure 4.11: Nonlinear interaction from degenerate four-wave mixing with two-beam excitation. (a) Schematic diagram of three-wave mixing with two-independent laser beams of the same wavelength. (b) CCD image with raw data from scan beam, auxiliary beam, their respective generated second harmonic and the emitted sum-frequency signal.

by SP's on a flat metal surface, ensuring that propagating SP are not altered by intricate geometrical effects. With this powerful method, it is possible to discover the origins of plasmon-assisted second-harmonic generation. According to the analysis in the previous section, the nonlinear interactions observable with our setup can be limited to the creation of second harmonic photons. The definitions from Eqs. 4.1-4.6 can be further extended for interactions involving two-beam excitation. As a function of their wave-vectors, they can be distinguished using the following phase-matching conditions

$$2k_{f'}^{\omega}(\theta'_{in}) - k_f^{2\omega}(\theta_{out}) = \Delta_{f'f'-f} \quad (4.7)$$

$$k_f^{\omega}(\theta_{in}) + k_{f'}^{\omega}(\theta'_{in}) - k_f^{2\omega}(\theta_{out}) = \Delta_{ff'-f} \quad (4.8)$$

$$k_p^{\omega} + k_{f'}^{\omega}(\theta'_{in}) - k_f^{2\omega}(\theta_{out}) = \Delta_{pf'-f} \quad (4.9)$$

As before, the fundamental beam is incident at θ_{in} while θ_{out} is the exit angle of the generated second-harmonic radiation. Here, f' is an auxiliary beam, which was fixed to a given off-resonant angle of incidence θ'_{in} , while f was scanned (Fig. 4.11a). Using Eqs. 4.1-4.9, the wave-vectors of incident and exiting photons, which are functions of the angles θ_{in} and θ_{out} , can be related to the corresponding conversion processes. As such, each process can be identified by its unique matching combination.

In order to conduct an experimental investigation of SFG and SHG with plasmonic participation, the main focus is the pf -interaction (Eq. 4.2), involving a plasmon and a photon from one single beam, and the pf' -interaction (Eq. 4.9), where the photon is provided by a second beam. Both are expected to occur close to the SPR-angle.

A map of the second-harmonic intensity produced by the two-beam excitation is shown in Fig. 4.12 as a function of incident and exit angles. It can be compared to the matching conditions given by Eqs. 4.1-4.9 to discriminate the different conversion processes. Fig. 4.12a) shows the generated second-harmonic light of two beams with a delay $\tau = 1$ ps.

This ensures, that the beams do not interact. For the investigation of mixing interaction between photons and plasmons, the auxiliary beam f' is fixed at $\theta_{\text{in}} = 43.7^\circ$, which is off-resonant to the plasmon-angle. The scan beam f is scanned from 40° to 50° .

The strictly photonic conversion process $f f - f_{2\omega}$, where two incident photons of frequency ω become a 2ω photon, occurs over the whole angle range, thereby forming the diagonal line. The second-harmonic light generated by the auxiliary beam $f' f' - f_{2\omega}$ exits at a constant angle of $\theta_{\text{out}} = 43.2^\circ$. There is half a degree offset of the exit angles θ_{out} for both beams compared with their respective θ_{in} due to the dispersion in silver and glass.

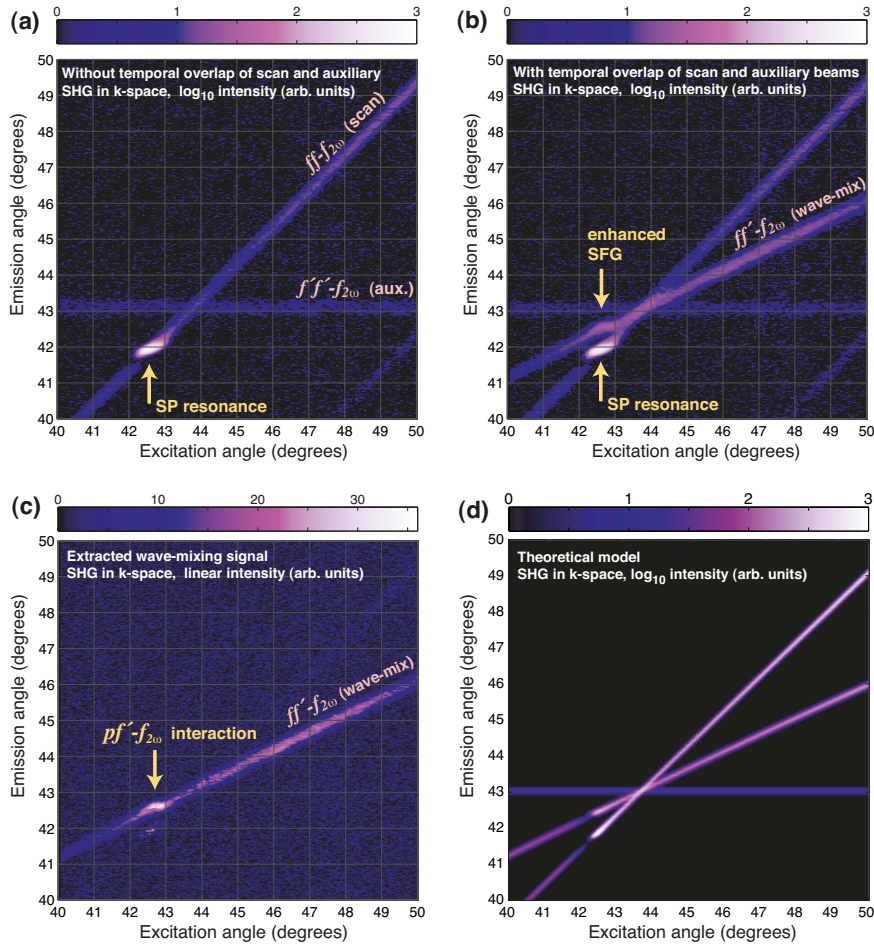


Figure 4.12: Resulting SHG-radiation as a function of incident and exit angle for a fixed auxiliary beam. (a) shows the SHG of two beams, that are not overlapping in time. The increased intensity when the scan-beam is adjusted to the SP-resonance is visible. In (b) the beams have a zero delay and the wave-mixing process and enhanced SFG are clearly visible. The mixing signal of the two incident beams is extracted in (c) by subtracting (a) from (b) and the $pf'f - f_{2\omega}$ interaction is identified. The theoretical calculation is shown in (d).

When the scan beam approaches the angle for the surface plasmon resonance ($\theta_{\text{in}} = 42.6^\circ$), the harmonic intensity momentarily decreases, but for larger angles θ_{in} increases two orders of magnitude due to the plasmonic field enhancement. Because of the angular width of the incident beam, plasmons p are generated over a slightly extended range of incident angles and can then participate in nonlinear conversion processes. This leads to the observed horizontal elongation, which is spread over 0.5° of incident angles. Following the previous section, it is identified as the $pp-f_{2\omega}$ conversion of two fundamental plasmons p into a harmonic photon [29], which emerges at a constant exit angle $\theta_{\text{out}} = 42.2^\circ$. At angles very near to the diagonal, the $pf-f_{2\omega}$ interaction is also thought to occur (Eq. 4.2) and can hence not be discriminated from the $pp-f_{2\omega}$ interaction. Therefore, only the second-harmonic that considerably deviates from the diagonal trend can precisely be assigned to the $pp - f_{2\omega}$ wave-vector-matching conditions.

Fig. 4.12b) shows the same excitation setup with auxiliary beam f' and scan beam f overlapping in time ($\tau = 0$). The photonic SFG of the two beams $f f' - f_{2\omega}$ is visible as an additional diagonal component. This wave-mixing signal shows, as seen in Fig. 4.12a) for the scan beam, a horizontal elongation at the scan beam's SP-excitation angle of incidence. This feature is evaluated in Fig. 4.12c). The mixing signal is extracted by subtracting an intensity map of a measurement having a non-zero delay from one taken at zero delay. Elongation and increased intensity of the mixing signal at $\theta_{\text{in}} = 42.7^\circ$ signify the $pf' - f_{2\omega}$ process, where an auxiliary beam photon f' and a plasmon p each of frequency ω become a 2ω photon. As in the former case, the horizontal component is caused by the angular width of both incident beams, thus the scan-beam excites plasmons p over a 0.5° range of incident angles. Since the auxiliary beam f' is held at a fixed angle and the SP's excited by the scan beam f have a constant wave-vector, the generated second-harmonic can only be emitted in one direction. This combination of incident and exit angle, i.e. the related wave-vectors, together with a boost in harmonic intensity is clear evidence of the predicted conversion process.

To confirm our results theoretically, a plane-wave Fabry-Pérot model was used following the analysis in Chapter 2 and 3. It considers an accumulated nonlinear polarization from both interfaces [73, 155]. The nonlinear polarization was calculated at both interfaces from the field components normal to the surface, considering the contributions of two Gaussian beams, that were incident with angles θ_{in} and θ'_{in} . The dielectric function for silver ϵ_{m} was measured by white-light ellipsometry and the remaining model parameters were derived from the experimental setup, while the relative phase between auxiliary and scan beam was randomly dithered. To ensure correct exit angles θ_{out} for the generated

second-harmonic light, the matching conditions Eqs. 4.1-4.9 were applied.

Fig. 4.12d) shows the theoretical calculation for two-beam excitation, which is in good agreement with the experimental results. The SFG is clearly visible as additional diagonal component and the SPR leads to strong harmonic intensity at $\theta_{\text{in}} = 42.3^\circ$. Also present is the drop in the SHG-intensity from the scan beam for angles θ_{in} just below the surface plasmon resonance. A slight horizontal broadening away from the diagonal in terms of incident angle is visible for scan- and SFG-beam, whose characteristic strongly depends on the beam waist and therefore the precision of the exciting beam's wave-vector.

The use of this auto-correlation technique ensures pulse overlap between auxiliary and scan beam even at large angular separations between both beams. This enables the study pf - f -interaction far from the resonance. In addition, exit angles and profiles of the emission can be studied: analogous to section 4.2.1, the presence of a plateau in the emission angle would be further evidence of pf - f -interaction (not just field enhancement).

Fig. 4.13 shows a map of incident and exit angles for different positions of the auxiliary beam. In Fig. 4.13a), the pp - f -interaction, already known from 4.2.1 is visible. Fig 4.13b) identifies the different contributions and shows a summary of the expected interactions. In Fig. 4.13c), the pf - f -interaction is analyzed for an auxiliary beam incident at 41.7° . It can be seen, that the emission angle of the pf - f -interaction is nearly constant, which makes sense because the auxiliary beam also is at a constant angle. The surface plasmons are generated at a constant k -vector, even though the angle of the scan beam is being varied: because the scan beam has a Gaussian profile, and finite divergence, plasmons are generated over a wider range of incident angles. So, the emission angle of SHG remains essentially constant because of the constant plasmon wave-vector. Note how the profile of the pf - f -interaction is very narrow in terms of k -vector compared to off-resonant excitation. The width relates to the SP propagation length along the interface.

Hence, wave-mixing between a plasmon, generated by the scan beam, and a photon from the auxiliary beam is visible and clearly identified. In Fig. 4.13d), the auxiliary beam is moved to the plasmon angle, which leads to strongly increased harmonic emission. Fig. 4.13e) again shows the intensity map for the auxiliary beam moved to an off-resonant position at a larger incident angle of 46.9° . The horizontal component, which identifies the constant emission angle of the pf - f -interaction, is likewise visible. Additional information can be obtained by analyzing the measured full width half maximum (FWHM) of the SHG

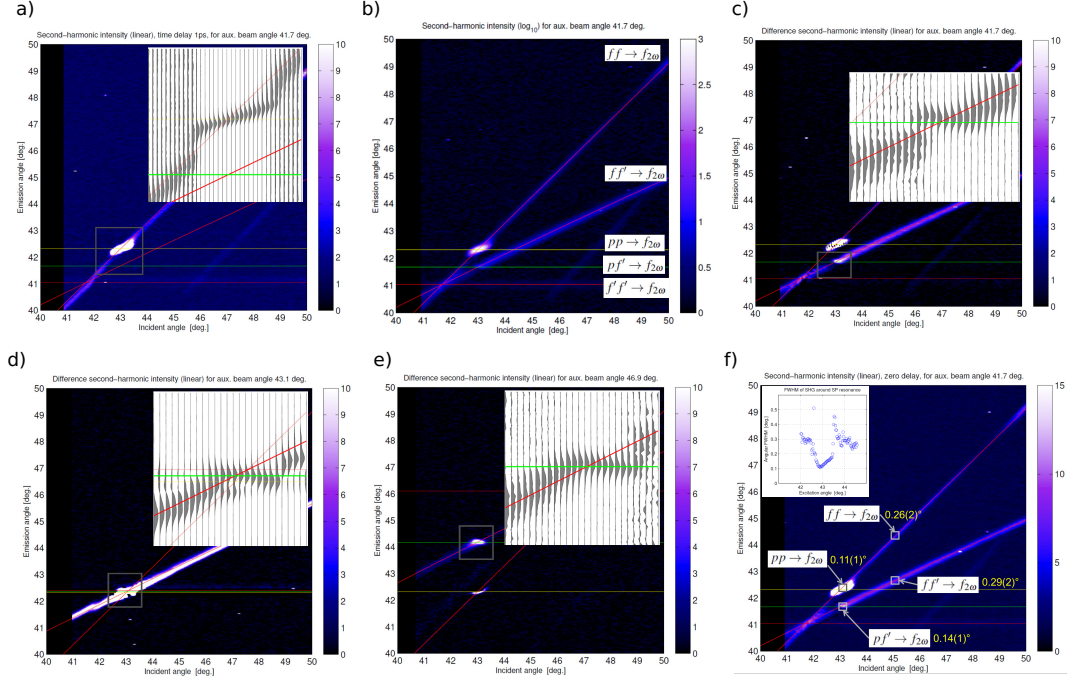


Figure 4.13: Resulting SHG-radiation as a function of incident and exit angle for variation of the auxiliary beam. (a) shows the SHG of two beams, that are not overlapping in time. The inset shows the established $pp-f$ -interaction. In (b) the beams have a zero delay and the wave-mixing process and enhanced SFG are clearly visible. The mixing signal of the two incident beams is extracted in (c) by subtracting (a) from (b) and the $pf'-f_{2\omega}$ -interaction is identified. (d) shows the harmonic signal for an auxiliary beam, that hits the plasmon resonance and (e) for an incident angle of 46.9°. In (f), the full width half maximum as a function of exit angle is analyzed for the different interactions, the inset shows the FWHM around the SP resonance.

emission profile:

$$\begin{aligned}
 ff - f & \text{ produces FWHM of } 0.26^\circ \\
 ff' - f & \text{ produces FWHM of } 0.29^\circ \\
 pf' - f & \text{ produces FWHM of } 0.14^\circ \\
 pp - f & \text{ produces FWHM of } 0.11^\circ
 \end{aligned}$$

SHG is driven by the fundamental field and hence the SHG emission depends only on the fundamental's beam divergence. Far from the SP resonance, the SHG is purely photonic and the resulting FWHM is 0.26° for the $ff-f$ -interaction and 0.29° for the $f'f'-f$ -interaction. For the scan beam at the SP resonance, where the $pp-f$ process must dominate due to field-enhancement, the emission FWHM is narrow: 0.11°. This narrow emission is due to the intrinsic width of the SP mode in k -space, which relates inversely to the SP propagation length (Eq. 2.19). For the wave-mixing process, $pf-f$, an intermediate FWHM

of 0.14° can be measured, which essentially comes from a cross-correlation of the photon mode with the SP mode. With a time delay of 1 ps, there are in principle two single-beam measurements that do not influence each other.

However, near the SP resonance, three interactions can occur: $ff-f$, $pf-f$ and $pp-f$. Even a single beam has a finite angular width and will essentially undergo wave-mixing from different (angular) parts of the same beam. Far from the SP resonance, no SP are excited and therefore, the SHG is purely photonic. Approaching the SP resonance, then some of the beam converts to SP, which then mix with photons from the auxiliary beam in $pf-f$ interaction. At the resonance, the centre of the beam is exciting SP, thus yielding huge field enhancement and which leads to the $pp-f$ -interaction dominating.

The mixing process between ω SP and ω photon was clearly isolated by comparing an effective one beam measurement (where both beams were not overlapping in time) with a two-beam measurement (that enabled interaction). While the common photonic SHG was measurable over the entire angular range, plasmon-driven SFG was limited to the regime where SP's are excited and could therefore be clearly distinguished.

A series of 2D- k -space spectroscopic measurements of SHG and degenerate SFG from a gold film in the Kretschmann and the Otto configuration has been performed. The nonlinear sources contributing to SHG have been identified and their strength has been quantified. Furthermore, the nonlinear interactions which generate second harmonic radiation have been investigated. They could be characterized by their unique signature in k -space due to the fact, that only a well-defined combination of wave-vectors can take an active part in SFG and SHG. In particular the $pp-f_{2\omega}$ and $pf'-f_{2\omega}$ interactions have been observed. The results are in good agreement with our theoretical calculations. Accordingly, a useful tool has been demonstrated that can be applied to investigate particle-quasiparticle nonlinear interactions.

5 | Long-Range Surface Modes On Thin Films

Common surface plasmon polaritons, investigated in the previous chapters, propagate at the interface between two media and usually have short propagation lengths of only a few microns (Fig. 5.1) [36]. In contrast, thin films with symmetric cladding in terms of the dielectric function are known to support long range surface waves (LRSW) such as waveguide-modes in transparent media or long-range surface plasmon polaritons (LRSP) in metallic thin films [75, 79, 83, 86]. These LRSWs are surface confined coupled modes, which can yield propagation lengths of hundreds of microns up to the centimeter regime [80, 88]. The linear and nonlinear properties of LRSP on thin metal films have been investigated in detail [90–92, 156, 157].

However, intrinsically absorbing materials are usually not considered as optical elements as attenuation accompanies any effort to guide or focus light. As a surprising result from electrodynamic theory, solutions for propagating surface waves in a thin-film configuration can even be found for such strongly absorbing materials [158]. Thus, absorbing films can support low-loss surface waves which have been reported for semiconductors, transition metals, metal oxides, and dichalcogenides as long-range surface exciton polaritons (LRSEP) [84]. Their linear propagation properties have been confirmed from the ultraviolet to the infrared [76, 78, 159–166].

The propagation lifetime of LRSWs can be further increased as the thickness of the absorbing film is reduced. Calculations for a film of absorbing material that is embedded in a transparent medium even show that the propagation lifetime of LRSW becomes arbitrarily long in the limit of vanishing film thickness [87]. The electric field is near to zero inside the absorbing film and thus in large part propagating inside the transparent cladding where it does not suffer losses. This effect only requires of the dielectric function to be dominated by its imaginary part at the desired optical frequency.

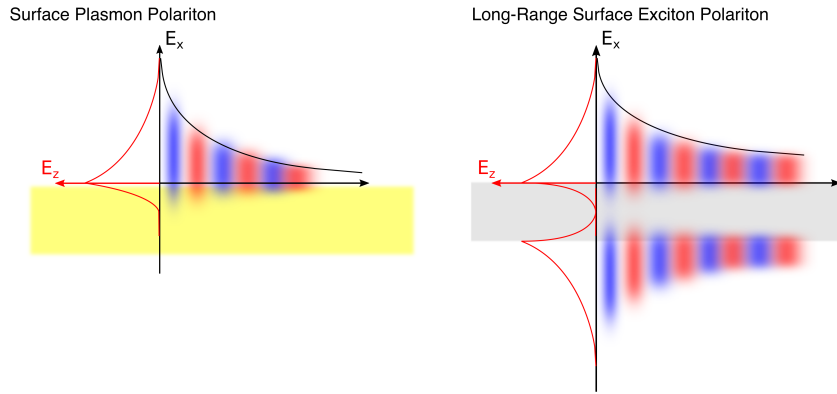


Figure 5.1: Schematic comparison of a surface plasmon polariton, that is confined to the interface between a metal and a dielectric (on the left) and a long-range surface wave on a thin film with symmetric cladding(on the right). The components of the electric field in propagation (E_x) and the confinement to the surface (E_z) are also shown.

Close to an absorption resonance, the nonlinear susceptibility of a material can greatly exceed those values found off resonance which could make absorbing thin films also interesting for nonlinear optics [85, 167, 168]. This compelling aspect of absorbing materials –their intrinsic nonlinear susceptibility– has not yet been studied in the context of LRSW. To employ absorbing materials as nonlinear optical media, one needs to find a way to have light interacting with the medium over a long propagation distance, i.e. polarizing it over many wave cycles, but without the associated absorption. Observations further show that the excitation of LRSW leads to a dramatic increase in the yield of second-harmonic generation which is caused by a local field-enhancement. These results imply that intrinsically absorbing materials can indeed be considered as low-loss optical media for doing surface-wave optics in the nonlinear regime.

In this Chapter, the propagation of surface-confined LRSWs is explored in thin chromium and molybdenum films by using the Otto configuration for efficient coupling to the far-field. The coupling to LRSW and their propagation lifetime and hence interaction length are investigated and questions regarding the overall effective nonlinearity that the system can achieve will be discussed. Furthermore, the enhancement of the electric field which drives the nonlinear sources is determined and the contribution of the different sources (see Chapter 4) are identified. Finally, the phase-matching between the relevant modes as well as the efficient coupling to the far-field are examined. Understanding these factors will be the key to propelling absorbing materials into applications such as electrooptic modulation and frequency conversion.

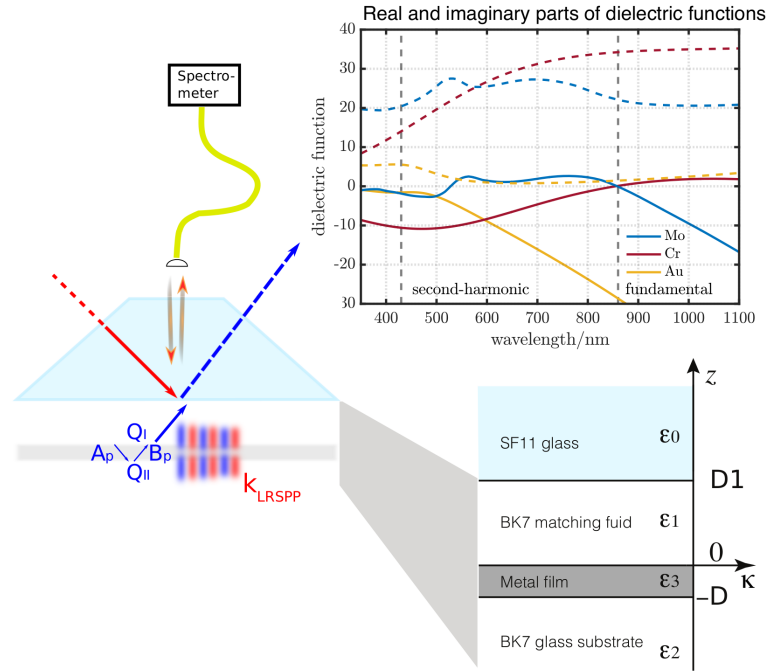


Figure 5.2: Excitation configuration for long-range surface waves. On a high-index coupling prism (SF11) follows a tunable layer of BK7 matching fluid, a thin sample film and BK7 substrate for a symmetric cladding around the sample. The coupling gap of thickness D_1 is controlled via white-light interferometry. The inset shows the real (solid lines) and imaginary (dashed lines) parts of the dielectric functions for the investigated materials, Molybdenum (Mo), Chromium (Cr) and Gold (Au) [146, 169, 170].

5.1 Theoretical Analysis

The study of SHG from LRSWs requires characterization of the LRSW mode in terms of its wave-vector, propagation length, and its excitation by an evanescent field. The enhancement of the driving electric field at the resonance, its confinement to the surface and the contributions of the different nonlinear source terms in the bulk material and at the surfaces have to be examined.

As in chapter 2 and 3, a stack of four isotropic, non-scattering optical media is considered. To ensure a symmetric cladding and still provide evanescent coupling, a configuration similar to the Otto configuration was employed (Fig. 5.2). It consists of a high-index SF11-glass coupling prism (ϵ_0), BK7 matching fluid (ϵ_1) as adjustable spacer layer of thickness D_1 , the absorbing film (ϵ_3) of thickness D , and the BK7-glass substrate.

LRSW can be found by piecing together plane-waves in the media $i = \{1, 3, 2\}$, and solving for the wave-vectors and amplitude that fulfill the boundary conditions of Maxwell's equations, as shown in section 3.2, Eq. 3.22:

$$\tanh(k_{3,z}D)(\epsilon_1\epsilon_2k_{3,z}^2 + \epsilon_3^2k_{1,z}k_{2,z}) + (k_{3,z}(\epsilon_1k_{2,z} + \epsilon_2k_{1,z})\epsilon_3) = 0$$

with a field profile in the media given by

$$\begin{aligned} E_{i,x} &= [\exp(i\omega t - \mathbf{k}_{i,z} \cdot \mathbf{r}) + \exp(i\omega t + \mathbf{k}_{i,z} \cdot \mathbf{r})] \left| \frac{k_{i,z}}{k_0} \right| E_i \\ E_{i,z} &= [\exp(i\omega t - \mathbf{k}_{i,x} \cdot \mathbf{r}) + \exp(i\omega t + \mathbf{k}_{i,x} \cdot \mathbf{r})] \left| \frac{k_{i,x}}{k_0} \right| E_i \end{aligned}$$

For symmetric materials $\epsilon_1 = \epsilon_2$, Eq. 3.22 can be split into two discrete solutions

$$\begin{aligned} \tanh(k_{3,z}D) &= -\frac{k_{1,z}\epsilon_3}{k_{3,z}\epsilon_1} \\ \tanh(k_{3,z}D) &= -\frac{k_{3,z}\epsilon_1}{k_{1,z}\epsilon_3}, \end{aligned} \tag{5.1}$$

defining a long-range mode and a short-range mode, respectively. Solutions of Eq. 5.1 have the form

$$k_{sw} = \beta + i\alpha, \tag{5.2}$$

where $k_{i,z} = \sqrt{\epsilon_i k_0^2 - k_{sw}^2}$ and β is a propagation quantity, defining wavelength and propagation direction of the surface wave. α describes the attenuation of the surface wave along its propagation. As defined in Eq. 2.19, α depends on the intrinsic and the radiative losses and is linked to the propagation length via

$$L_{sw} = \frac{1}{2\alpha} = \frac{1}{2(\Gamma_i + \Gamma_{rad})}.$$

To attend long propagation lengths, $\alpha \ll \beta$. As discussed above, solutions of Eq. 5.1 are not only valid for surface plasmons on metal films but can be found for many materials with an appropriate cladding. A comparison of the k_{SW} solutions for gold and molybdenum films [170] is shown in Fig. 5.3 at a wavelength of 855 nm. For increasing film thickness, the long-range propagation quantity β on a gold film proceeds from a plane wave solution in the cladding at $D = 0$, $\beta/k_{cladding} = 1$, to the single interface solution for a surface plasmon on infinite bulk gold. The attenuation α follows the same trend: Increasing film thickness leads to increased losses and hence lower propagation, converging to the bulk limit.

However, the long range mode in molybdenum films follows the solution for gold up to a film thickness of 60 nm. Then it starts decreasing to values even below $\beta/k_{cladding} = 1$,

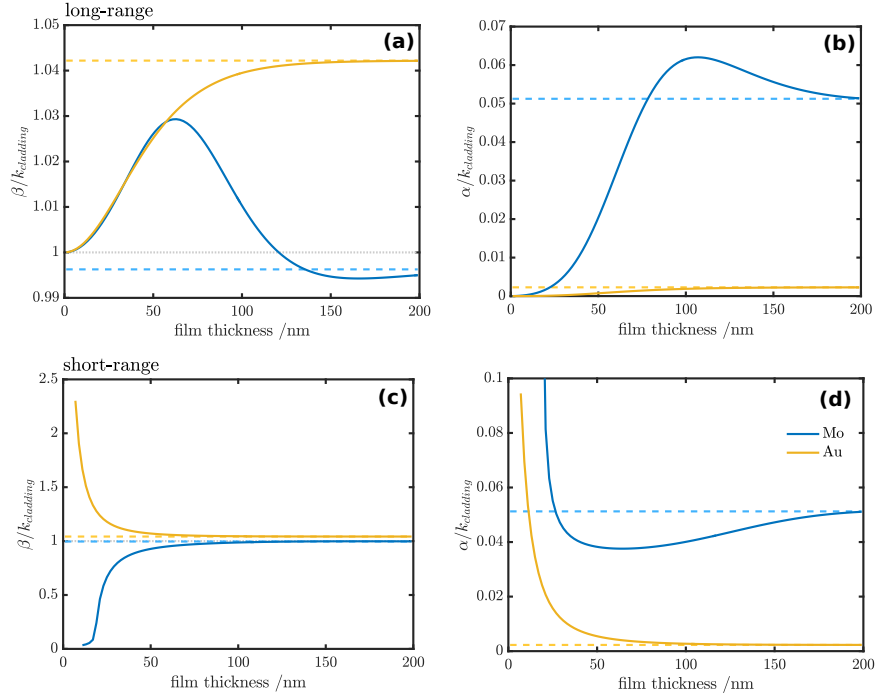


Figure 5.3: Real (a,c) and imaginary (b,d) parts of the calculated wave-vectors for long-range (a,b) and short-range (c,d) modes as a function of film thickness. Blue lines show the calculations for molybdenum and yellow lines for gold.

which is in the free-space propagating regime, and then also converges to the solution for a single interface. In contrast to gold, molybdenum does not support bound surface modes at a single interface for the given wavelength. Hence a cut-off thickness of ~ 120 nm is found above which no coupled mode solution exists. The values for α are only comparable to gold for very thin films below 20 nm thickness. Above this value, α strongly increases for Mo and converges to the single interface solution, at which it is ten times higher than α for gold. As a consequence, preferably thin films have to be used for long propagation lengths in molybdenum.

The short-range modes both show high losses especially for thin films and then converge likewise to the single interface solutions. While the propagation quantity β for gold converges to the single interface solutions from the upper side of 1 which describes bound modes, β for molybdenum approaches from the lower side of 1: No bound solution exists for the propagating short-range mode in molybdenum at the given values for cladding and wavelength.

For a profound analysis, the coupling properties to the LRSW in the excitation configuration have to be determined. As in Chapter 2, the excitation is polarized perpendicular

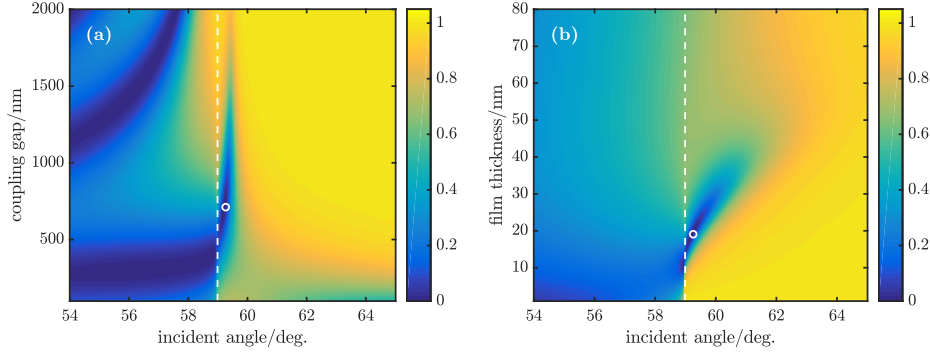


Figure 5.4: Calculated reflected intensity from thin molybdenum films. (a) shows the calculation for a 19 nm film and varying coupling gap. (b) shows different layer thicknesses at a constant gap size of 750 nm. The dashed white line marks the TIR angle and the circle identifies the parameters for optimum coupling efficiency.

with respect to the xz -plane (plane of incidence) while θ_{in} is defined to be the incident angle. The reflected intensity including multiple reflections inside the different layers can thus be calculated [145] by

$$\bar{r}_{02} = r_{01} + \frac{t_{01}\bar{r}_{12}t_{10}e^{2ik_{1,z}D_1}}{1 - r_{10}\bar{r}_{12}e^{2ik_{1,z}D_1}}$$

where the coupling prism is defined as medium 0 with ϵ_0 in analogy to section 2.2.1.

A plane-wave calculation at a wavelength of 855 nm for different coupling gap sizes at constant molybdenum film thickness of 19 nm, and for varying molybdenum film thickness at constant gap size of 750 nm, can be found in Fig. 5.4. The dashed white line identifies the angle of total internal reflection and the circle marks the optimum coupling parameters. Excitation of the LRSW, and its out-coupled wave in the far-field on the prism side, interferes with the direct TIR reflected wave of the fundamental which leads to a destructive interference, and hence the dip in reflection [32]. The LRSW resonance is found close to the TIR angle and the coupling efficiency shows a strong dependence on both, the coupling gap size and the film thickness.

5.2 Experimental Analysis

Experimental observations are presented, that show a remarkable boost in second-harmonic yield due to the excitation of LRSW in films of strongly absorbing materials. Our analysis indicates that the LRSW not only creates a local field-enhancement at the fundamental frequency which is driving the nonlinear response. It also leads to an increase of the interaction length, in comparison to the electromagnetic skin-depth of the bulk material. The

chromium and molybdenum films selected for this study have dielectric functions [146, 169, 170] that are dominated by their imaginary components in the near-infrared (see dielectric functions in Fig. 5.2). So although being electrical conductors, at these frequencies they operate well outside of the plasmonic regime. It is discussed here how the LRSW that these films support, have an electric field profile that is highly discontinuous at the film-cladding boundary. Furthermore, the driving field and the related nonlinear source terms are determined and quantified in the form of the nonlinear parameters from Chapter 3. The experimental results demonstrate that absorbing materials have the potential to become a viable alternative to conventional transparent nonlinear media.

5.2.1 Spectroscopic Measurements

For the linear measurements, the white-light setup from section 2.3.1 was applied, yet the centre angle of incidence had to be changed due to the high-index coupling prism. Fig. 5.5 shows the acquired spectra at different coupling gaps for a 19 nm molybdenum film and a 8 nm chromium film, respectively. Here, the white-light spectra were normalized to a reference sample consisting of the SF-11 coupling prism and BK7 matching fluid and a background measurement from a bare SF-11 coupling prism was subtracted. For larger gap sizes, the closest Fabry-Pérot modes are visible as broad absorption features to the left of the TIR line.

The long-range mode excitation is identified by its sharp absorption feature closely beyond the angle of total internal reflection (dashed red line). A spectral shift of the resonance can be seen when the gap size is varied and hence the coupling condition is changed as expected from the analysis in section 2.3.1: Shorter wavelengths require smaller gap sizes for efficient coupling because the out-coupled evanescent field decreases. Likewise broadening of the resonance can be observed for reduced coupling gap sizes in Fig. 5.5 a) and d) as predicted by the calculations in Fig. 5.4.

For the thinner chromium film, the resonance is narrower than for the molybdenum film, which signifies longer propagation lengths and also conforms with the calculation in Fig. 5.3. However, the LRSW-resonance is considerably sharper in terms of incident angle than the surface plasmon resonance from the semi-infinite films in Chapter 2. Another difference appears for shorter wavelengths: While the plasmonic resonance bends towards larger angles, the thin film resonance closely follows the edge of the total internal reflection. This can be related to the ratio of the refractive indices and thus the dispersion of the core material and the cladding material. The calculations in Fig. 5.5 c) and f) are in good agreement with their respective measurements.

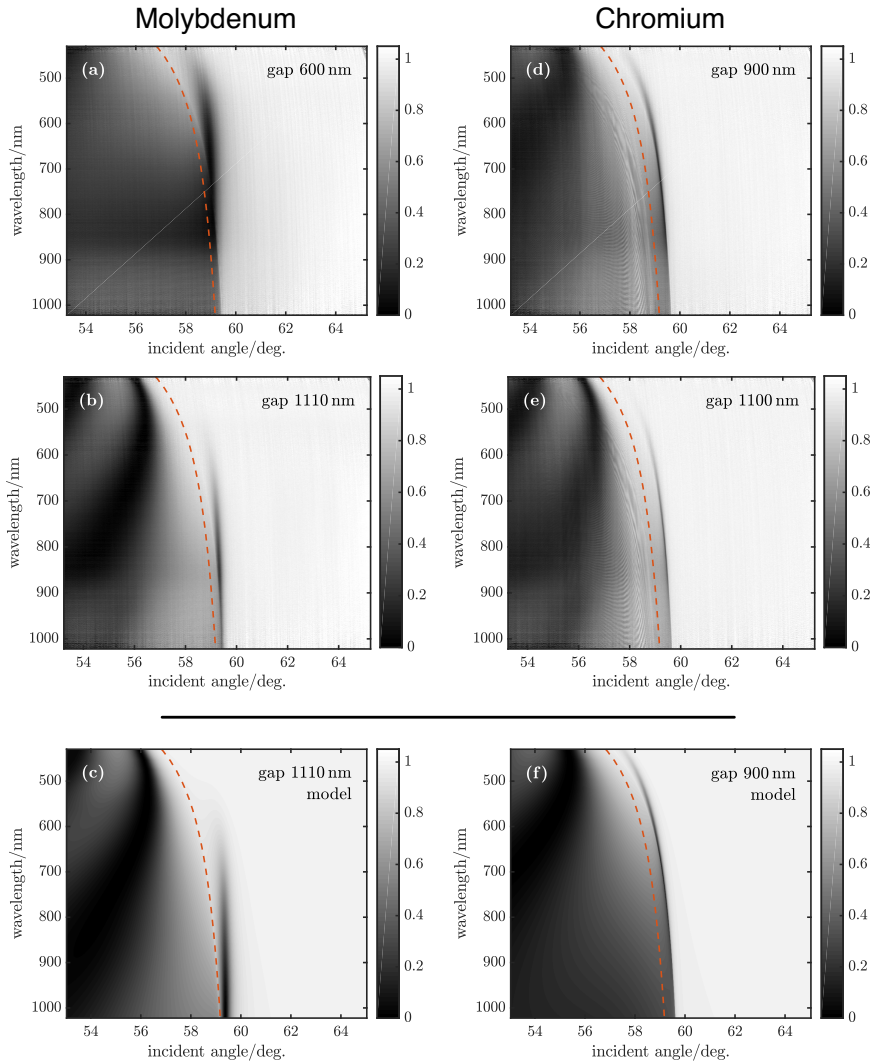


Figure 5.5: White-light measurements for thin films of chromium and molybdenum. A SF-11 coupling prism was followed by a tunable BK7 matching fluid spacer and a 19 nm molybdenum film, (a) and (b), and a 8 nm chromium film, (d) and (e), respectively, both on BK7-glass substrate. (c) and (f) show calculations for the correspondent gap sizes.

5.2.2 Excitation at High Intensities

In Chapter 4, the second harmonic yield from metallic layers was investigated and related to the plasmonic field enhancement at the surface [69]. With this knowledge, we can also identify the field enhancement provided by LRSWs by analyzing the out-coupled SHG. For this reason and to investigate the coupling properties aside from the plane-wave like white-light excitation, the setup from Fig. 1.4 was used as before in Chapters 2 and 4. A pulsed Ti:Sapphire laser with a wavelength of 855 nm and a pulse length 150 fs provided

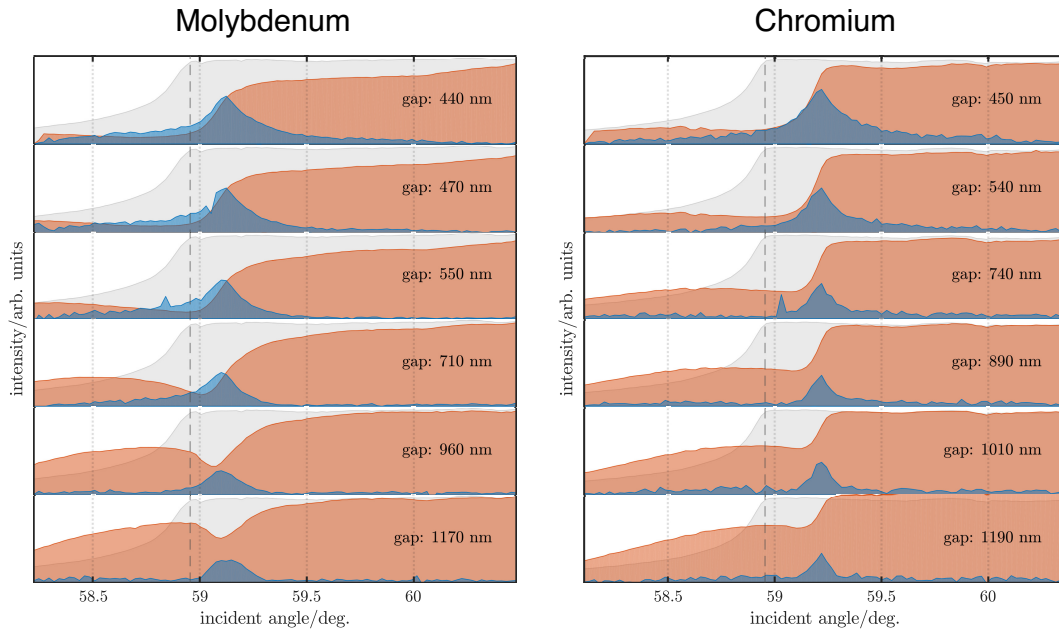


Figure 5.6: Reflected intensity and nonlinear yield for thin molybdenum and chromium films and different coupling gaps. The red-shaded areas show the reflected fundamental intensity, while the blue-shaded areas show the emitted second-harmonic intensity as a function of incident angle. A reference of a SF-11 prism with BK7 matching fluid only is shown in the background (gray). The dashed red line marks the TIR angle.

2 nJ pulses of 0.075° angular width.

Fig. 5.6 shows the experimental results from reflectivity measurements for a 19 nm molybdenum film and a 8 nm chromium film. As shown in Fig. 5.2, the dielectric functions of both materials are very similar at 855 nm wavelength, the real part being close to zero and the imaginary part being above 20. The red-shaded areas represent the reflected fundamental intensity. The characteristic absorption dip for both films lies close to the TIR angle, marked by the dashed red line, and partially overlaps with its respective edge.

In addition, the finite beam width leads to a broadening of the absorption feature compared to white-light measurements. The dip is less distinct than in the familiar plasmonic measurements of Chapter 2. The LRSW modes are very sharp in k -space while the width of the laser beam is a compromise between resolution in k -space and sufficient intensity for SHG in position space. Thus the convolution of laser beam and surface wave results in the broadened resonance. A measurement of the SF-11 coupling prism with BK7 matching fluid only is laid underneath to be geared to the TIR angle and to validate that the absorption feature is located in the regime of bound surface waves. As expected from the linear results in the previous section, the resonance for the thicker molybdenum film is broader

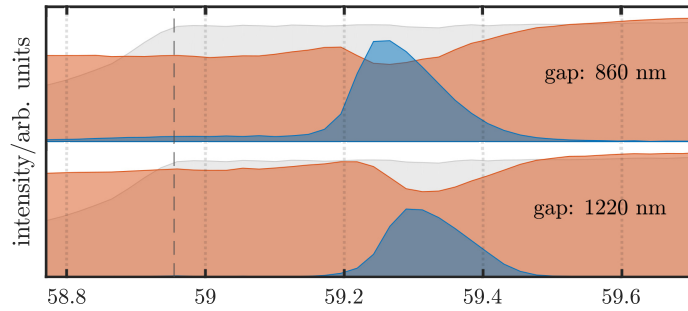


Figure 5.7: As a reference: **Reflected intensity and nonlinear yield for the SP resonance of a thin gold film** and different coupling gaps. The red-shaded areas show the reflected fundamental intensity and the blue-shaded areas the emitted second-harmonic intensity as a function of incident angle. A reference of a SF-11 prism with BK7 matching fluid only is shown in the background. The dashed red line marks the TIR angle.

and thus has better overlap with the incident beam. In the case of chromium, the dip is barely visible, as the resonance is too sharp to be resolved by the beam's finite width.

The emitted second-harmonic radiation is presented as blue-shaded areas in Fig. 5.6. The intensity of SHG shows a distinct peak as the incident angle of the fundamental beam is scanned. Its rise close to the position of the fundamental resonance is an unambiguous sign of LRSW-generated field enhancement: The excited LRSWs are strongly confined to the surfaces which boosts the local fields and hence leads to strongly increased harmonic emission. Decreasing coupling gaps lead to increasing harmonic intensities up to an optimum coupling thickness because they improve the coupling efficiency for short SHG wavelengths (as shown in the white-light measurements). The measured harmonic intensity for small gaps of 450 nm size is of the same order for both materials. In analogy to the linear analysis, broadening of the nonlinear radiation is observed for small gap sizes, while the resonance of the thicker molybdenum film is always broader compared to the thin chromium layer.

For very small coupling gaps, the harmonic emission even shifts across the TIR angle into the propagating regime. Here, the close proximity of the coupling prism gains influence which leads to increased radiative losses. Looking closely, a shift towards smaller incident angles can be observed for the linear resonance whereas the harmonic emission remains at a constant exit angle. This behavior will be discussed in the following section. A reference measurement for the SP resonance of a thin gold layer of 25 nm is presented in Fig. 5.7. The shapes of the linear dip and the harmonic peak are comparable to the previous measurements for molybdenum and chromium. The nonlinear yield on the contrary

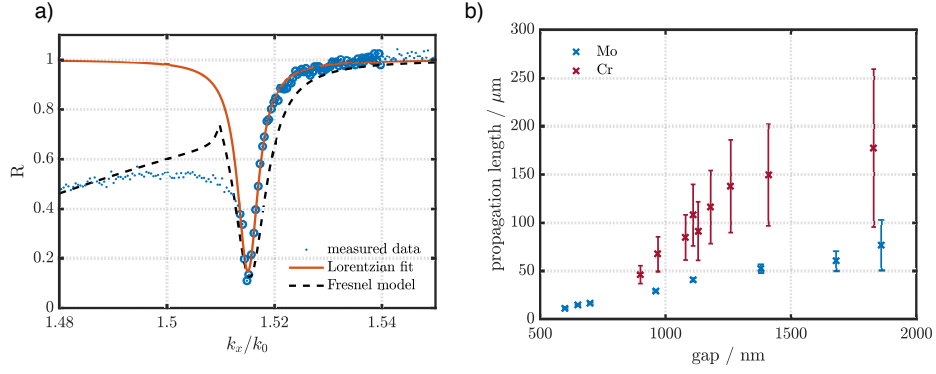


Figure 5.8: Experimentally obtained propagation lengths for thin molybdenum and chromium films. (a) Modeling of the surface wave resonance with the Fresnel model and a Lorentzian fit to obtain the propagation quantities β and α . (b) Propagation lengths for thin molybdenum (19 nm) and chromium (8 nm) films obtained with Lorentzian fits.

is a factor 20 higher for the excitation of LRSPPs in gold compared to the case of LRSWs in chromium or molybdenum.

5.2.3 Analysis of Propagation Lengths

The resonance at the fundamental wavelength can be analyzed to determine the LRSW's propagation length. The modal behavior of the system is better understood by using an approximate expression near the vicinity of the SPR (see section 2.2.1, Eq. 2.16), by introducing the Lorentzian function [32]

$$I_R = 1 - \frac{4\Gamma_i\Gamma_{rad}}{(k_x - \beta)^2 + \alpha^2}, \quad (5.3)$$

where Γ_i and Γ_{rad} are the internal and radiative damping terms established in Eq. 2.17. Fig. 5.8a) shows an example for a 19 nm molybdenum film and 960 nm BK7 coupling gap, that is fitted with the plane-wave Fresnel model and the Lorentzian to obtain the propagation quantities β and α . In this case, the extracted fit parameters yield $\beta = 1.515 k_0$ and $\alpha = 2.3 \cdot 10^{-3} k_0$, which, using Eq. 2.19, results in a propagation length of $\sim 60 \mu\text{m}$.

With this analysis, the propagation lengths from the white-light molybdenum and chromium measurements were determined and collected in Fig. 5.8b). Narrowing of the linear absorption feature is found for increasing coupling gaps which is interpreted as due to lower radiation losses and hence longer propagation lengths. This observation conforms with the results from the simple Fabry-Pérot theory and the linear Gaussian beam measurements. However, as the coupling efficiency strongly decreases for large gap sizes, the absorption feature shrinks which also leads to larger uncertainties of the results.

As expected from the white-light measurements, the thin chromium film supports much longer LRSW propagation lengths up to $200\ \mu\text{m}$ compared to the molybdenum film with a maximum of $70\ \mu\text{m}$.

5.2.4 Nonlinear Source Terms and Driving Electric Fields

As a surprising result the long propagation lengths for the chromium film do not yield higher conversion efficiencies for the SHG. An explanation can be given by the theoretical model from Chapter 3, which gives an insight into the harmonic source contributions and the out-coupling efficiencies. The LRSW resonance is very narrow in terms of its excitation wave-vector and thus requires larger coupling gaps for efficient coupling. As already analyzed in the previous chapters, the out-coupling of SHG is less efficient for large coupling gaps. In combination with the lower field confinement and hence local field enhancement of LRSW, this results in decreased harmonic conversion efficiencies of the SHG radiated to the far-field which will be discussed in greater detail in the following.

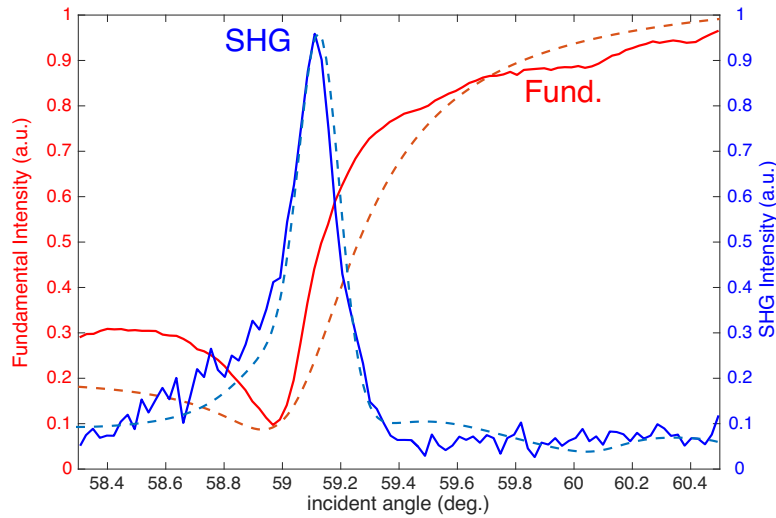


Figure 5.9: Comparison of linear and nonlinear thin molybdenum film measurements to the hydrodynamic model. The red curves show the linear reflectivity and the blue lines the second harmonic emission for the experiment (solid line) and the hydrodynamic model. The parameters were SF-11 coupling prism, 710 nm BK7 coupling gap, 19 nm molybdenum film on BK7 substrate, 855 nm wavelength and 0.075° angular beam width.

Cuts for the linear and nonlinear measurements of a 19 nm molybdenum film with 710 nm BK7 coupling gap are shown in Fig. 5.9. The Gaussian beam model matches the linear absorption dip well although the resonance is even narrower in the experiment, which can be related to small deviations in the gap size or the dielectric function of molyb-

denum. The second harmonic peak is matched very well by the hydrodynamic model and even its broadening towards smaller incident angles is reproduced. The following parameters were used to match the second harmonic peak:

\bar{b}	=	1.5	in – plane component of surface SHG
$\bar{\delta}'$	=	2.0	bulk SHG
$\bar{\gamma}$	=	2.5	bulk SHG
\bar{a}	=	0.1	out – of – plane component of surface SHG
n_0	=	$6.452 \cdot 10^{22} / \text{cm}^3$	electron number density

Compared to the gold measurements of a single interface SP in chapter 4, the out-of-plane component of the surface source in molybdenum is enhanced by one order of magnitude. The bulk sources are of the same order, while the in-plane component of the surface source in molybdenum is only one fourth. It is this change, and especially the strong out-of-plane component, that defines the particular shape of the harmonic emission. The sharp resonance of the long-range mode has a distinct wave-vector, which leads to harmonic emission that is almost independent of the coupling gap (as seen in terms of its exit angle). This explains the constant excitation angle of the SHG in the experimental results in Fig. 5.6 for different coupling gaps.

A comparison was made of calculations based on the hydrodynamic model for a 19 nm molybdenum film and a 25 nm gold film with varying gap sizes at 855 nm wavelength, see Fig. 5.10. For molybdenum, the linear resonance (left hand side) is found close to the TIR angle (white dashed line). It is broadened for small coupling gaps and partially overlaps with the propagation regime. An increasing gap size leads to a narrowing of the resonance, and hence longer propagation length of the LRESP mode. However, these are accompanied by decreased coupling efficiencies. The nonlinear calculation (on the right) produces a second harmonic radiation at a constant angle of incidence. Broadening of the resonance is observed for small gap sizes. The emission does not completely coincide with the linear resonance which bends towards smaller angles for decreasing gap sizes. The maximum intensity is found at a gap size of 750 nm which differs from the experiment, where the optimum was expected below 450 nm gap size. This deviation could result from the determination of the gap size by white-light interferometry. For gaps filled with matching fluid, which are on the order of the lowest interfering wavelengths, the interference spectra are not always explicit and thus the error increases.

However the theoretical predictions for a LRSPP of thin gold layer show a different behavior. Compared to LRSW in molybdenum, the linear resonance is found at larger incident angles, i.e. there is a greater separation from the propagating regime. With the

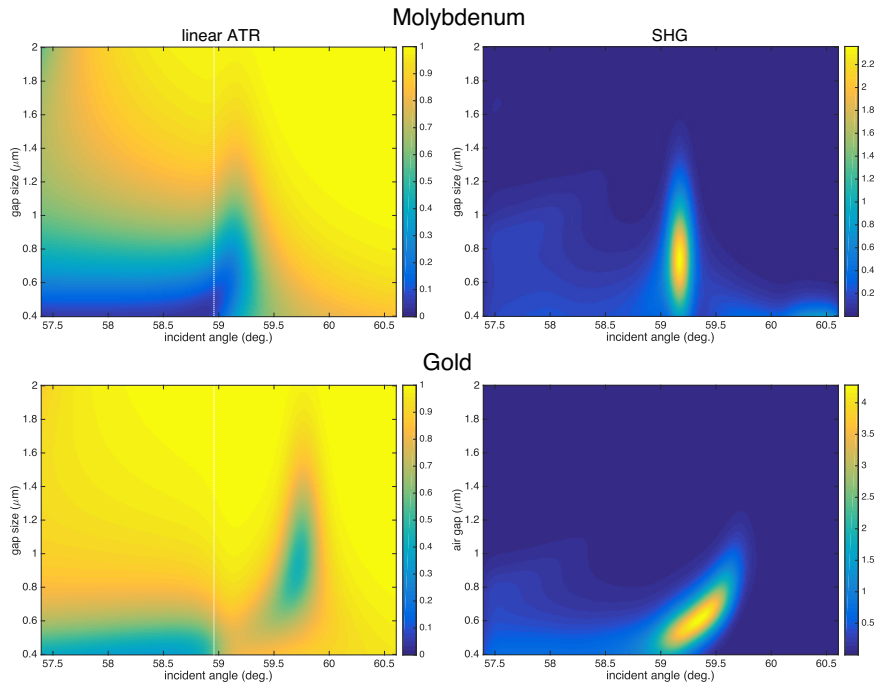


Figure 5.10: Comparison of theoretical calculations for a 19 nm molybdenum film and a 25 nm gold film both excited with by prism coupling (SF11) and symmetric claddings (BK7). The size of the coupling gaps was varied as well as the incident angle. The left images show the reflected intensity at 830 nm excitation wavelength and the right images show the second harmonic radiation coupled to the far-field.

given beam parameters, maximum coupling efficiencies of 60% can be obtained which is less than for the LRSW case. Here, the second harmonic clearly follows the fundamental resonance as a function of excitation angles. The out-coupling is more efficient at smaller gap sizes as expected from the results in Chapter 4 (where shorter wavelengths require smaller gap sizes for efficient coupling). The field enhancement, and hence the radiated second harmonic, are increased compared to the molybdenum film. As in the experiment, the harmonic yield for gold exceeds the yield obtained for molybdenum by a factor of 20.

Calculations of the driving field for the molybdenum film with a coupling gap of 660 nm are shown in Fig. 5.11. A strong enhancement of the intensity can be seen for the resonant excitation, (a) compared to off-resonant excitation in (e). Enhancement of the electric field can likewise be observed while undergoing the surface wave resonance (b) compared to off-resonant excitation (f). The high resolution analysis in (b) reveals that almost no electric field exists inside the molybdenum layer: It is confined in the cladding close to the interface. The components of the electric field, calculated for the inset in (a) are shown in (c), E_x , and (d), E_z . The E_z component of the electric field is identified to exhibit the

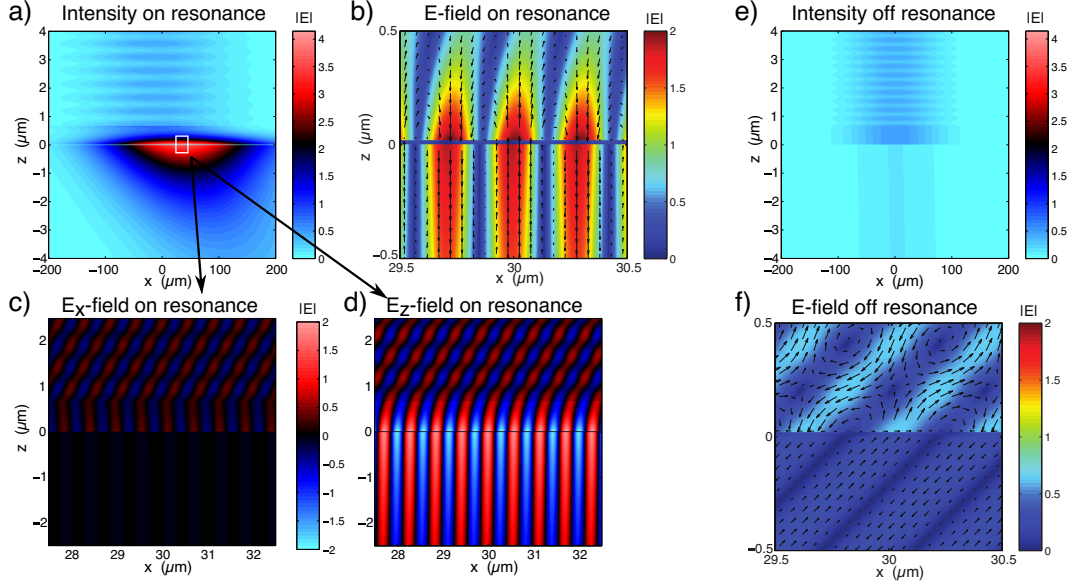


Figure 5.11: Calculations of the driving electric field (at 830 nm) for a 19 nm molybdenum film with a coupling gap of 660 nm. (a) Intensity and (b) electric field with field-vectors for resonant excitation. The E_x -component and the E_z -component of the electric field in the marked area of (a) are shown in (c) and (d), respectively. (e) shows the off-resonant intensity and (f) the off-resonant field calculations.

strongest enhancement and therefore is the driving source of the nonlinear radiation. This is in good agreement with the experiment and the hydrodynamic model which also resulted in a strong contribution of the out-of-plane surface source via its related nonlinear parameter \bar{a} driven by E_z .

In summary LRSWs were observed to have very sharp resonances as a function of incident angles. Thus propagation lengths of several hundreds of micrometers could be obtained for large coupling gaps which unfortunately led to decreased coupling efficiencies. As the out-coupling efficiency for SHG strongly depends on the transmission through the coupling gap, the out-coupled harmonic radiation was a factor of 20 lower for LRSWs (molybdenum) than for LRSPPs (thin gold), which was also 2 orders of magnitude lower than for SP's (thick gold). Still, LRSWs were shown to exhibit field enhancement at the interface which was on the same order of magnitude than for LRSPPs. Different coupling techniques, e.g. gratings could be used for efficient out-coupling of SHG in LRSW samples, which would also enable directed coupling of the narrow mode profiles to the far-field. Finally, the out-of-plane component of the nonlinear sources was identified to have the strongest contribution for LRSW samples which is in contrast to common SP samples.

6 | Anisotropic Emission of Oriented Nano-Platelets

With the achievements of the previous chapters, we can now characterize thin films of effective media that contain nano-particles in terms of their specific absorption and emission. Usually, absorption and emission of an atomic emitter are considered as isotropic. However, if the symmetry of an emitter is reduced, for example to a wire-like molecule, its optical transition dipole moment (TDM) is oriented along the molecule axis[109–111]. Anisotropic distributions of the TDM have thus been found in quantum confined systems and attributed to the symmetry and fine structure of the electronic states [112, 113, 171, 172]. Also planar molecular emitters like benzene have been shown to exhibit an in-plane degenerate TDM and a dark axis perpendicular to it. The existence of a bright plane and a dark axis has also been reported for wurzite CdSe/ZnS quantum dots (QDs) and nanorods[112, 113]. These directional emitters are very interesting e.g. for nanoparticle display technology to improve the out-coupling efficiency and reduce stray light image fading.

More recently, new two dimensional materials such as II-VI nano-platelets and belts as well as 2D transition metal dichalcogenides have emerged [96–99]. They have been found to exhibit the exciting property of being nearly ideal quantum wells more so than epitaxial quantum wells as they do not suffer from well width inhomogeneities, that result in trapping and localization. High carrier mobilities $>250\text{-}1000\text{ cm}^2/\text{Vs}$ [100, 101] and high exciton binding energies [98, 106, 107, 173] have been predicted and reported in these materials which were attributed to the influence of the strong dielectric confinement. It has also been demonstrated that these materials have very short (radiative) exciton lifetimes[102, 104, 105, 108].

However, the anisotropic distribution of internal TDMs in these materials has been less investigated [174]. Yet, the orientation and distribution of TDMs and their coupling to the density of photon states determine the emission characteristics and radiative rates.

Light-matter interaction and emission characteristics in semiconductors can be mediated by their dipole matrix element. It is determined by the Bloch functions (states) associated to the bands involved in an optical transition and the envelope function defining the selection rules [175]. Theoretical predictions for strongly anisotropic particles show further that the dielectric contrast between the nanoparticle and the surrounding ligands and matrix strongly alters the angular emission properties [114]. Together these dielectric and electronic effects yield anisotropic emission radiation patterns. This is in strong contrast to the case of highly symmetric spherical particles, such as PbSe dots, where isotropic internal dipole distribution and local fields result in isotropic emission [115].

In order to reconstruct their internal transition dipole distribution we applied two dimensional k -space spectroscopy on a monolayer of oriented CdSe nano-platelets. The absorption and emission characteristics are modeled including local field and local optical density of states effects as well as Fresnel effects. The platelets were excited in the energetically higher lying 2D continuum states where the absorption was found to have an isotropic transition dipole distribution. Surprisingly, the distribution of the TDM for the emitting heavy hole exciton is highly anisotropic. The emission can be characterized by a bright plane that coincides with the platelet plane and a quasi dark axis perpendicular to the platelet. This electronic effect leads to a strongly directed emission perpendicular to the platelet plane. Beyond these intrinsic electronic effects, the anisotropic shape of the nano-platelets induces dielectric effects that further concentrate the intrinsically enhanced emission perpendicular to the platelet. This is a fundamental advantage over wurtzite CdSe nano-rods where the bright plane is perpendicular to the dielectrically favored axis.

From these results one may conclude that CdSe nano-platelets are an interesting, realistic and efficient directional emitters for photonic applications. The origin of this strong anisotropy - going far beyond the shape effects introduced by local fields - will be discussed in this chapter as well as the implications paving the way to directionally emitting 2D fluorophores.

6.1 Analysis of Monolayer CdSe Nano-Particle Samples

Zinc-blend (ZB) CdSe nano-platelets of 4.5 monolayer (1.37 nm) thickness and $19.6 \cdot 9.6 \text{ nm}^2$ lateral size were deposited on $170 \text{ }\mu\text{m}$ thick fused silica substrates by a Langmuir-Blodgett technique. In this way, a monolayer of nano-platelets was obtained which lies flat on the substrate (platelet plane parallel to substrate plane) with a random lateral orientation. A

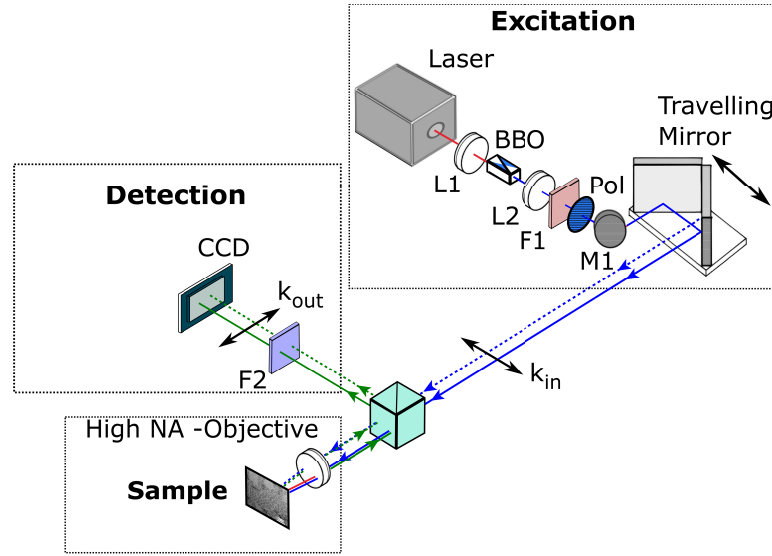


Figure 6.1: Simplified experimental setup with high-NA objective (NA = 1.49) which was applied in a confocal mode. The excitation was provided by a frequency-doubled pulsed Ti:Sapphire laser. Angle-dependent excitation was realized by a traveling mirror. The back aperture of the objective was imaged to a nitrogen-cooled CCD camera and the emitted photoluminescence was selected by a narrow bandpass filter.

reference sample of a monolayer of CdSe dots (ZB structure) with the same emission energy was produced as an isotropic emitter. Details, including the sample's absorption and emission spectra can be found in Appendix B.

These samples were introduced to an inverted microscope like setup (Fig. 6.1) with a high numeric aperture (1.49) immersion oil objective, thus producing a three layer system consisting of substrate/ligands and nano-crystals/air. The samples were excited by the second harmonic of a titanium sapphire laser (Coherent Mira, FWHM 150 fs, 75.4 MHz, 0.1 W/cm^2 excitation density) in the continuum of the nanoparticle absorption at 2.99 eV (415 nm). Angle dependent confocal excitation is realized by parallel displacement of the beam with respect to the optical axis of the objective. The back aperture of the infinity corrected objective is imaged to a sensitive CCD camera. This allows an angle-dependent and hence k -vector dependent detection of the (spectrally integrated) photoluminescence (PL) signal from the nanoparticle monolayer ensembles.

Figure 6.2 a) shows the concept of the experiment. An emitter placed in the sample plane may have an angular distribution of its emitting dipole. Here, out-of-plane (OP) dipoles are defined as z -oriented. In-plane (IP) dipoles lie in the x - y plane, i.e. parallel to the sample plane. The Hertzian radiation pattern of IP or OP dipoles in the focus of the objective can be related to a wave-vector distribution in the back focal plane. The emitted

radiation can be decomposed into its Cartesian components $\vec{k} = \vec{k}_x + \vec{k}_y + \vec{k}_z$ leading to a two dimensional projection of the radiation patterns in the k_x - k_y -space.

By introducing a polarizer, radiation oscillating parallel to the x-z plane is selected, thereby defining electric fields where \vec{E} and \vec{k} coincide in the x-z-plane as p-polarized. Radiation with \vec{E} pointing in x-direction and \vec{k} lying in the y-z-plane is thus s-polarized. The selection of cuts in the back focal plane (dashed white lines in Fig. 6.2 a) reduces the analysis to a 2D problem: k_x projections contain information about dipoles lying in- and out-of-plane (p-pol projection); k_y projections (s-pol) contain only radiation from IP dipoles. Figure 6.2 b) shows the result of a k-vector resolved emission of the oriented CdSe nano-platelets (excited at normal incidence). Figure 6.2 c) shows the reference sample of CdSe nano-dots. The measured intensity profiles of the k_x - and k_y -projections are plotted next to the CCD images where dashed lines indicate the selected regions (cuts). The k -scale is normalized to the wave-vector in air. Radiation with a wave vector $|k_{x,y}| > 1$ cannot couple into air, resulting in increased reflected intensity collected by the objective for these k -vectors.

The k -dependent emission profile is considerably different for platelets and dots. In s-polarization NPLs show triangular maxima, dots show rounded maxima with a steep decrease to the inside. S-polarization projections originate only from IP dipoles, their intensity profile merely depends on the dielectric function and thickness of the nano-crystal monolayer. In the following, the focus lies on cuts in k_x direction, as only p-polarization contains signal from in- as well as out-of-plane dipoles and thus reveals the transition dipole distribution in the studied monolayers. Here the emission profile of nano-platelets and dots is somewhat different. It will be shown that this is related to differing distributions of their emission transition dipoles. This allows one to gain direct access to the internal distribution of TDMs in the IP and OP directions, as we can model the measured angularly dependent emission and absorption characteristics.

6.1.1 Two-Dimensional k -space analysis

A multilayer system (glass - effective medium of oleic acid and nano-crystals - air) was used to model the k -vector dependent platelet emission (at the lowest 2.42 eV heavy hole exciton transition of CdSe platelets) and the absorption (into the 2D continuum at 2.99 eV). As the oriented CdSe platelets are surrounded by a ligand shell, consisting of oleic acid ligands, the nano-platelet monolayer samples form an anisotropic effective medium on top of the fused silica substrate. The anisotropic effective medium is modeled by approximating the platelets as oblate ellipsoids, comparable to what has been successful in Ref. [176].

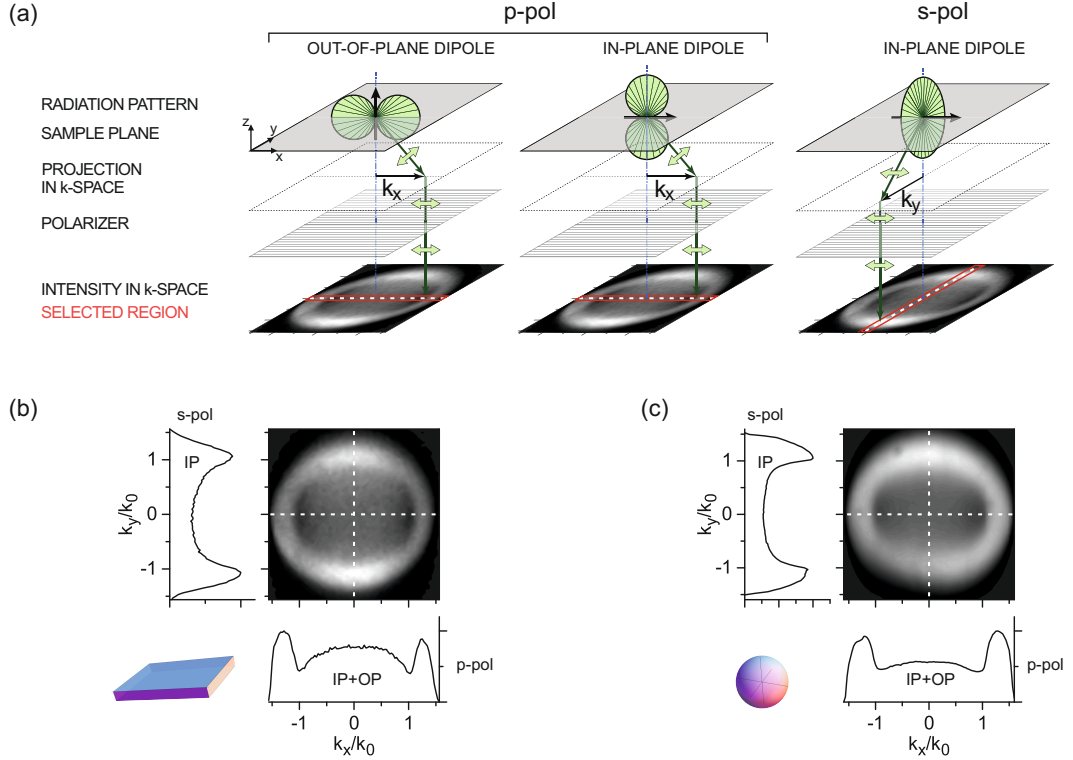


Figure 6.2: Polarization dependent in-plane and out-of-plane transition dipole contributions to radiative emission for nano-platelets and quantum dots. (a) By choosing one polarization axis, the back aperture image of a microscope objective can be analyzed with respect to in-plane (IP) and out-of-plane (OP) transition dipole emission. Cuts in k_x or k_y direction are well-defined and reduce the problem to a 2D geometry. (b) k -vector dependent emission of a monolayer of oriented nano-platelets and (c) a monolayer of dots. The profiles attached to the images display the cuts in k_y containing only emission from IP oriented dipoles, whereas cuts in k_x reveal the relative occurrence of IP and OP dipoles, i.e. the anisotropy of the dipole distribution.

In the present case they are modeled as aligned ellipsoids[177] to account for their orientation. A detailed discussion of effective medium theory can be found in Appendix B.

In a heterogeneous system a TDM couples into a different optical density of states as compared to air. For the coupling of IP and OP transition dipoles in the nano-crystal monolayers an effective density of states is used. According to Fermi's Golden Rule, the radiative rate of an emitter is proportional to the product of the Einstein coefficient A (proportional to the TDM $|\mu^2|$) and the density of (photon) states ρ yielding $\Gamma_r(\omega) = A(\omega)\rho(\omega) = \rho(\omega)\frac{\pi\omega}{3\hbar}\frac{|\mu(\omega)|^2}{\epsilon}$ with $\epsilon = \epsilon_r\epsilon_0$ [174, 178, 179]. Using the normalized density of states $\rho_0(\omega) = \omega^2(\epsilon\mu)^{3/2}/\pi$ a decomposition of the total radiative decay rate and the

TDM into IP and OP components is enabled. With the IP and OP Einstein coefficients:

$$\begin{aligned} A_{IP}(\omega) &= \rho_0(\omega) \frac{\pi\omega}{3\hbar} N_{r,IP} \frac{|\mu_{IP}(\omega)|^2}{\epsilon} \\ A_{OP}(\omega) &= \rho_0(\omega) \frac{\pi\omega}{3\hbar} N_{r,OP} \frac{|\mu_{OP}(\omega)|^2}{\epsilon} \end{aligned} \quad (6.1)$$

the PL emission originating from spontaneous heavy hole exciton recombination can be related to the density of photon states in the environment of the emitter. $N_{r,IP}|\mu_{IP}(\omega)|^2$ and $N_{r,OP}|\mu_{OP}(\omega)|^2$ are the IP and OP projections of the dipole strengths with respect to the principle axes of the dipole ellipsoid. $N_{r,IP}$ and $N_{r,OP}$ are the relative weights, which depend on its eccentricity. $\tilde{\rho}^{p,s}(\omega, k_{x,y}) = \frac{\rho^{p,s}(\omega, k_{x,y})}{\rho_0(\omega)}$ are the relative (photon) density of states with respect to free space for p and s polarization. They account for the alteration of the radiative rate in our heterogeneous system with respect to free space.

As cuts in the x -direction of the x - y -plane are used in the experimental analysis, only the x component of the rotationally symmetric external radiation pattern are taken into account, which is shown in Fig. 6.2. In this way the fits in Figs. 6.5 and 6.6 are obtained and one can derive the ratio of the IP transition dipole contribution in x direction to the OP contribution from z -oriented dipoles. From this two-dimensional (x - z -plane) IP to OP ratio one can calculate the three-dimensional ratio that also takes into account the (IP) dipoles oriented in the y direction. This corresponds to the true contribution of all OP and IP contributions to the total emission. The fraction R^{x-z} of IP and OP dipole contributions to the emission in the x - z plane is defined as

$$\begin{aligned} R_{IP}^{x-z} &= \frac{N_{r,IP}|\mu_{IP}(\omega)|^2}{N_{r,IP}|\mu_{IP}(\omega)|^2 + N_{r,OP}|\mu_{OP}(\omega)|^2} \\ R_{OP}^{x-z} &= \frac{N_{r,OP}|\mu_{OP}(\omega)|^2}{N_{r,IP}|\mu_{IP}(\omega)|^2 + N_{r,OP}|\mu_{OP}(\omega)|^2} \end{aligned} \quad (6.2)$$

and the 3D fraction of OP and IP contributions as:

$$R_{OP}^{3D} = \frac{1}{\frac{2}{R_{OP}^{x-z}} - 1} \quad (6.3)$$

$$R_{IP}^{3D} = 1 - R_{OP}^{3D} \quad (6.4)$$

With these equations, the fractional IP and OP contributions can be calculated with respect to 3D space.

The geometry used for k -space analysis consists of three dielectric layers schematically shown in Figure 6.3. Glass substrate, immersion oil and microscope objective are taken as one layer with (ϵ_1) followed by a thin sample layer (ϵ_2) of thickness D_{ML} , that contains either NPLs or QDs. The third layer is air (ϵ_3). As mentioned above, the plane of

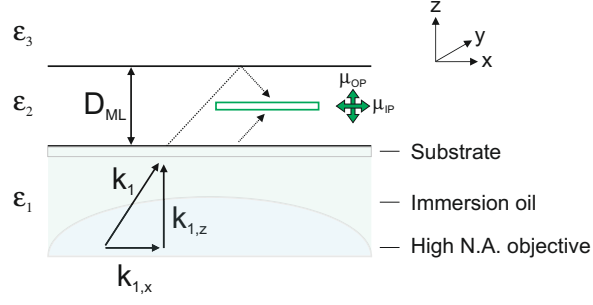


Figure 6.3: Scheme of k -space coupling geometry. Glass coupling layer consisting of substrate, immersion oil and objective (ϵ_1), sample layer (ϵ_2) and surrounding medium (air, ϵ_3). The thickness of the sample layer is determined by the thickness (diameter) of the NPLs (Dots) and their ligand lengths.

incidence is chosen to be the x - z -plane, which defines the s-polarized field to point in the y -direction.

With the vacuum wave-vector $k_0 = \frac{\omega}{c}$ and the wave-vector component parallel to the interface $k_x = \sqrt{\epsilon_1} k_0 \sin(\theta_{\text{in}})$, which is conserved between each layer, the perpendicular components are given by

$$k_{i,z} = \sqrt{k_0^2 \epsilon_i - k_x^2} \quad (6.5)$$

in media $i = 1, 2, 3$, respectively (see also Chapter 2).

If the emitter is placed in an uniaxial material the effective permittivity for the axis parallel ($\epsilon_{\text{eff}}^{IP}$) and the axis perpendicular to the interface ($\epsilon_{\text{eff}}^{OP}$) can be calculated. In the case of pure s-polarization, the electric field vector is parallel to the interface and its wave-vector is

$$k_{2,z}^s = \sqrt{k_0^2 \epsilon_2^s - k_x^2}, \text{ where } \epsilon_2^s = \epsilon_{\text{eff}}^{IP} \quad (6.6)$$

For p-polarized light, the electric field vector lies in the plane of incidence, and an angle-dependent dielectric function can be defined as

$$\epsilon_2^p(\theta_{\text{in}}) = \frac{\epsilon_{\text{eff}}^{IP} \epsilon_{\text{eff}}^{OP}}{\sqrt{(\epsilon_{\text{eff}}^{IP} \sin \theta_{\text{in}})^2 + (\epsilon_{\text{eff}}^{OP} \cos \theta_{\text{in}})^2}} \quad (6.7)$$

to take into account the anisotropy of the material. The respective wave-vector is then given by

$$k_{2,z}^p = \sqrt{k_0^2 \epsilon_2^p - k_x^2} \quad (6.8)$$

More details can be found in Appendix B.

For reciprocal (linear, time-invariant) media, the linear density of states is proportional

to the absorption rate for an identically oriented dipole [110].

$$\tilde{\rho}^{s,p}(\omega, k_x) = C_0 \left| \frac{E_x(\omega, k_x)}{E_0^{s,p}} \right|^2 + C_0 \left| \frac{E_y(\omega, k_x)}{E_0^{s,p}} \right|^2 + C_0 \left| \frac{E_z(\omega, k_x)}{E_0^{s,p}} \right|^2 \quad (6.9)$$

with

$$C_0 = \frac{1}{8\pi k_0^2} \frac{k_0}{k_{3,z}} \quad (6.10)$$

Now we can distinguish between in-plane and out-of-plane contributions to the density of electromagnetic modes $\tilde{\rho}^{p,s}(\omega, k_{x,y}) = \frac{\rho^{p,s}(\omega, k_{x,y})}{\rho_0(\omega)}$ in the emitter medium:

$$\begin{aligned} \tilde{\rho}_{IP}^s(\omega, k_x) &= C_0 \left| \bar{t}_{12}^s e^{\frac{1}{2} i k_{2,z}^s D_{ML}} (1 + r_{23}^s e^{i k_{2,z}^s D_{ML}}) \right|^2 \\ \tilde{\rho}_{IP}^p(\omega, k_x) &= C_0 \left| \frac{k_{2,z}^p}{\sqrt{\epsilon_2^p} k_0} \bar{t}_{12}^p e^{\frac{1}{2} i k_{2,z}^p D_{ML}} (1 - r_{23}^p e^{i k_{2,z}^p D_{ML}}) \right|^2 \\ \tilde{\rho}_{OP}^p(\omega, k_x) &= C_0 \left| \frac{k_x}{\sqrt{\epsilon_2^p} k_0} \bar{t}_{12}^p e^{\frac{1}{2} i k_{2,z}^p D_{ML}} (1 + r_{23}^p e^{i k_{2,z}^p D_{ML}}) \right|^2 \end{aligned} \quad (6.11)$$

where multiple reflections are taken into account by a Fabry-Pérot model (similar to the previous chapters).

$$\begin{aligned} \bar{t}_{12}^s &= \frac{t_{12}^s}{1 - r_{23}^s r_{21}^s e^{2i k_{2,z}^s D_{ML}}} \\ \bar{t}_{12}^p &= \frac{t_{12}^p}{1 - r_{23}^p r_{21}^p e^{2i k_{2,z}^p D_{ML}}} \end{aligned} \quad (6.12)$$

Here, D_{ML} is the thickness of medium 2. Following the definitions in Eq. 2.14, the Fresnel coefficients are given by

$$\begin{aligned} r_{ij}^s &= \frac{k_i - k_j}{k_i + k_j} \\ t_{ij}^s &= \frac{2k_i}{k_i + k_j} \\ r_{ij}^p &= \frac{k_i \epsilon_j - k_j \epsilon_i}{k_i \epsilon_j + k_j \epsilon_i} \\ t_{ij}^p &= \frac{2\sqrt{\epsilon_i} \sqrt{\epsilon_j} k_i}{k_i \epsilon_j + k_j \epsilon_i} \end{aligned}$$

for s- and p-polarization, respectively.

A combination of the IP and OP excitation and emission rates for s-polarization and p-polarization can now be fitted to the experimentally observed PL intensity to deduce the fraction of IP and OP dipole contributions.

$$\begin{aligned} S^s(\omega, k_x) &= C_1 \tilde{\rho}_{IP}^s(\omega, k_x) A_{IP}(\omega) \\ S^p(\omega, k_x) &= C_1 \left[\tilde{\rho}_{IP}^p(\omega, k_x) A_{IP}(\omega) + \tilde{\rho}_{OP}^p(\omega, k_x) A_{OP}(\omega) \right] \end{aligned} \quad (6.13)$$

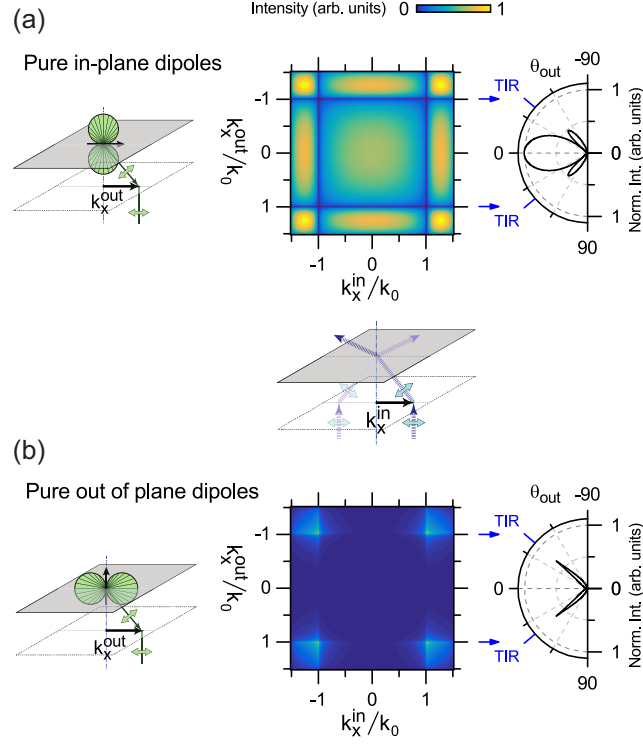


Figure 6.4: Simulated 2D k -space spectra of pure in-plane (a) and pure out-of-plane (b) transition dipoles: k_x -vector dependent dipole emission and excitation. Sketches of the in-plane and out-of-plane dipole radiation patterns are in the left column. The excitation geometry is shown in the center. The false color plots display the modeled p-polarized emission $I(k_x^{\text{out}})$ as a function of the excitation wave vector (k_x^{in}). The right column shows the emission patterns as a function of exit angle θ_{out} with respect to the surface normal of the sample plane. $k_x^{\text{out}} = \sin(\theta_{\text{out}})\sqrt{\epsilon_1}\omega/c$ and ϵ_1 is the permeability of the glass substrate at the emission frequency ω .

Figure 6.4 shows the theoretical predictions of the model for pure IP transition dipoles (a) and pure OP transition dipoles (b). The middle column of the figure displays the two-dimensional plots of the k -vector dependent luminescence intensity, which depends both on the excitation angle θ_{in} and emission angle θ_{out} . Angles and wave vectors are related by $k_x^a = \sin(\theta_a)\sqrt{\epsilon_1^a}\omega^a/c$ with $a = \text{in, out}$ and the permeability ϵ_1 of the glass substrate at the emission (out) our excitation (in) frequency ω^a . A sketch of the experimental geometry in excitation is shown in the middle. For pure IP or pure OP dipoles the 2D k -space images show the same behavior for absorption and emission, respectively. Pure IP and pure OP transition dipole orientations both lead to very specific emission patterns. However, they show only minor differences to the emission in their respective absorption patterns which result from variations of the materials dispersion relations at the excitation and emission frequencies.

Therefore the qualities of the IP and OP dipole emission/ absorption will be discussed using the corresponding angular emission patterns in the right hand column. Here the angular emission pattern is plotted versus its exit angle with respect to the surface normal of the plane. For the representation of the angle-dependent emission in the polar plots the Jacobian transformation from k_x^{out} to θ_{out} has been taken into account so that $\int I(k)dk = \int I(\theta)d\theta$. The two side lobes in the pure IP dipole emission pattern correspond to modes beyond the angle of total internal reflection (TIR) of the glass to air interface ($|k_x| = 1$). They can be observed on the back aperture of our objective due to the index matching immersion optics used. A perfectly in-plane oriented transition dipole has no electric field component in the z direction and we thus expect no emission or absorption at the TIR angle. In contrast, pure OP dipoles can only interact with the light field in a small region of angles seen as two lobes around the TIR angle.

6.2 Experimental Results and Discussion

Figure 6.5 (a) shows the measured p-polarized emission $I(k_x^{\text{out}})$ as a function of the excitation wave vector (k_x^{in}) for platelets (left) and a CdSe QD reference sample (right). They are obtained by plotting the cut in x direction of the back aperture image (see Figure 6.2 b) and c) for every excitation angle k_x^{in} . There are substantial differences between the nano-platelets and QDs: The 2D plot of the QDs is symmetric in excitation and emission. In contrast, the CdSe nano-platelets show more pronounced minima at $|k_x^{\text{out}}| = 1$ in their emission profile compared to the excitation profile. The angular emission $I(k_{\text{out}})$ changes in overall intensity but does not alter its shape as a function of excitation angle. This indicates that different dipoles are involved in the absorption process at 415 nm and the emission at 513 nm and the electronic system has no 'memory' of the exciting field's polarization. As seen in Figure 6.4 (b) out-of-plane transition dipoles only interact with the light field around the TIR angle ($|k_x| = 1$) and vanish for the range of angles and k -vectors $|k_x^{\text{out}}| \neq 1$. Hence nano-platelets must have a higher fraction of emitting IP transition dipoles compared to that of absorbing dipoles.

Now the experimental results can be compared to the theory (panel b) with all model parameters being determined by the measurement. It is important to note that the only free parameters (determined by least square routine) are the dipole distributions, i.e. the ratio of IP to OP dipole moments in absorption and emission. A very good agreement of the model can be observed with the experimental results in both cases. In the following, the emission and absorption transition dipole distributions of CdSe quantum dots and

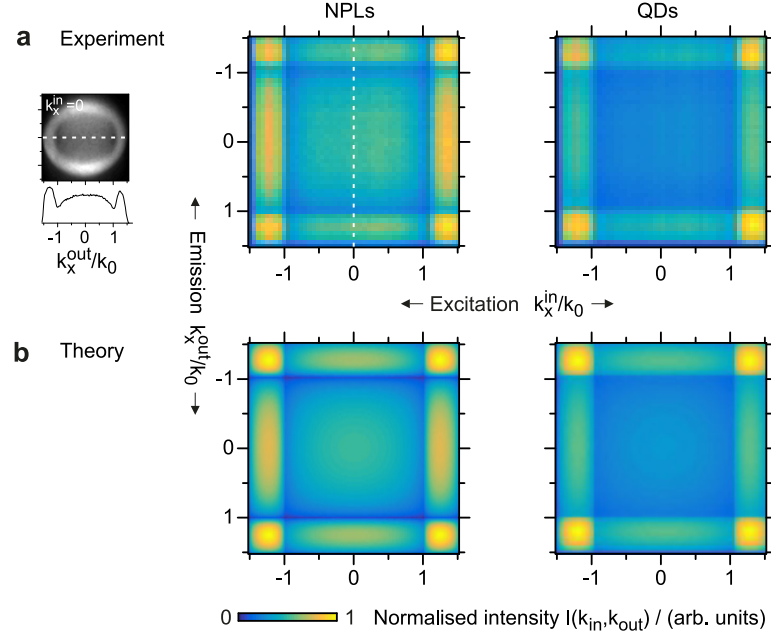


Figure 6.5: Comparison of calculated and experimental 2D k -space spectra for nano-platelet and quantum dot samples. (a) The experimental 2D k -space spectra of our nano-platelet and quantum dot samples are obtained by plotting p-polarized emission $I(k_x^{out})$ for every excitation wave vector (k_x^{in}). QDs' 2D spectra are symmetric, NPLs' less so. This indicates that NPLs have different transition dipole distributions for absorption and emission. (b) Calculated 2D k -space spectra. Isotropic distributions are obtained from the analysis for QD emission and absorption as well as for NPL absorption. Highly anisotropic distributions are evident for emitting NPL dipoles.

nano-platelets will be discussed in more detail.

Figure 6.6 a) and c) display the angle-dependent characteristics of platelets and dots for p-polarized excitation (blue frame) and emission (green frame). Figure 6.6 b) shows that the CdSe platelets are excited in the 2D absorption continuum, as the expected step-like, constant density of states is observed near the excitation laser energy. For CdSe dots it is also known that an excitation energy of 2.99 eV leads to continuum state absorption, Figure 6.6 d). Here the excited carrier states do not depend on the spatial quantum confinement. Thus the TDM distribution is isotropic.

The model results are shown as red curves in Fig. 6.6 a) and c). Experimental data and model are normalized to their total intensity, given by the integrated area under curve. The ratio of IP to OP transition dipoles can be deduced as described in detail in the previous section. An isotropic distribution of TDMs is expected to have 67% IP (due to two degenerate dipole orientations in x and y -direction) and 33% OP contributions. For ab-

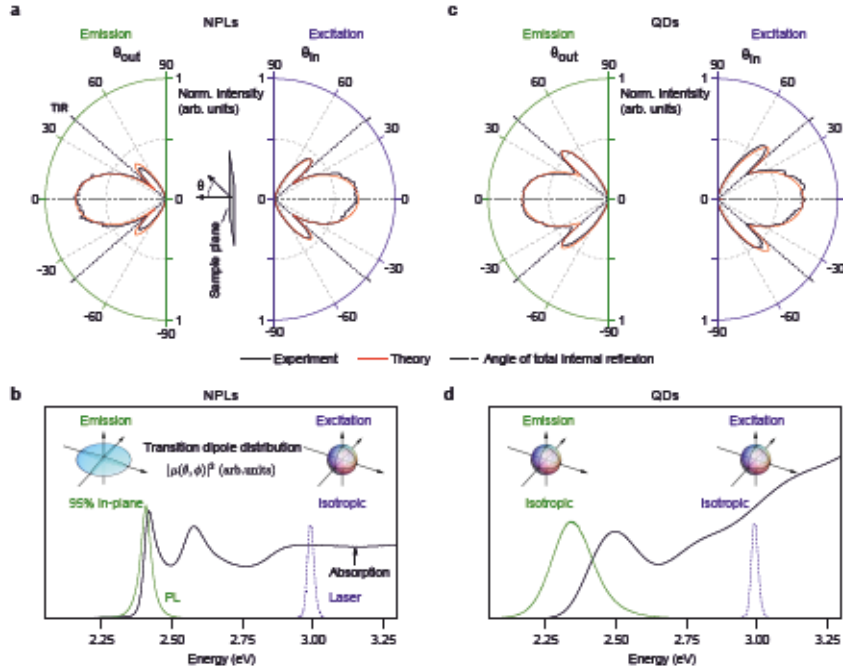


Figure 6.6: Angular dependent excitation and emission of CdSe nano-platelets and spherical quantum dot monolayers. (a) and (c): Polar plots of the angular dependent emission (θ_{out} , green frame) and excitation (θ_{in} , blue frame) along with theory curves. Data and model are normalized to their total intensity, i.e. area under curve. (b) and (d): Absorption and photoluminescence spectra of the studied nano-platelets and QDs along with the exciting laser. Insets: distributions of dipole moments for random orientation and for the strong anisotropic case of the emission of the oriented NPL monolayer calculated from our model.

sorption we find the dipole moments of dots to be 69% IP and 31% OP oriented. This reflects the fully isotropic nature of the absorption transition dipoles in ZB CdSe or PbSe nano-crystals [115]. With 70% IP and 30% OP orientation the distribution for platelets is likewise isotropic in the x - y -plane within our experimental error (5%). The small deviations of the excitation characteristics of dots and platelets (blue frames in Fig. 6.6 a) and c) are the result of dielectric effects. As mentioned above our nano-platelet monolayer samples form an anisotropic effective medium [176, 177] differing from the QD monolayer. Further, the QD and NPL monolayers have different thicknesses – determined by the nanocrystal thickness and the length of the oleic acid molecules.

For the emission of CdSe dots we observe a nearly ideal 68% IP to 32% OP ratio. So, the angular emission of dots does not differ from their excitation as the materials dispersion relations at the excitation and emission frequencies show only minor differences.

However, the angular dependent emission of CdSe nano-platelets is considerably dis-

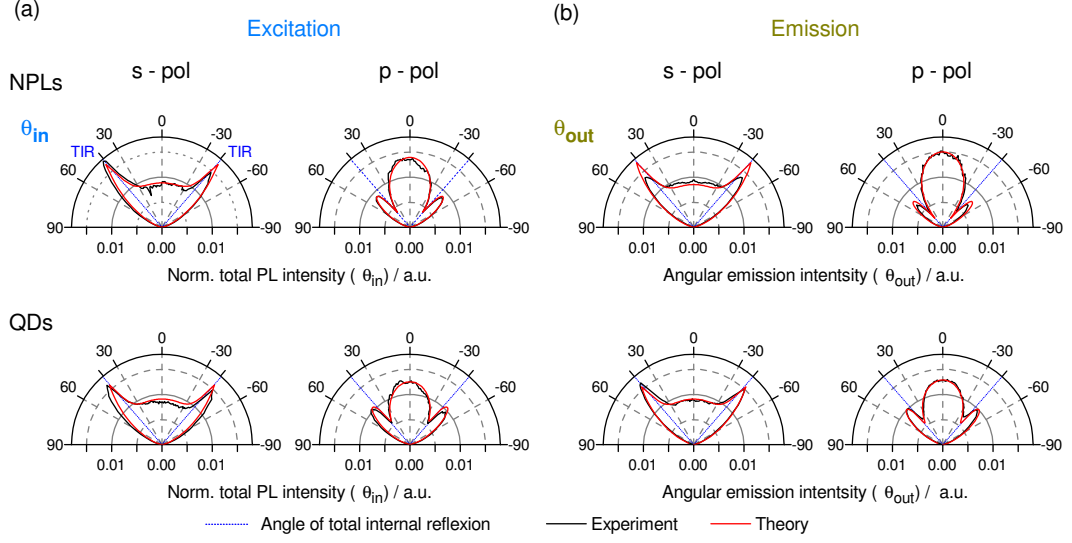


Figure 6.7: Angular dependent excitation (a) and emission (b) of monolayers of CdSe nano-platelets (upper images) and spherical quantum dots (lower images) for s-polarization and p-polarization. Data and model are normalized to their total intensity, i.e. area under curve.

tinct from its absorption. It also deviates strongly from the isotropic emission TDM distribution of the CdSe dots. From the model, a 95% IP to 5% OP distribution of the transition dipole is found for the CdSe nano-platelets' heavy hole emission. Due to the higher contribution of IP transition dipoles the emission of CdSe platelets is concentrated strongly along the surface normal. The ratio of the intensity within the angle of total internal reflection compared to the intensity of the side lobes increases from excitation to emission in Figure 6.6 a) from 3.5 to 5.0. Therefore NPLs can be considered as highly directional emitters. The strong anisotropic confinement in the CdSe nano-platelets has induced a predominant orientation of the TDM in a bright plane that coincides with the nano-platelets plane. The electronic origin of the anisotropy of the heavy hole transition in zinc blend nano-platelets is discussed in the next section and in greater detail in Appendix B.

The insets in Figure 6.6 b) and d) visualize the actual distributions of the TDMs for all cases. The measured 95% IP contribution for CdSe platelets leads to a strongly oblate shape, reflecting the bright plane.

For the sake of completeness, polar plots for s-polarization are also shown together with p-polarized excitation (a) and emission (b) in Fig. 6.7 for nano-platelets and dots. In s-polarization only minor deviations are observed between excitation and emission and also between nano-platelets and dots. This could be expected as in this detection

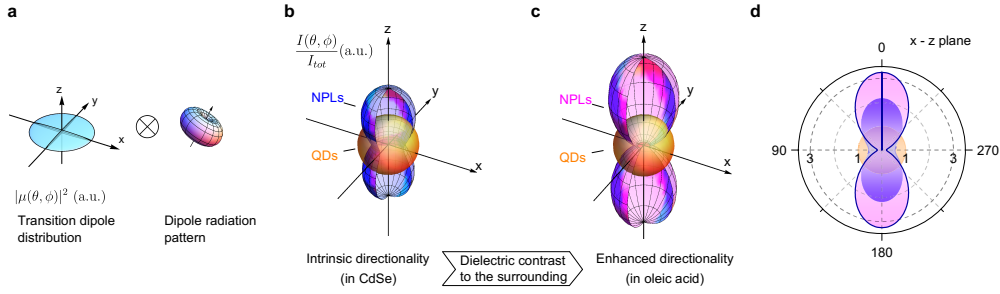


Figure 6.8: Radiation patterns of nano-platelet and quantum dot monolayer ensembles in isotropic media. (a) The transition dipole distribution $|\mu|^2(\theta, \phi)$ (shown here for platelets as derived from the fits in Figure 6.6) is convolved with the radiation pattern of a Hertzian dipole. The nanoparticle monolayers are oriented in the x,y plane. (b) The obtained radiation intensity pattern of nano-platelets (blue) and dots (orange) of the pure electronic contribution, as if the emitters were embedded in an infinite CdSe medium. (c) The external radiation patterns of platelets (magenta) and dots (orange) are calculated for an isotropic dielectric surrounding of oleic acid (with $n=1.46$) taking local field factors into account. The data in (b) and (c) is normalized to the total intensity I_{tot} emitted over 4π . (d) Comparison of radiation patterns of dots (orange) and NPLs with and without dielectric effects (blue and magenta) in the x - z plane. Clearly, platelets emit predominantly in direction of the surface normal, which corresponds to 0 and 180 degrees. Dielectric effects (magenta) further enhance this directionality.

configuration only IP dipoles can contribute to s-polarized emission. Differences in the dielectric surrounding for the excitation and emission wavelengths are hence the only source of deviations.

6.3 Analysis of Dielectric and Electronic Contributions

Up to now this analysis has concentrated on the external emission characteristics of the nano-particles embedded in a multilayer system. With the theoretical model the internal distribution of TDMs in the CdSe nano-platelets and QDs monolayers could be extracted. This allows the reconstruction of radiation intensity patterns of a monolayer nanocrystal ensemble in isotropic media. Figure 6.8 b) shows the case without dielectric contrast, which resembles excitons radiating into an infinite CdSe medium. It is given directly by the convolution of the internal dipole distribution $|\mu(\theta, \phi)|^2$ with the radiation pattern of a Hertzian dipole as indicated in (a). This pure electronic contribution to the radiation pattern is shown in (b) for NPLs in blue and for QDs in orange.

Now an isotropic surrounding is considered with dielectric contrast to CdSe. A medium

with the refractive index of a matrix in which nano-crystals are typically embedded is chosen: oleic acid $n=1.46$ [180]. These dielectric effects are described by local field factors $f_{x,y,z}$ of the NPLs [176] at the exciton emission energy. By averaging over the two in-plane components on the long axes of the platelets f_x and f_y the azimuthal random orientation of the NPL monolayer ensemble is taken into account and the field factor ellipsoid $|f(\theta, \phi)|^2$ is constructed (see Appendix B). The product [114, 181] of the field factor ellipsoid times the dipole distribution $|\mu(\theta, \phi)|^2$ is convolved with the radiation pattern of a Hertzian dipole to obtain the angular dependent radiation intensity of an emitter in an isotropic dielectric medium. The result is shown in 6.8 c) for NPLs in blue and QDs in orange. The cut through the x-z plane of the same data is plotted in (d). The intensity emitted perpendicular to the platelet is ~ 4 times higher than into the x-y plane.

Platelets have a highly anisotropic shape and high dielectric contrast to a typical ligand or polymeric surrounding. Their local field factors in-plane exceed the field factor for a field oscillating in the out-of-plane direction by almost an order of magnitude ~ 16 . The radiation from in-plane dipoles, i.e. the bright plane, is thus also favored by the dielectric effects so that in a realistic environment the emission becomes even more directed as seen in Figure 6.8 (b). On the other hand, CdSe QD monolayer ensembles emit isotropically since they have an isotropic dipole orientation. The local field factors of dots are isotropic as well.

The distance from the origin to a point on the surface of the 3D objects is proportional to the irradiance transmitted through the surface of a unit sphere at a given solid angle $I(\theta, \phi)$. The monolayer ensemble of NPLs (QDs) is placed in the center of the unit sphere and aligned to the x - y plane. To compare the radiation characteristics of the NPL and QD monolayer ensembles quantitatively we normalize to their total emitted power $I_{tot} = \int \int I(\theta, \phi) \sin \theta d\theta d\phi$. For a more detailed discussion on local field factors and radiation patterns see Appendix B.

It can be concluded from Figure 6.8 that the emission of the CdSe nano-platelets is highly directed normal to the platelet plane due to the existence of a bright plane of IP dipoles. This electronic effect is further intensified by the shape of the platelets in a dielectric surrounding and allows to use the CdSe platelets as a new type of directional emitters e.g. for display technology.

6.3.1 Microscopic Origin of the Anisotropy

In photoluminescence experiments, electron-hole recombination takes place between states near the band edges, as population excited in the continuum relaxes fast and radiation-

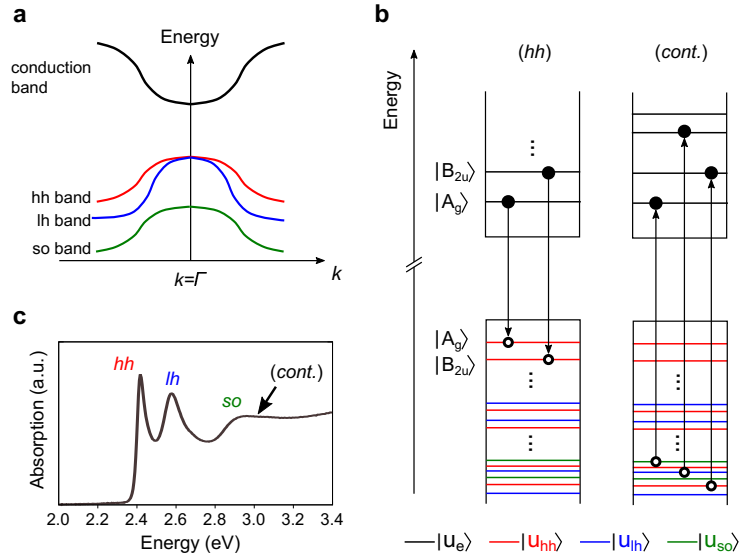


Figure 6.9: The contribution of different Bloch states determines the isotropic absorption and anisotropic emission of CdSe nano-platelets (a) A bulk zincblende (ZB) semiconductor has degenerate heavy-hole hh and light-hole lh sub-bands. The effective masses along the growth direction are heavier for hh than for lh , so the top of the valence band in NPLs is formed almost exclusively by hh states. (b) Schematic of the conduction band electron and valence band hole energy levels in a rectangular (D_{2h}) NPL with ZB crystal structure. Symmetry labels for envelope $|\nu\rangle$ and periodic parts $|u_j\rangle$ of a few states, $|\nu\rangle|u_j\rangle$, are given. The envelope functions, characterized by their basic symmetries ($|A_g\rangle$ and $|B_{2u}\rangle$), are shown on the left. The Bloch states are given color-coded at the bottom of (b). (hh): Dipole-allowed near-band-edge transitions (emission). ($cont.$): Dipole-allowed high energy transitions in absorption. In emission only hh levels (red) are involved, resulting in prevailing out-of-plane emission. In continuum absorption ($cont.$) hh , lh and split-off so holes are equally involved, which results in isotropic absorption. The corresponding transitions of (hh) and ($cont.$) are indicated in the NPL absorption spectrum in (c). In contrast to the bulk case shown in (a) the confinement lifts the degeneracy of the hh and lh .

less to the band-edge. As shown in Figure 6.9 (b) column (hh), this involves only emission from the heavy hole hh to which all excited higher excitons and electron-hole (e-h) pairs cool down. The emission dipoles of these hh excitons lie in the x - y plane and are thus IP. The intrinsic nature of the observed directed emission is thus related to the anisotropy of the electronic Bloch states governing the exciton transition dipole moment. This theoretical expectation is in excellent agreement with our measured 95% IP dipole orientation, considering our error margin of 5%.

Consequently, emission is mostly orthogonal to the NPL surface. Notice this is independent of the envelope function symmetry, and hence compatible with previous works

suggesting emission can have finite contribution from excited (B_{2u}) excitons [108]. On the other hand, our absorption experiments are performed at high energy. As shown in Figure 6.9 (b) column (*cont.*), optical transitions include any kind of hole state (hh , light-hole lh , split-off so or their mixture). On average, this means that the continuum absorption in our CdSe nano-platelets is isotropic with respect to the internal dipole distribution. This is again in agreement with our experimental results of nearly isotropic transition dipole distribution (70% in-plane to 30% out-of-plane) in absorption (ideally 67% to 33%). Details on Bloch states, envelope function and selection rules can be found in Appendix B.

By the means of two dimensional k -space spectroscopy we have demonstrated the directed emission of highly oriented CdSe nano-platelet monolayers. Our analysis shows that heavy hole exciton transition dipoles of the platelets' are oriented in a bright plane that coincides with the platelet plane. For nano-platelets the resulting out-of-plane directed emission is further favored by dielectric and local field effects. However, the transition dipole distribution in the platelets' 2D continuum has no preference: As the absorption and emission of quantum dot monolayers it is isotropic. We further showed that the observed anisotropic transition dipole distribution for the lowest hh excitons is directly related to the basic anisotropy of the electronic Bloch states governing the dipole moment. Hence k -space spectroscopy allows direct access to the internal Bloch states.

The combination of isotropic absorption and highly anisotropic emission makes CdSe nano-platelets an interesting directional emitter for photonic applications like in display technology or lasing, where directed emitters are desirable. As losses to non out-coupled modes (e.g. under oblique angles) are suppressed due to the directed emission, we expect a significant increase of the radiative out-coupling efficiency in displays. Gain media of oriented platelets in super structures for example are expected to have superior performance over random oriented or spherical nano emitters. Improved inversion conditions and reduction of losses through spontaneous emission might be achieved with high directional gain and flexible pump directions.

7 | k -Space Resolved Two-Photon Absorption in Oriented Nano-Platelets

Due to their large two-photon absorption (TPA) cross section, semiconductor nano-crystals are of current interest in many applications such as non-linear gain media [182], optical power limiting, photo-dynamic two-photon (TP) cancer therapy [183] or bio-labeling [184]. TPA has further become important in various applications, e.g. micro-fabrication, lithography, polymerization, data storage and spectroscopy [185–187]. Cell and animal in-vivo imaging [188] can also be realized by confocal two-photon imaging combining high spatial resolution and deep tissue penetration [189]. The scheme of TPA is shown in Fig. 7.1 a): Simultaneous absorption of two photons whose combined energy corresponds to the gap between electronic states leads to excitation from a lower state to a higher energy electronic state. This third-order nonlinear process depends on the square of the excitation intensity.

The combination of individual photon-emitters such as quantum dots, dye molecules, colloidal nano-particles and sub-wavelength-confined plasmon modes on metal films promises significantly enhanced emission while being excited at the plasmonic resonance [117–120, 122–124]. Thus improvements in numerous fields have been achieved such as sensing, microscopy, photovoltaics and spectroscopy [125–128]. Directed emission from coupling into the plasmonic mode has likewise been observed [116, 121, 122].

Plasmonic resonances in combination with TPA are of current interest in fluorescence microscopy, sensing applications and nano-lithography [129–134]. Highly oriented nano-platelets with their distinct radiation pattern (section 6.3) on top of plasmonic thin films promise boosted excitation and directed emission normal to the interface. In addition, nano-platelets are known for their extraordinary TPA cross-section [103].

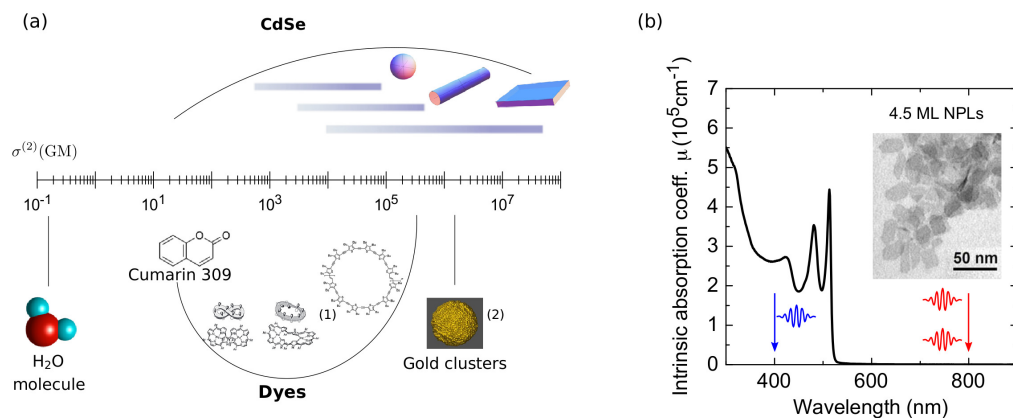


Figure 7.1: TPA cross-section and absorption spectrum of NPs. a) Comparison of two-photon absorption cross sections for different absorbers. CdSe nano-platelets have the largest reported cross section of up to $5 \cdot 10^7$ GM. b) Intrinsic absorption coefficient as a function of excitation wavelength. The characteristic 2D density of states can be seen in the absorption spectrum.

The preliminary work from Chapters 5 to 6 enables investigation and understanding of such samples which combine oriented nano-platelets with plasmonic layers. Therefore, the *k*-space setup from Chapter 6 (Fig. 6.1) is used for angle-dependent excitation and detection with spectral resolution. This enables simultaneous observation of the plasmonic resonance, SHG and photoluminescence.

The next section treats TPA excitation of oriented nano-platelets without plasmonic layers to characterize the excitation and emission patterns. The internal distribution of transition dipole moments (TDM) and the degree of in-plane orientation for this set of nano-platelet samples is determined as well. Differences between linear and TPA absorption are discussed in terms of their respective TDM distribution. Subsequently, a silicon dioxide covered silver layer is added (between the substrate and the NP monolayer) which enables plasmonic coupling. Surface plasmon enhanced excitation and directed emission into the plasmon mode are investigated and potential applications are discussed.

7.1 Two-Photon Absorption Of Oriented CdSe Nano-Platelets

CdSe nano-platelets have been identified to offer remarkably high TPA cross sections with respect to the particle volume [173] as compared to other semiconductor nanoparticles like CdSe or CdS dots and rods [176, 190]: TPA cross sections of up to $5 \cdot 10^7$ GM

(1 GM=1 Göppert Mayer= 10^{-50} cm⁴ s photon⁻¹) have been reached for CdSe nano-platelets which is way beyond typical two-photon absorbers which have cross sections smaller than 1000 GM[191]. Indeed, it is the largest ever reported for colloidal semiconductor nanocrystals [103]. Higher cross sections per particle or volume result in lower excitation intensities to obtain a sufficiently high response in TPA applications with the same amount of material. A comparison for different two-photon absorbers is shown in (Fig. 7.1 c).

Due to their strong confinement in normal (z -) direction, nano-platelets have a 2D density of states resulting in step-like TPA spectra with strong continuum absorption and a weak first excitonic resonance. In summary nano-platelets are extremely efficient and desirable broadband two-photon absorbers for applications in confocal two-photon imaging and non-linear opto-electronics.

7.1.1 Sample Characterization And Experimental Setup

The investigated Zinc-blend (ZB) CdSe nano-platelets had a thickness of 4.5 monolayer (1.37 nm). The lateral size of these NPLs in x and y direction (being determined by TEM-analysis, see inset in Fig. 7.1 b) has been averaged ($L = \sqrt{19.6 \cdot 9.6 \text{ nm}^2}$) accounting for the NP's random orientation inside this plane. The aspect ratio is then defined as $AR = n \cdot d_{ML}/L$. The lattice parameter for zinc blende CdSe[192] is twice the monolayer thickness $d_{ML} = 0.304$ nm with n being the number of CdSe monolayers. The studied NPLs are assumed to be cadmium-terminated on both basal planes as shown by Li et al. [192] and She et al.[182]. They consist of four Se and five Cd monolayers and their heavy hole emission is found at 513 nm (Fig. 7.1 b).

The NPLs were deposited on 170 μm thick fused silica substrates by a Langmuir technique. The sample can thus be modeled as a three layer system consisting of the glass substrate, a monolayer of nano-platelets and their ligands, and the surrounding air (Fig. 7.2):.

In Chapter 6, similar monolayer samples of CdSe nano-platelets have been shown to exhibit a high degree of in-plane (x - y -plane) transition dipole orientation. Now, the confocal k -space spectroscopy setup from Fig. 6.1 is applied to investigate angle dependent linear and two-photon absorption of these oriented CdSe nano-platelets. A Ti:Sapphire laser (FWHM 150 fs, 75.4 MHz, 0.1 W/cm² excitation density) provided p-polarized pulsed radiation at 830 nm wavelength for TPA excitation. For linear excitation, a beta barium borate (BBO) crystal was introduced for frequency doubling, resulting in an excitation wavelength of 415 nm.

The k -space analysis is performed using a high numeric aperture (1.49) immersion oil objective shown in Fig. 7.2. Excitation and detection are symmetric in the confocal

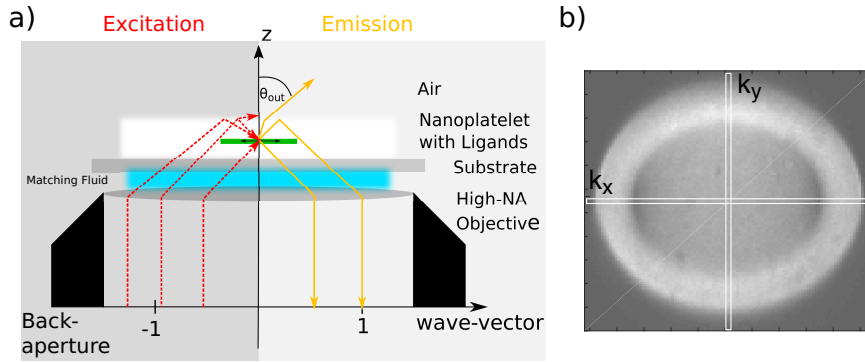


Figure 7.2: Excitation and emission scheme of oriented NPs. A high NA immersion oil objective is used to excite a sample of oriented nano-platelets. By projecting the back aperture of the objective onto a highly sensitive CCD camera, the wave-vector dependence of the emission and hence its angular emission pattern can be observed. Simultaneous variation of the excitation wave-vector in the back aperture enables 2D k -space spectroscopic measurements. Total internal reflection occurs for wave-vectors larger than the wave-vector in the surrounding air, ($k > 1$). b) shows a typical emission pattern for oriented nano-platelets. The k_x - and k_y -cuts can be referred to p-polarized and s-polarized emission, respectively.

setup. The beam position in the back aperture of the objective can be defined as wave-vector component and relates to the incident angle in the focus via a Fourier transform. The excitation and emission characteristics can hence be characterized by imaging the back aperture on a sensitive CCD camera. Furthermore, a polarizer is inserted in the detection to determine in-plane (IP) and out-of-plane (OP) contributions of the emission (see Fig. 6.2). Detailed information about the samples and the experimental configuration can be found in section 6.1 and in the Appendix B.

7.1.2 Transition Dipole Distributions for TPA Excitation

To determine the distribution of transition dipoles involved in the respective absorption and emission processes, we applied the analysis from Section 6.1.1. Here, all parameters are defined by the experimental setup except for the ratio of purely IP and OP oriented transition dipoles which is obtained by fitting the experimental results with a least square routine. According to this model, a ratio of 67% IP dipoles to 33% OP dipoles is expected for an isotropic transition dipole distribution.

A comparison of linear and TPA excitation and the related emission patterns is shown in Fig. 7.3. The case of linear excitation at a wavelength of 415 nm was discussed in detail in Chapter 6. Here, the absorption is nearly perfectly isotropic with a 3D-ratio of 70%IP

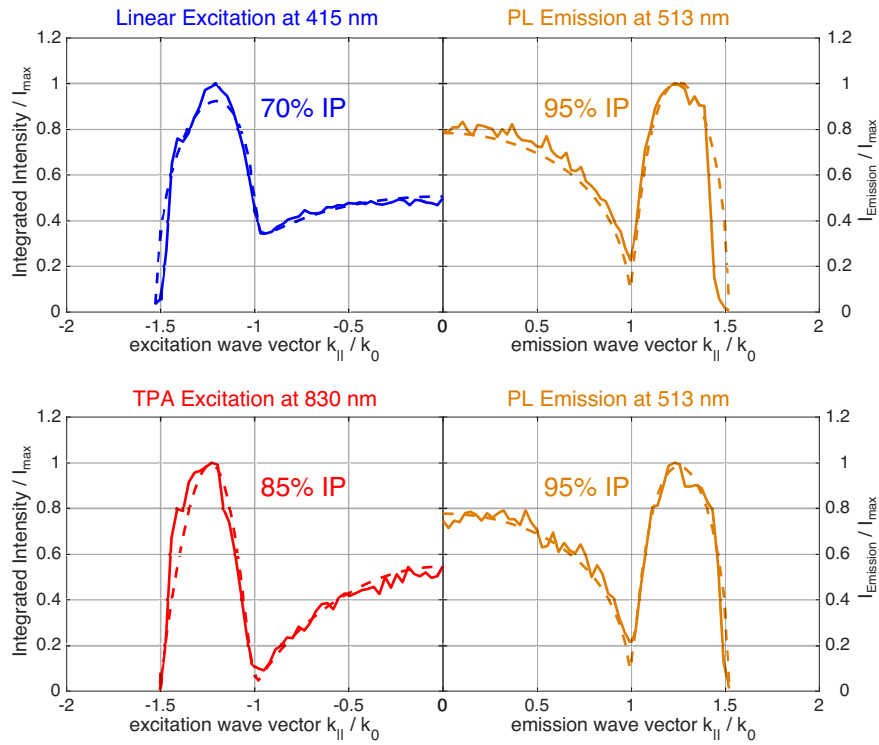


Figure 7.3: Comparison of linear and TPA excitation of oriented nano-platelets and the related emission patterns. The upper image shows linear excitation at a wavelength of 415 nm on the left and the related photoluminescent emission at a wavelength of 513 nm on the right. The lower image shows TPA excitation at a wavelength of 830 nm and the corresponding emission at a wavelength of 513 nm. The dashed lines correspond to our theoretical calculation and the insets contain the respective 3D-ratio of in-plane oriented transition dipoles.

and 30% OP transition dipoles (compare Eq. 6.4). For the emission, a highly anisotropic transition dipole distribution was found with 95% IP and only 5% OP dipoles. This results in strongly directed emission perpendicular to the nano-platelets. In photoluminescence experiments at room temperature, electron-hole recombination takes place between states near the band edges (see Appendix C). The excitonic emission is thus governed by the heavy hole transition which is only enabled by in-plane polarized light and accounts for the emission anisotropy. The absorption in the continuum in contrast includes heavy hole hh transitions as well as light hole lh and split-off so transitions which results in an isotropic distribution (see Chapter 6).

For two-photon absorption however, emission and excitation show anisotropic transition dipole distributions. The emission pattern is not altered compared to the case of linear excitation and shows the same ratio of 95% IP and 5% OP transition dipoles. This could be expected as the recombination process is still governed by the hh exciton. For

TPA excitation however, the model delivers a 85% IP to 15% OP ratio of the transition dipoles which reflects a considerable orientation. To account for the nonlinearity in the TPA process [193], the calculated intensities from Eq. 6.13 had to be squared to fit the experimental results leading to

$$\begin{aligned} S^s(\omega, k_x) &= (C_1 \tilde{\rho}_{IP}^s(\omega, k_x) A_{IP}(\omega))^2 \\ S^p(\omega, k_x) &= \left(C_1 \left[\tilde{\rho}_{IP}^p(\omega, k_x) A_{IP}(\omega) + \tilde{\rho}_{OP}^p(\omega, k_x) A_{OP}(\omega) \right] \right)^2 \end{aligned} \quad (7.1)$$

An explanation for the anisotropy in TPA excitation can be given regarding the probability of a TPA process taking place which is given by the 2nd order Fermi golden rule:

$$W_{TPA} = \frac{2\pi}{\hbar} \sum_{i,f} \left| \sum_m \frac{\langle f | \vec{e} \cdot \vec{p} | m \rangle \langle m | \vec{e} \cdot \vec{p} | i \rangle}{E_m - E_i - \hbar\nu} \right|^2 \delta(E_f - E_i - 2\hbar\nu) \quad (7.2)$$

where $|j\rangle$ is the wave function and E_j the energy in the initial ($j = i$), the intermediate ($j = m$), and the final ($j = f$) state. Here, \vec{e} is the light polarization vector and \vec{p} the momentum operator.

The initial states are in the valence band (hh -subband, lh -subband and so -subband) and the final states are in the conduction band (cb). Intermediate states for two-photon transitions are virtual, non-resonant, states, which are short-lived and hence energetically not well defined. The transition probability of such processes is proportional to the sum of perturbation terms involving all possible intermediate states and can thus be decomposed into a linear combination of resonant states. We can envisage the whole process as the sum of several paths through different non-resonant intermediate states $|m\rangle$.

The optical selection rules for these transitions are given by the matrix elements in the numerator. A detailed discussion of possible interband and intraband transitions and their optical orientation (which corresponds to the polarization of the optical excitation) can be found in Appendix C. It can be seen from the denominator and the δ -condition in Eq. 7.2, that the probability for transitions is maximized for intermediate states near the laser energy, where

$$E_m \approx \frac{E_f - E_i}{2} \quad (7.3)$$

A schematic representation of the decomposition into the different possible transitions can be found in Fig. 7.4. As discussed in Chapter 6 and the Appendix B, the luminescent emission takes place through recombination of the hh -exciton. This interband transition is interrelated to an optical orientation of the TDM inside the platelet-plane which causes the strong anisotropy of the emission pattern.

However, the decomposition of the TPA excitation comprises a multiplicity of transitions with different optical orientations. Their overall orientation is thus given by the

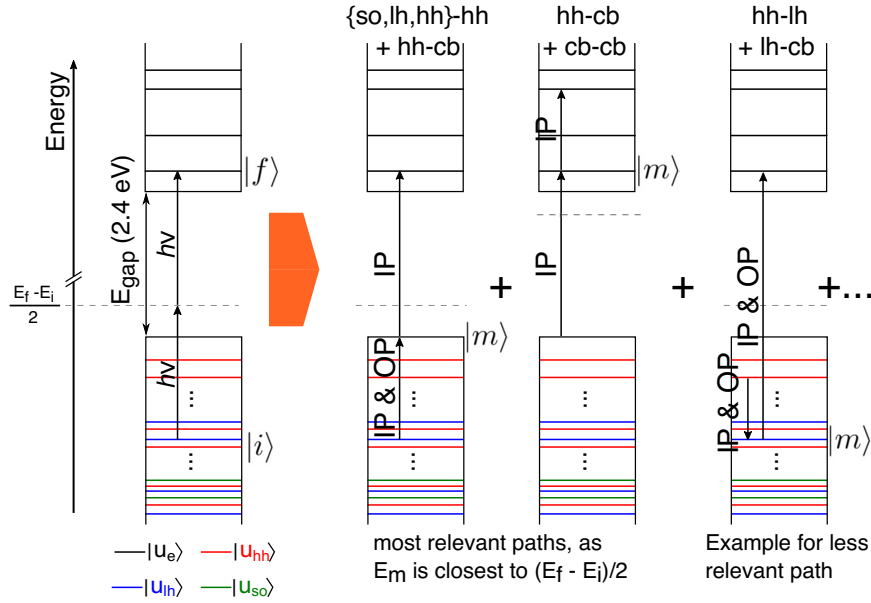


Figure 7.4: TPA excitation and its decomposition into possible transitions. Two-photon excitation from an initial state $|i\rangle$ to a final state $|f\rangle$ takes place through a virtual non-resonant state. The efficiency of this process is proportional to the sum of perturbational terms involving all possible intermediate states $|m\rangle$. In this connection, the transitions close to the $(E_f - E_i)/2$ and thus close to the bandgap energy have the highest probability. These contributions can further be analyzed in terms of their optical orientation (IP and OP), which directly relates to the polarization of the excitation. It should be noted that the displayed path are only examples of all the contributing linear combinations.

sum of allowed transitions weighted with their respective probabilities. As discussed before (Eq. 7.3), the transition probabilities are highest for energies near the laser energy (1.5 eV at 830 nm), which in our case are energies close to the bandgap energy (2.4 eV). The transitions with the highest probability, as shown in Fig. 7.4, are thus containing either hh - cb or cb - cb contributions which are optically in-plane oriented (see Appendix C for further details on selection rules and related orientations).

This analysis confirms our experimental results where the excitation by TPA shows a high degree of orientation. With a ratio of 85% IP transition dipoles, this orientation is considerably higher as for linear excitation (isotropic with 67% IP) but not yet fully oriented as in the luminescent emission with its ratio of 95% IP transition dipoles. This reflects the high, yet not exclusive, probability of transitions with optically in-plane orientation that are involved in TPA excitation of oriented nano-platelets.

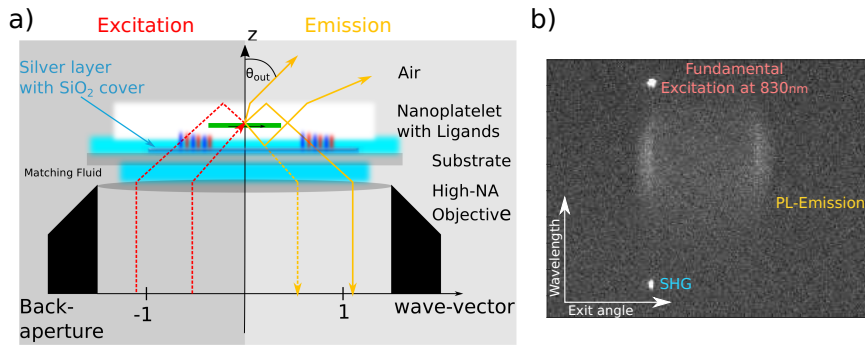


Figure 7.5: Excitation and emission scheme of oriented NPs on a thin silver layer. The sample consists of a 30 nm silver film, a 15 nm SiO₂ spacer and a monolayer of oriented CdSe nanoplatelets. In excitation, coupling to SP occurs by meeting the wave-vector of the resonance which is beyond the angle of total internal reflection, $k_{ex}/k_0 > 1$. SP-excitation through the emission is likewise possible. b) shows a CCD image with the fundamental excitation at a wavelength of 830 nm, the generated SHG at 415 nm and the PL-emission at 513 nm which is directed through coupling to the SP-mode

7.2 Surface Plasmon Enhanced TPA and Directed Emission

With the preliminary characterizations we can investigate the coupling of transition dipoles in oriented nano-platelets to propagating surface plasmons (SPs) in thin metal films. Enhancement of the excitation through the SP resonance, as well as directed emission into the plasmonic mode can thus be examined.

To enable coupling to SP, a thin silver layer is thermally evaporated onto the substrate and covered by a thin silicon dioxide (SiO₂) spacer to avoid quenching. Hereon, a monolayer of oriented nano-platelets is deposited by Langmuir technique as described in Chapter 6.

The excitation and detection scheme is shown in Fig. 7.5 a). Resonant excitation of SPs occurs for wave-vectors larger than that of the surrounding dielectric, which is air in this case ($k_{ex}/k_0 > 1$) and thus beyond the angle of total internal reflection (TIR). The wave-vector position of the SP resonance is strongly dependent on the dielectric functions of the silver layer and the glass used for the objective, and hence the wavelength of the excitation. Likewise, the width of the plasmonic resonance in terms of incident angle and its wave-vector projection depends on the dielectric functions. A raw image of the CCD camera at SP excitation is shown in Fig. 7.5 b). Here, the PL-emission pattern is strongly altered compared to Fig. 7.2 b) due to the sharp SP-resonance for TPA excitation and the

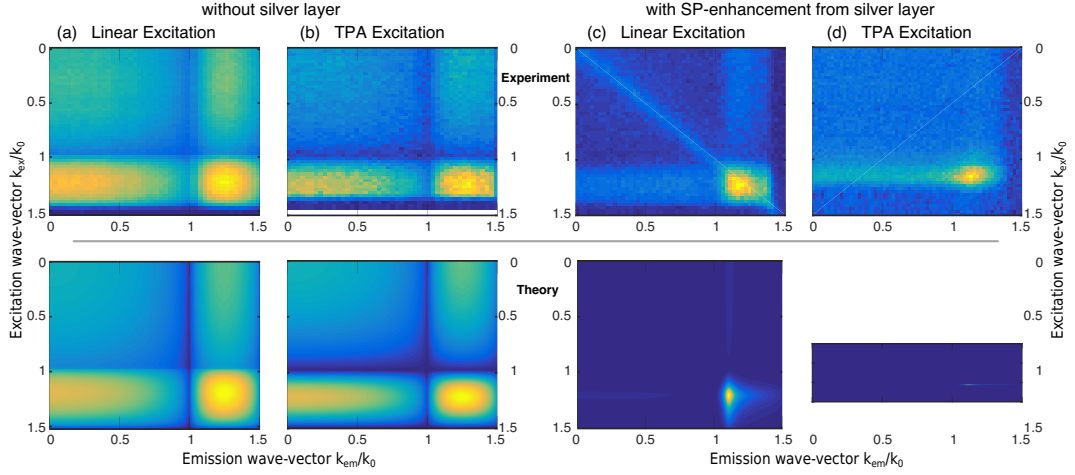


Figure 7.6: 2D k -space analysis of oriented NPs in linear and TPA excitation with and without plasmonic layer. The upper row shows the experimental results for the sample without silver layer (a and b) and for the one with additional silver layer (c and d). The lower row shows the respective simulations from the theory. Linear (a and c) and TPA (b and d) excitation measurements were performed for both samples and the corresponding k -space emission spectra were detected.

directed emission into the plasmonic mode. As in the previous experiments, we vary the excitation while simultaneously detecting the complete emission in terms of its k -space distribution.

2D k -space maps as a function of excitation and emission wave-vector are shown in Fig. 7.6. Here, the emission patterns of samples with and without plasmonic layer are compared for linear and TPA excitation, respectively. As expected from previous results for linear excitation without plasmonic layer, we observe isotropic absorption and anisotropic emission in (a). The latter can be identified by the strong decrease of emitted intensity at $k_{em}/k_0 = 1$ where OP dipoles only can radiate to the far-field. For TPA excitation in (b), absorption and emission are anisotropic which has been discussed in detail in the previous section. Our theoretical model matches the experimental results remarkably well.

A different behavior can be observed for the sample with additional silver layer and its SiO_2 cover, which enables coupling to propagating SPs. Here, the intensity of the emission is strongest, if both excitation and emission wave-vector are close to the plasmonic resonance. In this configuration the SiO_2 -layer affects the SP resonance, which is expected at $k_{\text{SP}}^{415\text{nm}}/k_0 \approx 1,18$ for linear excitation, $k_{\text{SP}}^{513\text{nm}}/k_0 \approx 1,1$ for the PL emission, and $k_{\text{SP}}^{830\text{nm}}/k_0 \approx 1,03$ for TPA excitation, each one normalized to the respective wave-vector k_0 in air. The emission normal to the sample ($k_{em}/k_0 \approx 0$), which is clearly visible for samples without silver layer, is almost completely suppressed. This is a clear

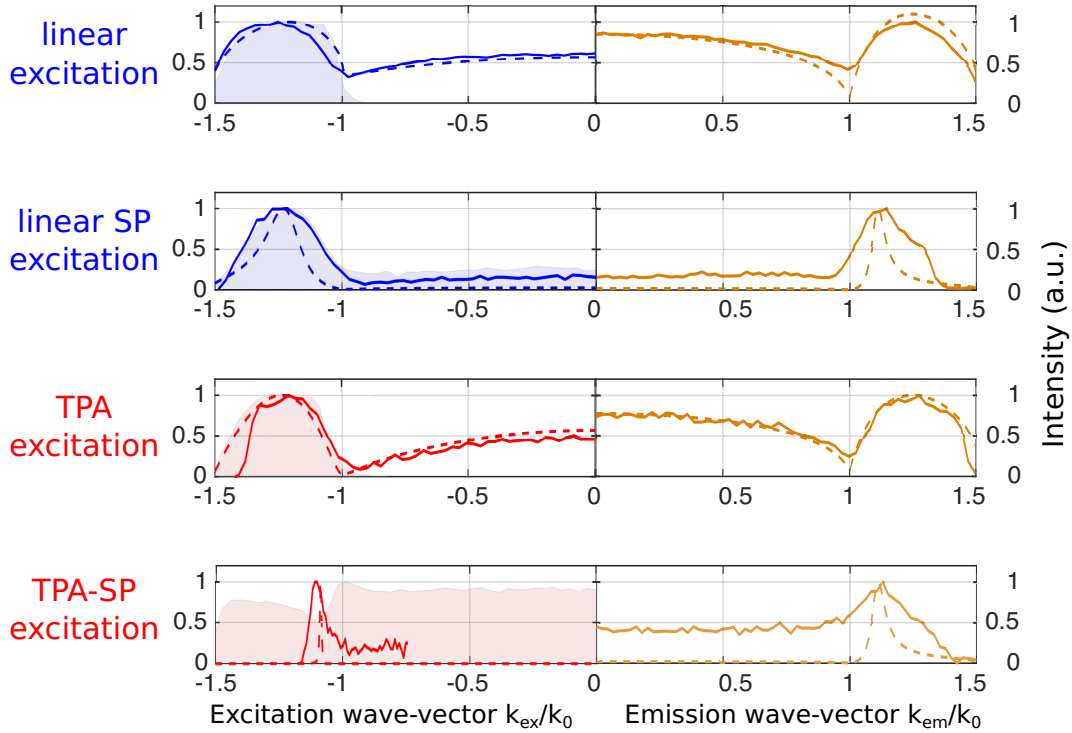


Figure 7.7: k -space cuts for excitation and emission of oriented NPs with and without plasmonic silver layer. The left-hand side shows the wave-vector dependence of the integrated emission for linear excitation and TPA excitation. SP-enhanced excitation through an additional silver layer is further compared to excitation without silver layer. The shaded areas refer to the reflected intensities of the laser used for excitation and the dashed lines to our theoretical calculations. The right-hand side shows the respective emission patterns as a function of exit angle k_{em}/k_0 .

evidence for SP-enhanced excitation of CdSe nano-platelets and the following directed emission into the plasmonic mode. It could be seen in Fig. 2.6 that the SP resonance is considerably broadened in the regime of the linear excitation (415 nm) and also of the emission (513 nm). This corresponds to the broadened SP resonance for linear excitation in (c). Here, the diagonal signal was identified to result from an internal reflection and is hence not characteristic for the emission.

For TPA excitation in the near-infrared (830 nm) in contrast, the SP resonance is expected to be very narrow (d). Indeed, the experimental results show a narrow peak in terms of excitation wave-vector while the emission is still as broad as for linear excitation. These characteristics are confirmed by our theoretical calculations in the lower row.

Fig. 7.7 shows cuts at the wave-vector positions of the respective resonances to illustrate the specific characteristic of SP-enhanced excitation and emission. Due to the di-

electric function of silver at the emission wavelength, the respective SP resonance is still relatively broad. Nevertheless, the emission on the right-hand side is significantly narrowed in terms of wave-vector if it is coupled to a plasmonic mode leading to a direction of the emission. Furthermore, the emission is basically limited to the region of the plasmonic resonance in contrast to the emission without plasmonic layer which has the specific anisotropic shape.

For TPA excitation, this difference is even stronger: A very narrow peak can be seen, which corresponds to the distinct SP resonance in the near-infrared. The plasmonic field enhancement is thus boosting the photoluminescent emission from the nano-platelets. The shaded background refers to the reflected intensity of the laser beam at the respective excitation wavelengths. For the sample without silver layer, the TIR edge is clearly visible. For excitation in the near-infrared with silver layer, the plasmonic resonance is clearly visible as a dip in the reflected intensity. At the wavelength of linear excitation, the corresponding dip is too broad to be distinguishable.

We have shown, that in contrast to linear absorption, the two-photon absorption in oriented nano-platelets is highly directed. This transition dipole orientation was referred to the probabilities of the involved processes and their selection rules. Furthermore, it was demonstrated that an additional silver layer covered with SiO_2 enables surface plasmon enhanced excitation and highly directed emission into the plasmonic mode. The combination of TPA and the plasmonic resonance even led to further concentration of the absorption range as a function of excitation wave-vector.

The integrated intensity of the detected emission for SP-enhanced excitation was weaker than for excitation without silver layer. Our NPs emitted at a wavelength of 513 nm which leads to a broadened SP resonance and is in a regime where the silver is lossy. For reflection measurements, it is thus preferable to use NPs which have their emission at larger wavelengths and provide better coupling to SP. For our platelets however, especially with TPA excitation, the SP leads to enhanced excitation while the emission does not efficiently couple to the SP. With the silver layer acting as a mirror, the emission into the upper half-space (air) is thus expected to be much increased. This effect will be subject of future measurements.

8 | Conclusion

Following the structure of this work, we will emphasize here the most important results of the individual chapters.

Surface Plasmons: Efficient optical access of surface plasmon polaritons (SP) from the far-field has traditionally been accomplished by using evanescent coupling in either the Otto or Kretschmann configurations. With a detailed characterization of these attenuated total internal reflection (ATR) coupling configurations we have determined how the efficient excitation of propagating SP depends on the setup parameters. Knowledge about linear coupling efficiency, its dependence on the coupling layer thickness, the excitation wavelength and the material properties is indispensable for all applications that exploit surface resonances. In Chapter 2 we have shown that the Otto and the Kretschmann coupling configuration, commonly regarded as identical in terms of plasmonic coupling, exhibit differing dependencies on the combination of excitation wavelength and coupling layer thickness. The optimum metal layer thickness for efficient coupling in the Kretschmann configuration lies around 45 nm as the dielectric contrast of the coupling prism and the dependence on the excitation wavelength compensate each other. For the Otto configuration in contrast, the coupling efficiency is very sensitive to the size of the coupling gap.

As a result, the Kretschmann configuration enables measurements (e.g. in sensing applications) over a wide spectral range without modifications of the setup. On the other hand, the Otto configuration with its tunable coupling gap can be used to investigate specific interactions in a selected wavelength region. In addition, both coupling methods also show perturbations to the SP momentum and lifetime in the limit of strong radiative damping. In the Otto geometry these deviations from the ideal SP are caused by the strong influence of the coupling layer and SP hybridization with a photonic mode. The Kretschmann geometry is only affected for very thin metal layers.

Our k -space measurements further revealed a strong connection between the angular

width of the plasmonic resonance, the waist of the excitation beam and the coupling efficiency. By comparing plane-wave excitation with excitation by a focussed laser beam, we could relate the absorption feature in the reflected intensity to the width of the plasmonic resonance and the SP propagation length. In combination with our theoretical model, we can determine intrinsic material properties of thin films and their environment which is the basis of sensing applications. Installed in an interferometer and combined with homodyne detection, the surface plasmon resonance provides a basis for quantum plasmonic sensing. These findings are not only valuable for applications but also for the analysis of plasmon-enhanced nonlinear interactions.

Nonlinear Plasmonics: To analyze SP-enhanced nonlinear interactions, a series of k -space spectroscopic measurements of second harmonic generation (SHG) and degenerate sum-frequency generation (SFG) from a gold film have been performed. We have experimentally demonstrated in Chapter 4, that the second-harmonic response in the in the Kretschmann and the Otto configuration differs markedly in its qualitative behavior (as a function of coupling strength), and quantitatively in its radiated nonlinear yield. These surprising results can be understood in terms of the nonlinear sources in the bulk metal and on the metal surfaces, how they are driven by the fundamental field and SP resonances, and the limitations imposed by the out-coupling efficiency of the second-harmonic to the far-field.

Our analysis using the hydrodynamic model of the metal film (Chapter 3), treated in the respective geometries, confirms that the harmonic out-coupling efficiency dominates in SHG yield from the Otto geometry, while the fundamental SP resonance governs the yield in the Kretschmann geometry. Even though the field enhancement is comparable for both coupling configurations, the intensity of SHG coupled to the far-field is one order of magnitude lower in the Otto configuration compared to the Kretschmann configuration. We have shown, that the hydrodynamic model enables a qualitative analysis of the experimental data as well as a quantitative calculation of the absolute second harmonic yield. Thus a first evaluation of the nonlinear parameters could be given, showing, that the in-plane surface source is stronger than predicted while the other parameters are in good agreement with the predictions from Rudnick and Stern [74]. To our knowledge, this is the first direct comparison of absolute values for SHG from the Otto and the Kretschmann configuration to the nonlinear parameters from the hydrodynamic model.

In addition, the plasmonic modes propagating at the surface were analyzed in terms of their wave-vector and its dependence on the thickness of the coupling layer. The match-

ing conditions of SP to the far-field radiation were also determined, which is especially important for the investigation of coupled modes in very thin films.

Furthermore, the nonlinear interactions which generate second harmonic radiation have been investigated for a gold film in the Kretschmann-geometry (4.2). They could be characterized by their unique signature in k -space due to the fact, that only a well-defined combination of wave-vectors can take an active part in SFG and SHG. The results from single-beam measurements revealed an interaction where two surface plasmons p annihilate to create a second harmonic photon ($pp-f_{2\omega}$). The surface plasmon thus plays an active role in the nonlinear conversion process.

For excitation with two independent laser beams, the mixing process between a plasmon p excited by the a beam and a photon f' provided by an auxiliary beam, the interaction $pf'-f_{2\omega}$, was clearly isolated. This plasmon-driven SFG was limited to the regime where SP's are excited and could therefore be clearly distinguished from the common photonic SHG which was measurable over the entire angular range, Thus we have demonstrated how 2D- k -space spectroscopy can identify the combinations of elementary excitations (photons, surface plasmons) which contribute to nonlinear frequency conversion in metal surfaces.

The interactions of photons and plasmons involved in second harmonic generation and degenerate sum-frequency generation could be identified and the nonlinear sources in the bulk material and at the surface could be quantified. Knowledge of the relevant nonlinear interactions that occur in nano-metallic structures is vital for the development of applications in quantum plasmonics, such as sub-wavelength sources of entangled surface plasmons. In future experiments, multilayer systems of silver and gold could be applied featuring desirable properties such as sharp resonances and hence increased interaction lengths. The combination with magnetic media can lead to increased nonlinearities which depend on the direction of the magnetic field.

Long-range surface waves in thin films: Long-range surface waves (LRSW) in thin films of molybdenum, chromium and gold were investigated in this thesis and compared in terms of linear coupling and nonlinear yield in Chapter 5. Compared to bulk SP, the LRSW resonance in thin films was observed to be much narrower which relates to their highly increased propagation lengths. Propagation lengths of several hundreds of micrometers could be obtained for large coupling gaps and very thin films. Surprisingly, the thin molybdenum and chromium films supported LRSW with long propagation lengths even in the near-infrared where these materials are very lossy. Intrinsically absorbing materials can

thus sustain low-loss surface waves. Provided that the configuration is chosen to be a film of absorbing material that is embedded in a transparent medium, the propagation lifetime of LRSW can even become arbitrarily long in the limit of vanishing film thickness which makes LRSW interesting in sensor applications and for micro-electronics.

Enhanced SHG from the excitation of LRSW was observed which is a strong evidence of field enhancement provided by the surface wave resonance. By means of our theoretical model we have identified the out-of-plane component of the nonlinear sources to have the strongest contribution for LRSW samples which is in contrast to bulk SP. However, the very sharp resonance of LRSW in terms of incident angle complicates excitation with expanded laser beams as the overlap of the modes and thus the coupling efficiency is decreased. The large coupling gaps required for efficient excitation of LRSW further reduced the out-coupling efficiency for SHG. The harmonic intensity coupled to the far-field from LRSW excitation (molybdenum) was measured to be only half of that for LRSP (thin gold), and even 2 orders of magnitude lower than for SP (thick gold).

By applying different coupling techniques such as gratings, the overlap with the narrow mode profile and thus the coupling efficiency to the far-field could be significantly increased. The combination of long propagation distances and the increased nonlinearity of absorbing materials opens the doors to using absorbing materials for doing nonlinear optics of surface waves. Furthermore, the sharp resonance of LRSW provides a basis for sensitive surface analysis with high angular resolution. Thin films of hybrid materials with tailored dielectric functions could further increase the propagation lengths, while incorporating gain media could pave the way for lasing or all-optical integrated circuits such as optical transistors.

Oriented nano-platelets: The distribution of transition dipoles in a monolayer of oriented semiconductor nano-particles has been characterized for one and two-photon absorption (TPA) and their respective photoluminescent emission. In Chapter 6, we have investigated the angular dependent excitation and emission of oriented CdSe nano-platelet monolayers. Our investigation has revealed photoluminescence with a strongly anisotropic k -space distribution. By the means of two dimensional k -space spectroscopy with high numerical aperture we have recovered the transition dipole distributions in our 2D nano-platelets for absorption and emission and thus revealed the origins of the emission anisotropy.

Analysis in both the evanescent and propagating regimes shows that this phenomenon is related to the anisotropy of the electronic Bloch states that govern the transition dipole moment of the exciton. Hence k -space spectroscopy allows direct access to the internal

Bloch states. Regarding the selection rules for the optical transitions and their orientation, we identified the emitting heavy hole exciton to form a bright plane of optically active dipoles aligned in the platelet plane. This alignment leads to a strongly directed emission perpendicular to the platelet plane, while the off-resonant absorption into the energetically higher 2D-continuum of states is isotropic. As such, the intrinsic nature of directed emission can be revealed by a reconstruction of the internal distribution of transition dipoles. For nano-platelets the resulting out-of-plane directed emission is further favored by dielectric and local field effects.

This contrasting combination of isotropic absorption and anisotropic emission makes CdSe nano-platelets an interesting directional emitter for photonic applications or lasing. Gain media of oriented platelets in hyper-structures are expected to have superior performance over random oriented or spherical nano emitters. Improved inversion conditions and a resulting reduction of losses through spontaneous emission might be achieved for platelets oriented perpendicular to the optical pump beam. Hybrid Maxwell-Garnett media containing nano-particles in a symmetric cladding could further support their own LRSW resonances leading to enhanced excitation and directed emission into this surface mode.

SP enhanced TPA in oriented nano-platelets: Our 2D- k -space measurements from Chapter 7 have shown, that in contrast to the isotropic linear absorption, the two-photon absorption in oriented nano-platelets is highly anisotropic. A transition that relies on the simultaneous absorption of two photons involves an intermediate virtual state. The orientation of such a transition can be determined by its decomposition into a linear combination of the allowed transition paths weighted with their respective transition probabilities. As this probability increases for states close to the photon energy, the absorption is governed by the heavy-hole states close to the band-edge, which relate to transition dipoles oriented in the platelet plane. Our angle-resolved TPA-analysis revealed a 85% in-plane (IP) orientation compared to 67% IP orientation for the (isotropic) linear absorption and 95% for the nearly perfectly oriented emission transition dipoles.

With the results from Chapters 2 to 6, we were able to investigate the coupling of highly oriented nano-particles to propagating surface plasmons. We have demonstrated that oriented nano-platelets on top of a silver layer covered with a SiO_2 -spacer show significantly enhanced emission while being excited at the SP resonance. Furthermore, the photoluminescent emission was also coupled to the plasmonic mode which resulted in high directionality in terms of its exit angle. While the SP resonance is broadened in

terms of wave-vector at the wavelength for linear excitation, the combination of TPA and SP resulted in a very narrow range of excitation wave-vectors.

In a next step, we want to determine the emission characteristics and particularly the intensity emitted into the upper half-space, which is air. Additional reflection from the silver layer is expected to lead to a considerable increase of the emitted intensity in this direction which does not interfere with, for example, two-photon excitation at larger wavelengths. This combination of surface plasmon enhanced excitation with highly directed emission could pave the way for an interesting class of semiconductor-based emitters for optical technologies. Nano-particles which show emission in the near-infrared could further improve the coupling to SP and hence the directionality of the emission.

We have demonstrated how two-dimensional k -space spectroscopy in the optical regime is a powerful tool for the analysis of surfaces and thin films. Beyond the determination of intrinsic material properties, such as the dielectric function, it provides an insight into the surface structure and additionally enables the characterization of the applied coupling configurations. Even the investigation of complex phenomena such as nonlinear particle interaction, the coupling to surface-confined modes or the distribution and orientation of transition dipole moments in semiconductor nano-particles was made possible by the means of k -space spectroscopy.

Publications

N. B. Grosse, J. Heckmann, and U. Woggon, "Nonlinear plasmon-photon interaction resolved by k-space spectroscopy," *Physical review letters*, **108**(13), 136802 (2012).

J. Heckmann, M.-E. Kleemann, N. B. Grosse, and U. Woggon, "The dual annihilation of a surface plasmon and a photon by virtue of a three-wave mixing interaction," *Opt. Express* **21**, 28856 (2013).

R. Scott●, J. Heckmann●, A.V. Prudnikau, A. Antanovich, A. Mikhailov, N. Owschimikow, M. Artemyev, J. I. Climente, U. Woggon, N. B. Grosse, and A. W. Achtstein, "Highly directed emission of CdSe nanoplatelets originating from strongly anisotropic 2D electronic structure," *Submitted to Nature Nanotechnology* (on January 26th 2017).

J. Heckmann, K. Pufahl, P. Franz, N. B. Grosse, X. Li, J. E. Sipe, and U. Woggon, "The plasmon-enhanced nonlinear yield in the Otto- and Kretschmann-Geometries," *Ready for submission to Physical Review B*.

K. Pufahl, P. Franz, J. Heckmann, N. B. Grosse, and U. Woggon, "A generalized view on long-range surface polaritons in slab waveguides," *in preparation*.

R. Scott●, J. Heckmann●, A.V. Prudnikau, A. Antanovich, A. Mikhailov, N. Owschimikow, M. Artemyev, J. I. Climente, U. Woggon, N. B. Grosse, and A. W. Achtstein, "Revealing the anisotropy in two-photon absorption of oriented CdSe nanoplatelets by 2D k -space spectroscopy," *in preparation*.

J. Heckmann●, R. Scott●, A.V. Prudnikau, A. Antanovich, A. Mikhailov, N. Owschimikow, M. Artemyev, J. I. Climente, U. Woggon, N. B. Grosse, and A. W. Achtstein, "Surface plasmon enhanced two-photon absorption and highly directed emission in oriented CdSe nanoplatelets," *in preparation*.

J. Heckmann, P. Franz, K. Pufahl, N. B. Grosse, and U. Woggon, "Absorptive materials for low-loss surface-wave optics," *in preparation*.

N. B. Grosse, J. Heckmann, K. Pufahl, and U. Woggon, "The quantum noise limit of surface-plasmon resonance sensing," *in preparation*.

- equally contributing authors

A | SHG in the Hydrodynamic Model

A.1 Conventions

The approach here largely follows that of J.E. Sipe, V.C.Y. So, M. Fukui, and G.I. Stegeman, "Analysis of second-harmonic generation at metal surfaces," Phys. Rev. B **21**, 4389 (1980) (hereafter referred to as SSFS) [73]. We give some of the development in more detail and also include a momentum relaxation time in the equations, which was not included in SSFS. Furthermore, the model was expanded to allow simulation of different excitation geometries, namely the Otto configuration, three-wave-mixing and Gaussian beam excitation.

Here, "cgs units," are used and the charge on the electron is taken to be $-e$.

A.2 The linear fields

The plane of incidence is defined to be the x - z -plane and the materials are aligned with the x - y -plane. All the fields at fundamental frequency are written as

$$f(\mathbf{r}, t) = f(\mathbf{r})e^{-i\omega t} + c.c. \quad (\text{A.1})$$

Here, ω is the frequency of the incident beam, later $\Omega = 2\omega$ will be used for the second harmonic frequency.

We consider a general configuration with 3 material layers for the Kretschmann configuration and with 4 layers for the Otto configuration, as an additional coupling layer is needed. The Kretschmann configuration consists of a glass coupling prism (M_0) onto which a thin metal film (M_3). SP's can be excited at the interface between the metal and the surrounding dielectric (M_2), which is air in this case. The arrangement in the

Kretschmann configuration is

$$\left. \begin{array}{l} z > 0 \quad \text{glass } M_0 \text{ with } \epsilon_0 \\ 0 > z > -D \quad \text{metal } M_3 \text{ with } \epsilon_3 \\ z < -D \quad \text{air } M_2 \text{ with } \epsilon_2 \end{array} \right\} \text{Kretschmann}$$

The Otto configuration is based on the same principle, however, the order of layers is inverted. A glass coupling prism (M_0) followed an adjustable air gap (M_1), that was used to vary the coupling to SP's on a metal-air-interface, resulting in

$$\left. \begin{array}{l} z > D_1 \quad \text{glass } M_0 \text{ with } \epsilon_0 \\ D_1 > z > 0 \quad \text{air } M_1 \text{ with } \epsilon_1 \\ 0 > z > -D \quad \text{metal } M_3 \text{ with } \epsilon_3 \\ z < -D \quad \text{substrate } M_2 \text{ with } \epsilon_2 \end{array} \right\} \text{Otto}$$

$\epsilon_0, \epsilon_1, \epsilon_3, \epsilon_2$ are the dielectric constants in their respective media. We will assume that ϵ_1 is real, but ϵ_3 will be complex.

We take an incident electric field

$$\mathbf{E}_{\text{inc}}(\mathbf{r}) = [(\hat{\mathbf{s}}E_{1-}^s + \hat{\mathbf{p}}_{1-}E_{1-}^p)e^{-ik_{1,z}z}]e^{i\boldsymbol{\kappa}\cdot\mathbf{R}} \quad (\text{A.2})$$

where, $\hat{\boldsymbol{\kappa}}$ is a real unit vector that lies in the x - y -plane, $\mathbf{R} = (x, y)$, while

$$k_x \equiv \kappa = k_0\sqrt{\epsilon_i} \sin \theta \quad (\text{A.3})$$

is the incident field's wave vector projection onto the interface under an incident angle θ .

$$k_{i,z} = \sqrt{k_0^2\epsilon_i - \kappa^2}, \quad (\text{A.4})$$

with $k_0 = \omega/c$, c being the speed of light, is the wave vector's component in the z -direction for the different media. The square roots in A.4 are defined as $\text{Im} \sqrt{Z} \geq 0$ and, for the case that $\text{Im} \sqrt{Z} = 0$, then $\text{Re} \sqrt{Z} \geq 0$ for a complex quantity Z .

The polarization is defined by $\hat{\mathbf{s}} = \hat{\boldsymbol{\kappa}} \times \hat{\mathbf{z}}$, a real unit vector in the xy -plane. It identifies the polarization direction for "s-polarized" light. Similarly the unit vector $\hat{\mathbf{p}}_-$ identifies the polarization direction of "p-polarized" light. In general, we take

$$\hat{\mathbf{p}}_{i\pm} = \frac{\kappa\hat{\mathbf{z}} \mp k_{i,z}\hat{\boldsymbol{\kappa}}}{k_0\sqrt{\epsilon_i}} \quad (\text{A.5})$$

The "-" sign in the subscript identifies the p-polarized direction for a "downward" propagating (or evanescent) wave in positive x -direction and negative z -direction, following the definitions of Born and Wolf.

There will be a reflected wave in medium 1, of the form

$$\mathbf{E}_{\text{refl}}(\mathbf{r}) = [\hat{\mathbf{s}} \bar{r}_{02}^s E_{1-}^s + \hat{\mathbf{p}}_{1+} \bar{r}_{02}^p E_{1-}^p] e^{ik_{1,z}z} e^{i\boldsymbol{\kappa} \cdot \mathbf{R}} \quad (\text{A.6})$$

and here \bar{r}_{02}^p and \bar{r}_{02}^s are respectively the s and p polarized overall slab Fresnel reflection coefficients. These are given by

$$\bar{r}_{02} = r_{01} + \frac{t_{01} \bar{r}_{12} t_{10} e^{2ik_{1,z}D_1}}{1 - r_{10} \bar{r}_{12} e^{2ik_{1,z}D_1}} \quad (\text{A.7})$$

with

$$\bar{r}_{12} = r_{13} + \frac{t_{13} r_{32} t_{31} e^{2ik_{3,z}D}}{1 - r_{31} r_{32} e^{2ik_{3,z}D}} \quad (\text{A.8})$$

where the r_{ij} and t_{ij} are the reflection and transmission Fresnel coefficients for a single interface. For s-polarization, those are given by

$$\begin{aligned} r_{ij}^s &= \frac{k_{i,z} - k_{j,z}}{k_{i,z} + k_{j,z}}, \\ t_{ij}^s &= \frac{2k_{i,z}}{k_{i,z} + k_{j,z}} \end{aligned} \quad (\text{A.9})$$

and for p-polarized light they are given by

$$\begin{aligned} r_{ij}^p &= \frac{k_{i,z}\epsilon_j - k_{j,z}\epsilon_i}{k_{i,z}\epsilon_j + k_{j,z}\epsilon_i}, \\ t_{ij}^p &= \frac{2\sqrt{\epsilon_i\epsilon_j}k_{i,z}}{k_{i,z}\epsilon_j + k_{j,z}\epsilon_i} \end{aligned} \quad (\text{A.10})$$

The reflectivity of the structure for light incident from medium 0 is thus $|\bar{r}_{02}^s|^2$ for s-polarized light and $|\bar{r}_{02}^p|^2$ for p-polarized light. The general form of A.7 is easily physically interpreted in terms of the different amplitude processes for how light can be reflected. In particular, the denominator describes ‘‘multiple bounces’’ within medium 3. Its zeros (in the complex plane) identify the ‘‘quasi-particles’’ of the system.

For an incident field A.2 there will also be a field in medium 2; it is given by

$$\mathbf{E}_{\text{trans}}(\mathbf{r}) = [\hat{\mathbf{s}} \bar{t}_{02}^s E_{1-}^s + \hat{\mathbf{p}}_{2-} \bar{t}_{02}^p E_{1-}^p] e^{-ik_{1,z}D_1} e^{-ik_{3,z}D} e^{-ik_{2,z}z} e^{i\boldsymbol{\kappa} \cdot \mathbf{R}} \quad (\text{A.11})$$

where \bar{t}_{02}^p and \bar{t}_{02}^s are respectively the s and p polarized overall slab Fresnel transmission coefficients, respectively, given by the transmitted fundamental field

$$\bar{t}_{02} = \frac{t_{01} \bar{t}_{12} e^{ik_{1,z}D_1}}{1 - r_{10} \bar{r}_{12} e^{2ik_{1,z}D_1}} \quad (\text{A.12})$$

with

$$\begin{aligned} \bar{t}_{12} &= \frac{t_{13} t_{32} e^{ik_{3,z}D}}{1 - \bar{r}_{30} r_{32} e^{2ik_{3,z}D}} \\ \bar{r}_{30} &= r_{31} + \frac{t_{31} r_{10} t_{13} e^{2ik_{3,z}D}}{1 - r_{10} r_{13} e^{2ik_{1,z}D_1}} \end{aligned} \quad (\text{A.13})$$

Although we label the field “trans”, in fact in many instances there is no propagating field radiated into medium 2; in exciting a surface plasmon, for example, $k_{2,z}$ has an imaginary part and the field evanescently decays in medium 2. But here, the formulas are completely general.

The field in the metal, medium 3, can be determined, and is given by

$$\begin{aligned} \mathbf{E}_3(\mathbf{r}) = & \hat{\mathbf{s}}(r_{32}^s e^{2ik_{3,z}D} e^{i\omega_3 z} + e^{-i\omega_3 z}) \frac{t_{13}^s}{1 - \bar{r}_{30}^s r_{32}^s e^{2ik_{3,z}D}} \frac{t_{01}^s}{1 - r_{10}^s \bar{r}_{12}^s e^{2ik_{1,z}D_1}} E_{1-}^s e^{i\boldsymbol{\kappa} \cdot \mathbf{R}} \\ & + (\hat{\mathbf{p}}_{3+} r_{32}^p e^{2ik_{3,z}D} e^{i\omega_3 z} + \hat{\mathbf{p}}_{3-} e^{-i\omega_3 z}) \frac{t_{13}^p}{1 - \bar{r}_{30}^p r_{32}^p e^{2ik_{3,z}D}} \frac{t_{01}^p}{1 - r_{10}^p \bar{r}_{12}^p e^{2ik_{1,z}D_1}} E_{1-}^p e^{i\boldsymbol{\kappa} \cdot \mathbf{R}} \end{aligned} \quad (\text{A.14})$$

where the polarization vectors are defined as

$$\begin{aligned} \hat{\mathbf{p}}_{3+} &= \frac{\kappa \hat{\mathbf{z}} - k_{3,z} \hat{\boldsymbol{\kappa}}}{k_0 \sqrt{\epsilon_3}} \\ \hat{\mathbf{p}}_{3-} &= \frac{\kappa \hat{\mathbf{z}} + k_{3,z} \hat{\boldsymbol{\kappa}}}{k_0 \sqrt{\epsilon_3}} \end{aligned} \quad (\text{A.15})$$

Combining these quantities and the polarization dependent Fresnel coupling coefficients to medium 3

$$\begin{aligned} C_s &= \frac{t_{13}^s}{1 - \bar{r}_{30}^s r_{32}^s e^{2ik_{3,z}D}} \frac{t_{01}^s e^{ik_{1,z}D_1}}{1 - r_{10}^s \bar{r}_{21}^s e^{2ik_{1,z}D_1}} \\ C_z &= \left(\frac{\kappa}{k_0 k_0 n_3} \right) \frac{t_{13}^p}{1 - \bar{r}_{30}^p r_{32}^p e^{2ik_{3,z}D}} \frac{t_{01}^p e^{ik_{1,z}D_1}}{1 - r_{10}^p \bar{r}_{21}^p e^{2ik_{1,z}D_1}} \\ C_\kappa &= \left(\frac{k_{3,z}}{k_0 n_3} \right) \frac{t_{13}^p}{1 - \bar{r}_{30}^p r_{32}^p e^{2ik_{3,z}D}} \frac{t_{01}^p e^{ik_{1,z}D_1}}{1 - r_{10}^p \bar{r}_{21}^p e^{2ik_{1,z}D_1}} \end{aligned} \quad (\text{A.16})$$

we can extract the components for the field in medium 3

$$\begin{aligned} \mathbf{E}_3(\mathbf{r}) = & \hat{\mathbf{s}}(e^{-ik_{3,z}z} + \rho_s e^{ik_{3,z}z}) C_s E_{1-}^s e^{i\boldsymbol{\kappa} \cdot \mathbf{R}} \\ & + \hat{\mathbf{z}}(e^{-ik_{3,z}z} + \rho_p e^{ik_{3,z}z}) C_z E_{1-}^p e^{i\boldsymbol{\kappa} \cdot \mathbf{R}} \\ & + \hat{\boldsymbol{\kappa}}(e^{-ik_{3,z}z} - \rho_p e^{ik_{3,z}z}) C_\kappa E_{1-}^p e^{i\boldsymbol{\kappa} \cdot \mathbf{R}} \end{aligned} \quad (\text{A.17})$$

where

$$\begin{aligned} \rho_s &= r_{32}^s e^{2ik_{3,z}D} \\ \rho_p &= r_{32}^p e^{2ik_{3,z}D} \end{aligned} \quad (\text{A.18})$$

A.3 The Bulk Metal Source and its Radiated Fields

For fundamental fields of the form A.1 there will be a second harmonic polarization

$$\mathbf{P}^{\text{II}}(\mathbf{r}, t) = \mathbf{P}^{\text{II}}(\mathbf{r}) e^{-i\Omega t} + c.c \quad (\text{A.19})$$

in the bulk metal, where $\Omega = 2\omega$, of the form

$$\mathbf{P}^{\text{II}}(\mathbf{r}) = \beta \mathbf{E}_3(\mathbf{r})(\nabla \cdot \mathbf{E}'_3(\mathbf{r})) + \gamma \nabla(\mathbf{E}_3(\mathbf{r}) \cdot \mathbf{E}'_3(\mathbf{r})) + \delta'(\mathbf{E}_3(\mathbf{r}) \cdot \nabla) \mathbf{E}'_3(\mathbf{r}) \quad (\text{A.20})$$

where we treat the metal as isotropic and the notation for the coefficients (β, γ, δ) is historical. For optical fields in the bulk metal where ϵ_3 is uniform we have $\nabla \cdot \mathbf{E}_3(\mathbf{r}) = 0$, and only the second two contributions will persist

$$\mathbf{P}^{\text{II}}(\mathbf{r}) = \gamma \nabla(\mathbf{E}_3(\mathbf{r}) \cdot \mathbf{E}'_3(\mathbf{r})) + \delta'(\mathbf{E}_3(\mathbf{r}) \cdot \nabla) \mathbf{E}'_3(\mathbf{r}) \quad (\text{A.21})$$

To expand the excitation beyond single plane waves, e.g. Gaussian beams, and enable interactions between incident fields, we have to consider all combinations for the E_3 components. Therefore, to distinguish the origin of both contributions, one field is marked as E'_3 .

The different contributions can be worked out using A.17, leading to

$$\begin{aligned} \mathbf{E}_3(\mathbf{r}) \cdot \mathbf{E}'_3(\mathbf{r}) = & e^{i(\boldsymbol{\kappa} + \boldsymbol{\kappa}') \cdot \mathbf{R}} \cdot \\ & \left(C_s E_{1-}^s C'_s E_{1-}^{s'} e^{-i(k_{3,z} + k'_{3,z})z} + \rho_s C_s E_{1-}^s C'_s E_{1-}^{s'} e^{i(k_{3,z} - k'_{3,z})z} \right. \\ & + C_s E_{1-}^s \rho'_s C'_s E_{1-}^{s'} e^{i(-k_{3,z} + k'_{3,z})z} + \rho_s C_s E_{1-}^s \rho'_s C'_s E_{1-}^{s'} e^{i(k_{3,z} + k'_{3,z})z} \\ & + C_z E_{1-}^p C'_z E_{1-}^{p'} e^{-i(k_{3,z} + k'_{3,z})z} + \rho_p C_z E_{1-}^p C'_z E_{1-}^{p'} e^{i(k_{3,z} - k'_{3,z})z} \\ & + C_z E_{1-}^p \rho'_z C'_z E_{1-}^{p'} e^{i(-k_{3,z} + k'_{3,z})z} + \rho_z C_z E_{1-}^p \rho'_z C'_z E_{1-}^{p'} e^{i(k_{3,z} + k'_{3,z})z} \\ & + C_\kappa E_{1-}^p C'_\kappa E_{1-}^{p'} e^{-i(k_{3,z} + k'_{3,z})z} - \rho_\kappa C_\kappa E_{1-}^p C'_\kappa E_{1-}^{p'} e^{i(k_{3,z} - k'_{3,z})z} \\ & \left. + C_\kappa E_{1-}^p \rho'_\kappa C'_\kappa E_{1-}^{p'} e^{i(-k_{3,z} + k'_{3,z})z} + \rho_\kappa C_\kappa E_{1-}^p \rho'_\kappa C'_\kappa E_{1-}^{p'} e^{i(k_{3,z} + k'_{3,z})z} \right) \end{aligned} \quad (\text{A.22})$$

from which we can calculate

$$\begin{aligned} \frac{1}{ik_0} \nabla(\mathbf{E}_3(\mathbf{r}) \cdot \mathbf{E}'_3(\mathbf{r})) e^{-i(\boldsymbol{\kappa} + \boldsymbol{\kappa}') \cdot \mathbf{R}} = & \left(e^{-i(k_{3,z} + k'_{3,z})z} (L_{I-}^\kappa \hat{\boldsymbol{\kappa}} + L_{I-}^z \hat{\mathbf{z}}) \right. \\ & + e^{i(k_{3,z} - k'_{3,z})z} (L_{I0a}^\kappa \hat{\boldsymbol{\kappa}} + L_{I0a}^z \hat{\mathbf{z}}) \\ & + e^{i(-k_{3,z} + k'_{3,z})z} (L_{I0b}^\kappa \hat{\boldsymbol{\kappa}} + L_{I0b}^z \hat{\mathbf{z}}) \\ & \left. + e^{i(k_{3,z} + k'_{3,z})z} (L_{I+}^\kappa \hat{\boldsymbol{\kappa}} + L_{I+}^z \hat{\mathbf{z}}) \right) \end{aligned} \quad (\text{A.23})$$

with

$$\begin{aligned}
 L_{I-}^{\kappa} &= \frac{\kappa + \kappa'}{k_0} (C_s E_{1-}^s - C'_s E_{1-}^{s'} + C_z E_{1-}^p - C'_z E_{1-}^{p'} + C_{\kappa} E_{1-}^p - C'_{\kappa}) \\
 L_{I-}^z &= -\frac{k_{3,z} + k'_{3,z}}{k_0} (C_s E_{1-}^s - C'_s E_{1-}^{s'} + C_z E_{1-}^p - C'_z E_{1-}^{p'} + C_{\kappa} E_{1-}^p - C'_{\kappa}) \\
 L_{I0a}^{\kappa} &= \frac{\kappa + \kappa'}{k_0} (\rho_s C_s E_{1-}^s - C'_s E_{1-}^{s'} + \rho_p C_z E_{1-}^p - C'_z E_{1-}^{p'} - \rho_{\kappa} C_{\kappa} E_{1-}^p - C'_{\kappa} E_{1-}^{p'}) \\
 L_{I0b}^{\kappa} &= \frac{\kappa + \kappa'}{k_0} (\rho'_s C_s E_{1-}^s - C'_s E_{1-}^{s'} + \rho'_p C_z E_{1-}^p - C'_z E_{1-}^{p'} - \rho'_{\kappa} C_{\kappa} E_{1-}^p - C'_{\kappa} E_{1-}^{p'}) \\
 L_{I0a}^z &= \frac{k_{3,z} - k'_{3,z}}{k_0} (\rho_s C_s E_{1-}^s - C'_s E_{1-}^{s'} + \rho_p C_z E_{1-}^p - C'_z E_{1-}^{p'} - \rho_{\kappa} C_{\kappa} E_{1-}^p - C'_{\kappa} E_{1-}^{p'}) \\
 L_{I0b}^z &= \frac{-k_{3,z} + k'_{3,z}}{k_0} (\rho'_s C_s E_{1-}^s - C'_s E_{1-}^{s'} + \rho'_p C_z E_{1-}^p - C'_z E_{1-}^{p'} - \rho'_{\kappa} C_{\kappa} E_{1-}^p - C'_{\kappa} E_{1-}^{p'}) \\
 L_{I+}^{\kappa} &= \frac{\kappa + \kappa'}{k_0} (\rho_s C_s E_{1-}^s - \rho'_s C'_s E_{1-}^{s'} + \rho_z C_z E_{1-}^p - \rho'_z C'_z E_{1-}^{p'} + \rho_{\kappa} C_{\kappa} E_{1-}^p - \rho'_{\kappa} C'_{\kappa} E_{1-}^{p'}) \\
 L_{I+}^z &= \frac{k_{3,z} + k'_{3,z}}{k_0} (\rho_s C_s E_{1-}^s - \rho'_s C'_s E_{1-}^{s'} + \rho_z C_z E_{1-}^p - \rho'_z C'_z E_{1-}^{p'} + \rho_{\kappa} C_{\kappa} E_{1-}^p - \rho'_{\kappa} C'_{\kappa} E_{1-}^{p'})
 \end{aligned} \tag{A.24}$$

Turning to the second term in A.21, since the ∇ operator will ultimately act on $\mathbf{E}_3(\mathbf{r})$, we can write

$$\nabla \rightarrow \hat{\mathbf{z}} \frac{\partial}{\partial z} + i\kappa \hat{\boldsymbol{\kappa}} \tag{A.25}$$

leading to

$$(\mathbf{E}_3(\mathbf{r}) \cdot \nabla) \rightarrow E_3^z(\mathbf{r}) \frac{\partial}{\partial z} + i\kappa E_3^{\kappa}(\mathbf{r}) \tag{A.26}$$

and

$$(\mathbf{E}_3(\mathbf{r}) \cdot \nabla) \mathbf{E}'_3(\mathbf{r}) = E_3^z(\mathbf{r}) \frac{\partial}{\partial z} \mathbf{E}'_3(\mathbf{r}) + i\kappa E_3^{\kappa}(\mathbf{r}) \mathbf{E}'_3(\mathbf{r}) \tag{A.27}$$

which can be simplified by collecting the different terms by vector components

$$\begin{aligned}
 \frac{1}{ik_0} (\mathbf{E}_3(\mathbf{r}) \cdot \nabla) \mathbf{E}'_3(\mathbf{r}) e^{-i(\kappa + \kappa') \cdot \mathbf{R}} &= [e^{-i(k_{3,z} + k'_{3,z})z} (L_{II-}^s \hat{\mathbf{s}} + L_{II-}^{\kappa} \hat{\boldsymbol{\kappa}} + L_{II-}^z \hat{\mathbf{z}}) \\
 &\quad + e^{i(k_{3,z} - k'_{3,z})z} (L_{II0a}^s \hat{\mathbf{s}} + L_{II0a}^{\kappa} \hat{\boldsymbol{\kappa}} + L_{II0a}^z \hat{\mathbf{z}}) \\
 &\quad + e^{i(-k_{3,z} + k'_{3,z})z} (L_{II0b}^s \hat{\mathbf{s}} + L_{II0b}^{\kappa} \hat{\boldsymbol{\kappa}} + L_{II0b}^z \hat{\mathbf{z}}) \\
 &\quad + e^{i(k_{3,z} + k'_{3,z})z} (L_{II+}^s \hat{\mathbf{s}} + L_{II+}^{\kappa} \hat{\boldsymbol{\kappa}} + L_{II+}^z \hat{\mathbf{z}})]
 \end{aligned} \tag{A.28}$$

with

$$\begin{aligned}
 L_{II-}^s &= \frac{\kappa'}{k_0} C_\kappa E_{1-}^p C'_s E_{1-}^{s'} - \frac{k'_{3,z}}{k_0} C_z E_{1-}^p C'_s E_{1-}^{s'} \\
 L_{II-}^\kappa &= \frac{\kappa'}{k_0} C_\kappa E_{1-}^p C'_\kappa E_{1-}^{p'} - \frac{k'_{3,z}}{k_0} C_z E_{1-}^p C'_\kappa E_{1-}^{p'} \\
 L_{II-}^z &= \frac{\kappa'}{k_0} C_\kappa E_{1-}^p C'_z E_{1-}^{p'} - \frac{k'_{3,z}}{k_0} C_z E_{1-}^p C'_z E_{1-}^{p'} \\
 L_{II0a}^s &= -\rho_p \left(\frac{\kappa'}{k_0} C_\kappa E_{1-}^p C'_s E_{1-}^{s'} + \frac{k'_{3,z}}{k_0} C_z E_{1-}^p C'_s E_{1-}^{s'} \right) \\
 L_{II0b}^s &= \rho'_s \left(\frac{\kappa'}{k_0} C_\kappa E_{1-}^p C'_s E_{1-}^{s'} + \frac{k'_{3,z}}{k_0} C_z E_{1-}^p C'_s E_{1-}^{s'} \right) \\
 L_{II0a}^\kappa &= -\rho_p \left(\frac{\kappa'}{k_0} C_\kappa E_{1-}^p C'_\kappa E_{1-}^{p'} + \frac{k'_{3,z}}{k_0} C_z E_{1-}^p C'_\kappa E_{1-}^{p'} \right) \\
 L_{II0b}^\kappa &= -\rho'_p \left(\frac{\kappa'}{k_0} C_\kappa E_{1-}^p C'_\kappa E_{1-}^{p'} + \frac{k'_{3,z}}{k_0} C_z E_{1-}^p C'_\kappa E_{1-}^{p'} \right) \\
 L_{II0a}^z &= -\rho_p \left(\frac{\kappa'}{k_0} C_\kappa E_{1-}^p C'_z E_{1-}^{p'} + \frac{k'_{3,z}}{k_0} C_z E_{1-}^p C'_z E_{1-}^{p'} \right) \\
 L_{II0b}^z &= \rho'_p \left(\frac{\kappa'}{k_0} C_\kappa E_{1-}^p C'_z E_{1-}^{p'} + \frac{k'_{3,z}}{k_0} C_z E_{1-}^p C'_z E_{1-}^{p'} \right) \\
 L_{II+}^s &= \rho_p \rho'_s \left(-\frac{\kappa'}{k_0} C_\kappa E_{1-}^p C'_s E_{1-}^{s'} + \frac{k'_{3,z}}{k_0} C_z E_{1-}^p C'_s E_{1-}^{s'} \right) \\
 L_{II+}^\kappa &= \rho_p \rho'_p \left(\frac{\kappa'}{k_0} C_\kappa E_{1-}^p C'_\kappa E_{1-}^{p'} - \frac{k'_{3,z}}{k_0} C_z E_{1-}^p C'_\kappa E_{1-}^{p'} \right) \\
 L_{II-}^z &= \rho_p \rho'_p \left(-\frac{\kappa'}{k_0} C_z E_{1-}^p C'_z E_{1-}^{p'} + \frac{k'_{3,z}}{k_0} C_z E_{1-}^p C'_z E_{1-}^{p'} \right)
 \end{aligned} \tag{A.29}$$

Now combining (A.23,A.28) in A.21 and defining

$$\mathbf{P}^{II}(\mathbf{r}) = \mathbf{P}^{II}(z) e^{i(\boldsymbol{\kappa} + \boldsymbol{\kappa}') \cdot \mathbf{R}} \tag{A.30}$$

we find

$$\begin{aligned}
 \mathbf{P}^{II}(z) &= \left[i e^{-i(k_{3,z} + k'_{3,z})z} (L_-^s \hat{\mathbf{s}} + L_-^\kappa \hat{\boldsymbol{\kappa}} + L_-^z \hat{\mathbf{z}}) \right. \\
 &\quad + i e^{i(k_{3,z} - k'_{3,z})z} (L_{0a}^s \hat{\mathbf{s}} + L_{0a}^\kappa \hat{\boldsymbol{\kappa}} + L_{0a}^z \hat{\mathbf{z}}) \\
 &\quad + i e^{i(-k_{3,z} + k'_{3,z})z} (L_{0b}^s \hat{\mathbf{s}} + L_{0b}^\kappa \hat{\boldsymbol{\kappa}} + L_{0b}^z \hat{\mathbf{z}}) \\
 &\quad \left. + i e^{i(k_{3,z} + k'_{3,z})z} (L_+^s \hat{\mathbf{s}} + L_+^\kappa \hat{\boldsymbol{\kappa}} + L_+^z \hat{\mathbf{z}}) \right] \tag{A.31}
 \end{aligned}$$

where

$$\begin{aligned}
 L_-^s &= k_0 \delta' L_{II-}^s \\
 L_-^\kappa &= k_0 \gamma L_{I-}^\kappa + k_0 \delta' L_{II-}^\kappa \\
 L_-^z &= k_0 \gamma L_{I-}^z + k_0 \delta' L_{II-}^z \\
 L_{0a}^s &= k_0 \delta' L_{II0a}^s \\
 L_{0a}^\kappa &= k_0 \gamma L_{II0a}^\kappa + k_0 \delta' L_{II0a}^\kappa \\
 L_{0a}^z &= k_0 \gamma L_{II0a}^z + k_0 \delta' L_{II0a}^z \\
 L_{0b}^s &= k_0 \delta' L_{II0}^s \\
 L_{0b}^\kappa &= k_0 \gamma L_{II0b}^\kappa + k_0 \delta' L_{II0b}^\kappa \\
 L_{0b}^z &= k_0 \gamma L_{II0b}^z + k_0 \delta' L_{II0b}^z \\
 L_+^s &= k_0 \delta' L_{II+}^s \\
 L_+^\kappa &= 2k_0 \gamma L_{I+}^\kappa + k_0 \delta' L_{II+}^\kappa \\
 L_+^z &= 2k_0 \gamma L_{I+}^z + k_0 \delta' L_{II+}^z
 \end{aligned} \tag{A.32}$$

Now, the propagation parameters for the radiated second harmonic field in medium 0 have to be defined

$$\begin{aligned}
 K_0 &= 2k_0 \\
 K &= \kappa + \kappa' \\
 \mathbf{K} &= \boldsymbol{\kappa} + \boldsymbol{\kappa}' \\
 W_i &= \sqrt{K_0^2 \mathcal{E}_i - K^2}, \text{ where } N_i = \sqrt{\mathcal{E}_i}
 \end{aligned} \tag{A.33}$$

and the unit vectors at Ω are defined following their definition at ω

$$\hat{\mathbf{K}} = \hat{\boldsymbol{\kappa}} \tag{A.34}$$

and thus the polarization vectors are given by

$$\begin{aligned}
 \hat{\mathbf{S}} &= \hat{\mathbf{K}} \times \hat{\mathbf{z}} = \hat{\mathbf{s}} \\
 \hat{\mathbf{P}}_{i\pm} &= \frac{K \hat{\mathbf{z}} \mp W_i \hat{\boldsymbol{\kappa}}}{K_0 N_i}
 \end{aligned} \tag{A.35}$$

and the related second harmonic Fresnel coefficients are

$$\begin{aligned}
 R_{ij}^s &= \frac{W_i - W_j}{W_i + W_j} \\
 T_{ij}^s &= \frac{2W_i}{W_i + W_j} \\
 R_{ij}^p &= \frac{W_i \mathcal{E}_j - W_j \mathcal{E}_i}{W_i \mathcal{E}_j + W_j \mathcal{E}_i} \\
 T_{ij}^p &= \frac{2N_i N_j W_i}{W_i \mathcal{E}_j + W_j \mathcal{E}_i}
 \end{aligned} \tag{A.36}$$

With this notation, a radiated harmonic field from a source

$$\mathbf{P}^{II}(\mathbf{r}, t) = \mathbf{P}^{II}(\mathbf{r})e^{i\Omega t} + c.c$$

with $\mathbf{P}^{II}(\mathbf{r})$ of the form (31,32), is given by

$$\mathbf{E}_0^{II(\text{bulk})}(\mathbf{r}) = (E_{0+}^{sII(\text{bulk})} \hat{\mathbf{S}} + E_{0+}^{pII(\text{bulk})} \hat{\mathbf{P}}_{0+}) e^{i\mathbf{K} \cdot \mathbf{R}} e^{iW_0 z} \tag{A.37}$$

with

$$\begin{aligned}
 E_{0+}^{sII(\text{bulk})} &= 2\pi i K_0 \frac{(K_0 \bar{T}_{10}^s T_{31}^s / K_{3,z})}{(1 - R_{32}^s \bar{R}_{30}^s e^{2iK_{3,z}D})} (A_s + R_{32}^s e^{2iw_3 D} B_s) \\
 E_{0+}^{pII(\text{bulk})} &= 2\pi i K_0 \frac{(K_0 \bar{T}_{10}^p T_{31}^p / K_{3,z})}{(1 - R_{32}^p \bar{R}_{30}^p e^{2iK_{3,z}D})} (A_p + R_{32}^p e^{2iw_3 D} B_p)
 \end{aligned} \tag{A.38}$$

with

$$\begin{aligned}
 \bar{T}_{10}^{s,p} &= \frac{T_{10}^{s,p} e^{iK_{1,z}D_1}}{(1 - R_{10}^{s,p} \bar{R}_{12}^{s,p} e^{2iK_{1,z}D_1})} \\
 \bar{R}_{12}^{s,p} &= R_{13}^{s,p} + \frac{T_{13}^{s,p} R_{23}^{s,p} T_{31}^{s,p} e^{iK_{3,z}D}}{(1 - R_{31}^{s,p} R_{23}^{s,p} e^{2iK_{3,z}D})} \\
 \bar{R}_{30}^{s,p} &= R_{31}^{s,p} + \frac{T_{31}^{s,p} R_{10}^{s,p} T_{13}^{s,p} e^{iK_{1,z}D_1}}{(1 - R_{10}^{s,p} R_{13}^{s,p} e^{2iK_{1,z}D_1})}
 \end{aligned} \tag{A.39}$$

The A's and B's are the second harmonic fields generated by the bulk source over the whole thickness D of the metal film, meanwhile allowing interference of the different angular components:

$$\begin{aligned}
 A_s &= \int_{-D}^0 e^{-K_{3,z}z'} \hat{\mathbf{S}} \cdot \mathbf{P}^{II}(z') dz' \\
 B_s &= \int_{-D}^0 e^{K_{3,z}z'} \hat{\mathbf{S}} \cdot \mathbf{P}^{II}(z') dz' \\
 A_p &= \int_{-D}^0 e^{-K_{3,z}z'} \hat{\mathbf{P}}_{3+} \cdot \mathbf{P}^{II}(z') dz' \\
 B_p &= \int_{-D}^0 e^{K_{3,z}z'} \hat{\mathbf{P}}_{3-} \cdot \mathbf{P}^{II}(z') dz'
 \end{aligned} \tag{A.40}$$

First the s-polarization quantities are evaluated

$$\begin{aligned}
 A_s &= iK_0 \int_{-D}^0 \left(e^{-i(K_{3,z}+k_{3,z}+k'_{3,z})z'} L_-^s + e^{i(-K_{3,z}+k_{3,z}-k'_{3,z})z'} L_{0a}^s \right. \\
 &\quad \left. + e^{i(-K_{3,z}-k_{3,z}+k'_{3,z})z'} L_{0b}^s + e^{i(-K_{3,z}+k_{3,z}+k'_{3,z})z'} L_+^s \right) dz' \\
 &= K_0 \left[\frac{e^{i(K_{3,z}+k_{3,z}+k'_{3,z})D} - 1}{K_{3,z} + k_{3,z} + k'_{3,z}} L_-^s + \frac{e^{i(K_{3,z}-k_{3,z}+k'_{3,z})D} - 1}{K_{3,z} - k_{3,z} + k'_{3,z}} L_{0a}^s \right. \\
 &\quad \left. + \frac{e^{i(K_{3,z}+k_{3,z}-k'_{3,z})D} - 1}{K_{3,z} + k_{3,z} - k'_{3,z}} L_{0b}^s + \frac{e^{i(K_{3,z}-k_{3,z}-k'_{3,z})D} - 1}{K_{3,z} - k_{3,z} - k'_{3,z}} L_+^s \right] \quad (A.41) \\
 B_s &= K_0 \left[\frac{e^{i(-K_{3,z}+k_{3,z}+k'_{3,z})D} - 1}{-K_{3,z} + k_{3,z} + k'_{3,z}} L_-^s + \frac{e^{i(-K_{3,z}-k_{3,z}+k'_{3,z})D} - 1}{-K_{3,z} - k_{3,z} + k'_{3,z}} L_{0a}^s \right. \\
 &\quad \left. + \frac{e^{i(-K_{3,z}+k_{3,z}-k'_{3,z})D} - 1}{-K_{3,z} + k_{3,z} - k'_{3,z}} L_{0b}^s + \frac{e^{i(-K_{3,z}-k_{3,z}-k'_{3,z})D} - 1}{-K_{3,z} - k_{3,z} - k'_{3,z}} L_+^s \right]
 \end{aligned}$$

then the p-polarization quantities with

$$\begin{aligned}
 \hat{\mathbf{P}}_{3+} \cdot \mathbf{P}^{II}(z) &= ie^{-i(k_{3,z}+k'_{3,z})z} L_-^{p+} + ie^{i(k_{3,z}-k'_{3,z})z} L_{0a}^{p+} + ie^{i(-k_{3,z}+k'_{3,z})z} L_{0b}^{p+} + ie^{i(k_{3,z}+k'_{3,z})z} L_+^{p+}, \\
 \hat{\mathbf{P}}_{3-} \cdot \mathbf{P}^{II}(z) &= ie^{-i(k_{3,z}+k'_{3,z})z} L_-^{p-} + ie^{i(k_{3,z}-k'_{3,z})z} L_{0a}^{p-} + ie^{i(-k_{3,z}+k'_{3,z})z} L_{0b}^{p-} + ie^{i(k_{3,z}+k'_{3,z})z} L_+^{p-}
 \end{aligned} \quad (A.42)$$

and

$$\begin{aligned}
 L_-^{p+} &= \frac{KL_-^z - K_{3,z}L_-^\kappa}{K_0N_3}, \\
 L_{0a}^{p+} &= \frac{KL_{0a}^z - K_{3,z}L_{0a}^\kappa}{K_0N_3}, \\
 L_{0b}^{p+} &= \frac{KL_{0b}^z - K_{3,z}L_{0b}^\kappa}{K_0N_3}, \\
 L_+^{p+} &= \frac{KL_+^z - K_{3,z}L_+^\kappa}{K_0N_3}, \\
 L_-^{p-} &= \frac{KL_-^z + K_{3,z}L_-^\kappa}{K_0N_3}, \\
 L_{0a}^{p-} &= \frac{KL_{0a}^z + K_{3,z}L_{0a}^\kappa}{K_0N_3}, \\
 L_{0b}^{p-} &= \frac{KL_{0b}^z + K_{3,z}L_{0b}^\kappa}{K_0N_3}, \\
 L_+^{p-} &= \frac{KL_+^z + K_{3,z}L_+^\kappa}{K_0N_3}
 \end{aligned} \quad (A.43)$$

which gives

$$\begin{aligned}
 A_p &= iK_0 \int_{-D}^0 \left(e^{-i(K_{3,z}+k_{3,z}+k'_{3,z})z'} L_-^{p+} + e^{i(-K_{3,z}+k_{3,z}-k'_{3,z})z'} L_{0a}^{p+} \right. \\
 &\quad \left. + e^{i(-K_{3,z}-k_{3,z}+k'_{3,z})z'} L_{0b}^{p+} + e^{i(-K_{3,z}+k_{3,z}+k'_{3,z})z'} L_+^{p+} \right) dz' \\
 &= K_0 \left[\frac{e^{i(K_{3,z}+k_{3,z}+k'_{3,z})D} - 1}{K_{3,z} + k_{3,z} + k'_{3,z}} L_-^{p+} + \frac{e^{i(K_{3,z}-k_{3,z}+k'_{3,z})D} - 1}{K_{3,z} - k_{3,z} + k'_{3,z}} L_{0a}^{p+} \right. \\
 &\quad \left. + \frac{e^{i(K_{3,z}+k_{3,z}-k'_{3,z})D} - 1}{K_{3,z} + k_{3,z} - k'_{3,z}} L_{0b}^{p+} + \frac{e^{i(K_{3,z}-k_{3,z}-k'_{3,z})D} - 1}{K_{3,z} - k_{3,z} - k'_{3,z}} L_+^{p+} \right] \quad (\text{A.44}) \\
 B_p &= K_0 \left[\frac{e^{i(-K_{3,z}+k_{3,z}+k'_{3,z})D} - 1}{-K_{3,z} + k_{3,z} + k'_{3,z}} L_-^{p-} + \frac{e^{i(-K_{3,z}-k_{3,z}+k'_{3,z})D} - 1}{-K_{3,z} - k_{3,z} + k'_{3,z}} L_{0a}^{p-} \right. \\
 &\quad \left. + \frac{e^{i(-K_{3,z}+k_{3,z}-k'_{3,z})D} - 1}{-K_{3,z} + k_{3,z} - k'_{3,z}} L_{0b}^{p-} + \frac{e^{i(-K_{3,z}-k_{3,z}-k'_{3,z})D} - 1}{-K_{3,z} - k_{3,z} - k'_{3,z}} L_+^{p-} \right]
 \end{aligned}$$

A.4 The Surface Sources and Their Radiated Fields

For the surface sources, we only consider the contribution near the interface, where the linear field will be enhanced by surface plasmon excitation. This is $z = 0$ for the Otto configuration and $z = -D$ for the Kretschmann configuration. The traditional approach to describe the surface source, going back to Rudnick and Stern, is to put the source in the surrounding dielectric, just beyond the metal surface, but to characterize its response in terms of the linear fields on the metal side of the interface.

Starting with the Kretschmann configuration, the linear fields in medium 3 at $\mathbf{r} = \mathbf{R} - D\hat{\mathbf{z}}$ are evaluated:

$$\begin{aligned}
 E_3^s(\mathbf{R} - D\hat{\mathbf{z}}) &= (e^{ik_{3,z}D} + \rho_s e^{-ik_{3,z}D}) C_s E_{1-}^s e^{i\kappa \cdot \mathbf{R}} \\
 E_3^z(\mathbf{R} - D\hat{\mathbf{z}}) &= (e^{ik_{3,z}D} + \rho_p e^{-ik_{3,z}D}) C_z E_{1-}^p e^{i\kappa \cdot \mathbf{R}} \\
 E_3^\kappa(\mathbf{R} - D\hat{\mathbf{z}}) &= (e^{ik_{3,z}D} - \rho_p e^{-ik_{3,z}D}) C_\kappa E_{1-}^p e^{i\kappa \cdot \mathbf{R}}
 \end{aligned} \quad (\text{A.45})$$

And the effective dipole moment per unit area source, placed outside the metal, is given by

$$\begin{aligned}
 \mathbf{Q}_{Kr}(\mathbf{R}) &= \mathbf{Q}^T(\mathbf{R}) + \hat{\mathbf{z}}Q^z(\mathbf{R}), \text{ where} \\
 \mathbf{Q}_{Kr}^T(\mathbf{R}) &= -\Gamma^T \mathbf{E}_3^T(\mathbf{R} - D\hat{\mathbf{z}}) E_3^{z'}(\mathbf{R} - D\hat{\mathbf{z}}) \\
 Q_{Kr}^z(\mathbf{R}) &= -\Gamma^z E_3^z(\mathbf{R} - D\hat{\mathbf{z}}) E_3^{z'}(\mathbf{R} - D\hat{\mathbf{z}})
 \end{aligned} \quad (\text{A.46})$$

with

$$\mathbf{E}_3^T(\mathbf{R} - D\hat{\mathbf{z}}) = \hat{\mathbf{s}} E_3^s(\mathbf{R} - D\hat{\mathbf{z}}) + \hat{\kappa} E_3^\kappa(\mathbf{R} - D\hat{\mathbf{z}})$$

Expressions for Γ^T and Γ^z will be given below; an explicit minus sign is introduced in A.46 because historically $\hat{\mathbf{z}}$ is taken to point from metal to air, whereas here, it points from air to metal. Combining (A.45,A.46) leads to

$$\mathbf{Q}_{Kr}(\mathbf{R}) = \hat{\mathbf{s}}Q_{Kr}^s e^{i(\kappa+\kappa')\cdot\mathbf{R}} + \hat{\boldsymbol{\kappa}}Q_{Kr}^\kappa e^{i(\kappa+\kappa')\cdot\mathbf{R}} + \hat{\mathbf{z}}Q_{Kr}^z e^{i(\kappa+\kappa')\cdot\mathbf{R}} = \mathbf{Q}_{Kr} e^{i(\kappa+\kappa')\cdot\mathbf{R}} \quad (\text{A.47})$$

where

$$\begin{aligned} Q_{Kr}^s &= -\Gamma^T(1+r_{32}^s)(1+r_{32}^{p'})e^{i(k_{3,z}+k'_{3,z})D}C_sE_{1-}^sC'_zE_{1-}^{p'} \\ Q_{Kr}^\kappa &= -\Gamma^T(1-r_{32}^p)(1+r_{32}^{p'})e^{i(k_{3,z}+k'_{3,z})D}C_\kappa E_{1-}^pC'_zE_{1-}^{p'} \\ Q_{Kr}^z &= -\Gamma^z(1+r_{32}^p)(1+r_{32}^{p'})e^{i(k_{3,z}+k'_{3,z})D}C_zE_{1-}^pC'_zE_{1-}^{p'} \end{aligned} \quad (\text{A.48})$$

The SHG field in medium 0 from this source is then given by

$$\mathbf{E}_0^{(Kr,\text{surface})}(\mathbf{r}) = (E_{0+}^{s(Kr,\text{surface})}\hat{\mathbf{S}} + E_{0+}^{p(Kr,\text{surface})}\hat{\mathbf{P}}_{0+})e^{i\mathbf{K}\cdot\mathbf{R}}e^{iW_0z} \quad (\text{A.49})$$

where

$$\begin{aligned} E_{0+}^{s(Kr,\text{surface})} &= 2\pi i \frac{\bar{T}_{10}^s T_{31}^s e^{iK_{3,z}D}}{(1-\bar{R}_{30}^s R_{32}^s e^{2iK_{3,z}D})} \left(\frac{K_0 T_{23}^s}{K_{2,z}} \right) (K_0 Q_{Kr}^s) \\ E_{0+}^{p(Kr,\text{surface})} &= 2\pi i \frac{\bar{T}_{10}^p T_{31}^p e^{iK_{3,z}D}}{(1-\bar{R}_{30}^p R_{32}^p e^{2iK_{3,z}D})} \left(\frac{K_0 T_{23}^p}{K_{2,z}} \right) \left(\frac{K(K_0 Q_{Kr}^z) - K_{2,z}(K_0 Q_{Kr}^\kappa)}{K_0 N_2} \right) \end{aligned} \quad (\text{A.50})$$

For the Otto configuration, the linear fields in medium 1 at $\mathbf{r} = \mathbf{R} - 0\hat{\mathbf{z}}$ have to be evaluated:

$$\begin{aligned} E_3^{sOt}(\mathbf{R} - 0\hat{\mathbf{z}}) &= (1 + \rho_s)C_s E_{1-}^s e^{i\kappa\cdot\mathbf{R}} \\ E_3^{zOt}(\mathbf{R} - 0\hat{\mathbf{z}}) &= (1 + \rho_p)C_z E_{1-}^p e^{i\kappa\cdot\mathbf{R}} \\ E_3^{\kappa Ot}(\mathbf{R} - 0\hat{\mathbf{z}}) &= (1 - \rho_p)C_\kappa E_{1-}^p e^{i\kappa\cdot\mathbf{R}} \end{aligned} \quad (\text{A.51})$$

Contrary to the Kretschmann case, the nonlinear source term that points from the metal to air, as well as the source term. That points from the air to the metal and the reflection there has to be taken into account. Hence,

$$\begin{aligned} Q_{Ot,\text{down}}^s &= \Gamma^T(1+r_{32}^s e^{2ik_{3,z}D})(1+r_{32}^{p'} e^{2ik'_{3,z}D})C_s E_{1-}^s C'_z E_{1-}^{p'} \\ Q_{Ot,\text{down}}^\kappa &= \Gamma^T(1-r_{32}^p e^{2ik_{3,z}D})(1+r_{32}^{p'} e^{2ik'_{3,z}D})C_\kappa E_{1-}^p C'_z E_{1-}^{p'} \\ Q_{Ot,\text{down}}^z &= \Gamma^z(1+r_{32}^p e^{2ik_{3,z}D})(1+r_{32}^{p'} e^{2ik'_{3,z}D})C_z E_{1-}^p C'_z E_{1-}^{p'} \\ Q_{Ot,\text{up}}^s &= -\Gamma^T(1+r_{32}^s e^{2ik_{3,z}D})(1+r_{32}^{p'} e^{2ik'_{3,z}D})C_s E_{1-}^s C'_z E_{1-}^{p'} \\ Q_{Ot,\text{up}}^\kappa &= -\Gamma^T(1-r_{32}^p e^{2ik_{3,z}D})(1+r_{32}^{p'} e^{2ik'_{3,z}D})C_\kappa E_{1-}^p C'_z E_{1-}^{p'} \\ Q_{Ot,\text{up}}^z &= -\Gamma^z(1+r_{32}^p e^{2ik_{3,z}D})(1+r_{32}^{p'} e^{2ik'_{3,z}D})C_z E_{1-}^p C'_z E_{1-}^{p'} \end{aligned} \quad (\text{A.52})$$

The total surface sources in Otto configuration are

$$\begin{aligned}
 Q_{Ot}^s &= Q_{Ot,\text{up}}^s + \bar{R}_{12}^s Q_{Ot,\text{down}}^s \\
 Q_{Ot}^\kappa &= Q_{Ot,\text{up}}^\kappa + \bar{R}_{12}^p Q_{Ot,\text{down}}^\kappa \\
 Q_{Ot}^z &= Q_{Ot,\text{up}}^z + \bar{R}_{12}^p Q_{Ot,\text{down}}^z
 \end{aligned} \tag{A.53}$$

This leads to the second harmonic field in medium 0

$$\mathbf{E}_0^{(Ot,\text{surface})}(\mathbf{r}) = (E_{0+}^{s(Ot,\text{surface})} \hat{\mathbf{S}} + E_{0+}^{p(Ot,\text{surface})} \hat{\mathbf{P}}_{0+}) e^{i\mathbf{K}\cdot\mathbf{R}} e^{iK_{1,z}z} \tag{A.54}$$

where

$$\begin{aligned}
 E_{0+}^{s(Ot,\text{surface})} &= 2\pi i \left(\frac{K_0 \bar{T}_{10}^s}{K_{1,z}} \right) (K_0 Q_{Ot}^s) \\
 E_{0+}^{p(Ot,\text{surface})} &= 2\pi i \left(\frac{K_0 \bar{T}_{10}^p}{K_{1,z}} \right) \left(\frac{K(K_0 Q_{Ot}^z - K_{1,z}(K_0 Q_{Ot}^\kappa))}{K_0 N_1} \right)
 \end{aligned} \tag{A.55}$$

A.5 The Total Fields and the Second Harmonic Reflection Coefficients

Adding the contributions from bulk and surface, we get the total second harmonic fields radiated into medium 0:

$$\mathbf{E}_0^{\text{II}}(\mathbf{r}) = (E_{0+}^{s\text{II}} \hat{\mathbf{S}} + E_{0+}^{p\text{II}} \hat{\mathbf{P}}_{0+}) e^{i\mathbf{K}\cdot\mathbf{R}} e^{iK_{1,z}z} \tag{A.56}$$

For the Kretschmann configuration, this leads to

$$\begin{aligned}
 E_{0+}^{s\text{II}, Kr} &= \frac{\bar{T}_{10}^s}{(1 - \bar{R}_{30}^s R_{32}^s e^{2iK_{3,z}D})} \\
 &\quad \left[\left(\frac{K_0 T_{31}^s}{K_{3,z}} \right) (A_s + R_{32}^s e^{iK_{3,z}D} B_s) + \left(\frac{K_0 T_{23}^s}{K_{2,z}} \right) T_{31}^s e^{iK_{3,z}D} (K_0 Q_{Kr}^s) \right] \\
 E_{0+}^{p\text{II}, Kr} &= \frac{\bar{T}_{10}^p}{(1 - \bar{R}_{30}^p R_{32}^p e^{2iK_{3,z}D})} \\
 &\quad \left[\left(\frac{K_0 T_{31}^p}{K_{3,z}} \right) (A_p + R_{32}^p e^{iK_{3,z}D} B_p) + \left(\frac{K_0 T_{23}^p}{K_{2,z}} \right) T_{31}^p e^{iK_{3,z}D} \left(\frac{K(K_0 Q_{Kr}^z) - K_{2,z}(K_0 Q_{Kr}^\kappa)}{K_0 N_2} \right) \right]
 \end{aligned} \tag{A.57}$$

For the Otto configuration, the harmonic fields can be written as

$$\begin{aligned}
 E_{0+}^{sII, Ot} &= \frac{\bar{T}_{10}^s}{(1 - \bar{R}_{30}^s R_{32}^s e^{2iK_{3,z}D})} \left(\frac{K_0 T_{31}^s}{K_{3,z}} \right) (A_s + R_{32}^s e^{iK_{3,z}D} B_s) + \left(\frac{K_0 \tilde{T}_{10}^s}{K_{1,z}} \right) (K_0 Q_{Ot}^s) \\
 E_{0+}^{pII, Ot} &= \frac{\bar{T}_{10}^p}{(1 - \bar{R}_{30}^p R_{32}^p e^{2iK_{3,z}D})} \left(\frac{K_0 T_{31}^p}{K_{3,z}} \right) (A_p + R_{32}^p e^{iK_{3,z}D} B_p) \\
 &\quad + \left(\frac{K_0 \tilde{T}_{10}^p}{K_{1,z}} \right) \left(\frac{K(K_0 Q_{Ot}^z) - K_{1,z}(K_0 Q_{Ot}^k)}{K_0 N_1} \right)
 \end{aligned} \tag{A.58}$$

In the ‘‘cgs units’’ being employed here, the Poynting vector is $\frac{(\mathbf{E} \times \mathbf{B})}{4\pi}$, so the power incident for s-polarized light is

$$P^s(\omega) = \frac{n_1 |E_{0+}^s|^2}{2\pi} A^{\text{beam}}(\omega) \tag{A.59}$$

where $A^{\text{beam}}(\omega)$ is the area of the incident beam. For such an excitation, the power radiated at 2ω is

$$P^s(2\omega) = \frac{n_1 |E_{0+}^{sII}|^2}{2\pi} A^{\text{beam}}(2\omega) \tag{A.60}$$

where $A^{\text{beam}}(2\omega)$ is the area of the beam at 2ω .

In the plane wave approximation, for an incident beam of area $A^{\text{beam}}(\omega)$, the area projected on the surface will be $A^{\text{surface}} = A^{\text{beam}}(\omega) / \cos \theta$, where $\cos \theta$ follows from (4),

$$\cos \theta = \frac{k_{1,z}}{k_0} \tag{A.61}$$

Similarly, $A^{\text{beam}}(2\omega) = A^{\text{surface}} \cos \Theta$, where $\cos \Theta$ follows from

$$\cos \Theta = \frac{K_{1,z}}{K_0} \tag{A.62}$$

So with

$$\begin{aligned}
 A^{\text{beam}}(2\omega) &= A^{\text{surface}} \cos \Theta \\
 &= A^{\text{beam}}(\omega) \frac{\cos \Theta}{\cos \theta} \\
 &= A^{\text{beam}}(\omega) \frac{K_{1,z} k_0}{K_0 k_{1,z}}
 \end{aligned} \tag{A.63}$$

the radiated intensity in s-polarization is

$$P^s(2\omega) = \frac{N_1 |E_{0+}^{sII}|^2}{2\pi} \frac{K_{1,z} k_0}{K_0 k_{1,z}} A^{\text{beam}}(\omega) \tag{A.64}$$

and thus the conversion efficiency per unit incident power is

$$\frac{P^s(2\omega)}{[P^s(\omega)]^2} = \frac{2\pi N_1 |E_{0+}^{sII}|^2 K_{1,z} k_0}{n_1^2 |E_{0-}^s|^4 K_0 k_{1,z}} \frac{1}{A^{beam}(\omega)} \quad (\text{A.65})$$

Similarly, for incident p-polarized light and p-polarized SHG, the conversion efficiency per unit incident power is

$$\frac{P^p(2\omega)}{[P^p(\omega)]^2} = \frac{2\pi N_1 |E_{0+}^{pII}|^2 K_{1,z} k_0}{n_1^2 |E_{0-}^p|^4 K_0 k_{1,z}} \frac{1}{A^{beam}(\omega)} \quad (\text{A.66})$$

The nonlinear parameters to match these conversion efficiencies to the experimental results are deduced following the works of Rudnick and Stern [74], and Sipe et al. [73].

B | Anisotropy in the Emission of CdSe-Nano-Platelets

B.1 Sample Analysis

Zincblend (ZB) CdSe core only NPLs with the first exciton absorption bands around 512 nm (4.5 Monolayers (ML)) and $(19.6 \pm 2.6) \times (9.6 \pm 1.6) \text{ nm}^2$ lateral size as well as ZB CdSe quantumdots (of similar absorption and emission wavelengths) were synthesized as in Ref. [194]. They are covered with oleic acid ligands. A TEM image of the sample is shown in Fig. B.2 a along with a histogram on their lateral size distribution (b). The area fill factor of platelets is measured to be $\sim 40\%$.

The monolayers of quantum dots and in-plane oriented nano platelets (NPLs) on $170 \mu\text{m}$ fused silica microscope cover slips were obtained using a Langmuir technique. The TEM image clearly demonstrates the in-plane orientation of our platelets in a monolayer.

B.1.1 Influence of the Effective Medium

As the platelets and dots are surrounded by oleic acid ligands local field effects arise and an effective medium consisting of CdSe particles and oleic acid is formed. This medium is anisotropic due to the orientation of the particles in a monolayer. Hence we calculate the direction dependent depolarization factors of the platelets assuming NPLs to be oblate ellipsoids with the semiaxes $a_{i,j,k}$ [115, 176, 177, 195].

$$L_i = \int_0^\infty \frac{a_i a_j a_k}{2(s + a_i^2)^{3/2} (s + a_j^2)^{1/2} (s + a_k^2)^{1/2}} ds \quad (\text{B.1})$$

For the semiaxes $a_{i,j,k}$ we insert the results of our TEM analysis on the lateral platelet dimensions $l_x/2$, $l_y/2$ and thickness $d_{NPL}/2$ for the short axis of the ellipsoid. $d_{NPL} = 4.5 \cdot d_{ML}$ is the thickness of the platelets, assuming a cadmium-termination on both basal planes[182, 192] with $d_{ML} = 0.304 \text{ nm}$, the half lattice parameter for zinc blende

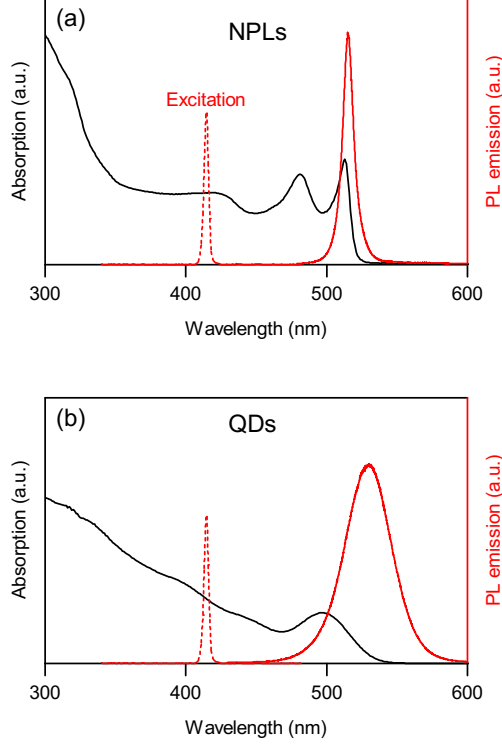


Figure B.1: PL and Absorption spectra of the nano-platelets (a) and quantum dots (b) used in the k -space spectroscopy. The spectrum of the excitation laser at 415 nm is shown as a dashed line.

CdSe[192]. We obtain $L_{x,y,z} = 0.04, 0.11, 0.85$ by cyclic permutation of the semi-axes. For spheres (QDs) we take $L_x = L_y = L_z = 1/3$ [177]. Following Sihvola et al.[177] the effective permittivity of an anisotropic medium of aligned ellipsoids at the frequency ω in the direction i is:

$$\epsilon_{eff}^i(\omega) = \epsilon(\omega) + \frac{F_V[\epsilon_s(\omega) - \epsilon(\omega)]\epsilon(\omega)}{\epsilon(\omega) + (1 - F_V)[\epsilon_s(\omega) - \epsilon(\omega)]L_i} \quad (\text{B.2})$$

where F_V is the volume fraction of the semiconductor particles with permittivity ϵ_s in the host material with permittivity ϵ . We insert $L_i = L_z$ for the out of plane direction $\epsilon_{eff}^{OP} = \epsilon_{eff}^z$.

To take the lateral random in-plane azimuthal orientation of the nano-platelets in the monolayer into account we analyze the expectation value of the effective permittivity over all in plane directions. Integration over a quarter circle ($\pi/2$) exploiting the symmetry of

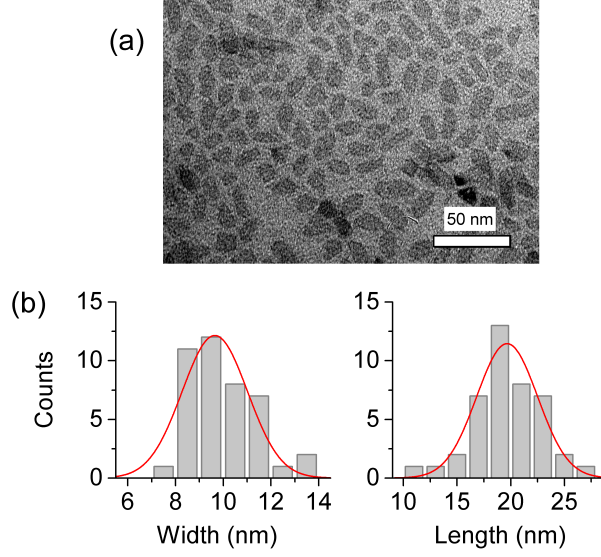


Figure B.2: TEM image and size of the CdSe nano-platelets. (a) TEM image of 4.5 ML nano-platelets brought to the TEM grid with the same technique as used to produce the sub-monolayer of oriented NPLs on quartz substrates for angle dependent PL measurements. (b) Gaussian fits to the distribution of short and long lateral size of the platelets result in $(l_x \times l_y) = (19.6 \pm 2.6) \times (9.6 \pm 1.6) \text{ nm}^2$. The average area of the platelets $A_{NPLs} = 200 \text{ nm}^2$ is calculated by taking the area of each NPL and then averaging over the ensemble.

the in plane depolarization gives:

$$\epsilon_{eff}^{IP}(\omega) = \langle \epsilon_{eff}^i(\omega) \rangle_\phi = \frac{2}{\pi} \int_0^{\frac{\pi}{2}} \epsilon(\omega) + \frac{F_V[\epsilon_s(\omega) - \epsilon(\omega)]\epsilon(\omega)}{\epsilon(\omega) + (1 - F_V)[\epsilon_s(\omega) - \epsilon(\omega)](L_x \sin \phi + L_y \cos \phi)} d\phi \quad (\text{B.3})$$

The dielectric function $\epsilon_s(\omega)$ of ZB CdSe bulk at 415 nm for excitation and at 515 nm (535 nm) for emission of our NPLs (QDs) is taken from Ninomiya et al.[196]. The optical permittivity of oleic acid surrounding is assumed to be constant $\sqrt{\epsilon} = n_{OA} = 1.46$ [180]. As Rowland et al.[197] show, the dielectric function of nano-platelets at their excitonic resonance does not differ strongly from that of bulk and can be used, in our case, for effective medium modeling. To express the volume fraction F_{NPL} in the monolayer we use an effective lateral extension $\langle l_{NPL} \rangle = \sqrt{A_{NPL}}$ (for lateral azimuthal random orientation in the monolayer) with A_{NPL} the platelet area. We assume our NPLs to be covered on all facets by their oleic acid ligands.

$$F_{NPL} = \frac{d_{NPL} A_{NPL}}{(\langle l_{NPL} \rangle + 2l_{OA} + l_{OA,a})^2 \underbrace{(d_{NPL} + 2l_{OA} + l_{OA,b})}_{D_{ML,NPL}}} \quad (\text{B.4})$$

Here $l_{OA} = 2.1 \text{ nm}$ [198] is the length of an oleic molecule, $l_{OA,xy}$ and $l_{OA,z}$ are additional

ligand excess lengths in the in-plane (index xy) and perpendicular (index z) direction, respectively, which are related to the fact that there is a slight ligand excess in the layer.

For our CdSe/ZnS quantum dots of 4 nm diameter d_{QD} the volume fraction in the monolayer is:

$$F_{QD} = \frac{\frac{4\pi}{3} \left(\frac{d_{QD}}{2}\right)^3}{(d_{QD} + 2l_{OA} + l_{OA,a})^2 \underbrace{(d_{QD} + 2l_{OA} + l_{OA,b})}_{D_{ML,QD}}}. \quad (\text{B.5})$$

With $l_{OA,xy} = 3.2$ nm and $l_{OA,z} = 0$ nm for NPLs (QDs) and $l_{OA,xy} = 0$ nm and $l_{OA,z} = 0$ nm for QDs we find volume fractions to be 16 % for NPL and 13 % for our quantum dot monolayers. The thickness of the monolayers of NPLs ($D_{ML,NPL}$) and QDs ($D_{ML,QD}$) needed for our k -space analysis (see section 6.1.1) are hereby determined by the length of the ligands and the thickness (diameter) of the nanoparticles. We also remark that the estimate of the surface coverage in Figure B.2 of $\sim 40\%$ is in good agreement with the 41% resulting from the above used excess length and platelet size.

B.1.2 In and Out-of Plane Local Field Factors for Radiation Pattern Calculation

The local field factor in the direction i of a nanoparticle is given by [114, 115, 176, 177, 195, 199]:

$$f_i(\omega) = \frac{1}{1 + L_i(\epsilon_{SC}(\omega)/\epsilon_M(\omega) - 1)} \quad (\text{B.6})$$

with the dielectric functions $\epsilon_{SC,M}(\omega)$ of the semiconductor inclusion (SC) and the surrounding (isotropic) matrix (M) at a given frequency ω . The depolarization factors L_i are as defined in eq. B.1.

In spherical coordinates, with azimuth angle ϕ and polar angle θ , the electric field amplitude of a field E is

$$\vec{E}(\phi, \theta) = E_0 \cdot \begin{pmatrix} \sin \theta \cos \phi \\ \sin \theta \sin \phi \\ \cos \theta \end{pmatrix} \quad (\text{B.7})$$

is reduced by the field factors to:

$$\vec{E}_{lf} = \begin{pmatrix} E_x \\ E_y \\ E_z \end{pmatrix} = \begin{pmatrix} f_x & 0 & 0 \\ 0 & f_y & 0 \\ 0 & 0 & f_z \end{pmatrix} \cdot \vec{E}(\phi, \theta) \quad (\text{B.8})$$

so that the field intensity becomes:

$$I_{lf}(\phi, \theta) = I_0 \left(|f_x|^2 \sin^2 \theta \cos^2 \phi + |f_y|^2 \sin^2 \theta \sin^2 \phi + |f_z|^2 \cos^2 \theta \right) \quad (\text{B.9})$$

As our NPLs are laterally, azimuthally randomly oriented in the measured ensemble in the monolayer we calculate the expectation value of the local field intensity factor $|f(\phi, \theta)|^2 = I_{lf}(\phi, \theta)/I_0$ as a function of θ by integrating over all azimuthal angles ϕ :

$$\langle |f|^2(\theta) \rangle_\phi = \frac{\int_0^{2\pi} |f(\phi, \theta)|^2 d\phi}{\int_0^{2\pi} d\phi} \quad (\text{B.10})$$

So that

$$\begin{aligned} \langle |f(\omega)|^2(\pi/2) \rangle_\phi &= |f(\omega)|_{IP}^2 \\ \langle |f(\omega)|^2(0) \rangle_\phi &= |f(\omega)|_{OP}^2 \end{aligned} \quad (\text{B.11})$$

are the in-plane averaged local field factors the frequency ω for a monolayer of oriented NPLs in an isotropic surrounding in the directions parallel (IP) and perpendicular (OP) to the monolayer.

B.1.3 Radiation Patterns

We define the dipole distribution in our NPL or QD monolayer ensembles as an ellipsoid with the semiaxes $\tilde{N}_{r,IP} = N_{r,IP}|\mu_{IP}(\omega)|^2$ for both in-plane directions (x and y axes) and $\tilde{\mu}_{r,OP} = N_{r,OP}|\mu_{OP}(\omega)|^2$ for the z-axis:

$$|\mu(\theta, \phi)|^2 = \frac{\tilde{\mu}_{r,IP}^2 \tilde{\mu}_{r,OP}}{\sqrt{(\tilde{\mu}_{r,IP} \tilde{\mu}_{r,OP} \cos \phi \sin \theta)^2 + (\tilde{\mu}_{r,IP} \tilde{\mu}_{r,OP} \sin \phi \sin \theta)^2 + (\tilde{\mu}_{r,OP}^2 \cos \theta)^2}} \quad (\text{B.12})$$

The local field factor ellipsoid $|f|^2(\theta, \phi)$ is obtained by replacing $\tilde{\mu}_{r,IP}$ and $\tilde{\mu}_{r,OP}$ in equation B.12 by $|f(\omega)|_{IP}^2$ and $|f(\omega)|_{OP}^2$, respectively.

We express the radiance of a Hertzian dipole of strength $|\mu|^2$ in spherical coordinates for θ from 0 to π and ϕ from 0 to 2π as $\tilde{D}(\theta, \phi, r) = |\mu|^2 R(r) D(\theta, \phi)$. Its angle dependent emission characteristics are given as:

$$D(\theta, \phi) = C_2 (1 - \cos^2 \theta) \quad (\text{B.13})$$

The constant C_2 is chosen so that $D(\theta, \phi)$ is in units of $\text{W}/\text{sr}(\text{Cm})^2$, i.e radiant intensity per dipole moment squared.

We now consider a unit sphere (with radius r) containing a monolayer ensemble of NPLs or QDs in its center. The irradiance transmitted through the surface of the sphere at

a given solid angle is then $I^r(\theta, \phi)$. To compare the radiation characteristics of the NPL and QD monolayer ensembles we assume their total emitted power $I_{tot} = \int \int I^r(\theta, \phi) d\Omega$ with $d\Omega = \sin \theta d\theta d\phi$ to be identical.

To obtain the intra platelet radiation pattern $I^r(\theta, \phi)$ we do not need to take dielectric effects into account as we know the internal dipole distribution from our experiments and analysis. We analyze the convolution of the dipole distribution ellipsoid $|\mu(\theta, \phi)|^2$ with the angle dependent radiation pattern of a Hertzian dipole $D(\theta, \phi)$.

$$I^r(\theta, \phi) = \int_0^\pi \int_0^{2\pi} |\mu(\theta - \theta', \phi - \phi')|^2 \cdot D(\theta', \phi') d\Omega' \quad (\text{B.14})$$

The radiation pattern with taking the local field factors into account is obtained by

$$I_{lf}^r(\theta, \phi) = \int_0^\pi \int_0^{2\pi} |\mu(\theta - \theta', \phi - \phi')|^2 \cdot f(\theta - \theta', \phi - \phi')^2 \cdot D(\theta', \phi') d\Omega', \quad (\text{B.15})$$

with $d\Omega' = \sin \theta d\theta' d\phi'$.

B.2 Analysis Of Optical Interband Transitions

The optical anisotropy of ZB NPLs can be explained from their characteristic electronic structure. One can describe the NPL as a cuboid with dimensions $L_x \geq L_y \gg L_z$. For a qualitative study, we can restrict to a simple effective mass description, disregarding band coupling. The wave function of confined carriers is then given by $\Psi_i = f_{\nu,n}^i |u_i\rangle$, where $i = e, hh, lh$, so indicates electron, heavy hole, light hole or split-off hole, respectively. $f_{\nu,n}^i$ is the envelope function, defined over the entire NPL, whose point symmetry is ν and its main quantum number is n . $|u_i\rangle$ is the band-edge periodic function at the Γ point, defined over the unit cell.

Considering the strong confinement along the growth direction, the energy of a carrier j is roughly given by $E^j \approx E_\Gamma^j + \frac{\hbar^2 \pi^2}{2m_{[001]}^j L_z^2}$, where E_Γ^j is the energy splitting from the top of the valence band at the Γ point, and $m_{[001]}^j$ the effective mass along the growth direction. Unlike in wurtzite semiconductors, the top of the valence band in bulk ZB semiconductor has degenerate hh and lh subbands, as $E_\Gamma^{hh} = E_\Gamma^{lh}$. However, the effective masses along the growth direction are heavier for hh than for lh . For CdSe, $m_{[001]}^{hh} = 0.33$ and $m_{[001]}^{lh} = 0.13$. [200] As a result, the top of the valence band is formed almost exclusively by hh states, with lh states and split-off holes split by hundreds of meV, as noted in different experiments. [98, 201] Notice that owing to the large energetic separation between hh and lh states, low-energy levels are expected to have weak $hh - lh$ coupling. A diagram of the electron and hole energy levels resulting from the above considerations is plotted in B.3(a).

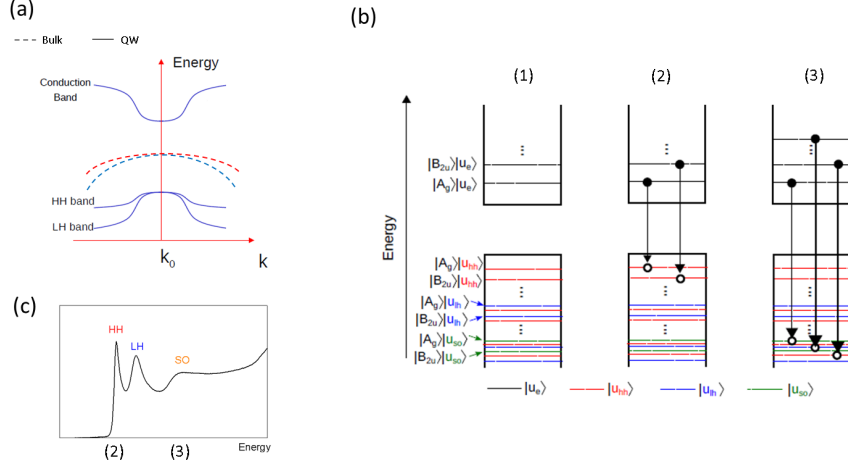


Figure B.3: The contribution of different Bloch states determines the isotropic absorption and anisotropic emission of CdSe nano-platelets (a) Schematic of the conduction band electron and valence band hole energy levels in a rectangular (D_{2h}) NPL with ZB crystal structure. Symmetry labels for envelope and periodic parts of a few states, $|\nu\rangle|u_j\rangle$, are given. (b) Dipole-allowed near-band-edge transitions. (c) Dipole-allowed high energy transitions. In (b) only hh levels are involved, which results in prevailing out-of-plane emission. In (c), hh , lh and split-off holes are equally involved, which results in isotropic emission.

The levels are labeled by the corresponding envelope and periodic function symmetries. For the envelope part, we take into account that the NPL belongs to the D_{2h} point group and obtain the ensuing symmetry for an increasing number of nodes along the weakest confinement direction, L_x .

The probability of interband optical transitions taking place in such a system is proportional to the transition dipole moment $|\mu_{ej}|$, with $j = hh, lh, so$. From the wave functions Ψ_i defined above, one obtains $|\mu_{ej}| = \langle f_{\nu_e, n_e}^e | f_{\nu_j, n_j}^j \rangle \langle u_e | \boldsymbol{\mu} | u_j \rangle$. The envelope integral provides selection rules, as only transitions fulfilling δ_{ν_e, ν_j} will be allowed. In turn, the unit cell integral defines the orientation of the absorbed/emitted light. Drawing a parallel between the symmetries of ZB crystal and those of the hydrogen atom, $|u_e\rangle$ is found to s -like symmetry, $|u_{hh}\rangle$ has mixed p_x and p_y symmetry, and $|u_{lh}\rangle$ ($|u_{so}\rangle$) mixed p_x , p_y and p_z character.[202] Here x and y are in-plane directions, while z is the $[001]$ direction (orthogonal to the NPL plane). Therefore, a heavy hole exciton $\Psi = \Psi_e \Psi_{hh}$ forms an in-plane electronic dipole, the integral $\langle u_e | \boldsymbol{\mu} | u_{hh} \rangle$ is non-zero only for (x, y) -polarized light and emission takes place mostly orthogonal to the NPL surface. By contrast, light hole and split-off hole excitons have finite dipole projection along z , so that $\langle u_e | \boldsymbol{\mu} | u_{lh} \rangle$ ($\langle u_e | \boldsymbol{\mu} | u_{so} \rangle$) is finite in all space directions.

We are now in a condition to interpret our measurements. In room temperature photoluminescence experiments, electron-hole recombination takes place between states near the band edges. As shown in B.3(b), this involves hh only. Consequently, emission is mostly orthogonal to the NPL surface. Notice this is independent of the envelope function symmetry, and hence compatible with previous works suggesting emission can have finite contribution from excited (B_{2u}) excitons.[108] On the other hand, our absorption experiments are performed at high energy. As shown in B.3(c), conduction band electrons are now able to recombine with any kind of hole state (or their mixture). On average, this means absorption is isotropic.

B.2.1 Theoretical Considerations

Periodic functions of electrons and holes

For ZB crystals with spin-orbit interaction, it is customary to define the periodic Bloch functions in a basis of spherical harmonic functions with well defined total (orbital plus spin) angular momentum and its z-projection, $|J, J_z\rangle$.[202] For conduction electrons, which have s -like symmetry, the orbital angular momentum is $l = 0$. Hence, $J = l + \sigma = 1/2$. $|u_e\rangle$ (including spin) can then take the following forms:

$$|\frac{1}{2}, \frac{1}{2}\rangle_e = |S\rangle|\uparrow\rangle \quad |\frac{1}{2}, -\frac{1}{2}\rangle_e = |S\rangle|\downarrow\rangle$$

For valence band holes, which have p -like symmetry, the orbital angular momentum is $l = 1$. Hence, $J = 3/2, 1/2$. For $J = 3/2$, $J_z = \pm 3/2$ projections correspond to the heavy hole subband. $|u_{hh}\rangle$ can then take the following forms:

$$|3/2, 3/2\rangle = -\frac{1}{\sqrt{2}}|(X + iY)\rangle|\uparrow\rangle \quad |3/2, -3/2\rangle = \frac{1}{\sqrt{2}}|(X - iY)\rangle|\downarrow\rangle.$$

In turn, $J = 3/2$ with $J_z = \pm 1/2$ projections correspond to light hole subband. $|u_{lh}\rangle$ can then be:

$$|3/2, 1/2\rangle = \sqrt{\frac{2}{3}}|Z\rangle|\uparrow\rangle - \frac{1}{\sqrt{6}}|(X + iY)\rangle|\downarrow\rangle \quad |3/2, -1/2\rangle = \sqrt{\frac{2}{3}}|Z\rangle|\downarrow\rangle + \frac{1}{\sqrt{6}}|(X - iY)\rangle|\uparrow\rangle.$$

Last, $J = 1/2$ corresponds to the split-off subband. $|u_{so}\rangle$ can then be:

$$|1/2, 1/2\rangle = \frac{1}{\sqrt{3}}|Z\rangle|\uparrow\rangle + \frac{1}{\sqrt{3}}|(X + iY)\rangle|\downarrow\rangle \quad |1/2, -1/2\rangle = -\frac{1}{\sqrt{3}}|Z\rangle|\downarrow\rangle + \frac{1}{\sqrt{3}}|(X - iY)\rangle|\uparrow\rangle.$$

Polarization of interband transitions

The oscillator strength of a transition between a conduction band level and valence band one is proportional to $|\mu_{ej}|^2 = |\langle f_{\nu_e, n_e}^e | f_{\nu_j, n_j}^j \rangle \langle u_e | \boldsymbol{\mu} | u_j \rangle|^2$. The integral over the

unit cell $\langle u_e | \boldsymbol{\mu} | u_j \rangle$ defines the polarization of the emitted/absorbed light, as we show next. $\boldsymbol{\mu} = q \vec{r}$ stands for the dipole moment of the electromagnetic radiation, with q the electric charge. $|u_j\rangle$ functions are given in the previous section. Besides, the cubic symmetry of zinc-blende crystals leads to $\langle S|x|X\rangle = \langle S|y|Y\rangle = \langle S|z|Z\rangle = K$, with all other integrals being zero. Note that, while in bulk x , y and z directions are equivalent, in the presence of confinement z is taken as the $([001])$ direction. This is in line with the surface normal $[001]$ of the platelets. With these considerations, one can compare $\langle u_e | \boldsymbol{\mu} | u_j \rangle$ for different kinds of interband transitions. For transitions involving hh levels, $|\langle u_e | \boldsymbol{\mu} | u_{hh} \rangle|^2$ can take the following values:

$$|\langle 1/2, 1/2 | \boldsymbol{\mu} | 3/2, 3/2 \rangle|^2 = |\langle 1/2, -1/2 | \boldsymbol{\mu} | 3/2, -3/2 \rangle|^2 = q^2 K^2 \begin{pmatrix} \frac{1}{2} \\ \frac{1}{2} \\ 0 \end{pmatrix} \quad (\text{B.16})$$

$$|\langle 1/2, 1/2 | \boldsymbol{\mu} | 3/2, -3/2 \rangle|^2 = |\langle 1/2, -1/2 | \boldsymbol{\mu} | 3/2, 3/2 \rangle|^2 = 0.$$

For transitions involving lh levels, $|\langle u_e | \boldsymbol{\mu} | u_{lh} \rangle|^2$ can take the following values:

$$|\langle 1/2, 1/2 | \boldsymbol{\mu} | 3/2, 1/2 \rangle|^2 = |\langle 1/2, -1/2 | \boldsymbol{\mu} | 3/2, -1/2 \rangle|^2 = q^2 K^2 \begin{pmatrix} 0 \\ 0 \\ \frac{2}{3} \end{pmatrix} \quad (\text{B.17})$$

$$|\langle 1/2, 1/2 | \boldsymbol{\mu} | 3/2, -1/2 \rangle|^2 = |\langle 1/2, -1/2 | \boldsymbol{\mu} | 3/2, 1/2 \rangle|^2 = q^2 K^2 \begin{pmatrix} \frac{1}{6} \\ \frac{1}{6} \\ 0 \end{pmatrix}.$$

Last, for transitions involving so levels, $|\langle u_e | \boldsymbol{\mu} | u_{so} \rangle|^2$ can take the following values:

$$|\langle 1/2, 1/2 | \boldsymbol{\mu} | 1/2, 1/2 \rangle|^2 = |\langle 1/2, -1/2 | \boldsymbol{\mu} | 1/2, -1/2 \rangle|^2 = q^2 K^2 \begin{pmatrix} 0 \\ 0 \\ \frac{1}{3} \end{pmatrix}, \quad (\text{B.18})$$

$$|\langle 1/2, 1/2 | \boldsymbol{\mu} | 1/2, -1/2 \rangle|^2 = |\langle 1/2, -1/2 | \boldsymbol{\mu} | 1/2, 1/2 \rangle|^2 = q^2 K^2 \begin{pmatrix} \frac{1}{3} \\ \frac{1}{3} \\ 0 \end{pmatrix}.$$

Equation (B.16) shows that transitions between electron and hh are enabled only by in-plane (x, y) polarized light, hence there are only IP transition dipoles. That is, light is emitted orthogonal to such plane. Since the levels near the top of the valence band in NPLs are of hh character, this explains the fact that most photoluminescence emission

propagates orthogonal to the NPL plane. By contrast, Eqs. (B.17) and (B.18) show that transitions between electron and lh or so holes are enabled by any light polarization. For high energy interband transitions, like those in the absorption measurements we report, the final state can be of hh , lh or so character (or mixed character) with similar likelihood. In such a case $\overline{|\mu_{ej}|^2} = \sum_j |\mu_{ej}|^2 / 3 = q^2 K^2 (1/3, 1/3, 1/3)$. That is, the polarization and the propagation of light is isotropic, as indeed observed in our experiment.

C | Orientation of TPA in CdSe-Nano-Platelets

C.1 Two-Photon Absorption Probability

The probability of a TPA process taking place is given by the 2nd order Fermi golden rule [194]:

$$W_{TPA} = \frac{2\pi}{\hbar} \sum_{i,f} \left| \sum_m \frac{\langle f | \vec{e} \cdot \vec{p} | m \rangle \langle m | \vec{e} \cdot \vec{p} | i \rangle}{E_m - E_i - \hbar\nu} \right|^2 \delta(E_f - E_i - 2\hbar\nu) \quad (\text{C.1})$$

where $|j\rangle$ is the wave function and E_j the energy in the initial ($j = i$), the intermediate ($j = m$), and the final ($j = f$) state. Here, \vec{e} is the light polarization vector and \vec{p} the momentum operator. Initial states are in the valence band (the heavy-hole *hh*, light-hole *lh* and split-off *so* subbands) and final states are in the conduction band *cb*. The virtual intermediate states in TPA-processes are in any band.

The matrix elements in Eq. C.1 represent the optical selection rules and the numerator gives a rough idea of the intensity of a given process. From the denominator, we can determine that the probability for a TPA process is maximized for intermediate states near the laser energy. In our case, this corresponds to half the energy between initial state and final state

$$E_m \approx \frac{E_f - E_i}{2}. \quad (\text{C.2})$$

The virtual intermediate states are short-lived and hence energetically not well defined. The probability of a TPA process taking place is proportional to the sum of perturbation terms involving all possible states $|m\rangle$ and can hence be modeled as a linear combination of several paths through different non-resonant states $|m\rangle$. As mentioned before, the perturbational contribution of a path to the overall transition probability is larger, the closer the intermediate state is to the energy of the absorbed photon. In any case, the state should

never be exactly resonant, as then we would have a first order transition, which is the case for sequential TPA, rather than for non-resonant TPA.

C.2 Selection Rules

Using the envelope function approximation, the dipole matrix elements for one photon can be expanded as:

$$\langle a|\vec{p}|b\rangle = \langle f_a|\langle u_a|\vec{p}|u_b\rangle|f_b\rangle = \langle f_a|f_b\rangle\langle u_a|\vec{p}|u_b\rangle + \langle f_a|\vec{p}|f_b\rangle\langle u_a|u_b\rangle \quad (\text{C.3})$$

where $f_{\nu,n}^i$ is the envelope function, defined over the entire NPL, whose point symmetry is ν and its main quantum number is n . $|u_i\rangle$ is the band-edge periodic function at the Γ point, defined over the unit cell (see Appendix B). Here, $\langle f_a|f_b\rangle\langle u_a|\vec{p}|u_b\rangle$ is finite for interband transitions ($a \neq b$) because $\langle u_a|\vec{p}|e_b\rangle$ would not fulfill the angular momentum conservation. $\langle f_a|\vec{p}|f_b\rangle\langle u_a|u_b\rangle$ is finite for intraband transitions ($a = b$) as Bloch functions of different bands are orthogonal, $\langle u_a|u_b\rangle = \delta_{a,b}$.

For further analysis, the Bloch functions of the cb , hh , lh and so bands in zinc-blende are taken, where

$$\begin{aligned} |u_{cb}\rangle &\rightarrow |J = 1/2, J_z = \pm 1/2\rangle_{cb} = |S\rangle |\pm 1/2\rangle \\ |u_{hh}\rangle &\rightarrow |J = 3/2, J_z = \pm 3/2\rangle_{hh} = \mp \frac{1}{\sqrt{2}} |X \pm iY\rangle |\pm 1/2\rangle \\ |u_{lh}\rangle &\rightarrow |J = 3/2, J_z = \pm 1/2\rangle_{lh} = \sqrt{3/2} |\pm 1/2\rangle \mp \frac{1}{\sqrt{6}} |X \pm iY\rangle |\mp 1/2\rangle \\ |u_{so}\rangle &\rightarrow |J = 1/2, J_z = \pm 1/2\rangle_{so} = \pm \frac{1}{\sqrt{3}} |Z\rangle |\pm 1/2\rangle + \frac{1}{\sqrt{3}} |X \pm iY\rangle |\pm 1/2\rangle \end{aligned} \quad (\text{C.4})$$

For interband transitions $\langle a|\vec{p}|b\rangle = \langle f_a|f_b\rangle\langle u_a|\vec{p}|u_b\rangle$, f_a and f_b must have the same symmetry within the D_{2h} point group of a rectangular platelet for a finite probability. $\langle u_a|\vec{p}|u_b\rangle \propto \langle u_a|\vec{r}|u_b\rangle$ determines the optical orientation of the transition.

Table C.1: Orientation of relevant interband transition for two-photon absorption.

	$ u_{cb}\rangle$	$ u_{hh}\rangle$	$ u_{lh}\rangle$	$ u_{so}\rangle$
$\langle u_{cb} $		x,y	x,y,z	x,y,z
$\langle u_{hh} $	x,y		x,y,z	x,y,z
$\langle u_{lh} $	x,y,z	x,y,z		x,y
$\langle u_{so} $	x,y,z	x,y,z	x,y	

From these expressions and the fact, that non-zero elements in Td-symmetry are either $\langle S|y|X\rangle = \langle S|y|Z\rangle = \langle S|z|Z\rangle$ or $\langle X|y|Z\rangle$, we can determine the table C.1 of possible transitions and their respective orientations. The first row of this table has already been used for the linear absorption process in Chapter 6 and Appendix B.

For intraband transitions $\langle a|\vec{p}|b\rangle = \langle f_a|\vec{p}|f_b\rangle \langle u_a|u_b\rangle$, u_a and u_b must have the same symmetry for finite transition probabilities as they belong to the same sub-band. Here, $\langle f_a|\vec{p}|f_b\rangle \propto \langle f_a|\vec{r}|f_b\rangle$ determines the optical orientation of the transition. As our photon energies are of 1.5 eV, the most relevant intraband transitions are z-forbidden as can be seen from the table C.2.

Table C.2: Orientation of relevant intraband transition for two-photon absorption.

	$ u_{cb}\rangle$	$ u_{hh}\rangle$	$ u_{lh}\rangle$	$ u_{so}\rangle$
$\langle u_{cb} $	x,y	x,y	x,y,z	x,y,z
$\langle u_{hh} $	x,y	x,y	x,y,z	x,y,z
$\langle u_{lh} $	x,y,z	x,y,z	x,y	x,y
$\langle u_{so} $	x,y,z	x,y,z	x,y	x,y

The most relevant paths are those where E_m is closest to the energy of the absorbed photon (1,5 eV). Considering the gap size (2,4 eV), this suggests that the hh -band is either initial or intermediate state as shown in Fig. C.1. In both cases, z-polarization is forbidden in at least one of the steps. Several other paths are possible but presumably less likely based on energetic considerations. Some of them imply z-polarization, others do not. The highest probability for TPA paths and thus the highest contribution to the orientation is found for paths that involve either cb - cb or hh - cb transitions, both of which are forbidden for z-polarized light due to the particular symmetry of zinc-blende nano-platelets.

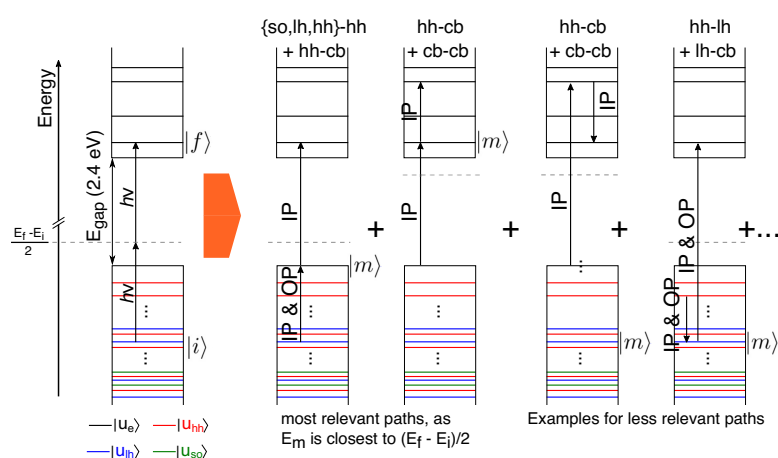


Figure C.1: TPA excitation and its decomposition into possible transitions. Two-photon excitation from an initial state $|i\rangle$ to a final state $|f\rangle$ takes place through a virtual non-resonant state. The efficiency of this process is proportional to the sum of perturbational terms involving all possible intermediate states $|m\rangle$. In this connection, the transitions close to the $(E_f - E_i)/2$ and thus close to the bandgap energy have the highest probability. These contributions can further be analyzed in terms of their optical orientation (IP and OP), which directly relates to the polarization of the excitation. It should be noted that the displayed path are only examples of all the contributing linear combinations.

Bibliography

1. Walls, J. & Smith, R. Surface science techniques. *Vacuum* **45**, 649–652 (1994).
2. Desjonquères, M.-C. & Spanjaard, D. Concepts in surface science. *Springer Ser. Surf. Sci* **40** (1995).
3. Lüth, H. *Solid Surfaces, Interfaces and Thin Films* (Springer Berlin Heidelberg, 2010).
4. Castner, D. G. & Ratner, B. D. Biomedical surface science: Foundations to frontiers. *Surface Science* **500**, 28–60 (2002).
5. Prutton, M. Introduction to surface physics. *Clarendon Press* (1994).
6. Chen, J., Li, Z., Yue, S. & Gong, Q. Ultracompact surface-plasmon-polariton splitter based on modulations of quasicylindrical waves to the total field. *Journal of Applied Physics* **109** (2011).
7. Bubert, H. *et al. Surface and Thin-Film Analysis* (Wiley Online Library, 2002).
8. Pendry, J. *Low Energy Electron Diffraction: the Theory and its Application to Determination of Surface Structure* Academic Press, London and New York. 1974.
9. Seah, M. P. & Dench, W. A. Quantitative electron spectroscopy of surfaces: A standard data base for electron inelastic mean free paths in solids. *Surface and Interface Analysis* **1**, 2–11 (1979).
10. Sherwood, P., Briggs, D & Seah, M. Practical surface analysis. *Auger and X-ray Photoelectron Spectroscopy* **1**, 555 (1990).
11. Carette, J. D. *et al. Electron spectroscopy for surface analysis* (Springer Science & Business Media, 2012).
12. Dürig, U., Pohl, D. W. & Rohner, F. Near-field optical-scanning microscopy. *Journal of Applied Physics* **59**, 3318–3327 (1986).
13. Heinzlmann, H. & Pohl, D. W. Scanning near-field optical microscopy. *Applied Physics A Solids and Surfaces* **59**, 89–101 (1994).

BIBLIOGRAPHY

14. Hecht, B. *et al.* Scanning near-field optical microscopy with aperture probes: Fundamentals and applications. *The Journal of Chemical Physics* **112**, 7761–7774 (2000).
15. Wagner, C. D. & Muilenberg, G. *Handbook of X-ray photoelectron spectroscopy* (Perkin-Elmer, 1979).
16. Van Grieken, R. & Markowicz, A. *Handbook of X-ray Spectrometry* (CRC Press, 2001).
17. Holy, V., Baumbach, T. & Pietsch, U. *High-Resolution X-Ray Scattering from Thin Films and Multilayers* (Springer Berlin Heidelberg, 1999).
18. Shen & Y.R. *Principles of nonlinear optics* Wiley-Interscience, New York. 1984.
19. Azzam, R. M. & Bashara, N. M. *Ellipsometry and polarized light* (North-Holland. sole distributors for the USA and Canada, Elsevier Science Publishing Co., Inc., 1987).
20. Kneipp, K. *et al.* Single Molecule Detection Using Surface-Enhanced Raman Scattering (SERS). *Physical Review Letters* **78**, 1667–1670 (1997).
21. Tompkins, H. G. E. A. I. *Handbook of Ellipsometry* (ed Tompkins, H. G. E. A. I.) 902 (William Andrew, 2005).
22. Vidal, F. & Tadjeddine, A. Sum-frequency generation spectroscopy of interfaces. *Reports on Progress in Physics* **68**, 1095–1127 (2005).
23. Aussenegg, F. R., Leitner, A., Lippitsch, M. E., Reinisch, H. & Riegler, M. Novel aspects of fluorescence lifetime for molecules positioned close to metal surfaces. *Surface Science* **189-190**, 935–945 (1987).
24. Myszka, D. G. & Rich, R. L. Implementing surface plasmon resonance biosensors in drug discovery. *Pharmaceutical Science & Technology Today* **3**, 310–317 (2000).
25. Pozzi, F. *et al.* in *Nanoscience and Cultural Heritage* 161–204 (Atlantis Press, Paris, 2016).
26. Voelker, U. & Betzler, K. Domain morphology from k-space spectroscopy of ferroelectric crystals. *Phys. Rev. B* **74**, 132104(1)–132104(4) (2006).
27. Shankaran, D, Gobi, K & Miura, N. Recent advancements in surface plasmon resonance immunosensors for detection of small molecules of biomedical, food and environmental interest. *Sensors and Actuators B: Chemical* **121**, 158–177 (2007).
28. Homola, J. Surface Plasmon Resonance Sensors for Detection of Chemical and Biological Species. *Chemical Reviews* **108**, 462–493 (2008).

29. Grosse, N. B., Heckmann, J. & Woggon, U. Nonlinear plasmon-photon interaction resolved by k-space spectroscopy. *Physical Review Letters* **108** (2012).
30. Heckmann, J., Kleemann, M.-E., Grosse, N. B. & Woggon, U. The dual annihilation of a surface plasmon and a photon by virtue of a three-wave mixing interaction. *Optics express* **21**, 28856–61 (2013).
31. Kolin, D. L., Ronis, D. & Wiseman, P. W. k-Space Image Correlation Spectroscopy: A Method for Accurate Transport Measurements Independent of Fluorophore Photophysics. *Biophysical Journal* **91**, 3061–3075 (2006).
32. Raether, H. in *Surface Plasmons on Smooth and Rough Surfaces and on Gratings* 4–39 (Springer Berlin Heidelberg, 1988).
33. Maier, S. A. *Plasmonics: fundamentals and applications* (Springer Science & Business Media, 2007).
34. Dornhaus, R., Benner, R. E., Chang, R. K. & Chabay, I. Surface plasmon contribution to SERS. *Surface Science* **101**, 367–373 (1980).
35. Homola, J., Yee, S. S. & Gauglitz, G. Surface plasmon resonance sensors: review. *Sensors and Actuators B: Chemical* **54**, 3–15 (1999).
36. Dawson, P., Puygranier, B. A. F. & Goudonnet, J.-P. Surface plasmon polariton propagation length: A direct comparison using photon scanning tunneling microscopy and attenuated total reflection. *Physical Review B* **63**, 205410 (2001).
37. Borejdo, J., Calander, N., Gryczynski, Z & Gryczynski, I. Fluorescence correlation spectroscopy in surface plasmon coupled emission microscope. *Optics express* **14**, 7878–7888 (2006).
38. Catchpole, K. R. & Polman, A. Plasmonic solar cells. *Optics express* **16**, 21793–800 (2008).
39. Pala, R. A., White, J., Barnard, E., Liu, J. & Brongersma, M. L. Design of plasmonic thin-film solar cells with broadband absorption enhancements. *Advanced Materials* **21**, 3504–3509 (2009).
40. Vala, M., Chadt, K., Piliarik, M. & Homola, J. High-performance compact SPR sensor for multi-analyte sensing. *Sensors and Actuators, B: Chemical* **148**, 544–549 (2010).
41. Atwater, H. A. & Polman, A. Plasmonics for improved photovoltaic devices. *Nat. Mater.* **9**, 865–865 (2010).
42. Shen, H. & Maes, B. Combined plasmonic gratings in organic solar cells. *Optics Express* **19**, A1202 (2011).

BIBLIOGRAPHY

43. Munday, J. N. & Atwater, H. A. Large integrated absorption enhancement in plasmonic solar cells by combining metallic gratings and antireflection coatings. *Nano Letters* **11**, 2195–2201 (2011).
44. Green, M. A. & Pillai, S. Harnessing plasmonics for solar cells. *Nature Photonics* **6**, 130–132 (2012).
45. Salomon, A., Gordon, R. J., Prior, Y., Seideman, T. & Sukharev, M. Strong coupling between molecular excited states and surface plasmon modes of a slit array in a thin metal film. *Physical Review Letters* **109**, 1–5 (2012).
46. Palomba, S. *et al.* Optical negative refraction by four-wave mixing in thin metallic nanostructures. *Nature Materials* **11**, 34–38 (2011).
47. Meng, L. *et al.* Optimized grating as an ultra-narrow band absorber or plasmonic sensor. *Optics letters* **39**, 1137–40 (2014).
48. Zhang, X. & Liu, Z. Superlenses to overcome the diffraction limit. *Nature Materials* **7**, 435–441 (2008).
49. Kawata, S., Inouye, Y. & Verma, P. Plasmonics for near-field nano-imaging and superlensing. *Nature Photonics* **3**, 388–394 (2009).
50. Fang, L., Pan, L., Wang, C. & Luo, X. Superlens imaging lithography for high aspect ratio sub-wavelength pattern employing trilayer resist process. *Microelectronic Engineering* **110**, 35–39 (2013).
51. Gallinet, B., Siegfried, T., Sigg, H., Nordlander, P. & Martin, O. J. F. Plasmonic Radiance: Probing Structure at the Angstrom Scale with Visible Light. *Nano Letters* **13**, 497–503 (2013).
52. Fan, W., Lawrie, B. J. & Pooser, R. C. Quantum plasmonic sensing. *Physical Review A - Atomic, Molecular, and Optical Physics* **92**, 1–5 (2015).
53. Kretschmann, E. & Raether, H. Notizen: Radiative Decay of Non Radiative Surface Plasmons Excited by Light. *Zeitschrift für Naturforschung A* **23**, 2135–2136 (1968).
54. Otto, A. Excitation of nonradiative surface plasma waves in silver by the method of frustrated total reflection. *Zeitschrift für Physik* **216**, 398–410 (1968).
55. Arakawa, E. T., Williams, M. W., Hamm, R. N. & Ritchie, R. H. Effect of Damping on Surface Plasmon Dispersion. *Physical Review Letters* **31**, 1127–1129 (1973).
56. Ferguson, P., Wallis, R. F., Belakhovsky, M., Jadot, J. P. & Tomkinson, J. Surface plasma waves in silver and gold. *Surface Science* **76**, 483–498 (1978).

57. Pollard, R. J., Bradberry, G. W. & Sambles, J. R. A STUDY OF THE THIN METAL FILM/FLUID INTERFACE USING SURFACE PLASMON-POLARITONS. *Physics* **63**, 803–806 (1987).
58. Fukui, M. & Oda, K. STUDIES ON METAL FILM GROWTH THROUGH INSTANTANEOUSLY OBSERVED ATTENUATED TOTAL REFLECTION SPECTRA. *Applied Surface Science* **34**, 882–889 (1988).
59. Rothenhäusler, B. & Knoll, W. Surface-plasmon microscopy. *Nature* **332**, 615–617 (1988).
60. Barnes, W. L., Dereux, A. & Ebbesen, T. W. Surface plasmons subwavelength optics. *Nature* **424**, 824–830 (2003).
61. Cheng, Z. *et al.* Plain silver surface plasmon resonance for microarray application. *Analytical Chemistry* **87**, 1466–1469 (2015).
62. Nielsen, M. P. *et al.* Adiabatic Nanofocusing in Hybrid Gap Plasmon Waveguides on the Silicon-on-Insulator Platform. *Nano Letters* **16**, 1410–1414 (2016).
63. Nie, S. Probing Single Molecules and Single Nanoparticles by Surface-Enhanced Raman Scattering. *Science* **275**, 1102–1106 (1997).
64. Altewischer, E., van Exter, M. P. & Woerdman, J. P. Plasmon-assisted transmission of entangled photons. *Nature* **418**, 304–306 (2002).
65. Palomba, S. & Novotny, L. Nonlinear Excitation of Surface Plasmon Polaritons by Four-Wave Mixing. *Physical Review Letters* **101**, 056802 (2008).
66. Renger, J., Quidant, R., van Hulst, N. & Novotny, L. Surface-Enhanced Nonlinear Four-Wave Mixing. *Physical Review Letters* **104**, 046803 (2010).
67. Kauranen, M. & Zayats, A. V. Nonlinear plasmonics. *Nature Photonics* **6**, 737–748 (2012).
68. Mesch, M., Metzger, B., Hentschel, M. & Giessen, H. Nonlinear Plasmonic Sensing. *Nano Letters* **16**, 3155–3159 (2016).
69. Naraoka, R., Okawa, H., Hashimoto, K. & Kajikawa, K. Surface plasmon resonance enhanced second-harmonic generation in Kretschmann configuration. *Optics Communications* **248**, 249–256 (2005).
70. Bloembergen, N. & Pershan, P. S. Light Waves at the Boundary of Nonlinear Media. *Physical Review* **128**, 606–622 (1962).

BIBLIOGRAPHY

71. Bloembergen, N., Chang, R. K., Jha, S. S. & Lee, C. H. Optical Second-Harmonic Generation in Reflection from Media with Inversion Symmetry. *Physical Review* **174**, 813–822 (1968).
72. Simon, H. J., Mitchell, D. E. & Watson, J. G. Optical Second-harmonic Generation with Surface Plasmons in Silver films. *Physical Review Letters* **33**, 1531–1534 (1974).
73. Sipe, J. E., So, V. C. Y., Fukui, M. & Stegeman, G. I. Analysis of second-harmonic generation at metal surfaces. *Physical Review B* **21**, 4389 (1980).
74. Rudnick, J. & Stern, E. A. Second-harmonic radiation from metal surfaces. *Physical Review B* **4**, 4274–4290 (1971).
75. Economou, E. N. Surface Plasmons in Thin Films. *Physical Review* **182**, 539–554 (1969).
76. Yang, F., Sambles, J. R. & Bradberry, G. W. Long-range surface modes supported by thin films. *Phys Rev B* **44** (1991).
77. Sellai, A. & Elzain, M. Characteristics of a dielectric-metal-dielectric plasmonic waveguide. *Physica E: Low-Dimensional Systems and Nanostructures* **41**, 106–109 (2008).
78. Giannini, V, Zhang, Y, Forcales, M & Rivas, J. G. Long-range surface polaritons in ultra-thin films of silicon. *Optics express* **16**, 19674–85 (2008).
79. Berini, P. Long-range surface plasmon polaritons. *Advances in Optics and Photonics* **1**, 484 (2009).
80. Sarid, D. Long-Range Surface-Plasma Waves on Very Thin Metal Films. *Physical Review Letters* **47**, 1927–1930 (1981).
81. Takahara, J, Yamagishi, S, Taki, H, Morimoto, A & Kobayashi, T. Guiding of a one-dimensional optical beam with nanometer diameter. *Optics letters* **22**, 475–477 (1997).
82. Kovacs, G. J. & Scott, G. D. Optical excitation of surface plasma waves in layered media. *Physical Review B* **16**, 1297–1311 (1977).
83. Burke, J. J., Stegeman, G. I. & Tamir, T. Surface-polariton-like waves guided by thin, lossy metal films. *Physical Review B* **33**, 5186–5201 (1986).
84. Yang, F., Sambles, J. R. & Bradberry, G. W. Long-range coupled surface exciton polaritons. *Physical Review Letters* **64**, 559–562 (1990).
85. Bloom, D. M., Yardley, J. T., Young, J. F. & Harris, S. E. Infrared up-conversion with resonantly two-photon pumped metal vapors. *Applied Physics Letters* **24**, 427–428 (1974).

86. Lenac, Z & Tomas, M. S. ATTENUATION OF LONG-RANGE SURFACE POLARITONS IN A THIN METALLIC SLAB WITH A DIELECTRIC COATING. *Surface Science* **154**, 639–657 (1985).
87. Yang, F., Bradberry, G. W. & Sambles, J. R. Long-range surface mode supported by very thin silver films. *Physical Review Letters* **66**, 2030–2032 (1991).
88. Negm, S. & Talaat, H. Radiative and non-radiative decay of surface plasmons in thin metal films. *Solid State Communications* **84**, 133–137 (1992).
89. Norrman, A., Setälä, T. & Friberg, A. T. Long-range higher-order surface-plasmon polaritons. *Physical Review A - Atomic, Molecular, and Optical Physics* **90**, 1–8 (2014).
90. Stegeman, G. I., Burke, J. J. & Hall, D. G. Nonlinear optics of long range surface plasmons. *Applied Physics Letters* **41**, 906–908 (1982).
91. Reinisch, R. & Neviere, M. Guided-wave resonance and enhanced nonlinear-optical effects. *Phys Rev B* **26**, 5987–5988 (1982).
92. Quail, J., Rako, J. & Simon, H. Optical second-harmonic generation with long-range surface plasmons. *Physical review letters* **50**, 1987–1989 (1983).
93. West, J. L. & Halas, N. J. Engineered Nanomaterials for Biophotonics Applications: Improving Sensing, Imaging, and Therapeutics. *Annual Review of Biomedical Engineering* **5**, 285–292 (2003).
94. Caruge, J. M., Halpert, J. E., Wood, V., Bulović, V. & Bawendi, M. G. Colloidal quantum-dot light-emitting diodes with metal-oxide charge transport layers. *Nature Photonics* **2**, 247–250 (2008).
95. Rajesh, Ahuja, T. & Kumar, D. Recent progress in the development of nano-structured conducting polymers/nanocomposites for sensor applications. *Sensors and Actuators B: Chemical* **136**, 275–286 (2009).
96. Joo, J., Son, J. S., Kwon, S. G., Yu, J. H. & Hyeon, T. Low-Temperature Solution-Phase Synthesis of Quantum Well Structured CdSe Nanoribbons. *Journal of the American Chemical Society* **128**, 5632–5633 (2006).
97. Ithurria, S. & Dubertret, B. Quasi 2D Colloidal CdSe Platelets with Thicknesses Controlled at the Atomic Level. *Journal of the American Chemical Society* **130**, 16504–16505 (2008).
98. Achtstein, A. W. *et al.* Electronic Structure and Exciton–Phonon Interaction in Two-Dimensional Colloidal CdSe Nanosheets. *Nano Letters* **12**, 3151–3157 (2012).

BIBLIOGRAPHY

99. Wang, Z. *et al.* Unidirectional launching of surface plasmons with subwavelength metallic gratings around the plasmonic critical angle. *Applied Physics Letters* **101** (2012).
100. Kaasbjerg, K., Thygesen, K. S. & Jacobsen, K. W. Phonon-limited mobility in *n*-type single-layer MoS₂ from first principles. *Phys. Rev. B* **85**, 115317 (11 2012).
101. Perera, M. M. *et al.* Improved Carrier Mobility in Few-Layer MoS₂ Field-Effect Transistors with Ionic-Liquid Gating. *ACS Nano* **7**, 4449–4458 (2013).
102. Naeem, A. *et al.* Giant exciton oscillator strength and radiatively limited dephasing in two-dimensional platelets. *Phys. Rev. B* **91**, 121302 (12 2015).
103. Scott, R. *et al.* Two Photon Absorption in II–VI Semiconductors: The Influence of Dimensionality and Size. *Nano Letters* **15**, 4985–4992 (2015).
104. C. Poellmann, C. *et al.* Resonant internal quantum transitions and femtosecond radiative decay of excitons in monolayer WSe₂. *Nat. Mat.* **14**, 889 (2016).
105. Wang, H. *et al.* Radiative lifetimes of excitons and trions in monolayers of the metal dichalcogenide MoS₂. *Phys. Rev. B* **93**, 045407 (4 2016).
106. Cheiwchanamngij, T. & Lambrecht, W. R. L. Quasiparticle band structure calculation of monolayer, bilayer, and bulk MoS₂. *Phys. Rev. B* **85**, 205302 (20 2012).
107. Chernikov, A. *et al.* Exciton Binding Energy and Nonhydrogenic Rydberg Series in Monolayer WS₂. *Phys. Rev. Lett.* **113**, 076802 (2014).
108. Achtstein, A. W. *et al.* p-State Luminescence in CdSe Nanoplatelets: Role of Lateral Confinement and a Longitudinal Optical Phonon Bottleneck. *Physical Review Letters* **116** (2016).
109. Lieb, E. H. in *Condensed Matter Physics and Exactly Soluble Models* 473–474 (Springer Nature, 2004).
110. Novotny, L. & Hecht, B. *Principles of Nano-Optics* (Cambridge University Press (CUP), Cambridge, 2006).
111. Pellant, I. & Valenta, J. *Luminescence Spectroscopy of Semiconductors* (Oxford, 2012).
112. Empedocles, S., Neuhauser, R. & Bawendi, M. Three-dimensional orientation measurements of symmetric single chromophores using polarization microscopy. *Nature* **399**, 126–130 (1999).
113. Koberling, F. *et al.* Fluorescence Anisotropy and Crystal Structure of Individual Semiconductor Nanocrystals. *J. Phys. Chem. B* **107**, 7463 (2003).

114. Pukhov, K. K., Basiev, T. T. & Orlovskii, Y. V. Spontaneous emission in dielectric nanoparticles. *JETP Letters* **88**, 12–18 (2008).
115. Cunningham, P. D., Boercker, J. E., Placencia, D. & Tischler, J. G. Anisotropic Absorption in PbSe Nanorods. *ACS Nano* **8**, 581–590 (2014).
116. Lakowicz, J. R., Malicka, J., Gryczynski, I. & Gryczynski, Z. Directional surface plasmon-coupled emission: A new method for high sensitivity detection. *Biochemical and Biophysical Research Communications* **307**, 435–439 (2003).
117. Nomura, W., Ohtsu, M. & Yatsui, T. Nanodot coupler with a surface plasmon polariton condenser for optical far/near-field conversion. *Applied Physics Letters* **86**, 1–3 (2005).
118. Neal, T., Okamoto, K. & Scherer, A. Surface plasmon enhanced emission from dye doped polymer layers. *Optics express* **13**, 5522–5527 (2005).
119. Mertens, H., Biteen, J. S., Atwater, H. A. & Polman, A. Polarization-Selective Plasmon-Enhanced Silicon Quantum-Dot Luminescence. *Nano Letters* **6**, 2622–2625 (2006).
120. Akimov, a. V. *et al.* Generation of single optical plasmons in metallic nanowires coupled to quantum dots. *Nature* **450**, 402–406 (2007).
121. Ming, T. *et al.* Experimental evidence of plasmaphores: Plasmon-directed polarized emission from gold nanorod - Fluorophore hybrid nanostructures. *Nano Letters* **11**, 2296–2303 (2011).
122. Su, H., Zhong, Y., Ming, T., Wang, J. & Wong, K. S. Extraordinary Surface Plasmon Coupled Emission Using Core / Shell Gold Nanorods. *The Journal of Physical Chemistry C* **116**, 6–11 (2012).
123. Manjavacas, A., Abajo, F. J. G. D. & Nordlander, P. Quantum plexcitonics: Strongly interacting plasmons and excitons. *Nano Letters* **11**, 2318–2323 (2011).
124. Vasa, P. *et al.* Optical stark effects in J-aggregate-metal hybrid nanostructures exhibiting a strong exciton-surface-plasmon-polariton interaction. *Physical Review Letters* **114**, 1–6 (2015).
125. Pockrand, I., Swalen, J. D., Santo, R., Brillante, a. & Philpott, M. R. Optical properties of organic dye monolayers by surface plasmon spectroscopy. *The Journal of Chemical Physics* **69**, 4001 (1978).
126. Biteen, J. S., Lewis, N. S., Atwater, H. A., Mertens, H. & Polman, A. Spectral tuning of plasmon-enhanced silicon quantum dot luminescence. *Applied Physics Letters* **88**, 1–4 (2006).

BIBLIOGRAPHY

127. Standridge, S. D., Schatz, G. C. & Hupp, J. T. Distance dependence of plasmon-enhanced photocurrent in dye-sensitized solar cells. *Journal of the American Chemical Society* **131**, 8407–8409 (2009).
128. Pasqualotto, E. *et al.* Plasmonic platforms for innovative surface plasmon resonance configuration with sensing applications. *Microelectronic Engineering* **111**, 48–353 (2013).
129. He, R.-Y. *et al.* Surface plasmon-enhanced two-photon fluorescence microscopy for live cell membrane imaging. *Optics Express* **17**, 5987–5997 (2009).
130. Moh, K. J., Yuan, X.-C., Bu, J., Zhu, S. W. & Gao, B. Z. Radial polarization induced surface plasmon virtual probe for two-photon fluorescence microscopy. *Optics Letters* **34**, 971–973 (2009).
131. Lin, C.-Y. *et al.* Surface plasmon-enhanced and quenched two-photon excited fluorescence. *Optics express* **18**, 12807–17 (2010).
132. Wissert, M. D., Ilin, K. S., Siegel, M., Lemmer, U. & Eisler, H. J. Coupled nanoantenna plasmon resonance spectra from two-photon laser excitation. *Nano Letters* **10**, 4161–4165 (2010).
133. Chiu, K.-C., Lin, C.-Y., Dong, C. Y. & Chen, S.-J. Optimizing silver film for surface plasmon-coupled emission induced two-photon excited fluorescence imaging. *Optics express* **19**, 5386–96 (2011).
134. Li, Y. *et al.* Two-surface-plasmon-polariton-absorption based nanolithography. *Applied Physics Letters* **102**, 2011–2015 (2013).
135. Zenneck, J. Über die Fortpflanzung ebener elektromagnetischer Wellen längs einer ebenen Leiterfläche und ihre Beziehung zur drahtlosen Telegraphie. *Annalen der Physik* **328**, 846–866 (1907).
136. Sommerfeld, A. Über die Ausbreitung der Wellen in der drahtlosen Telegraphie. *Annalen der Physik* **333**, 665–736 (1909).
137. Ritchie, R., Arakawa, E., Cowan, J. & Hamm, R. Surface-Plasmon Resonance Effect in Grating Diffraction. *Physical Review Letters* **21**, 1530–1533 (1968).
138. Gaylord, T. & Moharam, M. Analysis and applications of optical diffraction by gratings. *Proceedings of the IEEE* **73**, 894–937 (1985).
139. Vanlabekke, D., Baida, F. & Vigoureux, J. A Theoretical Study of Near Field Detection and Excitation of Surface Plasmons. *Ultramicroscopy* **71**, 351–359 (1998).

140. Homola, J., Koudela, I. & Yee, S. S. Surface plasmon resonance sensors based on diffraction gratings and prism couplers: sensitivity comparison. *Sensors and Actuators, B: Chemical* **54**, 16–24 (1999).
141. Temnov, V. V. *et al.* Femtosecond nonlinear ultrasonics in gold probed with ultrashort surface plasmons. *Nature Communications* **4**, 1468 (2013).
142. Razdolski, I. *et al.* Nonlinear Surface Magnetoplasmonics in Kretschmann Multilayers. *ACS Photonics* **3**, 179–183 (2016).
143. Jackson, J. D. *Electrodynamics* (Wiley Online Library, 1975).
144. Simon, H. J., Mitchell, D. E. & Watson, J. G. Surface plasmons in silver films—a novel undergraduate experiment. *American Journal of Physics* **43**, 630–636 (1975).
145. Fabry, C. & Perot, A. Theorie et applications d' une nouvelle methode de spectroscopie interferentielle. *Ann. Chim. Phys* **16**, 115 (1899).
146. Johnson, P. B. & Christy, R. W. Optical Constants of the Noble Metals. *Physical Review B* **6**, 4370–4379 (1972).
147. Sipe, J. E. The ATR spectra of multipole surface plasmons. *Surface Science* **84**, 75–105 (1979).
148. Sipe, J. E. Bulk-selvedge coupling theory for the optical properties of surfaces. *Physical Review B* **22**, 1589 (1980).
149. Schaich, W. L. & Mendoza, B. Simple model of second-harmonic generation. *Physical Review B* **45**, 14279–14292 (1992).
150. Jensen, H. R., Raymond, R. & Coutaz, J. L. Hydrodynamic study of surface plasmon enhanced non-local second-harmonic generation. *Appl. Phys. B* **64**, 57–63 (1997).
151. Tzeng, C. & Lue, J. Nonlinear optical generation from noble metals and aluminum films in various geometric configurations. *Phys. Rev. A* **39**, 191–196 (1989).
152. Wang, F. X. *et al.* Surface and bulk contributions to the second-order nonlinear optical response of a gold film. *Physical Review B* **80**, 4–7 (2009).
153. Wang, C.-Y. *et al.* Giant colloidal silver crystals for low-loss linear and nonlinear plasmonics. *Nature Communications* **6**, 7734 (2015).
154. Boyd, R. W. nonlinear susceptibility of composite optical materials Maxwell garnet model.pdf. **46** (1992).
155. Shen, Y. Surfaces probed by nonlinear optics. *Surface Science* **299**, 551–562 (1994).

BIBLIOGRAPHY

156. Kolthammer, W. S. *et al.* Harmonic generation in thin films and multilayers. *Physical Review B - Condensed Matter and Materials Physics* **72**, 1–15 (2005).
157. Gielis, J. J. H., Gevers, P. M., Aarts, I. M. P., van de Sanden, M. C. M. & Kessels, W. M. M. Optical second-harmonic generation in thin film systems. *Journal of Vacuum Science & Technology A: Vacuum, Surfaces, and Films* **26**, 1519 (2008).
158. Kovacs, G. J. Surface polariton in the ATR angular spectra of a thin iron film bounded by dielectric layers. *Journal of the Optical Society of America* **68**, 1325 (1978).
159. Bryan-Brown, G., Elston, S. & Sambles, J. Coupled surface excitations on palladium-coated gratings. *Thin Solid Films* **207**, 252–257 (1992).
160. Albuquerque, E. L. & Fulco, P. Far-Infrared ATR from Surface Exciton Polaritons. *physica status solidi (b)* **182**, 357–364 (1994).
161. Wu, Z.-C., Arakawa, E. T., Inagaki, T., Thundat, T. & Schowalter, L. J. Experimental observations of a long-range surface mode in metal island films. *Physical Review B* **49**, 7782–7785 (1994).
162. Wood, E., Sambles, J., Pudonin, F. & Yakovlev, V. Degenerate long range surface modes, supported on thin nickel films. *Optics Communications* **132**, 212–216 (1996).
163. Yang, F. & Sambles, J. R. Determination of the optical permittivity and thickness of absorbing films using long range modes. *Journal of Modern Optics* **44**, 1155–1163 (1997).
164. Soller, B. J. & Hall, D. G. Direct observation of a propagating, planar-waveguide surface mode in a discontinuous film of metal nanoparticles. *Optics Letters* **25**, 1071 (2000).
165. Arnold, C., Zhang, Y. & Rivas, J. G. Long range surface polaritons supported by lossy thin films. *Applied Physics Letters* **96**, 113108 (2010).
166. Arnold, C., Zhang, Y. & Rivas, J. G. Modified light emission from emitters coupled to long-range guided modes in strongly absorbing layers. *Optics Express* **20**, 27554 (2012).
167. Lidorikis, E., Busch, K., Li, Q., Chan, C. T. & Soukoulis, C. M. Optical nonlinear response of a single nonlinear dielectric layer sandwiched between two linear dielectric structures. *Physical Review B* **56**, 15090–15099 (1997).
168. Boyd, R. W. *Nonlinear optics* 613 (Academic Press, 2008).

169. Rakić, A. D., Djurišić, A. B., Elazar, J. M. & Majewski, M. L. Optical properties of metallic films for vertical-cavity optoelectronic devices. *Applied Optics* **37**, 5271 (1998).
170. Werner, W. S. M., Glantschnig, K. & Ambrosch-Draxl, C. Optical Constants and Inelastic Electron-Scattering Data for 17 Elemental Metals. *Journal of Physical and Chemical Reference Data* **38**, 1013–1092 (2009).
171. Leonard, S. W. *et al.* Tunable two-dimensional photonic crystals using liquid crystal infiltration. *Physical Review B* **61**, R2389–R2392 (2000).
172. Asatryan, A. A. *et al.* Two-dimensional local density of states in two-dimensional photonic crystals. *Optics Express* **8**, 191 (2001).
173. Scott, R. *et al.* Time-Resolved Stark Spectroscopy in CdSe Nanoplatelets: Exciton Binding Energy, Polarizability, and Field-Dependent Radiative Rates. *Nano Letters* **16**, 6576–6583 (2016).
174. Schuller, J. A. *et al.* Orientation of luminescent excitons in layered nanomaterials. *Nature Nanotechnology* **8**, 271–276 (2013).
175. Basu, B. K. *Theory of Optical Processes in Semiconductors* (Oxford University Press, 1997).
176. Achtstein, A. W. *et al.* Linear Absorption in CdSe Nanoplates: Thickness and Lateral Size Dependency of the Intrinsic Absorption. *The Journal of Physical Chemistry C* **119**, 20156–20161 (2015).
177. Sihvola, A. & Kong, J. Effective permittivity of dielectric mixtures. *IEEE Transactions on Geoscience and Remote Sensing* **26**, 420–429 (1988).
178. Loudon, R. *The Quantum Theory of Light* 3rd ed. (Oxford Univ. Press, 2000).
179. Taminiau, T. H., Karaveli, S., van Hulst, N. F. & Zia, R. Quantifying the magnetic nature of light emission. *Nature Communications* **3**, 979 (2012).
180. The Merck Index- An Encyclopedia of Chemicals, White House Station NY, 2006. <https://www.rsc.org/Merck-Index>.
181. Dolgaleva, K. & Boyd, R. W. Local-field effects in nanostructured photonic materials. *Advances in Optics and Photonics* **4**, 1 (2012).
182. She, C. *et al.* Low-Threshold Stimulated Emission Using Colloidal Quantum Wells. *Nano Letters* **14**, 2772–2777 (2014).

BIBLIOGRAPHY

183. Chou, K.-L., Won, N., Kwag, J., Kim, S. & Chen, J.-Y. Femto-second laser beam with a low power density achieved a two-photon photodynamic cancer therapy with quantum dots. *Journal of Materials Chemistry B* **1**, 4584 (2013).
184. Wang, F., Banerjee, D., Liu, Y., Chen, X. & Liu, X. Upconversion nanoparticles in biological labeling, imaging, and therapy. *The Analyst* **135**, 1839–54 (Aug. 2010).
185. Mahr, H, Rabin, H & Tang, C. Two-photon absorption spectroscopy. *Quantum electronics: A treatise*. **1**, 285–361 (1975).
186. Wu, E.-S., Strickler, J. H., Harrell, W. R. & Webb, W. W. *Two-photon lithography for microelectronic application* in *Optical/Laser Microlithography V* (ed Cuthbert, J. D.) (SPIE-Intl Soc Optical Eng, 1992).
187. Cumpston, B. H. *et al.* Two-photon polymerization initiators for three-dimensional optical data storage and microfabrication. *Nature* **398**, 51–54 (1999).
188. Petryayeva, E., Algar, W. R. & Medintz, I. L. Quantum dots in bioanalysis: a review of applications across various platforms for fluorescence spectroscopy and imaging. *Applied spectroscopy* **67**, 215–52 (Mar. 2013).
189. Biju, V., Itoh, T., Anas, A., Sujith, A. & Ishikawa, M. Semiconductor quantum dots and metal nanoparticles: syntheses, optical properties, and biological applications. *Analytical and bioanalytical chemistry* **391**, 2469–95 (Aug. 2008).
190. Achtstein, A. W., Hennig, J., Prudnikau, A., Artemyev, M. V. & Woggon, U. Linear and Two-Photon Absorption in Zero- and One-Dimensional CdS Nanocrystals: Influence of Size and Shape. *The Journal of Physical Chemistry C* **117**, 25756–25760 (2013).
191. Makarov, N. S., Campo, J., Hales, J. M. & Perry, J. W. Rapid, broadband two-photon-excited fluorescence spectroscopy and its application to red-emitting secondary reference compounds. *Optical Materials Express* **1**, 551 (2011).
192. Li, Z. & Peng, X. Size/Shape-Controlled Synthesis of Colloidal CdSe Quantum Disks: Ligand and Temperature Effects. *J. Am. Chem. Soc.* **133**, 6578–6586 (2011).
193. Gryczynski, I., Gryczynski, Z. & Lakowicz, J. R. Two-Photon Excitation by the Evanescent Wave from Total Internal Reflectio. *Analytical Biochemistry* **76**, 69–76 (1997).
194. Achtstein, A. W. *et al.* Electroabsorption by 0D, 1D, and 2D Nanocrystals: A Comparative Study of CdSe Colloidal Quantum Dots, Nanorods, and Nanoplatelets. *ACS Nano* **8**, 7678–7686 (2014).

195. Van de Hulst, H. C. *Light Scattering by Small Particles* (Dover Publications: New York, 1981).
196. Ninomiya, S. & Adachi, S. Optical properties of cubic and hexagonal CdSe. *J. Appl. Phys.* **78**, 4681 (1995).
197. Rowland, C. E. *et al.* Picosecond energy transfer and multiexciton transfer outpaces Auger recombination in binary CdSe nanoplatelet solids. *Nature Materials* **14**, 484–489 (2015).
198. Disch, S. *The spin structure of magnetic nanoparticles and in magnetic nanostructures* ISBN 978-3-89336-704-7 (Forschungszentrum Jülich GmbH, 2010).
199. Hens, Z. & Moreels, I. Light absorption by colloidal semiconductor quantum dots. *J. Mater. Chem.* **22**, 10406–10415 (21 2012).
200. Adachi, S. *HANDBOOK ON PHYSICAL PROPERTIES OF SEMICONDUCTORS* (Kluwer Academic Publishers, Boston, 2004).
201. Ithurria, S. *et al.* Colloidal nanoplatelets with two-dimensional electronic structure. *Nat. Mater.* **10**, 936–941 (Dec. 2011).
202. Yu, P. & Cardona, M. *Fundamentals of Semiconductors* (Springer, Berlin, 1996).

List of Figures

1.1	<i>k</i> -space spectroscopy excitation and detection scheme	3
1.2	Illustration of surfaces waves	5
1.3	Absorption and emission characteristics of oriented NPs	7
1.4	Experimental setup for <i>k</i> -space spectroscopy	10
2.1	Geometry of a surface wave, that is confined to the interface between a metal and a dielectric	13
2.2	AFM image and SP dispersion relation from a thermally evaporated gold film	14
2.3	Excitation scheme for the Otto and the Kretschmann configuration	15
2.4	Calculated reflected intensities as a function of wavelength and incident angle for the Otto and the Kretschmann configuration	18
2.5	Experimental Setup for linear measurements with white-light excitation	19
2.6	White-light reflection measurements for varying coupling layer thickness in the Otto and the Kretschmann configuration	20
2.7	Comparison of coupling efficiencies as a function of wavelength and coupling layer thickness for the Otto and the Kretschmann configuration	21
2.8	Comparison of measured reflected intensities and calculations at 855 nm wavelength for Gaussian beam excitation in the Kretschmann configuration and in the Otto configuration	23
2.9	Measured and calculated coupling efficiency for the Kretschmann configuration and the Otto configuration at 855 nm wavelength	25
3.1	Excitation configurations with position of nonlinear sources	28
3.2	Calculated reflected intensity for a thin film in the Otto configuration	34

LIST OF FIGURES

4.1	Comparison of theory and experimental data for fundamental coupling and second harmonic emission in the Otto and the Kretschmann configuration	37
4.2	SHG yield and fundamental impedance matching in the Otto and Kretschmann configurations	39
4.3	Exemplary calculated SHG for overly large values of the nonlinear parameters $\bar{\delta}'$ and \bar{a}	41
4.4	Absolute harmonic conversion efficiency as a function of the nonlinear parameters \bar{b} and $\bar{\gamma}$	42
4.5	Comparison of the harmonic peak positions for experimental data and theory	43
4.6	Feynman diagrams and nonlinear phase-matching conditions for surface plasmons (p) and photons (f) interacting for SHG	45
4.7	Optical path and CCD image for one-beam excitation in the Kretschmann configuration with a silver sample	47
4.8	Revealing pp - f interaction by analyzing incident and exit angles of second harmonic radiation	48
4.9	Fundamental and second harmonic radiation from a 57 nm silver sample .	49
4.10	Experimental setup for two-beam excitation.	50
4.11	CCD image and nonlinear interactions for two-beam excitation	51
4.12	Resulting SHG-radiation as a function of incident and exit angle for fixed auxiliary beam.	52
4.13	Resulting SHG-radiation as a function of incident and exit angle for variation of the auxiliary beam	55
5.1	Schematic comparison of a surface plasmon polariton and a long-range surface wave	58
5.2	Excitation configuration for long-range surface waves and dielectric functions for Mo, Cr and Au	59
5.3	Real and imaginary parts of the calculated wave-vectors for long-range and short-range modes as a function of film thickness	61
5.4	Calculated reflected intensity from thin molybdenum films as a function of layer thickness	62
5.5	White-light measurements for thin films of chromium and molybdenum at different coupling gap sizes	64
5.6	Reflected intensity and nonlinear yield for thin molybdenum and chromium films and different coupling gaps	65

5.7	Reflected intensity and nonlinear yield for a thin gold films and different coupling gaps	66
5.8	Experimentally obtained propagation lengths for thin molybdenum and chromium films by applying a lorentzian fit	67
5.9	Comparison of linear and nonlinear thin molybdenum film measurements to the hydrodynamic model	68
5.10	Comparison of theoretical calculations for a 19 nm molybdenum film and a 25 nm gold film for varying coupling gaps	70
5.11	Calculation of the driving electric field for a 19 nm molybdenum film with a coupling gap of 660 nm	71
6.1	Experimental setup for confocal investigation of oriented CdSe nano-platelets	75
6.2	Polarization dependent in-plane and out-of-plane transition dipole contributions to radiative emission for nano-platelets and quantum dots	77
6.3	Scheme of the k -space coupling geometry for oriented monolayer samples	79
6.4	Simulated 2D k -space spectra of pure in-plane and pure out-of-plane transition dipoles	81
6.5	Comparison of calculated and experimental 2D k -space spectra for nano-platelet and quantum dot samples	83
6.6	Angular dependent excitation and emission of CdSe nano-platelets and spherical quantum dot monolayers	84
6.7	Angular dependent excitation and emission of monolayers of CdSe nano-platelets and spherical quantum dots in s- and p-polarization	85
6.8	Radiation patterns of nano-platelet and quantum dot monolayer ensembles in isotropic media	86
6.9	The contribution of different Bloch states determines the isotropic absorption and anisotropic emission of CdSe nanoplatelets	88
7.1	TPA cross-section and absorption spectrum of NPs	92
7.2	Excitation and emission scheme of oriented NPs	94
7.3	Comparison of linear and TPA excitation of oriented nano-platelets and the related emission patterns	95
7.4	TPA excitation and its decomposition into possible transitions	97
7.5	Excitation and emission scheme of oriented NPs on a thin silver layer	98
7.6	2D k -space analysis of oriented NPs with and without plasmonic layer	99

LIST OF FIGURES

7.7	<i>k</i> -space cuts for excitation and emission of oriented NPs with and without plasmonic layer	100
B.1	PL and Absorption spectra of the nano-platelets (a) and quantum dots (b) used in the <i>k</i> -space spectroscopy	128
B.2	TEM image and size of the CdSe nano-platelets	129
B.3	The contribution of different Bloch states determines the isotropic absorption and anisotropic emission of CdSe nano-platelets	133
C.1	TPA excitation and its decomposition into possible transitions	140